

13 December 2013 | \$10

Science

The Thousand-Year
Graveyard

EDITORIAL

- 1291** Reading the Bones
George J. Armelagos
>> News story p. 1306

NEWS OF THE WEEK

- 1296** A roundup of the week's top stories

NEWS & ANALYSIS

- 1299** Lick Observatory in Trouble as Austerity Starts to Bite
- 1300** New Results Send Mars Rover on a Quest for Ancient Life
>> Science Podcast;
<http://scim.ag/SciCuriosity>
- 1302** Advocates Protest the Cost of a Hepatitis C Cure
- 1303** Fossilized Teeth Offer Mouthful on Ancient Microbiome
- 1304** Cavefish Study Supports Controversial Evolutionary Mechanism
>> Report p. 1372
- 1305** Europe Readies Peerless Star Mapper

NEWS FOCUS

- 1306** The Thousand-Year Graveyard
>> Editorial p. 1291; Multimedia
- 1311** Stefan Behnisch and the Good Client

LETTERS

- 1315** Health Information and the Like
A. Reddi
Response
S. Aral et al.
Setting the Course for a Green Internet
R. Bolla et al.
Finding Best Practices for Fossil Fuel Extraction
J. L. Deichmann and A. Alonso
- 1316** CORRECTIONS AND CLARIFICATIONS

BOOKS ET AL.

- 1319** Complexity and the Arrow of Time
C. H. Lineweaver et al., Eds.,
reviewed by D. W. McShea
- 1320** Tracks and Shadows
H. W. Greene, reviewed by F. Bonier

POLICY FORUMS

- 1321** The Bioethics Commission on Incidental Findings
A. Gutmann
- 1323** What Role for Short-Lived Climate Pollutants in Mitigation Policy?
J. K. Shoemaker et al.

PERSPECTIVES

- 1325** The Hidden Codes That Shape Protein Evolution
R. J. Weatheritt and M. M. Babu
>> Report p. 1367
- 1326** Colloid Science Collides with Liquid Crystals
N. L. Abbott
>> Report p. 1351
- 1327** My Oldest Sister Is a Sea Walnut?
A. Rokas
>> Research Article p. 1336
- 1329** An Enzymatic Route to H₂ Storage
I. A. C. Pereira
>> Report p. 1382
- 1330** Coming to an Airport Near You
A. R. McLean
>> Research Article p. 1337
- 1332** Improving Biologic Drugs via Total Chemical Synthesis
L. C. Hsieh-Wilson and M. E. Griffin
>> Report p. 1357
- 1333** Finding the Right Partner in a 3D Genome
P. P. Rocha et al.
- 1335** Retrospective: Michael Neuberger (1953–2013)
J. E. Sale et al.

CONTENTS continued >>



page 1311



page 1321

ON THE WEB THIS WEEK

>> Science Podcast

Listen to stories on fear-enhanced odor detection, the latest news from the Curiosity mission, and more.

>> Science Digital First

Explore the history of disease in a thousand-year graveyard, in a special multimedia news feature with video, slideshows, and graphics, at www.sciencemag.org.



COVER

Remains of an older woman buried in the mid-1800s at Badia Pozzeveri graveyard in Altopascio, Italy. She is one of several skeletons entombed in lime, probably to quell infection during an epidemic. Archaeologists are currently studying skeletons buried over the course of 1000 years at this site for clues to ancient health and disease. For further information, see pages 1291 and 1306 and a special multimedia package at <http://scim.ag/1000yrgrave>.

Photo: Francesco Coschino

DEPARTMENTS

- 1289** This Week in Science
1292 Editors' Choice
1294 Science Staff
1393 New Products
1394 Science Careers

RESEARCH ARTICLES

- 1336** The Genome of the Ctenophore *Mnemiopsis leidyi* and Its Implications for Cell Type Evolution

J. F. Ryan et al.

Analysis of the genome of the sea walnut reveals insights into the early evolution of the animal kingdom.

Research Article Summary; for full text:

<http://dx.doi.org/10.1126/science.1242592>

>> Perspective p. 1327

- 1337** The Hidden Geometry of Complex, Network-Driven Contagion Phenomena

D. Brockmann and D. Helbing

A model based on effective rather than geographical distance can reveal the origin, timing, and likely spread of epidemics.

>> Perspective p. 1330; Video

REPORTS

- 1343** Detection of a Noble Gas Molecular Ion, $^{36}\text{ArH}^+$, in the Crab Nebula

M. J. Barlow et al.

- 1346** Phosphorus in the Young Supernova Remnant Cassiopeia A

B.-C. Koo et al.

Spectroscopic observations of the remains of stellar explosions confirm that argon-36 and phosphorus are produced in such energetic events.

- 1349** Nondestructive Detection of an Optical Photon

A. Reiserer et al.

An atom in a cavity can be used for the nondestructive detection of optical photons.

- 1351** Effect of Collective Molecular Reorientations on Brownian Motion of Colloids in Nematic Liquid Crystal

T. Turiv et al.

Colloidal particles in a nematic liquid crystal experience anomalous and anisotropic Brownian motion.

>> Perspective p. 1326

- 1354** Detection and Structure of HOON: Microwave Spectroscopy Reveals an O–O Bond Exceeding 1.9 Å

K. N. Crabtree et al.

Spectroscopy reveals an isomer of nitrous acid previously considered too unstable to observe.

- 1357** Erythropoietin Derived by Chemical Synthesis

P. Wang et al.

Chemical synthesis of a glycoprotein hormone provides a sample uniformly substituted with specific sugar chains.

>> Perspective p. 1332

- 1360** The Missing Mountain Water: Slower Westerlies Decrease Orographic Enhancement in the Pacific Northwest USA

C. H. Luce et al.

Weakening westerly winds since 1950 have decreased streamflows across the Pacific Northwest United States.

- 1364** Long-Term Dynamics of Adaptation in Asexual Populations

M. J. Wiser et al.

Even in a constant environment, over 50,000 generations, evolutionary fitness continues to increase in bacterial cultures.

- 1367** Exonic Transcription Factor Binding Directs Codon Choice and Affects Protein Evolution

A. B. Stergachis et al.

Transcription factor binding within protein-coding regions of DNA constrains how the protein can evolve.

>> Perspective p. 1325

- 1372** Cryptic Variation in Morphological Evolution: HSP90 as a Capacitor for Loss of Eyes in Cavefish

N. Rohner et al.

Preexisting but “hidden” variations in eye size provide a substrate for natural selection in fish reared in the dark.

>> News story p. 1304

- 1375** Progressive Specification Rather than Intercalation of Segments During Limb Regeneration

K. Roensch et al.

Salamanders regenerate limb segments using the same molecular hierarchy observed in development.

- 1379** EMRE Is an Essential Component of the Mitochondrial Calcium Uniporter Complex

Y. Sancak et al.

A final but essential protein component involved in maintaining mitochondrial calcium levels is discovered.

- 1382** Direct and Reversible Hydrogenation of CO₂ to Formate by a Bacterial Carbon Dioxide Reductase

K. Schuchmann and V. Müller

Enzymes from anaerobic bacteria can catalyze the storage of hydrogen in the form of formic acid.

>> Perspective p. 1329

- 1385** Genetic and Molecular Basis of Drug Resistance and Species-Specific Drug Action in Schistosome Parasites

C. L. L. Valentim et al.

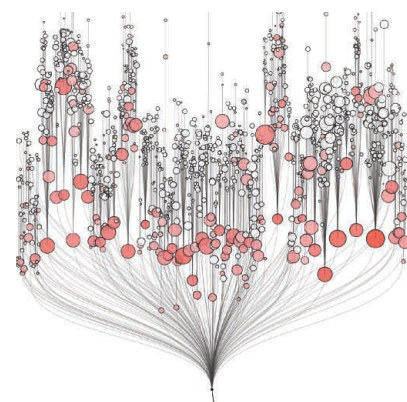
Mutations in a distinctive sulfotransferase are responsible for oxamniquine resistance in a human blood fluke.

- 1389** Fear Learning Enhances Neural Responses to Threat-Predictive Sensory Stimuli

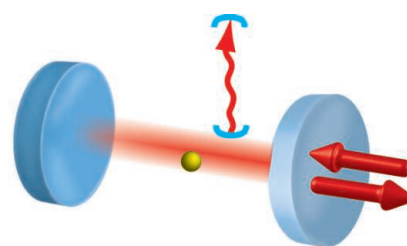
M. D. Kass et al.

The response of mouse olfactory sensory neurons was selectively increased when an odor was linked to discomfort.

>> Science Podcast



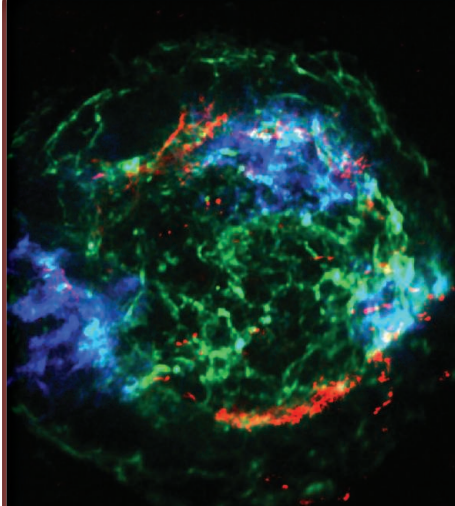
pages 1330 & 1337



page 1349

SCIENCE (ISSN 0036-8075) is published weekly on Friday, except the last week in December, by the American Association for the Advancement of Science, 1200 New York Avenue, NW, Washington, DC 20005. Periodicals Mail postage (publication No. 484460) paid at Washington, DC, and additional mailing offices. Copyright © 2013 by the American Association for the Advancement of Science. The title SCIENCE is a registered trademark of the AAAS. Domestic individual membership and subscription (51 issues): \$149 (\$74 allocated to subscription). Domestic institutional subscription (51 issues): \$990; Foreign postage extra: Mexico, Caribbean (surface mail) \$55; other countries (air assist delivery) \$85. First class, airmail, student, and emeritus rates on request. Canadian rates with GST available upon request, GST #1254 88122. Publications Mail Agreement Number 1069624. Printed in the U.S.A.

Change of address: Allow 4 weeks, giving old and new addresses and 8-digit account number. Postmaster: Send change of address to AAAS, P.O. Box 96178, Washington, DC 20090-6178. Single-copy sales: \$10.00 current issue, \$15.00 back issue prepaid includes surface postage; bulk rates on request. Authorization to photocopy material for internal or personal use under circumstances not falling within the fair use provisions of the Copyright Act is granted by AAAS to libraries and other users registered with the Copyright Clearance Center (CCC) Transactional Reporting Service, provided that \$30.00 per article is paid directly to CCC, 222 Rosewood Drive, Danvers, MA 01923. The identification code for Science is 0036-8075. Science is indexed in the Reader's Guide to Periodical Literature and in several specialized indexes.



We Are Stardust

Most of the universe's chemical elements were produced in stars, with the heaviest elements being produced when stars explode. Barlow *et al.* (p. 1343) used the Herschel Space Observatory to obtain sub-millimeter spectra of the Crab Nebula, the remains of a stellar explosion that was witnessed on Earth in 1054 AD, and detected the first evidence of a noble gas-containing molecular ion in space— $^{36}\text{ArH}^+$. Koo *et al.* (p. 1346) obtained near-infrared spectroscopic observations of the remains of another stellar explosion, Cassiopeia A, with the Palomar 5-m Hale telescope, and found evidence that a substantial amount of phosphorus was formed in the explosion. Among the six elements essential for life (hydrogen, carbon, nitrogen, oxygen, phosphorus, and sulfur), only the origin of phosphorus remained to be confirmed by observation.

Confusing Colloids in Liquid Crystals

In a simple fluid, particle diffusion such as the motion of colloidal particles shows a change in the mean squared displacement that is proportional with time. Within a nematic liquid crystal, diffusion of the molecules may show anisotropic behavior. Turiv *et al.* (p. 1351; see the Perspective by Abbott) asked what happens to colloidal particles in a nematic liquid crystal. At short times, anomalous diffusion was observed with motion both slower and faster than the long-term behavior, indicative of a complex coupling between the diffusive motion of the colloidal particles and the motion of the liquid crystal molecules.

Up and Down

Climate change is expected to have significant impacts on Earth's hydrological cycle, owing to changes, for example, in air temperature,

weather patterns, and land surface evaporation. In the Pacific Northwest of the United States, decreases in stream flow have been attributed to increased temperatures. Luce *et al.* (p. 1360, published online 29 November) show that these changes in stream flow are not likely to have been caused by temperature change, however, but rather by decreasing precipitation in the mountains where the streams originate.

The Fit Get Fitter

Advances in modern biology have allowed us to measure evolutionary fitness and estimate the rate of fixation of beneficial mutations. Drawing on the Long-Term Evolution Experiment, studying the evolution of *Escherichia coli* in a constant environment, Wiser *et al.* (p. 1364, published online 14 November) demonstrate that even after 50,000 generations over 20 years, gains in fitness show no evidence of leveling off. Instead, fitness is following a power-law relationship that is dependent on epistasis and clonal interference.

Eye to Eyeless

To what extent does adaptation rely on de novo mutation, as opposed to preexisting variation? It has been proposed that heat shock protein 90 (HSP90) can act to maintain cryptic variation by correcting misfolded proteins, until the system is taxed under stress conditions. Focusing on the cavefish *Astyanax mexicanus*, Rohner *et al.* (p. 1372) provide evidence that this mechanism contributed to morphological evolution in a natural setting where cryptic variation in eye size was masked by HSP90 in the ancestral river but revealed when the fish were reared and selected in caves.

Fear Factor

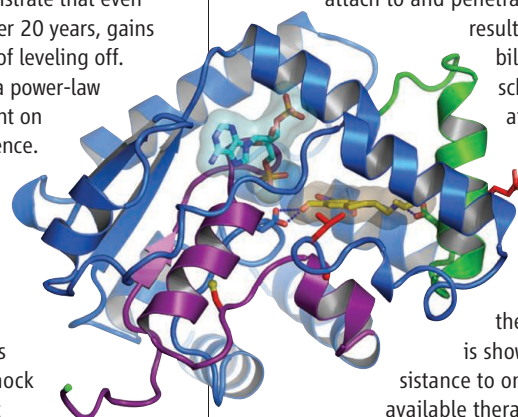
It has generally been assumed that the most basic aspects of peripheral sensory processing do not change even if they are paired with reward or punishment. A smell should still smell the same, a color should still look the same, and any changes observed would be likely to occur downstream of the primary sensory processing areas. However, using longitudinal in vivo neurophysiology in transgenic mice, Kass *et al.* (p. 1389) observed that neurotransmitter release from olfactory sensory neurons themselves was selectively enhanced for threat-predictive odors after fear conditioning.

Nondestructive Photon Detection

The click of a photon detector is the usual method for detecting a photon and can be sufficiently sensitive to detect even a single photon. Such a detection process is, however, destructive—the photon is annihilated. Reiserer *et al.* (p. 1349, published online 14 November) describe an experimental system capable of detecting a single photon without destroying it.

Blood Fluke Resistance

The larval stages of the blood fluke *Schistosoma mansoni* are disseminated via a replicative cycle in freshwater snails. When people come into contact with contaminated water, the larvae attach to and penetrate the skin. The



resulting disease, bilharzia or schistosomiasis, afflicts approximately 67 million people in Africa and South America. Unfortunately, the parasite is showing resistance to one of the available therapeutic drugs,

oxamniquine, which means that schistosome control relies on a single drug, praziquantel. Valentim *et al.* (p. 1385, published online 21 November) analyzed the genetic and molecular basis of resistance to oxamniquine through a combination of genetic linkage mapping, genome sequencing, functional genomics analysis, and x-ray crystallography.

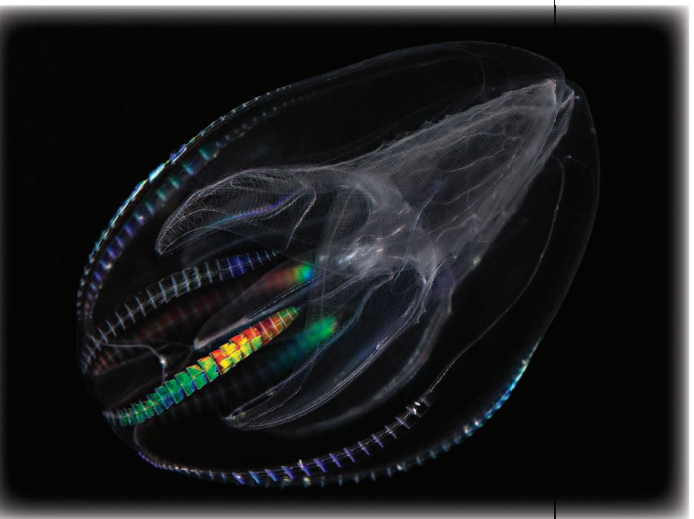
Limb Regeneration Mirrors Development

Salamanders regenerate the right amount of limb after cutting anywhere along its length. A long-discussed explanation suggests that the regenerating tissue first sets the fingertips as a boundary and then regenerates everything in between. However, Roensch *et al.* (p. 1375) report that the limb regenerates in the opposite order. Similar to the processes followed during development, the regenerating salamander limb first establishes a field of cells with the identity of the cut site, and then cells progressively commit to alternate fates as they grow closer to the tip of the regenerated limb.

Additional summaries

The Base of the Animal Tree?

The identity of the most basal lineages of the animal kingdom evolutionary tree has long been contested. **Ryan *et al.*** (p. 1336; see the



Perspective by **Rokas**) sequenced the genome of the ctenophore the warty comb jelly or sea walnut, *Mnemiopsis leidyi*, and conclude that ctenophores alone, not sponges or the clade consisting of both ctenophores and cnidarians, are the most basal extant animals. The results suggest a specific evolutionary process that likely occurred—including repeated gains and loss of mesoderm, expansion of genes associated with the cell cycle, growth signaling, apoptosis, and epithelial and neural cell types. Furthermore, previous hypotheses regarding the evolution of animals may require re-evaluation.

Predicting Disease Dissemination

In combating the global spread of an emerging infectious disease, answers must be obtained to three crucial questions: Where did the disease emerge? Where will it go next? When will it arrive? **Brockmann and Helbing** (p. 1337; see

the Perspective by **McLean**) analyzed disease spread via the “effective distance” rather than geographical distance, wherein two locations that are connected by a strong link are effectively close. The approach was successfully applied to predict disease arrival times or disease source using data from the the 2003 SARS viral epidemic, 2009 H1N1 influenza pandemic, and the 2011 food-borne enterohaemorrhagic *Escherichia coli* outbreak in Germany.

A Glimpse of HOON

Bonds between two oxygen atoms are relatively weak, as manifested in the sometimes explosive reactivity of O₂ and various peroxides. Thus, although nitrous acid (HONO) can be rearranged on paper to an isomer with an O-O rather than N-O bond, nitrosyl-O-hydroxide (HOON) has been considered too unstable to be observed. **Crabtree *et al.***

(p. 1354) used microwave spectroscopy to detect HOON formation in a dilute gaseous mixture of NO and OH in neon. Isotopic substitutions enabled determination of its structure, which included an unusually long O-O bond.

EPO via Total Synthesis

Erythropoietin (EPO) is a hormone involved in the production of red blood cells. Synthetic EPO produced via genetically engineered cell cultures is used to treat anemia and—more controversially—to boost athletic performance. EPO is a glycoprotein, and though its protein component is well-defined, both natural and synthetic EPO exhibit a wide range of attached oligosaccharides. **Wang *et al.*** (p. 1357; see the Perspective by **Hsieh-Wilson and Griffin**) prepared an EPO sample by a chemical synthesis that maintains a uniform pattern of attached sugars throughout, which may prove helpful in the analysis of how variation in the sugar components of EPO impact function.

Transcription Factor Binding Sites

Transcription factors (TFs) are proteins that bind to DNA to control gene transcription. **Stergachis *et al.*** (p. 1367; see the Perspective by **Weatheritt and Babu**) examined TF binding within the human genome in more than 80 cell types. Nearly 15% of coding regions simultaneously specify both amino acid sequence and TF recognition sites. The distribution of the TF binding sites evolutionarily constrains how codons within these regions can change, independent of encoded protein function. Thus, TF binding may represent a widespread and strong evolutionary force in coding regions.

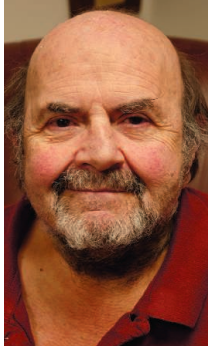
EMRE Emerges

Concentrations of calcium within mitochondria are tightly regulated and modulate physiological mitochondrial functions, including control of metabolism and cell death. **Sancak *et al.*** (p. 1379, published online 14 November) complete the molecular characterization of the mitochondrial calcium uniporter (MCU), the multicomponent channel that allows concentration of calcium within the organelle. They identified a small protein termed “essential MCU regulator”—or EMRE—which was required for calcium transport activity of the fully assembled uniporter.

Making CO₂ Work for You

Converting carbon dioxide (CO₂) to formic acid (HCOOH) is an attractive substrate for the storage and recovery of hydrogen (H₂) for use as fuel. Because CO₂ is relatively stable, however, its hydrogenation typically requires extreme conditions. **Schuchmann and Müller** (p. 1382; see the Perspective by **Pereira**) isolated a hydrogen-dependent carbon dioxide reductase from *Acetobacterium woodii* that is nearly 2000-fold more effective than the fastest known chemical catalysts. The process, which relies on the formation of formate as a chemical intermediate, also works well in whole-cell systems of *A. woodii* when certain metabolic pathways are inhibited. The enzyme, whether isolated or present in host bacteria, may lead to the design of more efficient fuel cells capable of functioning under less harsh conditions than fuel cells based on chemical reactions alone.

CREDIT: STEFAN SIEBERT/BROWN UNIVERSITY



George J. Armelagos is a Goodrich C. White Professor in the Department of Anthropology at Emory University, Atlanta, GA. E-mail: antga@emory.edu.

Reading the Bones

THE MODERN ERA OF DISEASE EMERGENCE AND REEMERGENCE IS ATTRIBUTED TO ISSUES RANGING from the deterioration of the environment, which brings humans in contact with pathogens that jump species barriers, to globalization, which is expanding the reach of pathogens beyond their former geographic boundaries. The transition from foraging to agriculture about 10,000 years ago accelerated the emergence of infectious disease. But it was the rise in social inequalities within and between societies that created disparities in disease risks and access to treatments, conditions that are still evident in today's world. The calls for improving surveillance, research, vaccines, and behavioral change are indeed urgent, but what is also worrisome is the lack of an evolutionary perspective in formulating new strategies to confront this modern disease-scape. Paleopathology—the study of ancient diseases—not only provides an archaeological record of the adaptations and lifeways of ancient peoples, it is a source of information on the evolutionary epidemiology of infectious diseases. Reading the bones of the ancient dead can guide how we confront infectious diseases today.

The genomic analysis of pathogens in human remains, together with knowledge from oral history and tradition, provides a framework for understanding the emergence of modern diseases. As described in the News story on p. 1306, analysis of the graveyard of the Abbey of St. Peter in the province of Lucca, Italy, is revealing how epidemics such as the plague spread through Europe. It was once thought that a mutation in *Yersinia pestis*, the source of the Black Death, caused the plague's lethality, which wiped out about half of the European population during the Middle Ages. But paleopathologists working in conjunction with microbiologists and geneticists are discovering that the ancient pathogen is similar to the modern-day microbe. This raises the question of why the bacterium was so deadly in the past. The team has also discovered a mass grave, where they hope to recover DNA of *Vibrio cholerae* from the remains. This pathogen killed nearly 100,000 people in a worldwide pandemic in 2012. By understanding the evolution of this bacterium, scientists hope to discover the genetic changes that are associated with extreme virulence.

The Italian project, like many other sites, involves remarkable support by the local inhabitants and human remains that are available for study. This contrasts with the situation in the United States. The Native American Graves Protection and Repatriation Act (NAGPRA) of 1990 requires that human remains affiliated with tribes must be returned to those tribes for reburial. It was the result of a compromise among organizations representing Native Americans, the scientific community, museums, and preservation interests. In many cases, NAGPRA has stimulated constructive interactions by all stakeholders. However, the Act hampers potential research and, although conceived with good intentions, is at times ambiguous. As a result of such legislation, the opportunities offered in Italy and other sites outside the United States have attracted many U.S. paleopathologists and bioarchaeologists. This is extremely unfortunate, as there is much to be learned from analysis of the ancient DNA of Native Americans. Understanding the origin and spread of smallpox, measles, typhoid, and other outbreaks in the New World will not only test long-held hypotheses about how disease devastated Native Americans, but should reveal the virulence of strains, how diseases spread, and how populations recovered. These are precisely the issues that researchers need answers to in considering future pandemics.

To expand the sources of ancient remains in the United States, the scientific community must increase its engagement with the public, policy-makers, and tribal communities in ways that clearly explain how access to human remains, in an ethical and respectful manner, holds great potential for understanding the diseases that affect their own health. Different ecological settings that characterize archaeological sites offer opportunities to examine patterns of disease, as well as adaptive potentials and constraints. Ancient bones can help us deal with diseases in the future, and scientists should have an opportunity to study them.

— George J. Armelagos

10.1126/science.1249076



PLANT SCIENCE

Neuroexcitatory Starfruit



The starfruit (*Averrhoa carambola*), so named for the starlike shape generated when the fruit is cut in cross section, adds a tropical note to diverse diets. However, those with kidney failure have an unusual reaction to ingesting starfruit that includes hiccups, mental confusion, and seizures. Garcia-Cairasco *et al.*, analyzing the response of kidney-damaged rats to starfruit extracts, have now identified the toxic element. The key compound is not the nephrotoxic oxalic acid, known to be present in the fruit, but rather is a molecule somewhat like phenylalanine, which the authors have named caramboxin. When injected into rat brains, caramboxin has a neuroexcitatory effect. Experiments with brain slices showed that caramboxin has properties of a glutamatergic receptor agonist. With this potent natural product, the starfruit may be useful for more than gracing a salad. — PJH

Angew. Chem. Int. Ed. **52**, 10.1002/anie.201305382 (2013).

INFECTIOUS DISEASE

Nonrandom and Nonoverlapping

Evolutionary pressure from pathogens appears to have generated diversity in alleles of immune response genes known as *human leucocyte antigen* (*HLA*). It remains unclear, however, how this mechanism resulted in the dominance of certain *HLA* allele combinations. Penman *et al.* investigated particular associations of *HLA* alleles with protection against death from specific pathogens using a mathematical model for the simple case of a two-locus two-allele system. The model reveals that a pathogen population evolves, which extirpates homozygote hosts and then enters dynamic coevolutionary cycling of heterozygotes. The consequence is that strain structure evolves in the pathogen population as a result of this immune selection and results in nonrandom and nonoverlapping associations among the *HLA* immune recognition alleles of the host. — CA

Proc. Natl. Acad. Sci. U.S.A. **10**, 10731/pnas.1304218110 (2013).

ECONOMICS

Learning by Doing

Many have championed the importance of formal education for industrial innovation and technical change in a modern economy. On-the-job training, however, or learning by doing, is critical as well. Despite this importance, theorists and managers still lack fine-grained details about how such knowledge is acquired, aggregated, transmitted, and embodied in a production process. Levitt *et al.* studied an auto

assembly plant that was, in many respects, starting over, having just completed major changes in assembly line layout, in types of vehicle assembled, and into new production teams. Over the course of a year, they tracked hundreds of line workers and the 189,000 vehicles they made. They measured hundreds of features on each vehicle, from the torque applied to a bolt to defects in the fit of parts, and the timing of each production step. Defect rates and production times both improved dramatically over the first 7 weeks, at which point a second shift began working on the same line. Despite minimal overlap between first- and second-shift workers, second-shift defect rates began, and remained,



slightly better than for the first shift, who had a 7-week head start. Features that were more defect-prone in shift one were similarly more defect-prone in shift two. Defect rates and production time spiked up again when new styles of vehicle were introduced. The authors discuss the

importance of institutional systems to harness and apply this knowledge, and speculate as to why workers might voluntarily “overshare” their hard-earned and valuable knowledge with management. — BW

J. Politi. Econ. **121**, 643 (2013).

EDUCATION

Women in Physics

Women continue to be underrepresented in physical science classes and careers. Hazari *et al.* tested five hypotheses regarding what factors might affect women’s interest: having a single-sex class, having a female teacher, having a

female scientist guest speaker, discussing the work of female scientists, and discussing the underrepresentation of women in physics. Based on data from the Persistence Research in Science and Engineering project, which surveyed a sample of over 7000 U.S. college students, individuals were identified as being part of the treatment or control groups by virtue of having experienced, or not experienced, each of the five hypotheses. Next, students were matched so that the females in both treatment and control groups had equal prior physical science career interest, and students were asked to rate the likelihood that they would choose a

career in physical sciences. Women who were exposed to discussions about the underrepresentation of women in the physical sciences were more likely to choose a career in physics than those who were not. Such student-centered discussions afford more opportunities for female students to picture themselves as physical scientists. On the other hand, the lack of support for the other hypotheses invalidates the common belief that female role modeling is necessary for attracting women. — FB

Phys. Rev. ST Phys. Educ. Res. **9**, 020115 (2013).

ENVIRONMENTAL SCIENCE

Nanosilver Lining

From socks to children's toys, nanoparticles of metallic silver (i.e., "nanosilver") are being incorporated into more and more consumer



products for their antimicrobial properties. But as these products are used or reach the end of their life cycle and enter the waste stream, they can have negative impacts on natural or engineered microbial communities, such as those in wastewater treatment plants or compost reactors. Gitipour *et al.* analyzed the impact that realistic low levels of silver nanoparticles had on the microbial communities responsible for biodegrading disposed organic matter during composting. In compost treated with nanosilver or free silver ions, the species present in the bacterial communities differed from a control reactor without any added silver; however, the physical properties of the aged compost and leachate were nearly identical between treatments. Statistical analysis of DNA sequencing data suggests that functional redundancy within the bacterial communities played an important role in maintaining efficient biodegradation. Furthermore, strong associations with organic matter may explain why spectroscopic analyses could not detect surface reactions of silver nanoparticles with abundant anions such as chloride, potentially limiting the bioavailability and toxicity of silver in the compost. — NW

Environ. Sci. Technol. **10.1021/es402510a** (2013).

SIGNALING

Nuclear Receptor Partner

Drugs that activate glucocorticoid nuclear hormone receptors are commonly used in the clinic for their anti-inflammatory actions, or to slow the growth of some cancers. The ways in which these receptors, which function as transcription factors in the nucleus, modulate a broad set of genes that make up a quarter of the genome are not fully understood. Revollo *et al.* show that another transcription factor, HES1 (hairy and enhancer of split-1), has a general role to restrain glucocorticoid-dependent gene expression. HES1 is well known for its function during development in another signaling pathway, the Notch signaling pathway. Revollo *et al.* show that in adult mice, HES1 acts at glucocorticoid-responsive genes to inhibit transcription and

that it also strongly influences the range of genes that are responsive to glucocorticoids. In order to regulate many of its targets, it appears that a primary effect of the glucocorticoid receptor is to first repress transcription of the gene encoding HES1. This relieves inhibition by HES1 and allows the glucocorticoid receptor to activate its targets and produce its wide-ranging effects that support physiological responses to stress. — LBR

Sci. Signal. **6**, 10.1126/scisignal.2004389 (2013).

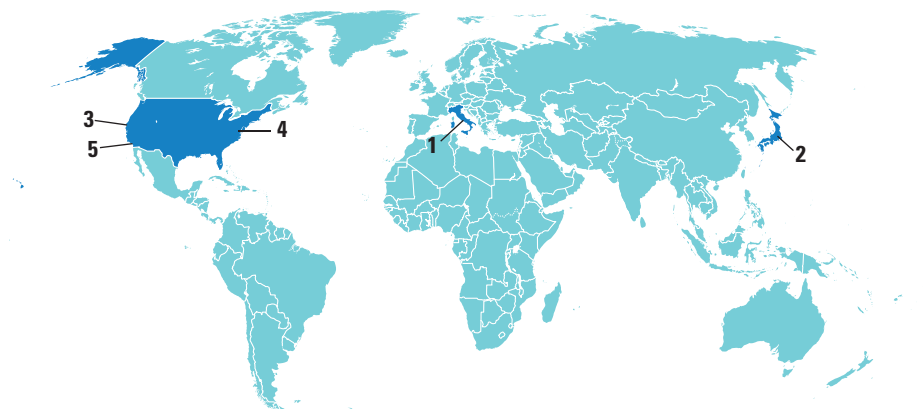
APPLIED PHYSICS

Enhancing Diamond

The thermal, mechanical, optical, and transport properties of diamond make it an ideal material for applications in high-end power electronics and high-frequency devices. More recently, the quantum properties of the various individual defects in diamond, particularly the nitrogen vacancy defect, also make it attractive for quantum information processing and quantum optical applications. Melville *et al.* demonstrate the potential to enhance that functionality even further by epitaxially growing a single-crystal europium oxide (EuO) layer on a diamond substrate. The EuO layer is a low-temperature ferromagnet and provides the possibility of controlling the properties of diamond magnetically. Varying the growth parameters of the EuO layer to manipulate the strain or expanding the search for other compatible functional oxides provides the opportunity of adding further control knobs for the already multipurpose diamond. — ISO

Appl. Phys. Lett. **103**, 222402 (2013).

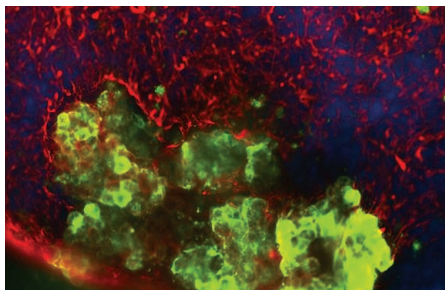
AROUND THE WORLD



Rome 1

Disputed Stem Therapy Revived

A controversial stem cell treatment may have another shot at a clinical trial funded by the Italian government after a ruling last week from a regional administrative court. The



Second chance. An attempt to treat brain diseases using stem cells (green) may yet enter clinical trials.

ruling suspends the September decision of a federal scientific committee to not finance the trial. The committee concluded that the treatment, which uses bone marrow stem cells purported to treat neurodegenerative diseases, has no scientific foundation.

The treatment has been developed by the Stamina Foundation, which asked the regional court to invalidate the panel. The new ruling implies that the committee experts were not impartial in their decision—a claim that angers the Italian scientific community. “It does not respect the rule of the scientific method and offends scientists who spend their career to find a cure to diseases,” says Maria Grazia Roncarolo, scientific director of the San Raffaele Scientific Institute in Milan and member of the committee that decided against the trials. Health Minister Beatrice Lorenzin told the Italian media that she will appoint a new expert panel to assess Stamina’s protocols.

Tokyo 2

Scientists Oppose Secrecy Law

To the chagrin of many scientists, Japan’s Diet adopted a state secrets law on 6 December that threatens imprisonment for those who leak or publish information deemed sensitive by the government. Nobel laureates Toshihide Maskawa, a physicist at Nagoya University, and Hideki Shirakawa, a chemist formerly at the University of Tsukuba, were among 30 scholars who issued a 28 November statement warning that the law threatens constitutional rights, including freedom of the press, of thought and expression, and of academic research. By 6 December, more than 3000 academics had signed on, and the Japan Scientists’ Association expressed similar concerns.

Despite widespread public protest, the ruling coalition used its Diet majority to pass the legislation. Under the new law, government employees leaking “secrets” could be jailed for up to 10 years; journalists publishing them could get 5-year sentences. Many



Objector. Nobel laureate Toshihide Maskawa is among the scientists who oppose Japan’s secrecy law.

worry that the vague definition of state secret could be used to restrict access to, among other things, information surrounding nuclear accidents.

Opponents now hope to limit the law’s implementation and to get the next administration to repeal it. http://scim.ag/_secrecy

Mountain View, California 3

23andMe Drops Health-Related Tests

In response to a warning from the U.S. Food and Drug Administration (FDA), the company 23andMe will no longer provide health information to people who purchase its DNA testing kit. According to a 5 Decem-



ber announcement, current customers will still have access to a 23andMe database noting the health issues associated with their DNA, but customers who purchased its Personal Genome Service (PGS) on or after 22 November will receive only information about their ancestry and their raw genetic data without interpretation.

“I am highly disappointed that we have reached this point,” CEO Anne Wojcicki wrote on the 23andMe blog, adding that the company is seeking FDA clearance to reinstate the health tests soon.

While the 23andMe website maintains that it does not provide medical advice, recent marketing has emphasized the service’s medical uses, says Cecile Janssens, an epidemiologist at Emory University in Atlanta. “It used to be more about what science knows about your DNA,” she says. “But in the past year they really went on a different track. It is more about health recommendations now.” <http://scim.ag/23Health>

Washington, D.C. 4

Panel Calls for End to Gene Therapy Review

After 4 decades of vetting clinical trials of gene therapy for novel risks, it’s time to relax a bit, says a report issued last week by an expert panel at the U.S. National Academies.

CREDITS (LEFT TO RIGHT): COURTESY OF CHRISTINA TU/SUE & BILL GROSS STEM CELL RESEARCH CENTER; UC IRVINE; WIKIMEDIA COMMONS; KEITH SIMMONS/FLICKR

Downloaded from www.sciencemag.org on December 13, 2013

The Recombinant DNA Advisory Committee (RAC), established in 1974, was a response to public concern that genetic engineering, particularly human gene transfer trials, might run amok.

RAC has done a good job, reviewers found. But the group chaired by law professor Lawrence Gostin of Georgetown University in Washington, D.C., now urges the National Institutes of Health, which houses RAC and uses its advice, to phase out the committee. It recommends creating a new panel modeled on RAC to watch over human subject research “that is so novel, and carries significant unknown risks, that the normal regulatory apparatus lacks the capacity to conduct an adequate review.” RAC should focus only on “exceptional” cases until it is replaced, they conclude. http://scim.ag/_RAC

San Diego, California 5

New Prize for New Livers

A contest will award \$1 million to the first team of scientists that can grow a bioengineered liver advanced enough to keep a large mammal alive for 90 days. The Methuselah Foundation’s “New Organ Liver Prize,” announced 5 December at the World Stem Cell Summit in San Diego, is designed to encourage more researchers to focus on liver tissue engineering. The competition is open to teams around the world and has a deadline of 31 December 2018.

According to the contest rules, teams must keep at least three out of four trial animals alive with transplanted, lab-grown livers, and these animals must also maintain a healthy weight and be able to eat and move normally. The liver has to be grown from scratch. Transplanting functional livers from other experimental animals into trial animals won’t qualify. Allowed are “reseeding” techniques, in which a donor liver is stripped of its cells and new cells—matching those of the recipient—are grown on it.

The Springfield, Virginia-based foundation says it also plans to launch prizes for kidney, heart, pancreas, and lungs.

NOTED

Merriam Webster last week **declared “science” the 2013 Word of the Year**. The dictionary chose its winner from among the top lookups on Merriam-Webster.com based on the increase in searches over the previous year. With a 176% increase, “science” beat out “cognitive” for first place.

NEWSMAKERS

Three Q’s

European scientists are celebrating a windfall in funding for the European Union’s flagship research program: Horizon 2020 is set to receive almost €70 billion over the next 7 years, a nearly 30% increase over its predecessor, Framework Programme 7. *Science* caught up with the bonanza’s chief architect, European research commissioner **Máire Geoghegan-Quinn**, last week at the commission’s headquarters in Brussels.



Q: How will things change for scientists under Horizon 2020?

M.G.-Q.: Horizon 2020 is putting a lot of research money into finding answers to societal challenges [such as climate change]. It’s

challenging all the disciplines to step outside their comfort zones.

Q: Has research policy become more important in Europe?

M.G.-Q.: For everybody, unemployment is the big issue. And where are the good jobs? They are going to be in research and innovation: high-quality, well-paid jobs that are secure for the future. And when I visit universities, academics say that E.U. money used to be the icing on the cake, but that’s no longer the case—it’s absolutely, fundamentally important to their budget now.

Q: Your 5-year term ends next October. How do you make sure Horizon 2020 stays relevant?

M.G.-Q.: When the Seventh Framework Programme started in 2007, there was no such thing as a climate change challenge or a food security issue. FP7 was very much like a straitjacket. One of the things that we

Random Sample

Following Mawson’s Cold Trail

“I was attacked by sea lions this morning,” says Chris Turney by satellite phone from the Southern Ocean. It’s all in a day’s work for Turney, a climate scientist with the University of New South Wales in Australia, who boarded a Russian icebreaker heading south toward Antarctica on 27 November. Turney is leading a group of nearly 40 scientists and doctoral students and a handful of media representatives on the Australasian Antarctic Expedition (AAE) 2013. The team will spend the month retracing the steps of Australian geologist Douglas Mawson’s original 1911 to 1914 expedition over the frozen continent.

The trip is more than just an adventure. It aims to investigate how poleward-shifting westerly winds affect the Southern Ocean, the Antarctic ice sheet, and the plants and animals of sub-Antarctic islands. AAE’s scientific team will duplicate and extend the data that Mawson and his companions collected in surveying work marred by mishaps, brushes with starvation, and the deaths of two explorers. “Having observations a century ago covering several years is unique,” says Turney of the extensive and little-studied data sets.

The expedition hopes to kindle public interest in science by highlighting Mawson’s saga of adventure and survival. “We’re using some of the latest technology to take people with us virtually,” Turney explains. Follow the adventure at www.spiritofmawson.com.



Chris Turney with snares crested penguins on Snares Island, New Zealand, on the way to Antarctica.



Reptiles Tout Alluring Snouts

In what could be the first example of tool use among reptiles, researchers have discovered that both alligators and crocodiles use twigs and sticks to attract nest-building birds. Behavioral ecologist Vladimir Dinets of the University of Tennessee, Knoxville, first noticed in 2007 that mugger crocodiles (*Crocodylus palustris*) at a zoo in India balanced small sticks on their snouts near a rookery where egrets compete for sticks to build their nests. He observed the same strategy in alligators (*Alligator mississippiensis*) in Louisiana: They displayed sticks much more frequently near egret rookeries and during the nest-building season, he and colleagues report online in *Ethology Ecology & Evolution*. Although Dinets observed only one attack over a year, two co-authors who have worked for 13 years at a wildlife park in Florida have seen multiple attacks after alligators lured birds with sticks. <http://scim.ag/reptool>

>>NEWSMAKERS

worked strongly on is ensuring that Horizon 2020 is flexible, so if issues arise that we haven't even thought about now, at least the program will be able to respond to that. http://scim.ag/_Quinn

Scientist Behind 'Drowning Polar Bear' Paper Settles Lawsuit

A long saga is finally over for marine ecologist **Charles Monnett**, whose observations of drowned polar bears were featured in Al Gore's *An Inconvenient Truth* and attracted scrutiny from climate change skeptics. Monnett has resigned from the U.S. Bureau of Ocean Energy Management (BOEM) under terms of a settlement released last week. BOEM had investigated Monnett for alleged "integrity issues" over management of research grants.



Monnett

The controversy started in 2006 when Monnett, who was researching the impact of Alaskan offshore drilling on whales, published a paper noting drowned polar bears—presumably trying to swim long distances between ice packs. The observations became a cause célèbre for environmentalists objecting to Arctic drilling. BOEM, then known as the Minerals Management Service, probed Monnett's science and his grant management (*Science*, 5 August 2011, p. 681) and eventually reprimanded him for leaking internal e-mails about an Arctic oil and gas exploration plan. Under the settlement, signed in October, BOEM has also retracted a letter of reprimand and paid Monnett \$100,000.

FINDINGS

Diets Induce Quick-Change In Gut Microbes

Almost monthly a new study suggests a link between bacteria living in the gut and diseases from obesity to autism, at least in mice. But connecting human health to gut microbes has been a struggle, in

BY THE NUMBERS

13,200+ Signatures on a petition from Italian scientists protesting a proposed law to restrict use of animals in scientific research.

http://scim.ag/_petition

100,000 Number of individuals whose DNA the new Saudi Human Genome Program intends to sequence over the next 5 years.

part because it's difficult to have people change their diets for the weeks or months researchers thought it would take to alter an intestine's microbes and see an effect.

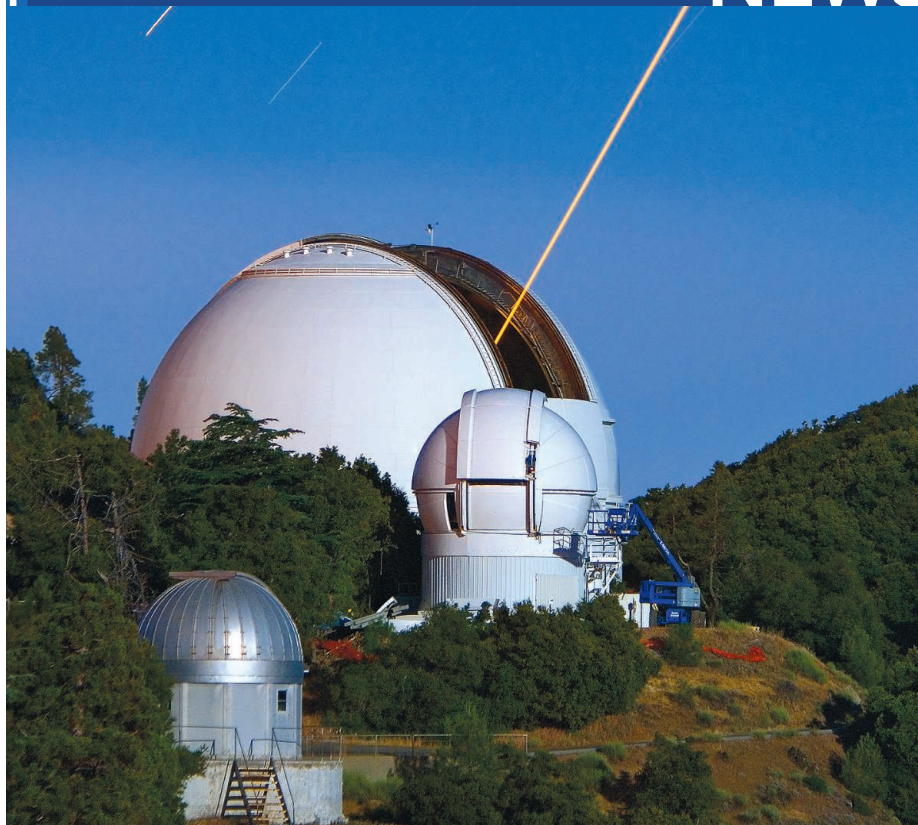
Yet, with the right diet, it actually takes just 3 days to shift the abundance and activity of different gut bacteria, according to a study in *Nature* this week. Computational biologist Lawrence David of Duke University in Durham, North Carolina, and his colleagues asked 10 people to eat only meats, eggs, and cheeses or else a high-fiber vegetarian diet for 5 days. Fecal samples from



Eat up. A plant-based meal for testing the effects of diet on the microbiome.

before, during, and after the diets revealed reproducible changes in bacterial makeup, paving the way for short-term tests of various microbiome-health hypotheses. "It's a landmark study," says Rob Knight, a microbial ecologist at the University of Colorado, Boulder. "It changes our view of how rapidly the microbiome can change."

CREDITS (TOP TO BOTTOM): DON SPECHT; (INSET) VLADIMIR DINETS; AP/FILE; LAWRENCE DAVID



ASTRONOMY

Lick Observatory in Trouble As Austerity Starts to Bite

One of the most iconic astronomical institutions in the United States—the 125-year-old Lick Observatory on Mount Hamilton near San Jose, California—is facing the threat of closure. Astronomers affiliated with the observatory say that the University of California’s Office of the President (UCOP) plans to cut its funding as part of an effort to control costs across the UC system. UCOP’s decisions threaten not just Lick, the astronomers say, but also the future of Lick’s parent organization, the University of California Observatories (UCO).

“I am absolutely heartbroken and crushed by what’s going on,” says Steven Vogt, an astronomer at UCO who has worked at Lick since 1978. Already, several prominent astronomers have left UCO because of the uncertainty. “We are hemorrhaging good people right and left,” Vogt says. Other U.S. astronomers say UCOP’s decisions—although tough to swallow—are an unavoidable consequence of belt-tightening.

In addition to running Lick Observatory, UCO is responsible for building instruments

and software for both Lick and the W. M. Keck Observatory in Hawaii, home to two of the world’s largest telescopes, which UC owns jointly with the California Institute of Technology. UCO’s astronomers and technical staff members are also developing instruments for the Thirty Meter Telescope (TMT) project (*Science*, 23 October 2009, p. 512). Based at UC Santa Cruz, UCO is now funded through an annual budget of \$7.5 million provided by UCOP.

Starting next July, however, UCOP will no longer pay for the salaries of UCO’s 11 faculty and staff members, which account for about \$2.5 million of UCO’s budget. UCOP has directed UC Santa Cruz to pick up that tab, says UCO’s interim director, Sandra Faber, leaving UC Santa Cruz officials worried about how they will meet the financial burden. Faber and her colleagues have also been told that UCOP will ramp down funding for Lick starting in 2016, leading to a complete cutoff after 2018. Unless UCO can find an alternative way to cover Lick’s \$1.3 million annual

Distress signal. A laser test at Lick, which astronomers say is rapidly losing staff members.

budget, the observatory—which is home to six telescopes, with a new 2.4-meter Automated Planet Finder scheduled to come online next year—will have to close down.

The cuts follow the recommendations of a UC board set up in 2012 by Steven Beckwith, an astronomer at UC Berkeley who serves as vice president for research and graduate studies within UCOP. The board’s charge was to review UCO’s activities and suggest ways to optimize UC’s overall investments in astronomy. In its report, issued in June, it recommended that UC direct its astronomy dollars to Keck and the TMT project while converting Lick from a research-and-training observatory into a public museum supported by funds from outside the UC system.

“This is about much more than UC’s budget problems,” says Garth Illingworth, a UCO astronomer. He and others also blame a perception by university faculty and administrators that UCO staff members enjoy privileged status. They have a lighter teaching load than professors at UC astronomy departments. They also hold 11-month appointments, meaning they receive salaries for most of the year, while their UC departmental colleagues typically receive just 9 months of university salary. “I don’t want to minimize the rancor this has caused,” Faber says.

Illingworth says that UCO astronomers have provided UC with unmatched scientific value. For decades, the organization has been the birthing ground for instruments that have advanced optical and infrared astronomy, helping observers at both Lick and Keck rack up an impressive string of firsts, such as this year’s discovery by Vogt and his colleagues of three exoplanets in the habitable zone of a star. A 2011 review by an external committee—led by astronomer Robert Kennicutt of the University of Cambridge in the United Kingdom—gave both UCO and Lick Observatory top billing. “UC leadership in astronomy through observations on the Keck and Lick telescopes has produced some of the most important astronomical discoveries of the past 15 years, including ground-breaking work in exoplanets, cosmology and black holes,” the review said, calling UCO “[t]he assembly of what arguably is the leading ground-based optical astronomical instrumentation group in the world.”

Beckwith would not comment on the board's recommendations. Board member James Bullock, an astronomer at UC Irvine, says the board was forced to make tough choices because UCOP officials had made up their minds to slash UCO's overall budget. "It came down to this: Given the budget cuts, we can't do everything, so let's focus on Keck and TMT," Bullock says. He adds that some board members thought that "there's too much money being spent on Lick for the science that it produces"—a view he says he does not share.

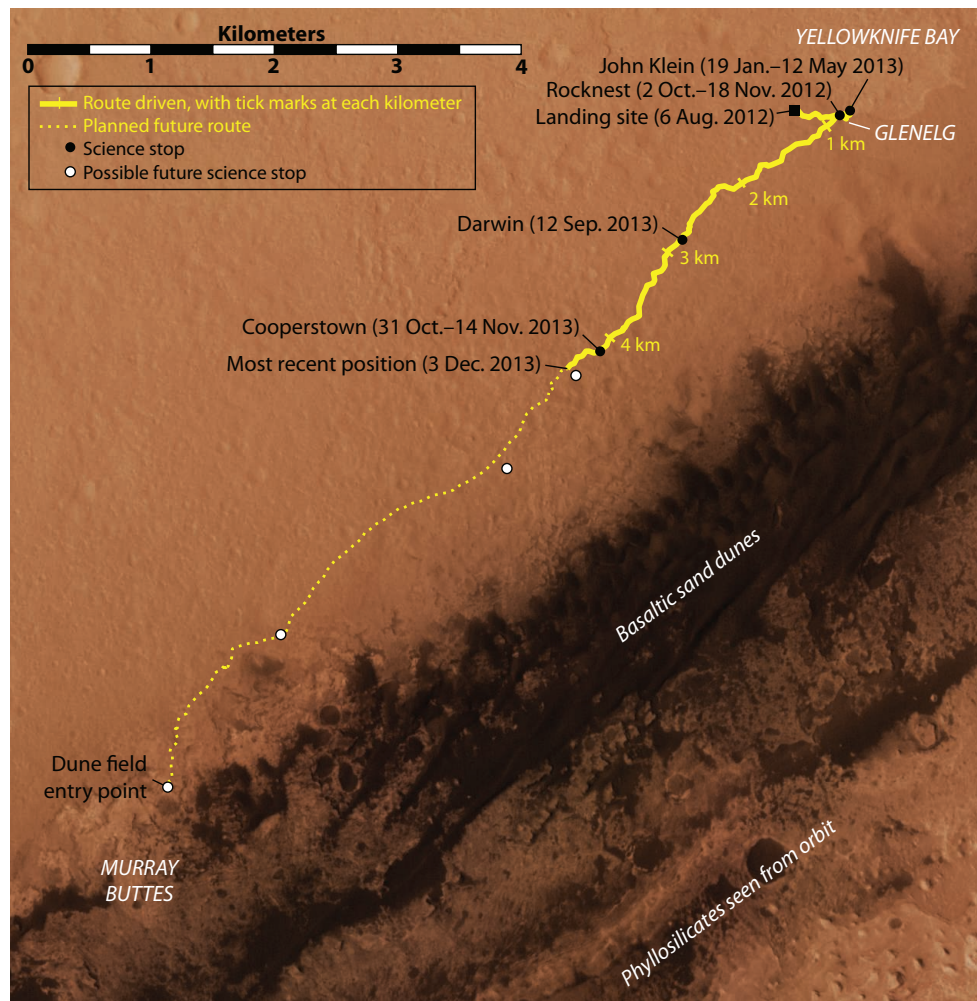
The board also debated whether the 11-month appointments for UCO faculty can be sustained in the future, Bullock says. "Some feel that the money budgeted to guarantee those positions should be spread around," he says. He denies that these discussions have been driven by envy, even though UCO professors "do have a nice deal," he says. "The broader problem is that the budget is being cut."

Lick's uncertain future and the doubts about who will pay UCO salaries have already taken a toll. Michael Bolte stepped down as UCO director last year. A prominent instrument builder at UCO—Rebecca Bernstein, who was leading the development of a spectrograph for the TMT project—was recently lured away by the rival Giant Magellan Telescope project. "That was a big blow to us," Illingworth says.

The decision to end UC's support of Lick is "tragic and myopic," says John Wareham, Lick's deputy director until September of this year. He opted for retirement partly out of frustration over the administration's moves against Lick and UCO. "Lick provides students with the ability to work with large, powerful telescopes and to build instruments that are compatible with those research-grade devices," he says, adding that it is far more difficult for UC students to get access to Keck's telescopes. "If Lick closes, one could predict a significant negative impact on the university's ability to recruit astronomy students for generations to come."

Faber says that UCO is making a concerted effort to look for alternate funding for Lick, including tapping potential private donors. "This is not a dead observatory," she says, pointing to ongoing instrumentation projects such as a \$2.5 million next-generation adaptive optics system that is being developed for the observatory's 3-meter Shane Telescope. "This is our primary training ground for future astronomers. We will find a way to keep it going."

—YUDHIJIT BHATTACHARJEE



PLANETARY SCIENCE

New Results Send Mars Rover On a Quest for Ancient Life

When the Curiosity rover landed in Gale crater 16 months ago, its goal was to find a place on Mars that was habitable 4 billion years ago. It quickly identified a lake mud that fit the bill, and now a spate of new findings is driving the mission in a new direction: searching for actual traces of ancient life. Leaders of the 400-strong Curiosity science team say their latest discoveries, published online earlier this week in *Science* (<http://scim.ag/SciCuriosity>), are narrowing down how and where to look for "molecular fossils"—organic matter that might have come from ancient martian microbes.

"Our mission is turning a corner," says Curiosity project scientist John Grotzinger of the California Institute of Technology (Caltech) in Pasadena. "We are beginning to map a way forward, a way to explore deliberately for organic matter."

Curiosity's new analyses of sediment from the bed of a long-vanished lake hint that Mars harbors substantial amounts of organic carbon compounds, although no one is yet willing to attribute them to ancient life. And in a martian first, Curiosity has determined how recently surface rocks have been exposed by erosion. That opens the way to more systematic searches for molecular fossils, by showing scientists how to maximize their chances of finding organic matter that was only recently exposed to the ravaging rain of cosmic rays that pours down on Mars.

The last time Curiosity scientists reported on the hunt for organic matter, things were a bit of a mess (*Science*, 12 April, p. 138). Perchlorate compounds—powerful oxidizers when heated—turned out to be ubiquitous on Mars. And because

CREDIT: EMILY LAKDAWALLA/THE PLANETARY SOCIETY

Curiosity so far. The Mars rover landed in August of last year, scooped dust at Rocknest, drilled rock at Yellowknife Bay, and is headed for Mount Sharp.

Curiosity's onboard test for organic matter involves heating finely powdered rock by hundreds of degrees, any organic carbon compounds would be oxidized to carbon dioxide before the carbon's original form could be determined. A few small molecules did survive, but they seemed to come from a contaminant that leaks into Curiosity's Sample Analysis at Mars (SAM) instrument package.

SAM team members now report that their contamination problem is behind them. The contamination "can't explain it all," says SAM team member Daniel Glavin of NASA's Goddard Space Flight Center in Greenbelt, Maryland. By analyzing empty sample containers, varying the amount of sample, and flushing out samples before analysis, the SAM team has concluded that the contaminant now accounts for only 1% to 3% of the carbon appearing as carbon dioxide.

The remaining 97% may well have come from martian organic matter. The SAM authors reached that conclusion after Curiosity took its first look beneath the planet's surface. At a site called Yellowknife Bay, which has a rock outcrop that seems to have been the bottom mud of an ancient lake, the probe drilled 5 centimeters into the rock. The team then compared samples of windblown dust scooped off the surface with samples of rock powder from the borehole. The dust had been exposed to organics-destroying solar ultraviolet, cosmic rays, and radiation-activated perchlorates for many millions of years. The lakebed had long been shielded by encasing rock.

When SAM heated the samples, the lakebed samples emitted more carbon dioxide than equal-size dust samples did, and their carbon dioxide came off at lower temperatures. Those observations suggested that heating the dust had simply decomposed naturally occurring, inorganic carbonate minerals, but that heating the lakebed samples may have burned organic matter. Most telling, as carbon dioxide from the lakebed surged, the level of oxygen gas from decomposing perchlorates dropped. On seeing those data, one SAM team member reportedly declared, "This is combustion of organic carbon, folks."

Curiosity's Glavin says the results are "exciting," but he and the rest of the SAM team are cautious in print. So is organic geochemist Mark Sephton of Imperial College London, who is not on the Curiosity team. The results

are "very consistent with organic carbon," he says, but he adds that so far they are "tantalizing" rather than definitive.

Tempering the excitement is Glavin's ready admission that "we can't say anything about the origin of this [organic] carbon." That's because a nonbiological source is close at hand: Tons of organic matter fall on Mars every year in meteorites and cosmic dust. Researchers estimate that these organic compounds, made not by living things but by chemical processes in space, could be maintaining surface carbon at between about 10 parts per million (ppm) and several hundred ppm—enough at the high end to account for all of the roughly 500 ppm of carbon that Curiosity has detected in the lakebed samples.

What's more, the ancient environment around Gale crater does not appear to have been very hospitable to life, new analyses reported in the *Science* papers suggest. The lakebed deposits—which washed into the crater from surrounding high ground—show "very little evidence for chemical weathering" before arriving in the lake, says team member Scott McLennan of Stony Brook University in New York. That suggests that there was little liquid water around to alter the minerals and thus that "we're dealing with very arid and/or cold environments," McLennan says. The area may have resembled the hostile, hyperarid Atacama Desert of Chile, where water flows only during rare torrential rainstorms.

The muddy lake bottom might have been more hospitable. In their paper, Grotzinger and his Curiosity colleagues describe the bottom mud there as a "strikingly Earth-like habitable environment." But to survive in the mud of an oxygen-free planet, any microbes would have had to derive energy from the chemical imbalances between minerals in the sediment—"eating rock" in a process called chemolithotrophy.

On Earth, "fully convincing" chemolithotrophy is known only in

Online

sciencemag.org

Podcast interview
with author
Richard Kerr (http://scim.ag/pod_6164).

kilometers-deep rock exposed in South African gold mines, according to marine geochemist Steven D'Hondt of the University of Rhode Island in Narragansett. And levels of organic carbon there are minuscule compared

with the 500 ppm of carbon reported on Mars. So if the martian carbon is indeed organic, the best guess now is that either Curiosity has stumbled across the remains of an unexpected subsurface oasis, or most of the carbon comes from meteorites, or a bit of both.

Another of the recent results may make it easier to search for martian carbon—and ultimately sort out its origins. For the moment, carbon-hunters face a serious obstacle: Cosmic rays penetrate the rock to a depth of a meter or so, far beyond the reach of Curiosity's drill, and over millions of years destroy any organic matter.

Kenneth Farley of Caltech and colleagues demonstrate an elegant solution: a way to identify rock that has been buried for eons

beneath at least a couple meters of protective rock and only recently exposed by wind erosion. Using SAM's mass spectrometer, they measured isotopes of helium, neon, and argon that cosmic rays generate as they pass through rock. The fewer of these isotopes they find, the more recently the rock has been exposed near the surface. Using the technique, they show that the 4-billion-year-old lakebed rock drilled by Curiosity was uncovered between 30 million and 110 million years ago as winds sandblasted away 2 meters of overlying rock. An ideal drill site

"Our mission is turning a corner. We are beginning to map a way forward, a way to explore deliberately for organic matter ... on Mars."

**—JOHN GROTZINGER,
CALIFORNIA INSTITUTE OF TECHNOLOGY**



Pay dirt. Curiosity drilling revealed once-habitable lake muds and a hint of organics.

would be tens of millions of years fresher, but it's a start.

"It gives us a rational way to look for organics on Mars," Grotzinger says. So next time, Curiosity's handlers will just look for a sign of recent wind erosion, such as a step up in the rock, nuzzle the rover up to the step, and see just how freshly exposed the rock is. Voilà: a whole new approach to prospecting for past life on the Red Planet.

—RICHARD A. KERR

Advocates Protest the Cost of a Hepatitis C Cure

For disease advocates, the U.S. Food and Drug Administration's 6 December approval of what promises to become a blockbuster drug against the hepatitis C virus (HCV) was bittersweet news. Sofosbuvir, made by Gilead Sciences of Foster City, California, works better than anything on the market: It's effective against most HCV variants and will help rid the body of this liver-damaging virus more quickly and safely than existing drugs. What rankles advocates is its price—each pill costs \$1000, and the drug must be used for at

Borders (Médecins Sans Frontières [MSF]). "We are really convinced that this drug can revolutionize the way we treat HCV in low- and middle-income countries."

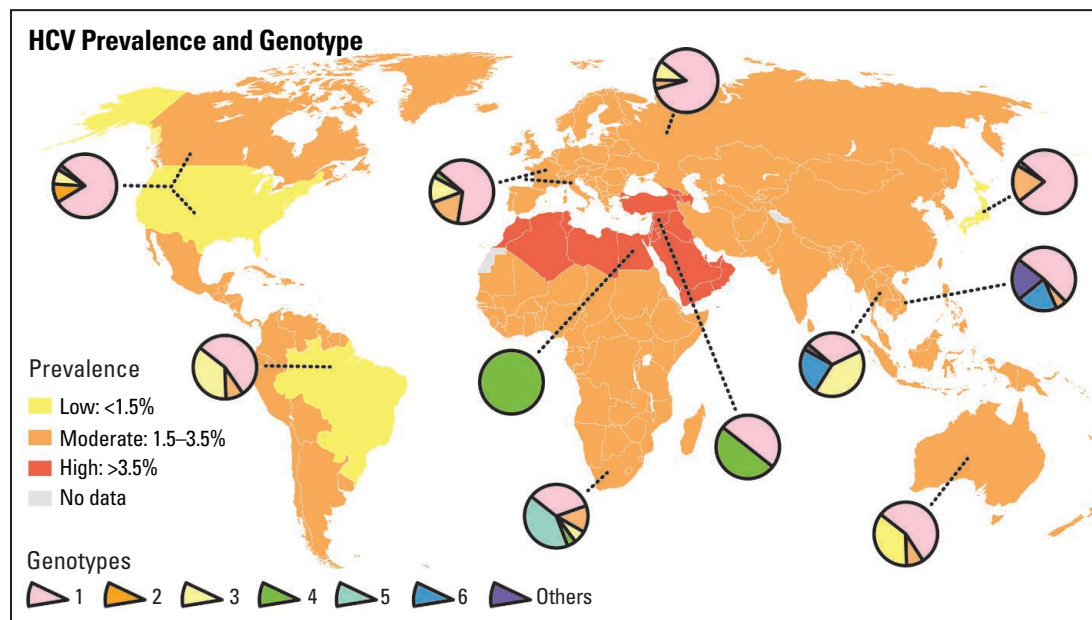
Meyer-Andrieux says that Gilead seems receptive to differential pricing, a strategy the company uses for its anti-HIV drugs. Gregg Alton, Gilead's executive vice president for corporate and medical affairs, wrote in an e-mail to *Science* that the company hopes "to develop an appropriate access and pricing strategy" and "greatly values" input from

than 50% of those with genotype 1, which infects about 70% of the estimated 3 million people in the United States with hepatitis C. In the past 3 years, three drugs have come to market that directly attack HCV and reduce treatment regimens to 12 to 28 weeks, but they are approved only to treat genotype 1, some have serious side effects, and cure rates are, at best, 80%.

Gilead's sofosbuvir cripples an HCV enzyme, polymerase, that the virus needs to copy itself. The drug cures roughly 90%

of genotype 1, 2, and 4 infections in 12 weeks with relatively minor side effects, when given with ribavirin and, for genotypes 1 and 4, interferon injections. It's also approved for use in combination with ribavirin for genotype 3, although efficacy is slightly lower and treatment takes 24 weeks.

The drug's performance in early studies led Gilead in January 2012 to pay a staggering \$11.2 billion to purchase the small company that first made it. But Meyer-Andrieux argues that the full-price sales of the drug in wealthy countries will offer the company ample



least 12 weeks—which will put it out of reach of most of the more than 100 million people in resource-limited countries who need it. "It doesn't matter how great these drugs are if no one can have them," says Tracy Swan, who works with the Treatment Action Group, a New York City nonprofit whose members successfully battled big pharma as leading AIDS activists in ACT UP.

In an unusual move, Swan and other HCV advocates have been imploring Gilead to offer a lower price to cash-strapped countries right from the start. They want to avoid a repeat of what happened during the early days of the AIDS epidemic, when it took years—and many protests and lawsuits—before the poor had access to lifesaving antiretroviral drugs. "We want the drug now—not in 15 years," says Isabelle Meyer-Andrieux, a clinician based in Geneva, Switzerland, who works for the Campaign for Access to Essential Medicines run by Doctors Without

advocates. "Providing treatment in resource-limited settings presents complex challenges and we understand the concerns that have been raised," he wrote.

HCV, which can cause life-threatening cirrhosis and liver cancer, infects an estimated 130 million to 185 million people—and 90% of them live in poorer countries (see map). It's mainly transmitted through contaminated blood transfusions or syringes shared by injecting drug users, but sexual transmission can occur, too. There are six main viral variants, called genotypes, which respond differently to treatments. New drugs are desperately needed.

Until 2011, the only treatment was an unpopular 48-week regimen that combined injections of interferon with ribavirin pills, which boosted the immune system and had some nonspecific antiviral effect but didn't directly attack HCV. The treatment often had severe side effects and cured fewer

profit. "They don't have to treat so many patients to reimburse the \$11 billion," she says. A 20 November investor report from Credit Suisse bank, subtitled "The HCV Revolution," suggests sofosbuvir's sales in wealthy countries in 2014 alone could total \$3 billion.

"The drugs are extremely cheap to make," contends Andrew Hill, a pharmacologist at the University of Liverpool in the United Kingdom. Based on the raw ingredients, the steps in the chemical synthesis, and molecular similarities to anti-HIV drugs, Hill and his colleagues concluded that it costs \$68 to \$136 to manufacture enough sofosbuvir to treat a person for 12 weeks. MSF suggests that diagnosing and curing an HCV infection should cost developing countries no more than \$500.

Hoping to pave the way for an inexpensive generic version of sofosbuvir, another nonprofit is challenging Gilead over its Indian

patent application, a strategy that also proved successful with anti-HIV drugs. The Initiative for Medicines, Access & Knowledge (I-MAK) in New York City filed an “opposition” to the Indian sofosbuvir patent application on 21 November, contending that sofosbuvir is a slight variation on an earlier patented drug that had activity against HCV and thus is not novel. Gilead did not respond to *Science*’s question about the I-MAK opposition.

Many expect that sofosbuvir will prove even more powerful when combined with one of several other anti-HCV drugs in late-stage development. Meyer-Andrieux of MSF says the group is also trying to establish differential pricing for those drugs, and ultimately hopes to convince companies to coformulate one pill that works against all genotypes. “We would very much like to take the best drugs and combine them and escape

from big pharma monopoly strategies,” Meyer-Andrieux says.

When a short course of pills can cure all HCV infections, demand for treatment will intensify further, says David Thomas, who treats hepatitis C at Johns Hopkins University in Baltimore, Maryland. Says Thomas: “I can’t imagine anyone who won’t want the cure.”

—JON COHEN

ANCIENT DNA

Fossilized Teeth Offer Mouthful on Ancient Microbiome

LONDON—In pretoothbrush populations, a thick, visible crust of calcium phosphate, food particles, and trapped microorganisms often marred gumlines. Dental calculus, or tartar, still plagues many, and dentists attack it with metal picks and abrasives. “It’s a meandering line of caramel-colored, cementlike material,” says Christina Warinner, an anthropologist at the University of Oklahoma, Norman. “It’s quite gross.”

It can also be a treasure for those studying ancient DNA. At a recent meeting here,* researchers noted that the microbial DNA preserved in ancient dental calculus—and in equally prosaic human coprolites (fossilized or preserved feces)—carries a record of the communities of bacteria that lived in and on people who died hundreds or thousands of years ago. “I think it’s the biggest untapped resource in ancient DNA,” says Laura Weyrich, a microbiologist at the University of Adelaide in Australia, who co-authored a paper on DNA in calculus from fossilized teeth earlier this year (*Science*, 22 February, p. 896). “We’ve just scratched the surface.”

The microbiome, the myriad bacteria that naturally inhabit our mouths, guts, and other tissues, is increasingly recognized as a vital component of human health—and disease. Researchers want to know how thousands of years of civilization have changed this invisible ecosystem, for good or for ill, and ancient samples can offer a window on the past. “By better understanding the natural [microbiome] state, we can better understand the diseases of civilization we’re struggling with today,” suggests Cecil Lewis, a molecular anthropologist at the University of Oklahoma, Norman.

They already have some tantalizing

results. At the meeting, Warinner noted that her studies of calculus from ancient humans show that genes associated with resistance to the antibiotic tetracycline, widespread in modern samples, were once scarce. And earlier this year, Lewis reported that 1400-year-old ancient coprolites found at a site in Mexico yielded DNA from spirochetes, a kind of bacteria not found in most modern human guts—but present in remote, rural populations recently studied in Africa and South America. “We have this spirochete found on two separate continents, with the commonality being rural populations—one of them from 1400

of biological material, she and Lewis are building a special “high-biomass” ancient DNA lab at Oklahoma.

As always in ancient DNA, contamination is a worry. Studying ancient dental calculus is “a good approach, but it’s not bulletproof,” says veteran ancient DNA researcher Eske Willerslev of the University of Copenhagen.

To sort environmental microbes from original inhabitants of the calculus, Weyrich “fries” fossilized samples under ultraviolet light for 15 minutes, then soaks them in bleach for another 5 to kill anything on the outside. The samples are then pulverized under sterile conditions and sequenced.

Researchers can also match the DNA of microorganisms they find in ancient samples with libraries of sequences of known microbial communities, such as the gut microbiome. “If you compare it to soil and water and the sample still looks gutlike, that’s a good sign,” Lewis says.

At her talk in London, Warinner also described comparing microorganisms from the inner dentin of a fossilized tooth, which is open to the environment after death, to those from the crust of preserved plaque just a few millimeters away. “They’re quite distinct,” Warinner said. Dental calculus “samples greatly resemble human oral microbiome samples ... whereas our dentin sample resembles things like ground water, soil, and leaf litter.”

Until now, archaeologists and conservators often removed calculus to better study a human skeleton’s teeth, and simply discarded it. “It was always the thing that got in the way,” says Amanda Henry of the Max Planck Institute for Evolutionary Anthropology in Leipzig, Germany. She hopes they’ll now put away their dental picks. “We had no idea how informative it could be.”

—ANDREW CURRY



Tooth pick. A researcher looking for ancient DNA samples dental calculus from a 1000-year-old tooth found in Peru.

years ago,” Lewis says. “Now we can ask, ‘Why is it there?’”

Well-preserved human coprolites are rare and prone to contamination. Calculus, on the other hand, is nearly ubiquitous on ancient human teeth. Researchers hope to dissect its fine layers to see how the microbiome changes over an individual’s lifetime, but it is so rich in genes that they can be overwhelmed. “In some samples, the DNA concentration in ancient dental calculus is as high as in fresh human liver,” Warinner says. To deal with the surfeit

*Ancient DNA: the first three decades, Royal Society, London, 18–19 November.



Fish-eye view. Hidden genetic variation in typical *Astyanax mexicanus* (top) may quickly lead to eye loss in cavefish populations (bottom).

EVOLUTION

Cavefish Study Supports Controversial Evolutionary Mechanism

To the classic case studies of evolution, such as Darwin's finches and the peppered moth, a small group of researchers would now add the Mexican tetra. This small, freshwater fish is mostly found as a drably colored inhabitant of creeks and rivers. But at least a half dozen times, populations have taken up residence in caves, where they have been transformed. They remain the same species, but are now eyeless and nearly albino.

On page 1372, a research team presents evidence that a controversial evolutionary mechanism was at work in the adaptation of the blind cavefish to their lightless environment. Nicolas Rohner, an evolutionary geneticist at Harvard Medical School in Boston, and his colleagues found that in the sighted tetras, a molecule called heat shock protein 90 (HSP90) masks variation in genes, such as those governing the size of the fish's eye. The team proposes that the stresses of cave life disturbed the function of HSP90 and unmasked the genetic variation, providing a rich template upon which natural selection acted. The study bolsters those who have long believed HSP90 is an evolutionary force, says Kazuo Takahashi, a quantitative geneticist at Okayama University in Japan. "Its impact is huge."

In 1998, biologist Susan Lindquist, now at

the Massachusetts Institute of Technology in Cambridge, and her colleagues were the first to propose that HSP90 acts as an evolutionary "capacitor," by analogy to the electrical storage device. They showed that some fruit flies making less HSP90 than normal developed bizarre-looking eyes, legs, and other traits. Lindquist suggested that HSP90 normally masks underlying mutations, which are revealed in its absence.

HSP90 is a so-called molecular chaperone, which ensures proteins take on and maintain their correct shape, even if their amino acid sequence varies slightly because of mutations. By doing this for proteins important for development, the researchers proposed, HSP90 could theoretically hide the existence of accumulated mutations. Reduce its presence in an embryo, and the effects of those mutations would appear—providing grist for natural selection. Skeptics criticized the fruit fly studies as too artificial, however, and similar findings in a plant by Lindquist's team won few converts.

Then Lindquist heard about the unusual Mexican blind cavefish and wondered if their eyes, like fruit fly eyes, were under HSP90's influence. She approached Rohner and his Harvard boss, developmental biologist Cliff Tabin, who had long studied these fish, and

convinced them to investigate.

When Rohner treated fish embryos with an inhibitor of HSP90, some fish developed larger or smaller eyes and eye sockets than untreated fish, consistent with the idea that the chaperone masked phenotypic variation. Breeding the small-eye fish resulted in young that had small eyes as well, indicating that the size was genetically based.

Rohner then looked for an environmental stressor that might naturally release such variation and found that the underground water was much less salty than the surface water. When he placed surface fish embryos in water of such low salinity, the adults developed eyes and eye sockets that varied in size. In caves, smaller eyes should require less energy to grow and use, and thus would likely be favored by natural selection, Rohner suggests. "What is beautiful about this paper is that the HSP90-dependent change resembles a natural adaptation," says Christine Queitsch, a geneticist at the University of Washington, Seattle.

To some biologists, the cavefish study is persuasive that HSP90 acts as an evolutionary capacitor in a natural setting. "This is a superb example of a full circle, starting from lab results, making a controversial hypothesis, and testing it in the wild," says Ritwick Sawarkar, a molecular biologist at the Max Planck Institute of Immunobiology and Epigenetics in Freiburg, Germany. This "will pave a way for further research in many other species in [the] wild." Lindquist is pleased as well. "It's a capstone, establishing that [HSP90] can explain a lot of complex evolution in higher organisms," she says.

Others are cautious. "The story of HSP90 and its relations with evolution is more complex," suggests Maria Pia Bozzetti, a geneticist at the University of Salento in Lecce, Italy. She suspects that the loss of HSP90 promotes new genetic variation by releasing mobile DNA elements called transposons.

Although the study showed that HSP90 is important to development, "its contribution to the evolution of eye loss is still unclear," says Takahashi, who thinks that many evolutionary capacitors may exist. Other distinctive aspects of the blind cavefish, such as their color, weren't under the chaperone's control. "HSP90 is by far the strongest candidate, but by no means the only candidate, to buffer variation," Sawarkar agrees. **—ELIZABETH PENNISI**

ASTRONOMY

Europe Readies Peerless Star Mapper

Think of it as 19th century astronomy, refined for the 21st. Victorian astronomers spent countless hours glued to brass transit telescopes, meticulously measuring the positions of stars. Such sky mapping—known as astrometry—went out of fashion in the 20th century, as scientists pursued exotic prey such as pulsars, quasars, gamma ray bursts, and black holes.

Now, it is decisively back in vogue. This month, a spacecraft called Gaia will roar into space from the European Space Agency's (ESA's) spaceport in Kourou, French Guiana. There, the €450 million satellite will systematically scan the sky, mapping the positions and motions of a billion stars in the Milky Way.

Gaia is following a path blazed in the early 1990s, when an orbiting ESA observatory called Hipparcos plotted high-accuracy positions of more than 118,200 stars and fixed another 2.5 million at lower accuracy. Hipparcos data are still yielding insights about the dynamics of our galaxy and the life histories of stars. But with 200 times the accuracy of Hipparcos, "Gaia is going to change everything," says Gerry Gilmore, U.K. principal investigator for Gaia and a professor in the University of Cambridge's Institute of Astronomy. "We'll find out what the Milky Way is made of and where it came from."

Gaia is due to take off on 19 December for a point in space known as L2, a gravitational null point 1.5 million kilometers from Earth. Once there, the spacecraft will rotate once every 6 hours, scanning the sky with its two telescopes. The scopes focus light onto a billion-pixel detector. Gaia can fix positions with an accuracy of five-billionths of a degree of arc—measured with an Earth-bound telescope, that's the width of a shirt button on the surface of the moon.

As it spins, the satellite will record stars' positions against the background of more distant stars; it will repeat the measurements 6 months later, when it has moved around to the other side of the sun. In a phenomenon

known as parallax, the stars will seem to shift position; nearby stars will shift more than distant ones do, allowing Gaia to calculate their distances. By repeating the measurements many times, Gaia will also be able to tell how stars are really moving through space.

The results should give astronomers front-row seats on an intricate cosmic ballet. Hipparcos data—which covered only part of the Milky Way near Earth—revealed that the overall gravity of the galaxy is not the only factor governing how stars move, as scientists had assumed. Instead, groups of stars coax one another into very complex collective motions. "They hunt in packs. This was a completely unexpected discovery," Gilmore says.

With Gaia's data on 1 billion stars—1% of the Milky Way's population—researchers will be able to study "some extremely complicated motions," says Michael Perryman of Princeton University, former project scientist for both Hipparcos

composition that Gaia's spectrophotometer can detect. In the galactic halo, the diffuse ball of stars that stretches far above and below the galactic disk, "you will see streams [of material] indicating it was part of a dwarf galaxy eaten by the Milky Way," says Timo Prusti, ESA's Gaia project scientist.

On a smaller scale, accurate distance fixes will help researchers calculate the true luminosities and sizes of individual stars—key data for studies of stellar evolution. And by detecting the wobbling of stars due to the pull of unseen orbiting companions, Gaia can look for exoplanets. Astronomers have detected hundreds of them from the ground by measuring wobbles back and forth along the line of sight. Gaia will make it possible for the first time to detect side-to-side wobbles as well. "It is very difficult to do, but we will have sufficient accuracy," Prusti says. Researchers estimate that Gaia could detect a thousand or more exoplanet systems and help determine the masses of planets discovered by other instruments, such as NASA's Kepler satellite.

Gaia will also play a key role in firming up the cosmic distance ladder, a suite of methods used for gauging distance far across the cosmos, beyond the range of parallax. One

key method uses stars called Cepheid variables, stars that pulse at a frequency that varies with their intrinsic brightness. Astronomers measure a Cepheid's period to derive its true brightness, then determine the distance to the star—and its host galaxy—by comparing its true brightness with what is observed. But this yardstick has shaky foundations, and astronomers would like to calibrate it with other distance measurements.

"The present way we do it is based on a few data points," Gilmore says—the handful of Cepheids that are close enough to measure with parallax. "Gaia will give precision measurements on some 4000 Cepheids," he says.

Astronomers are still mining Hipparcos's data 20 years after the mission ended. Prusti estimates that Gaia's will still be sparking discoveries 50 to 100 years after its instruments go dark. "We are really making building blocks for many fields of astronomy," he says.

—DANIEL CLERY

	Hipparcos	Gaia
Operation	1989–1993	2013–2018
Launch mass	500 kg	2030 kg
Sample population	100,000 (position)	1 billion (position) 150 million (radial velocity)
Position accuracy	2 milliarcseconds	24 microarcseconds

Megamappers. Hipparcos proved the value of space-based astrometry; Gaia will map the Milky Way.

and Gaia. The spiral arms are "a very complicated arena," Perryman says, in which stars bob up and down inside a galactic disk that is actually two disks, one thick and one thin. Extrapolating back from stars' current motions, astronomers hope to trace how the galaxy formed under the influence of dark matter, map out dark matter's 3D distribution, and even get hints as to what it is made of.

Gaia scientists will also be looking for evidence that the Milky Way has grown by consuming other small nearby galaxies. Such galaxies might have telltale differences in



The Thousand-Year Graveyard

Scientists uncover a tortured history of disease and death from the Middle Ages onward

BADIA POZZEVERI CHURCHYARD, ALTOPASCIO, ITALY—On a hot afternoon in July 2012, Giuseppe Vercellotti was digging up bones near the wall of an abandoned medieval church here, thinking about getting a cold drink, when he heard his students call his name. Faces glistening with sweat, they told him that they had found something strange buried half a meter down. Vercellotti took a look and saw a layer of lime, used in ancient times to squelch the stench of rotting corpses. When he tapped the hard layer with his trowel, it sounded hollow. “We immediately thought it was a mass grave,” says Vercellotti, a biological anthropologist at Ohio State University, Columbus, who co-leads a field school here. “We instructors were all excited and hopeful.”

But the students were apprehensive: “They all started talking about possible contagion,” Vercellotti says. Unconcerned, he leaned deep into the trench,

where he got a whiff of a pungent odor and spotted an elbow bone poking out of the lime that had sealed it like a cast. The layer spoke of bodies tossed into a pit and hastily covered with lime. Could this trench hold victims of the Black Death, the plague that killed half of Europe in the Middle Ages?

It was the end of the summer field season. So the team carefully covered the trench with tarps and went home, hoping that excavations in 2013 would show that they had struck gold. They had come to expect extraordinary finds in the graveyard of the now decrepit Abbey of St. Peter, where a bountiful store of ancient skeletons was laid to rest in a single place over 1000 years, from the 11th to the 19th centuries. The goal of the ongoing project is to read the history written in these bones: when and where these people were born, what they ate, what diseases they suffered and died from, and how their

Online
sciencemag.org



See special
multimedia
feature at <http://scim.ag/1000yrgrave>.

CREDIT: FRANCESCO COSCHINO



Hasty burial. An elderly woman, buried with a gold earring, was entombed in lime, suggesting she died during an epidemic.

health varied by social class and over time. “This is a superb opportunity to learn about life in the medieval period and how it evolved and changed over that time and into the Renaissance and Industrial era,” says project co-leader Clark Spencer Larsen, a biological anthropologist at Ohio State.

Helped by locals who house and feed 30 students for 6 weeks each summer, the interdisciplinary team of 12 researchers is now in its third year of excavations. Their work is set apart not just by the extraordinary site but also by the variety of tools used to learn the secrets of the bones, from scanning them with 3D computed tomography to extracting isotopes from the teeth. In an unusual

collaboration, this year the team brought along an ancient DNA expert to sample for ancient pathogens.

Because the abbey stood beside an ancient pilgrimage route, the results could help track the spread of disease through Europe. DNA from ancient microbes could also help today’s medical researchers keep one step ahead of fast-evolving diseases like cholera and influenza. “What you’re seeing at Badia Pozzeveri is hypothesis testing not only on bones, but also using pathogens and cultural factors,” says bioarchaeologist George Armelagos of Emory University in Atlanta, who is not part of the project. “It’s going to be the poster child for future work in bioarchaeology.”

The Burials Begin

1039 to 1300 C.E.

One afternoon while the students ate lunch, University of Pisa archaeologist Antonio Fornaciari gave a tour of the trenches, pointing to a freshly excavated stone wall beneath an asphalt parking lot in area 4000 (see graphic). In the 12th and 13th centuries, this wall ran along the inner sanctum of the monastery. Monks of the Camaldolese branch of the Benedictine order lived here, surrounded by a tall wall and moat, at the edge of marshes and oak woods, according to the town’s official history.

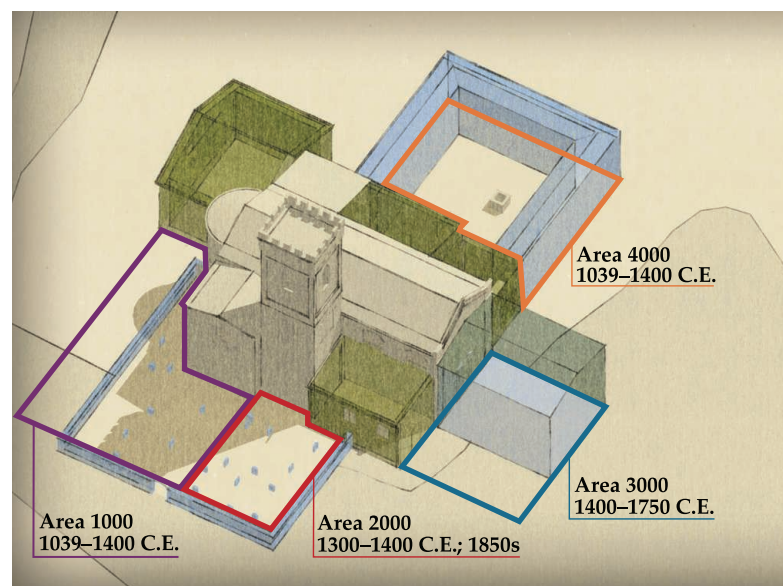
In this courtyard, the team found two partial skeletons, buried between 1200 and 1300 C.E. in a place of honor that suggests they were monks. The anthropologists are now examining their remains to answer a key question: Did monks have better health than farmers or peasants?

Stature is one clue to health, and most medieval Europeans were short. European men averaged 167 centimeters in the Middle Ages (compared with 178 cm today), and shrank by 5.4 cm by the

end of the period. The team thinks that with the rise in population, more people competed for food and resources. The bones at Badia Pozzeveri could confirm a trend toward scarcer food and worse health as the Middle Ages progressed.

The bones could also show whether monks were exceptions. Historical records suggest monks did eat better than peasants—and that both had poorer diets and health than nobles. To begin the analysis, Vercellotti laid out the leg bones of one monk on a table in the makeshift lab inside the church, below a ceiling covered with faded frescoes. He measured the lengths of thighbone and shinbone and made a “very preliminary” height estimate of 165 to 170 cm. A better estimate might give him a clue to the monks’ status: High-status medieval men buried in one churchyard in northern Italy averaged 171 cm, while lower status men averaged 164 cm, according to a study he published in 2011 in the *American Journal of Physical Anthropology*. The team has also dug up the likely remains of peasants, probably dating from the 11th century—two poorly preserved skeletons found outside the wall—and they’re hoping for more.

Pilgrims also passed right by the church as they followed the main highway of the Middle Ages, the Via Francigena or “road that comes from France.” Knights, clerics, and peasants all traveled this route, leaving traces such as two rare Islamic jugs from North Arabia, found



Through the ages. Over 1000 years, people were buried in different areas around the Abbey of St. Peter in Tuscany. The church complex evolved from its medieval heyday (transparent blue) to a smaller church (gray) and outer buildings (green).

in the cloister this summer. With the travelers came new diseases. Leprosy, for example, may have arrived from the Middle East with the Crusaders. It swept into Tuscany in the 12th century, when four leprosariums sprang up in the area, including one run by the monks. The pilgrims probably also spread many diseases including smallpox, measles, tuberculosis (TB), and typhus.

Those are just the sort of infectious company that Hendrik Poinar seeks. An ancient DNA expert at McMaster University in Hamilton, Canada, he jumped at the rare chance to get DNA from pathogens over time in a single location. He wants to see how many diseases people of each period had to combat and how fast pathogens evolved in different conditions, such as famine and war.

One morning, as Poinar watched, Vercellotti and a graduate student laid out one skull after another on a long table. Poinar looked at the excellently preserved teeth in a freshly excavated jaw. Teeth are a promising source of ancient DNA. “This is it—this is what we came for,” he said.

“Dig in,” said Vercellotti, holding a skull steady. Poinar adjusted his facemask, pulled up his rubber gloves, and yanked a tooth out of a jaw with pliers. “Skilled dentistry,” he joked. If he does get DNA from these teeth, he’ll test it for everything from leprosy to plague to TB.

Online: maps of the Via Francigena and a video reconstruction of the Badia Pozzeveri monastery through the ages.

The Worst Century

1300 to 1400 C.E.

The next day, Poinar knelt head down over a trench in area 2000, trying to excavate a jaw with teeth protruding from the wall of the pit. The team hadn’t yet gotten radiocarbon dates from this trench, but they thought it might be from the 14th century, a time of devastating infections including the Black Death, which killed half of Europe from 1348 to 1350. The teeth glistened in the dirt wall, but the jaw was firmly embedded. “I’ve been drooling over them for 4 days,” Poinar said.

Earlier that week, he had explained why. He gave a presentation in the church and flashed a slide about a news story about a plague-infected squirrel that closed campgrounds near Los Angeles. “Killer squirrels are coming!” he joked.

But it’s no joke to ask if killer strains of plague could return. In 2011, Poinar was part of a team that gathered ancient DNA from people who died in London between 1348 to 1349, apparently of plague. The scientists identified the cause of the Black Death as the bacterium *Yersinia pestis*, rather than anthrax or a mix of pathogens, as some had suspected. This ancient strain was almost identical to a *Y. pestis* strain that still circulates in small rodents in the southwestern United States, Africa, and Asia. But today, *Y. pestis*, although still deadly, infects only



Dental technicians. Hendrik Poinar (left) and Giuseppe Vercellotti extract ancient teeth from jaws for DNA analysis.

about 1000 to 3000 people annually and is transmitted slowly from person to person.

Why is this *Y. pestis* strain so much less virulent today, and why does it only rarely move from rodents to humans? Poinar is one of several geneticists in a neck-to-neck race to find out. They’re trying to learn when and why the Black Death strain jumped from rodents to humans, and what made it spread so rapidly. Was it mutations in the genome of *Y. pestis* or changes in the susceptibility of animal or human hosts—or both? “If we study humans before, during, and after the plague, we should see how the human genome responded to these repeated outbreaks and the response in bacteria,” Poinar says.

That’s why he is seeking the Black Death in Badia Pozzeveri, where cases were recorded in 1348 before the epidemic reached northern Europe. He’ll compare that strain—newly arrived from Asia—with that of the London victims to see if the plague evolved as it tore through Europe. He also can see if plague victims suffered from TB or other infections, to test the idea that 14th century people harbored so many pathogens that they were more susceptible to plague.

Another theory behind the deadliness of plague is that it was

hard for anyone in Europe to survive that terrible century. Before the plague hit, the continent had been pounded by bad weather, failing crops, famine, and war. Torrential rains in 1315 and 1316 flooded crops and caused the Great Famine. The Little Ice Age had begun, triggering frigid winters that destroyed more crops. In England, between 1348 and 1375, life expectancy at birth was only 17 years, according to parish records. Overall health, as shown by seven indicators in teeth and bones, plummeted to an all-time low in the 14th century, according to a study of 17,250 individuals from 100 locations in Europe by Ohio State economic historian Richard Steckel, Larsen, and their colleagues in the Global History of Health Project (*Science*, 1 May 2009, p. 588).

Disease may even have influenced the outcome of battles among the Italian city-states, which came right to the doorstep of



Buried treasure. Hendrik Poinar hopes to recover DNA from ancient microbes from a jaw stuck in the side of a pit.

the church at Pozzeveri. In September 1325, Florence's commander Ramon de Cardona camped at the abbey with most of his 3000 cavalry and 15,000 infantry. The nobles moved into the monastery itself, while the troops probably camped in a field west of the church, near what was then a large lake and swamp. Many got sick.

That may be why Cardona made a move that still puzzles historians: He lingered at Badia Pozzeveri for two long weeks while his rival, the legendary Castruccio Castracani from Lucca, recruited reinforcements. Castracani had far fewer troops at first. But by the time Cardona advanced on 23 September, Castracani's army outnumbered the Florentines, many of who retreated before the battle had even begun. It was a rout, and Castracani became a hero whose military victories were immortalized by Machiavelli.

Just what sickened Cardona's men? Fornaciari suspects malaria because they complained of *mala ariæ*, or bad air. He convinced Poinar to test for that disease, too. "One of our hopes is to discover if malaria is present in the medieval period," Fornaciari says, because it is not clear when the illness first reached Tuscany.

Another hope is to find the remains of those who died in that famous battle, because relatively few groups of soldiers killed in war have been found in Europe, Larsen says. Three spearheads have turned up so far in area 4000. Human remains would provide the first good physical "record of injuries from the kinds of weapons available in 1325," Larsen says. "They were doing some really horrible things to each other. They had this square hammer-headed mace for bashing in skulls."

Online: more images from the dig and a narrated slideshow on the quest for ancient pathogens.

Noble Secrets

1400 to 1600 C.E.

One July morning, project co-director Gino Fornaciari dropped by the church. There he found his former student, Vercellotti, examining teeth with Poinar. "Why are the teeth so good?" Poinar asked. Fornaciari replied: "They're young. The teeth are good because the normal age of death was 40." He pointed out that the tooth wear can also reveal whether someone ate many tough grains such as coarse millet, or a more refined, soft diet.

When it comes to reading the signature of disease and foul play in the bones of ancient people, Fornaciari is the master. A professor in the medical school at the University of Pisa and the father of team member Antonio Fornaciari, he's famous for investigating the lives and deaths of the ancient nobility of Italy, including the Medici of Florence, who lived just 60 km from Badia Pozzeveri.

This site offers him and the others a rare chance to examine the health of commoners as well as nobles during the Renaissance. They have already found people of various social classes, buried in area 3000 from 1500 to 1700. One woman was buried with her spectacles—an expensive and treasured accessory—and several skeletons were interred in a costly stone-lined vault inside the ancient church. But most of the bones were buried in wooden coffins outside the churchyard and probably were those of poorer rural people, whose daily lives are less well known than the nobility of cities.

Commoners' bones will provide a counterpoint to Fornaciari's work elsewhere revealing the woeful condition of the well-fed nobility. In Naples, he examined the mummy of Maria d'Aragona, a noblewoman who lived from 1503 to 1568 and was a famed beauty in her youth—but was obese at death. That fits with what he has learned about her fellow nobles' diet. In 2008, Fornaciari analyzed carbon and nitrogen ratios in bone collagen from other princes of Naples and the Medici of Florence, and found that they had as much nitrogen in their diet as carnivorous mammals. Clearly, Renaissance royalty ate unhealthy quantities of meat at a time when many rural people struggled to get enough calories.

Nor was rank a protection against horrific infectious diseases. When Fornaciari cut off a linen bandage from Maria d'Aragona's arm, he discovered a large ulcer. He examined the tissue with a scanning electron microscope and rinsed it with antibodies that fluoresce in the presence of the bacteria that cause

Behind the smile. Isabella d'Aragona (right) had teeth blackened by mercury, used as a treatment for syphilis. The mummy of Maria d'Aragona also revealed signs of the disease in an ulcer on her arm (below).



syphilis, *Treponema pallidum*. The tissue was so well preserved that he could detect the spiral shape of the bacteria; he sent tissue to Poinar to confirm the diagnosis. Poor Maria also harbored human papillomavirus in a venereal wart—the first diagnosis of this sexually transmitted, cancer-causing disease in the tissue of a mummy, Fornaciari reported in a 2006 paper.

Sexually transmitted diseases were common in Renaissance Italy. Syphilis raced through the country in the 1500s, possibly after Spanish sailors brought a new venereal form from the New World. Fornaciari also examined Maria's distant relative, Isabella d'Aragona, who was also buried in Naples. She was married to the Duke of Milan and is thought by many to be the model for Leonardo da Vinci's Mona Lisa. When Fornaciari looked closely at this lady's teeth, he found that they had been abraded to remove most of the enamel. The remaining enamel traces were black, a sign that she

had taken mercury, which was then used—ineffectively—to treat syphilis. Lab tests confirmed that the black patina had a high level of mercury and that Isabella d'Aragona was poisoned by her own medicine, dying at age 54 in 1524.

By comparing the teeth and bones of urban nobles with those of Pozzeveri peasants, the team hopes to see how social rank affected health. The teeth of the noblewomen are less worn, because they ate a softer diet with meat, whereas poorer women and children often ate coarse millet. Vercellotti and Larsen expect to see more disruptions in tooth growth, caused by lack of food during childhood, in the peasants. With the graveyard's large sample sizes, they hope to compare the men and women of Badia Pozzeveri to see who was better fed.

Online: medical files on Maria and Isabella d'Aragona and how archaeologists spot disease in skeletons.

The Mass Grave

1850s

Almost a year after Vercellotti first tapped his trowel on the bed of lime, he and a crowd of students set to the task of systematically uncovering the entombed skeletons in area 1000. They chipped away the cementlike lime and tried to avoid inhaling the powdery white dust. Once they broke through the shell in early July, they brushed and scooped away the soil, sometimes with teaspoons. They found that each skeleton was buried separately, but all were blanketed in lime.

One skeleton clutched a cross, head to the side, jaw agape. Another



Perfect fit. Giuseppe Vercellotti put a jaw and skull from the mass grave back together to study it.

had a twisted spine, likely evidence of scoliosis. All had been buried in shrouds and were lying in unusual positions as though they had been dumped hurriedly. Everything fit the hypothesis that they were victims of an epidemic.

The researchers carefully uncovered another exceptionally complete skeleton—an older woman, as shown by her frail bones and worn teeth. She was lying on her side, probably in the same position in which she died. In the soil beneath her, they could see the impression of her fingers and ear, and the lines left by her bodice's laces. "I loved excavating her," Vercellotti said. "She was beautiful," Gino Fornaciari

agreed. Beneath her skull, they found a single, golden hoop earring, and they began to call her the Lady with the Gold Earring.

That earring was a clue: This was no medieval matron. The hoop style, as well as buttons and fasteners for clothing found with other skeletons, showed that these people died in the mid-1800s—too late to be victims of the Black Death. So what did kill them?

To find out, Poinar and Vercellotti pulled teeth from their skulls and scooped soil from where their stomachs once lay, seeking to sample and identify the pathogen's DNA. They already have a working hypothesis: cholera.

In 1855, this terrible diarrheal disease, transmitted by the waterborne bacterium *Vibrio cholerae*, swept through Italy, part of a worldwide pandemic. Poinar is just as eager to find DNA from *V. cholerae* as from plague, because tracing the evolution of cholera is still urgent today.

Like other pathogens, *V. cholerae* keeps evolving into new forms, and it continues to erupt into worldwide pandemics. Since the 1960s, the seventh known pandemic has infected 3 million to 4 million people and killed nearly 100,000 every year, with a new strain causing particular devastation in Haiti recently. If researchers can trace the bacterium's evolutionary history, they might be able to identify the key mutations that trigger virulence or adaptation to different habitats, for example. This could help them design better vaccines or medicines.

Poinar has already sequenced a sample of mid-19th century cholera from the United States. The researchers gathered DNA from a cholera victim's intestines, which in 1849 were preserved in jars in the Mütter Museum in Philadelphia. Their unpublished results match that strain with those that caused pandemics from 1899 to 1923; all these strains differ from the El Tor strain that swept Haiti last year.

If Poinar gets cholera DNA from Pozzeveri, it will let him compare the Philadelphia *V. cholerae* genome with one from the same time but a different place.

After extracting DNA from many of the 40 teeth he gathered at the site, Poinar sent samples to the Lawrence Livermore National Laboratory in California. There, the DNA is being scanned with a new microarray that can detect DNA from 3000 different pathogens, including the microbes that cause plague, TB, malaria, syphilis, Lyme disease, and cholera.

Despite the unexpected bonus of a probable cholera epidemic, Poinar was still intent on finding plague victims. On his last day at the site, he kept going back to the medieval trench, where the teeth peeped tantalizingly from the wall. Vercellotti gently brushed dirt off the jaw and sprayed it with water, hoping to loosen the sediment. But the jaw wouldn't budge. He finally gave up. "Next year," he

promised. Poinar left Italy still haunted by hopes of a plague sample.

Two weeks later, when he returned to his lab in Canada, he got a tiny package from Vercellotti. It held the tooth he had wanted so badly. Vercellotti had managed to excavate it in the season's final week, and its DNA is now being analyzed.

—ANN GIBBONS

Online: video of the excavation of the Lady with the Gold Earring and a slideshow of one skeleton's story.

CREDIT: WILLIAM SCHERLIS

Stefan Behnisch

And the Good Client

The German architect is recognized for his smart, sustainable buildings.
But an innovative science lab also requires a good partner

The warning signs were there, Stefan Behnisch says. “We used to meet every 6 weeks with the college trustees, and suddenly I couldn’t meet with them,” recalls the burly 56-year-old German architect.

Amherst College, an elite liberal arts college in western Massachusetts, had hired Behnisch in 2010 to design a new integrated science building. The college wanted to replace the Merrill Science Center, an ugly box built in the 1960s that devours a quarter of Amherst’s total energy bill. In addition to a bigger and more energy-efficient building, trustees wanted one that would foster communication among faculty and students as well as enhance the nearly 200-year-old campus, which offers breathtaking views of the surrounding New England hills.

To make it happen, college leaders turned to Behnisch, who has won acclaim for designing innovative, sustainable, and attractive corporate and academic buildings throughout Europe and, more recently, in North America. “He unites high design and high performance, and he’s been at it for decades,” says Alan Brake, editor of *The Architect’s Newspaper*, a New York-based trade publication. Behnisch’s solution for Amherst (see p. 1313) was an airy, four-story structure of glass, steel, and concrete, terraced into a hill and chock-full of the latest energy-saving technologies.

Amherst brass were initially enthusiastic. President Biddy Martin called the design “a visionary testament to the power and importance of science education and research in a liberal arts college,” and the college’s director of admissions said it was “the single most important decision the college has made” to attract top students. Indeed, a standout building can give academic institutions an edge in the increasingly competitive race for talented students and world-class faculty. And a science building, often the largest academic structure on campus and its biggest consumer of energy, can be the ideal show place for a school’s commitment to sustainable architecture and innovation.

But the college’s enthusiasm waned once preliminary work began on the site, which stood in the center of campus near some temporary student housing. And on 1 May, Behnisch got a phone call that, despite the warning signs, caught him by surprise: Amherst was canceling the \$260 million project and ending its 3-year relationship with Behnisch.

The decision, Martin announced the next morning, was made because of steadily rising costs and concerns about the disruption to campus life during the 2 years of construction. In October, she announced that the college had chosen another site for the building and would select a new architect. Behnisch was disappointed, of course. And he strongly disagrees with how Martin described the project’s costs and construction plans. But the episode also served to remind him of the profession’s maxim that a good building requires a good client. “A good client is someone with whom you

can have a good discussion,” Behnisch explains. “You don’t seduce them. You try to convince them, and sometimes they convince you. There has to be a good match”—especially when the building is architecturally and technologically ambitious.

The family business

To an outsider, Behnisch’s decision to become an architect may have seemed pre-ordained. His father, Günter Behnisch, was one of Germany’s most prominent architects, having designed the main stadium for the ill-fated 1972 Olympic Games

in Munich and West Germany’s parliament building in Bonn. His sister, brother-in-law, and several cousins are also architects, as is his wife.

But Behnisch, whose physical bulk belies a soft-spoken demeanor and an understated personality, had to do it in his own way. “I didn’t want to follow their expectations,” he says. “Childish, I know, but that’s the way it is.”

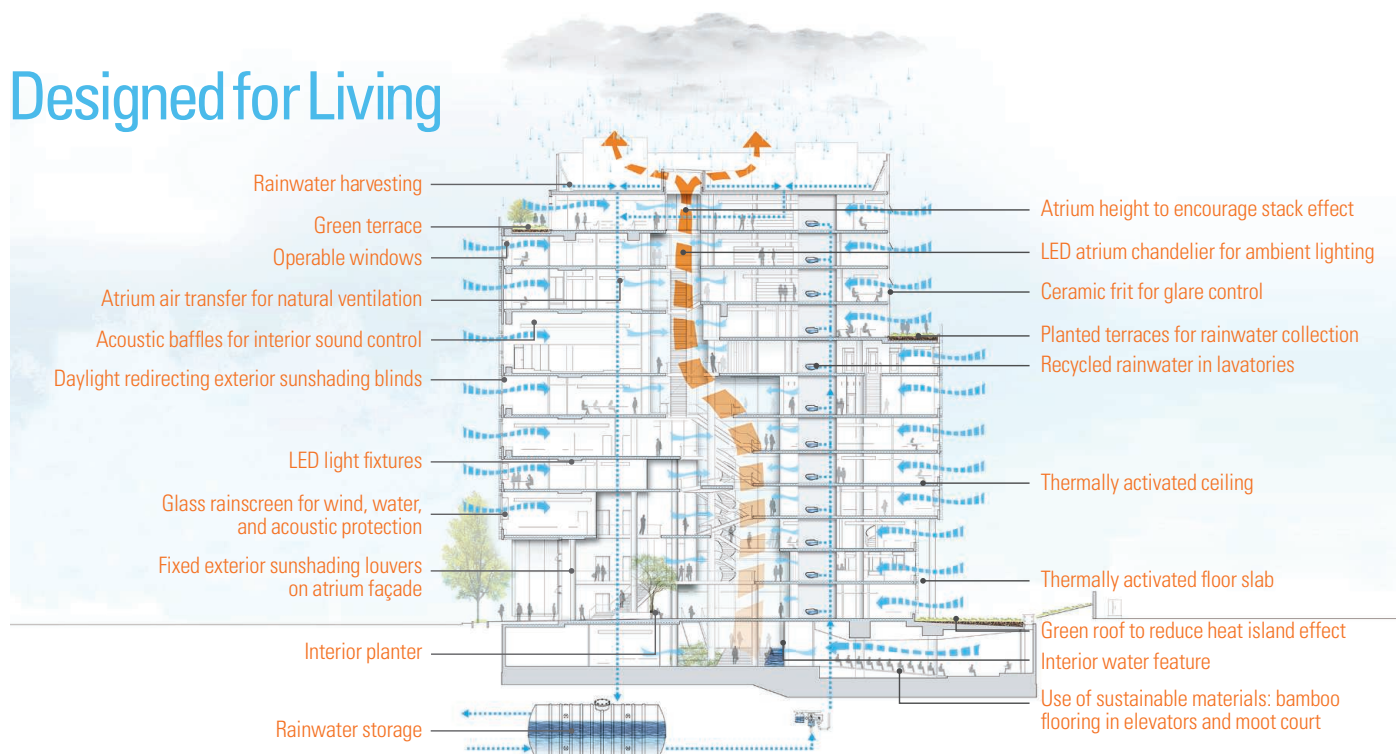
That independent streak led him to study philosophy with the Jesuits and then to earn an undergraduate degree in economics. Eventually, however, he returned to the fold, spending a year in the United States before joining his father’s firm in Stuttgart. In 1989, Behnisch founded his own firm, which now has satellite offices in Munich and Boston.

After designing dozens of critically acclaimed buildings for corporate and academic clients throughout Europe, including several laboratories, Behnisch crossed the Atlantic and made a splash with his first U.S. project. Robert Campbell, architecture critic for *The Boston Globe*, says the 12-story headquarters for the Genzyme



Looking ahead. Stefan Behnisch visited Harvard Yard in 2006 for ideas on how to design the science complex on the university’s new Allston campus.

Designed for Living



A healthy environment. A schematic (above) of the University of Baltimore's new law center features many of the components that Behnisch sees as essential

for a smart, sustainable building. The 12-story, \$114 million building (pictured below) opened in April 2013.

Corporation in Cambridge, Massachusetts, which opened in 2003, is "probably the best office space ever created" in the Boston area. Sustainable building guru Jerry Yudelson writes in a new book on the world's greenest buildings that Genzyme is proof "it's possible to construct an architecturally exciting, beautiful, and employee-friendly building that makes economic, social, and environmental sense."

Behnisch applied those same principles to his first research laboratory in North America, the \$80 million Terrence Donnelly Centre for Cellular and Biomolecular Research at the University of Toronto. The result is a skinny, 12-story tower—sited on a former loading dock—that has become one of the most popular spaces on campus since it opened in 2005. "It works wonderfully," says James Friesen, professor emeritus of microbiology and a prime mover behind the center, where he occupies a ninth-floor office that looks out on one of three indoor gardens.

Sustainable buildings

Although an office building or research lab can become a second home to those who work there, it has a far larger audience—those who pass it every day on their way to somewhere else. "Architecture is our living room. It's part of the public realm," Behnisch explained during a keynote address this fall in Chicago at a conference on building façades.

He had that larger audience in mind in the Amherst project. "Merrill had to disappear because it was too big, too ugly, and it's an energy hog," he says with characteristic bluntness.

Part of the challenge "was to make the building part of the landscape and not part of the built environment," he adds, so his 20,400-square-meter structure—5600 square meters larger than Merrill—was tucked into a terraced hillside to minimize its visual

footprint. Just as important, the new building would create additional vistas to the New England hills from inside and atop the building, rather than block those views, as Merrill does.

Another requirement—to make it more sustainable—was something that comes naturally to Behnisch. "Germany has been on the leading edge of sustainable design for decades, and Stefan is a leading proponent," says Brake of *The Architect's Newspaper*.

The new building abounded in energy-saving features (see diagram, above). They included green roofs merging into hillside foliage, LED lighting, radiant heating and cooling in the ceilings and floors, and exposed concrete slabs in the lab to reduce temperature fluctuations. A multistory atrium would admit daylight, improve ventilation, and encourage interaction between students and faculty.

Behnisch is a leading proponent of an industry-wide move to place more and more of a building's mechanical and environmental systems in its outer skin. "The façade is becoming a very complex structure," Behnisch told the architects, engineers, and builders gathered in Chicago. "It is ventilation, daylight enhancement, and sunshading. We also produce energy through the façade." The benefits of having smaller,

decentralized systems ripple across the building and include increasing usable space and improving the working environment. "It means we don't have as much noise as before," Behnisch explained. "We don't have the ductwork, and we don't need the air shafts."

One persistent criticism of sustainable buildings is that they cost more to erect. But Behnisch says that isn't necessarily true. "The construction manager [on the Amherst science building] calculated that it would be cheaper to build with the sustainability features than without them," he says. "Can you imagine that?"

Even if some features are more expensive initially, they may save



money in the long run. Speaking about the LED lighting for his latest building, a \$114 million law center at the University of Baltimore that opened in April, Behnisch says “we calculated that it would pay for itself in 4 years, and then every year after that they will save \$100,000.”

While the Amherst project gathered momentum, Behnisch was also engaged in what may be his biggest academic challenge: designing the science complex that will set the tone for the new, multibillion-dollar Allston campus at Harvard University. “When Harvard began planning its Allston campus, they looked at the bounce that MIT [Massachusetts Institute of Technology] had received for its Stata Center [a Frank Gehry–designed building for several academic departments that opened in 2004] and decided they would also look for well-known, internationally respected architects,” says James Collins, president of Payette, a Boston-based firm that specializes in science and high-tech buildings. (Collins also teamed with Behnisch on the Amherst project.) “And Stefan was on that list because of Genzyme and because of his passion and growing reputation for energy and performance.”

Behnisch’s original plans for Harvard, drawn up in 2006, featured a four-building science cluster that would be a focal point for Harvard’s growing efforts in stem cell research. The 2008 economic downturn caused officials to put the multibillion-dollar campus on hold, but the project has now kicked back into gear. The university’s School of Engineering and Applied Sciences is now expected to be the primary tenant for the science complex, and Behnisch is just beginning to meet with scientists before site work resumes next year.

The science complex will be the first visible result of a revised master plan that has been adjusted to reflect community sentiments. It has also created an internal competition that will shape the direction of the entire Allston campus. “If it is a successful building, the rest of the campus will be forced—or damned—to keep to the same standard,” Behnisch says. “And if it is not a good building, it will not be a good start for the Allston campus.”

An idea dies

For Amherst, Behnisch’s science center proved too much of a stretch. College officials declined repeated requests from *Science* to detail their thinking, but a spokesperson says the school has moved on. “We’ve turned the page,” says Peter Rooney, Amherst’s director of public affairs. “There were sound reasons for the shift in plans and

the new site. And we don’t want to be accused of being critical of Mr. Behnisch in public.”

However, insiders say a fierce debate took place behind closed doors between those who felt Behnisch’s innovative design was worth preserving and those who felt Amherst should stick to the tried and true. “It was a breakout building, that’s for sure,” says one knowledgeable observer who requested anonymity. Fitting such a large building into a small campus also proved to be a stumbling block. Behnisch had arranged for a two-step process. Faculty would move their labs and offices into the new building, located next to Merrill, once it was 70% completed. Merrill would then be torn down, and the rest of the building finished. That way, faculty would have to move only once.

But Behnisch’s efforts to address campus concerns weren’t enough. Faculty and students were already unhappy with the noise and congestion from preliminary site work, and some had complained that the building’s extensive use of glass didn’t afford them sufficient privacy. In addition, the leadership team that had hired Behnisch left midstream—Martin arrived in 2011, and the board of trustees turned over the next year.

Still, even as the tide began to turn against him, Behnisch hoped that his reputation for fiscal responsibility and collegiality would carry

the day. “He’s not a profligate spender,” says editor Brake. “He’s also no Howard Roark,” referring to the protagonist in *The Fountainhead*, Ayn Rand’s novel about an idealistic architect with a huge ego.

Instead, Behnisch says he watched with growing frustration as college officials pushed to make the building more conventional. “All the sustainable aspects were thrown out,” he says. “They didn’t want LED lighting. They didn’t want slab heating

and cooling, even though today it is state of the art, because they said it was too complex. In the end, the building died by a thousand cuts. And that was probably for the best.”

Robert Bogomolny, the president of the University of Baltimore and a huge fan of Behnisch’s work, says he can imagine the pressure on college leaders as the controversy escalated. But he thinks they made the wrong call.

“When you have an architect who’s asking you to do something you’ve never done before, there is a lot of room for tension,” he says. “But if you hire a world-class person, you ought to listen to him. I wish they would have let Stefan build his building, because it would have been better than what they are going to get now.”

—JEFFREY MERVIS



Not to be. Amherst has scrapped Behnisch’s plan for a new science building tucked into a hillside.



Successful debut. Behnisch’s first U.S. project, the Cambridge headquarters of the Genzyme Corporation, has become a benchmark for sustainable buildings.





LETTERS

edited by Jennifer Sills

Health Information and the Like

IN THEIR REPORT "SOCIAL INFLUENCE BIAS: A RANDOMIZED EXPERIMENT" (9 August, p. 647), L. Muchnik *et al.* explore whether Internet rating dynamics are influenced by the online community. They found that a comment that is initially slightly popular, regardless of credibility or quality, is more likely to garner even more "likes." The study results "demonstrate that whereas positive social influence accumulates, creating a tendency toward ratings bubbles, negative social influence is neutralized by crowd correction." This study reveals that social influence substantially biases ratings in systems designed to aggregate online opinions.

Social media sites that aggregate online opinions are increasingly popular among the public for dissemination of health information (1, 2). Unfortunately, a study examining the 2009 H1N1 epidemic found that tweets that had a negative sentiment about influenza vaccination were more likely to be retweeted than tweets supporting vaccination (3, 4). Also, unexpectedly, tweets promoting vaccine use increased the likelihood of negative tweets against vaccine use (3). Surprisingly,



in contrast to the findings by Muchnik *et al.*, it appears that "crowd correction" may actually obfuscate social media health communications in certain situations (5). Social influence bias in health communications could potentially be detrimental to public health.

Erroneous health information propagated by social media can endanger patient safety (6). Public health entities should consider the effects of social influence bias in health communications. In addition to promoting positive health messages on social media, public health strategies must also limit the spread of "popular" but erroneous health information (4).

ANAND REDDI

University of Colorado School of Medicine, Anschutz Medical Campus, Aurora, CO 80045, USA. E-mail: anand.reddi@gmail.com

References

1. B. W. Hesse *et al.*, *Arch. Intern. Med.* **165**, 2618 (2005).
2. W.-Y. S. Chou, Y. M. Hunt, E. B. Beckjord, R. P. Moser, B. W. Hesse, *J. Med. Internet. Res.* **11**, e48 (2009).
3. M. Salathé, D. Q. Vu, S. Khandelwal, D. R. Hunter, *EPJ Data Sci.* **2**, 10.1140/epjds16 (2013).
4. K. S. Yoshida, *ARS Technica*, "When it comes to vaccination, bad news is contagious" (<http://arstechnica.com/science/2013/04/when-it-comes-to-vaccination-bad-news-is-contagious/>).
5. M. Salathé, S. Khandelwal, L. A. Meyers, *PLOS Comput. Biol.* **7**, e1002199 (2011).
6. E. Campbell, M. Salathé, *Sci. Rep.* **3**, 10.1038/srep01905 (2013).

Response

REDDI'S THOUGHTFUL COMMENTS HIGHLIGHT the importance to global health policy of understanding the spread of health behaviors in society. Social media sites and online communication platforms are becoming increasingly popular sources for the dissemination of health information about prevention, medical conditions, and treatments. They are therefore central to the promulgation of beliefs about health threats and the efficacy of health interventions. To explain the critical points of divergence between our results and Reddi's conclusions, we must critically evaluate the scientific evidence.

First, ours is a randomized experiment, whereas the studies to which Reddi refers rely on observational data to make claims about information diffusion (the authors of those studies are careful to note that their evidence is predictive rather than causal). Our

approach, which randomly manipulates the ratings of online content, holds author and content effects constant, isolating the causal effect of upvoting or downvoting on opinion and behavior change. For example, the studies Reddi refers to analyze whether negative or positive content about vaccinations is more likely to be retweeted. They do not exclude several likely alternative explanations of retweeting behavior that may have nothing to do with whether negative tweets are actually changing people's opinions about vaccinations. The majority of Twitter users may already have a negative opinion of vaccinations, inspiring more retweets of such content.

The evidence Reddi cites shows that negative information spreads farther and faster. Our experiment shows that negative information is less likely to change people's opinions than positive information. These two claims

are not contradictory. In fact, they are complementary pieces of evidence in a broader story of information diffusion and behavior change. Observational data about and simulations of information diffusion are useful for understanding how information and awareness spread (1, 2), but causal inference is necessary to understand how information diffusion subsequently changes opinions and behavior (3–5). Combining causal analysis of

Letters to the Editor

Letters (~300 words) discuss material published in *Science* in the past 3 months or matters of general interest. Letters are not acknowledged upon receipt. Whether published in full or in part, Letters are subject to editing for clarity and space. Letters submitted, published, or posted elsewhere, in print or online, will be disqualified. To submit a Letter, go to www.submit2science.org.

behavior change with predictive analysis of information diffusion creates a powerful lens through which to understand the ebbs and flows of behaviors on our planet.

Second, analogies between ratings systems and Twitter will always remain loose at best. Collective opinion rating aggregates and presents the opinion of the community about specific content. Voters are likely motivated by the hope that their vote may influence the opinion of other readers. (Re)tweeting information on Twitter is also likely motivated by the desire to maximize publicity for certain information, the desire to become known as a curator of certain information, and the desire for personal exposure. Ratings are anonymous and do not push information to one's "followers," making these motivations less likely in ratings systems than on Twitter. The influence mechanisms in these scenarios differ as well. Twitter users are not privy to collective opinion on a topic when they tweet about it, whereas they are precisely aware of collective opinion when they vote on or rate an item. Thus, the motivations for diffusing information and rating it likely differ.

Perhaps more important, differences in the designs of these systems could drive differences between our results and results from studies of Twitter. Whereas the system we studied enables users to either upvote, downvote, or abstain, there is no feature analogous to the downvote on Twitter. The user can only choose to either retweet or not. Facebook operates similarly: One can like content, but not dislike it. Our results generalize to collective opinion aggregation and ratings systems; results from studies of Twitter likely generalize to microblogging and networked information dissemination systems.

SINAN ARAL,^{1*} LEV MUCHNIK,² SEAN TAYLOR³

¹MIT Sloan School of Management, Cambridge, MA 02142, USA. ²School of Business Administration, The Hebrew University of Jerusalem, Mount Scopus, Jerusalem, 91905, Israel. ³NYU Stern School of Business, New York, NY 10012, USA.

*Corresponding author. E-mail: sinan@mit.edu

References

1. E. Adar, L. A. Adamic, in *The 2005 IEEE/WIC/ACM International Conference on Web Intelligence* (Compiègne, France, 2005), pp. 207–214.
2. S. Aral, M. Van Alstyne, *Am. J. Soc.* **117**, 90 (2011).
3. S. Aral, L. Muchnik, A. Sundararajan, *Proc. Natl. Acad. Sci.* **106**, 21544 (2009).
4. C. R. Shalizi, A. C. Thomas, *Soc. Meth. Res.* **40**, 211 (2011).
5. S. Aral, L. Muchnik, A. Sundararajan, *Network Sci.* **1**, (2013).

Setting the Course for a Green Internet

IN HIS PERSPECTIVE "TOWARD A GREEN Internet" (29 March, p. 1533), D. Reforgiato Recupero reflects (partially) some of the ideas and even the wording of the ECONET project's Description of Work (DoW) (1), first published on 6 September 2010. However, the general philosophy of the ECONET Consortium is much broader than described in the Perspective, and we agree with the critical comment (2) that interest in reducing the impact of the Internet on the environment is not a recent development.

Apart from Data Centers, which were not part of the ECONET mandate, all network segments ranging from the home network to metro/transport and core networks were considered in the DoW, and optimization methods were considered for each [see (3), which is also the source for the figure shown in the Perspective]. ECONET has recently been working toward implementation of a Network Connectivity Proxy (4), which allows user

devices to be kept in a resting (low-energy) state by maintaining all vital network operations on their behalf. We have always emphasized the tradeoff between energy efficiency and performance: Examples of device-level and network-wide energy-aware optimal management and control strategies can be found in (5) and (6), respectively.

Finally, a fundamental aspect to our project that was not discussed in the Perspective is the need to provide standard interfaces between algorithms for management and control and a variety of hardware. The ECONET proposed solution—the Green Abstraction Layer (7)—is currently under consideration for standardization by the European Telecommunications Standards Institute. Although the ECONET project approaches its end after 3 years of activity, network power management technologies are becoming a reality in a number of network devices, as witnessed by industrial prototypes (8), which demonstrate reductions of at least 50% in power consumption.

RAFFAELE BOLLA^{1,2} ROBERTO BRUSCHI,^{2*} FLAVIO CUCCHIETTI,³ FRANCO DAVOLI^{1,2}

¹Department of Electrical, Electronic, Telecommunications Engineering, and Naval Architecture (DITEN), University of Genoa, 16126, Genoa, Italy. ²National Inter-University Consortium for Telecommunications (CNIT), University of Genoa Research Unit, 16126, Genoa, Italy. ³Telecom Italia Labs (TILabs), 10148, Torino, Italy.

*Corresponding author. E-mail: roberto.bruschi@cinit.it

References

1. ECONET (low-Energy CONsumption NETWORKs) Project, Grant Agreement no. 258454, Annex I, "Description of Work," European Commission, 6 September 2010 (available from the authors upon request).
2. Comment on D. Reforgiato Recupero, *Science* **339**, 1533 (2013); <http://comments.sciencemag.org/content/10.1126/science.1235623>.
3. R. Bolla, R. Bruschi, F. Davoli, F. Cucchietti, *IEEE Commun. Surveys Tutorials* **13**, 223 (2011).
4. R. Bolla, M. Gribaldi, R. Khan, M. Repetto, "Network connectivity proxy: An optimal strategy for reducing energy waste in network edge devices," *Proc. 24th Tyrrhenian International Workshop on Digital Communications (TIWDC 2013)—Green ICT*, Genoa, Italy, 23 to 25 September 2013.
5. R. Bolla, R. Bruschi, A. Carrega, F. Davoli, *IEEE/ACM Transactions Networking*, **10**, 1109/TNET.2013.2242485 (2013).
6. E. Niewiadomska-Szynkiewicz, A. Sikora, P. Arabas, J. Kołodziej, *Concurrency Comput. Practice Experience* **25**, 1738 (2013).
7. R. Bolla et al., *IEEE Internet Comput.* **17**, 82 (2013).
8. ECONET Demos (www.econet-project.eu/Public/Demo).

CORRECTIONS AND CLARIFICATIONS

News & Analysis: "Old dogs teach a new lesson about canine origins" by E. Pennisi (15 November, p. 785). The caption for the photograph of the buried dog in Illinois stated that the dog is 1000 years old; the dog is 8500 years old. The HTML and PDF versions online have been corrected.

Association Affairs: "What's so special about science (and how much should we spend on it?)" by W. H. Press (15 November, p. 817). In Fig. 2, the labels for Germany and Switzerland should be reversed, as well as the labels for Italy and Hungary and for Spain and Czech Republic. The HTML and PDF versions online have been corrected.

News of the Week: "Whose brain is it anyway?" (8 November, p. 678). The central brain in the caption was mislabeled as belonging to Conrad Heinrich Fuchs, but it was Carl Friedrich Gauss's. Also, the son of Rudolf Wagner who likely mixed up the brains 150 years ago was Hermann, not Thomas. The HTML and PDF versions online have been corrected.

Reports: "Femtosecond visualization of lattice dynamics in shock-compressed matter" by D. Milathianaki et al. (11 October, p. 220). Two equations were incorrect in the text. The correct equations are $\Delta\theta \sim \tan\theta_0 \sin^2\theta_0 \times \epsilon_r^n$ (sixth paragraph of text) and $\Delta\theta \sim -\tan\theta_0 \times \epsilon_r^n$ (seventh paragraph of text). The HTML and PDF versions online are correct.

Reports: "Functional extinction of birds drives rapid evolutionary changes in seed size" by M. Galetti et al. (31 May, p. 1086). Point 16 in Fig. 1 was slightly misaligned. The PDF and HTML versions online have been corrected.

Perspectives: "Toward a green Internet" by D. Reforgiato Recupero (29 March, p. 1533). The figure credit was missing. It should be "The original figure appears in: R. Bolla, R. Bruschi, F. Davoli, F. Cucchietti, *IEEE Commun. Surveys Tutorials* **13**, 223 (2011), as Figure 11 on p. 230." The HTML and PDF versions online have been corrected.

Finding Best Practices for Fossil Fuel Extraction

WE WERE HAPPY TO SEE N. BUTT ET AL. DRAW attention to the issue of fossil fuel extraction and its potential effects on biodiversity worldwide in their Policy Forum "Biodiversity risks from fossil fuel extraction" (25 October, p. 425). For years, diverse conservation non-

governmental organizations and academic institutions have been working with extractive industries to incorporate best practices into their operations (1, 2). Many of these efforts have been focused on conventional petroleum extraction methods, and lessons learned from research done alongside extraction have been incorporated into international standards for best practices (3). Biodiversity can only benefit from increased involvement of biologists in the identification, avoidance, and mitigation of the effects of fossil fuel exploration and production.

Given the progress made thus far toward understanding the effects of conventional petroleum extraction, we propose that applied ecological research for conservation should expand immediately to areas with proven nonconventional fossil fuel reserves (such as oil sands, oil and gas shale, and coal bed methane). As conventional fossil fuel reserves reach their peak, the petroleum industry is



actively stepping up their efforts to develop technologically and economically feasible extraction of nonconventional reserves (4). We call on ecologists and conservation biologists to become actively involved in this transition and to increase efforts to work side by side with national governments, extractive industries, and other stakeholders.

In addition, although we agree that north-

ern South America and the western Pacific are important areas for biodiversity, we worry that the analysis presented is far too simplistic to be able to make robust recommendations on where efforts for best-practice enforcement should be focused, particularly when it comes to prioritizing some highly biodiverse areas above others. Any analysis of the pressures of fossil fuel extraction should include analysis of pressures from other sources (such as agricultural activities, legal and illegal extraction of renewable natural resources, lack of rigor in national legislation, and lack of enforcement) that could exacerbate biodiversity loss even when best-practice extraction is used.

JESSICA L. DEICHMANN* AND ALFONSO ALONSO
Smithsonian Conservation Biology Institute, Washington, DC 20013–7012, USA.

*Corresponding author. E-mail: deichmannj@si.edu

References

1. A. Alonso, F. Dallmeier, G. P. Servat, Eds., *Monitoring Biodiversity: Lessons from a Trans-Andean Megaproject* (SI Scholarly Press, Washington, DC, 2013).
2. J. Robinson, *Conserv. Biol.* **26**, 1 (2012).
3. International Finance Corporation, *Guidance Note 6: Biodiversity Conservation and Sustainable Management of Living Natural Resources* (Washington, DC, 2012).
4. R. J. Brecha, *Energ. Pol.* **51**, 586 (2012).

PHYSICS

Unnecessary Complexity

Daniel W. McShea

Entropy, order, information, computation, emergence, and free energy. These words and phrases should be banned from interdisciplinary discussions of complexity in the history of the universe. Free energy should be banned because it has a precise meaning in physics, while there is no cognate concept in biology or in any of the strictly human sciences. Entropy, information, and computation, because they have technical usages in physics and very different meanings outside of that field. And order and emergence, because no one knows what they mean.

As one might guess, I didn't understand very much in the physics papers in *Complexity and the Arrow of Time*. On the other hand, the few glimmers I got suggested some fascinating lines of thought. Eric Chaisson offers data showing a trend in what he calls energy rate density, understood as a proxy for complexity, over the history of life (and even over the much longer history of the universe). That's saying something. Only two other trends on the scale of life's history have been documented quantitatively—those in body size and in hierarchy or nestedness (prokaryotic cell, eukaryotic cell, multicellular individual, colony). Energy rate density is a fine candidate for a third.

Other intriguing notions from the physicists: Marcelo Gleiser has a view of organisms as self-sustaining soliton-like structures. Charles Lineweaver argues that the source of all organismal complexity must lie ultimately in the physical environment. (Related to this, biologist David Krakauer's later chapter discusses the progressive transfer in evolution of information from environment to genome, or in the case of humans, to brains via learning.) And Paul Davies presents a new-to-me argument that cancers are morphologically, behaviorally, and genetically more complex than the host tissue in which they originate. He speculates that this complexity arises from a cassette of genes that was active in an ancient ecology, in the earliest multicellular lineages.

I found the biological and philosophical papers more accessible. Here are some

teasers. Paleontologist Simon Conway Morris notes the obvious increase in complexity in evolution, writing that "Once there were bacteria, now there is New York." But he raises the possibility that life has found and refined essentially all of the main workable solutions to the problems of survival and reproduction, that life's diversity has saturated complexity space, and that complexity is nearing its limits. (He carves out one exception, neural complexity, which may not have reached its apothecosis in humans.)

In another fun paper, Stuart Kauffman argues that the well-defined spaces in which physics typically represents change are not available in evolutionary biology, because in biology the relevant variables involve function. Thus the transformation of a fish lung into a swim bladder brought into existence a possible habitat for a parasite that might evolve to live exclusively in swim bladders. Yet in a space defined by the properties of the original fish lung, the unique properties of such a parasite could not even be plotted, much less predicted. In evolution, Kauffman notes, "Not only do we not know what WILL happen, we don't even know what CAN happen."

Also engaging is philosopher William Wimsatt's treatment of what he calls generative entrenchment, the dependence of later stages in embryonic development on earlier stages. Entrenchment makes complexity possible, he argues. When dependencies are strong, variation in early stages is so disastrously maladaptive that natural selection acts powerfully to stabilize those stages, to standardize them. (It is no accident, he points out, that "[t]he ways in which we are conceived and born are much more similar than the ways in which we mature and die.") And when early development is standardized, it acts as a stable foundation on which higher levels of complexity can be built. The same logic explains, Wimsatt argues, why we standardize parts in industrial processes and words and rules of syntax in language.

The volume closes on a skeptical note, with theologian and philosopher Philip Clayton expressing doubt that a unified, interdisciplinary science of complexity is possible:

"On more skeptical days, I suspect that these various sciences have little more in common than the fact that they describe phenomena that we like to call 'complex.'" I think that he is right, that unity is unlikely, and for a number of reasons. Consider a point made by Michael Ruse in his chapter on complexity and progress. Ruse identifies two radically different approaches to complexity, the Darwinian and the Spencerian. The Darwinians believe that any notion of complexity must have some aspect of adaptation built into it. Brains and eyes are complex not just because they are intricate and differentiated but because of what they can do. In contrast, the Spencerians think of complexity as a

perfectly good concept in its own right—as a purely structural notion, independent of adaptation. To the Darwinians, Spencerian complexity looks impoverished, ignoring what is most important about organisms (i.e., adaptation). To the Spencerians, Darwinian complexity looks confused,

like an attempt to weld two disparate notions into one, making investigation of the relationship between them impossible. How to connect these disparate approaches? The chasm between them looks unbridgeable.

Another reason to doubt that unity is possible has to do with the putative evolutionary trend in complexity. Again there are two very different strategies at work. One assumes there has been a trend in some important aspect of organisms and invites us to call it complexity. In this strategy, we seek to discover what complexity is, to find out what has been increasing. The second strategy involves no assumptions about a trend, nor even about the reality of any grand notion of complexity. Instead, we start with simple variables, ones that are measurable (e.g., counts of cell types or number of interactions among genes), and then measure them to see how they behave in the history of life. Following this strategy, we may someday be able to ask about a connection between these variables and some larger notion of complexity. But that is a downstream question, one we may not be able to deal with for some time. Like the Darwinian and Spencerian strategies, these two do not look reconcilable. (Although perhaps it would be fruitful to pursue both strategies, in parallel.)

One last thought. If interdisciplinary communication is going to work, we need to avoid the language of equations and formalisms and speak instead in the language of example and analogy. My experience is that there are

Complexity and the Arrow of Time

Charles H. Lineweaver, Paul C. W. Davies, and Michael Ruse, Eds.

Cambridge University Press, Cambridge, 2013. 369 pp. \$30, £21.99. ISBN 9781107027251.

The reviewer is at the Department of Biology, Box 90338, Duke University, Durham, NC 27708, USA. E-mail: dmcshea@duke.edu

very few concepts in science that cannot be translated without loss into everyday terms. It takes some work, and some art, but it can be done. We should all try harder. And then there are those troublesome words, the ones I said should be banned. My suggestion was somewhat tongue in cheek, but it's not a crazy idea. Actually, there is one more word to add to that list. No one knows what this word means, and it is used too often in an unscientific way, as a placeholder for the ineffable, the quasimystical, the truly awesome. It is complexity. It's time to ban that one too. Just kidding. (Or maybe I'm not.)

10.1126/science.1245386

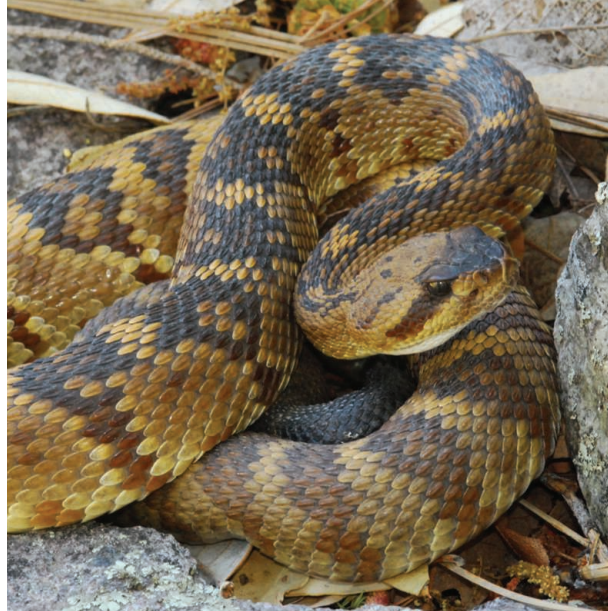
ECOLOGY

An Ode to Natural History

Frances Bonier

A mentor once cautioned me never to describe my research as “curiosity-driven,” lest I open my work up to critical attack. Such criticism centers on questioning the value of research without clear, direct benefits for human society. Funding agencies in many countries now call for increasingly tangible benefits of the research they support, and top academic jobs are increasingly targeted at systems, “-omics” (e.g., genomics, proteomics, and metabolomics), and computational biologists. All the while, opportunities for biologists driven by a curiosity about organisms in their natural environments are becoming scarce. Yet it is such curiosity that brought many of us to biology. And, as Harry Greene argues in *Tracks and Shadows*, human curiosity about nature might be fundamental to valuing and conserving biodiversity.

Greene's book reads as an ode to organismal biology; a defense of the value of basic natural history research; and a love story about snakes, wild places, and learning through the art of observation and inquiry. The book is far more than a memoir—as eclectic as its author (an ecologist at Cornell University), it encompasses biographical essays on friends and mentors, popular-



Appreciate, not eradicate. Black-tailed rattlesnakes (*Crotalus molossus*).

science writing about his beloved snakes, and philosophical ponderings of existential quandaries such as the meaning of wilderness and our place in nature. From vivid and touching stories about his experiences as an ambulance driver, to detailed descriptions of the biology and evolution of snakes, to appreciations on deserts and tropical forests, Greene engages readers from beginning to end.

Along this meandering path, common threads emerge: the importance of human relationships, an innate human curiosity for nature, and the complexity of our relationships with animals (particularly dangerous ones). Greene devotes much of his attention to this last theme, delving into the evolutionary history of our fascination for and fear of snakes, which he says derive from the multifaceted nature of our inter-

actions with these animals as food, competitors, and threats. In light of this complex relationship, he argues that snakes exemplify the links among research, education, and conservation. A quote borrowed from Senegalese environmentalist Baba Dioum summarizes Greene's basic thesis: “We will conserve only what we love, we will love only what we understand, and we will understand only what we are taught.” In his interpretation, natural history research provides the understanding that can create a deep appreciation for nature and motivate conservation, even in the case of snakes and other organisms with whom our relationships are complex and sometimes paradoxical.

Greene suggests that it is our innate fear of snakes and our ignorance of their lives as individuals that prevent many of us from appreciating them. His research and this book

address the second problem. In behavioral studies revolutionized by the use of telemetry for tracking individuals, he and his colleagues have documented sociality and maternal care in rattlesnakes, behaviors previously thought to be nonexistent in these “solitary” reptiles. By seeing in snakes behaviors that we value and understand, can we better appreciate them and even invest in conserving them? Perhaps so, but negative perceptions of venomous snakes remain the norm. “Rattlesnake roundups” are still held

every year in the American west and south, where thousands of rattlers are captured and killed in public spectacles [e.g., (1)]. Yet, snakes kill fewer than 10 people in the United States and Canada each year—fewer than are killed by domestic dogs (2). And, as Greene notes, these fatalities are often caused by bites from snakes that were intentionally handled. But such facts do little to counteract public opinion or our innate fear of snakes. Rather than combating deep-rooted negative perceptions with facts about relative risks, Greene promotes an approach of looking beyond our preconceptions and trying to understand what it means to be a predator. He reminds us that we, too, are predators with a long history of killing animals for food.

The book leaves us with questions to ponder but also with inspiration to indulge our curiosity for nature. This curiosity should not be viewed as an indulgence, nor curiosity-driven science in general seen as second tier to applied research. Instead, Greene argues, curiosity-driven investigations provide a critical contribution to the triumvirate of research, education, and conservation. As Greene writes, “In truth, we twenty-first-century humans are saddled with terrible dilemmas, willy-nilly shaping the future yet bereft of consensus over what to save, let alone how to do so. Amid shrinking resources, should we care more about pandas than crocodiles, especially if the latter eat us?” Driven by a curiosity for nature, and with efforts like *Tracks and Shadows*, perhaps we can learn to value the two equally.

References

1. <http://americanfestivalsproject.net/2009/03/18/the-worlds-largest-rattlesnake-roundup>.
2. A. Kasturiratne *et al.*, *PLOS Med.* 5, e218 (2008).

The reviewer is at the Biology Department, Queen's University, Kingston ON K7L 3N6, Canada. E-mail: bonierf@queensu.ca

10.1126/science.1247872

CREDIT: ROB DOBBS

ETHICS

The Bioethics Commission on Incidental Findings

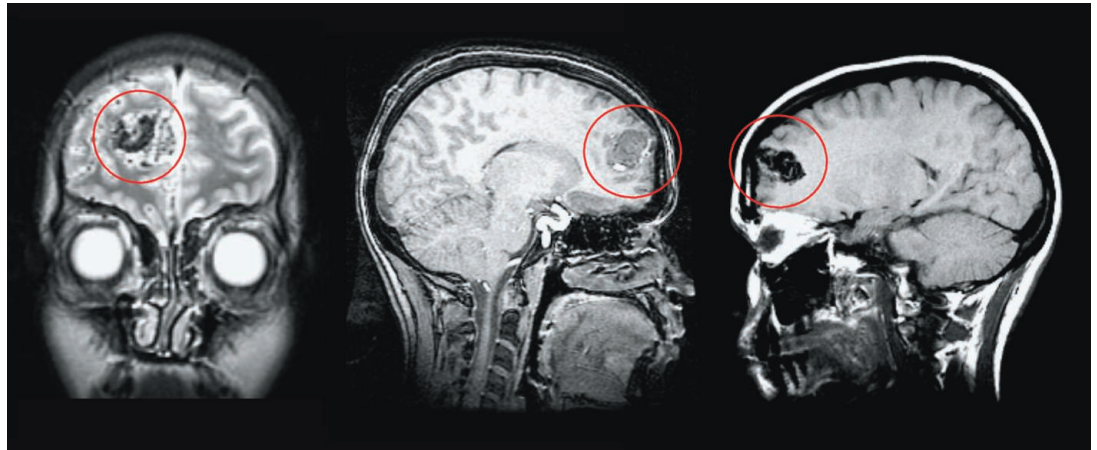
Amy Gutmann

Shared decision-making allows patients, participants, and consumers to decide what they do and do not want to know.

Dr. Sarah Hilgenberg believes that participating in a research study saved her life, although she had no reason to believe this when she enrolled. While examining functional magnetic resonance images collected during a memory study, researchers found an arteriovenous malformation, an abnormal connection between arteries and veins in her brain (see the image). Sarah had the mass surgically removed, and she recovered (1). Consider also a hypothetical case in which a routine computerized tomography angiogram turns up no clinically significant stroke warning signs but shows an unrelated nodule in the lung. During biopsy, the lung collapses, which leads to cardiac arrest and permanent anoxic brain injury. The nodule pathology report reveals benign inflammation.

Such discoveries—when physicians or researchers are looking for one thing and find something else—are known as incidental findings. Secondary findings raise related issues: They are not the primary target of testing, but (unlike incidental findings) they are actively sought. Improved technologies are making incidental and secondary findings increasingly common. They are becoming a growing certainty in clinical practice as well as in the distinct contexts of research and direct-to-consumer (DTC) testing.

A new report (2) by the U.S. Presidential Commission for the Study of Bioethical Issues offers specific recommendations across all three contexts and across a wide range of testing techniques (including large-scale genetic sequencing, testing of biological specimens, and imaging). These will help ensure that incidental and secondary findings are appropriately anticipated—so that



Functional magnetic resonance images showing an arteriovenous malformation in the brain of Sarah Hilgenberg (Reprinted by permission of S. Hilgenberg).

patients, research participants, and consumers are informed ahead of time about what to expect (including the unexpected)—and aptly communicated after they are found. When dealing with incidental findings, the commission's advice is to anticipate and communicate.

Unsettled Issues, Conflicting Advice

It would be rash—both ethically and practically speaking—to conclude that everything that can be sought should be sought, and reported, in all contexts. Results that are outside the original purpose for which a test or procedure is conducted might or might not possess important actionable implications for health and well-being. In some instances, incidental findings point to medical conditions for which there is currently no available treatment or might lead patients and their doctors to treat a condition that would be better left alone. Because there is no simple answer to the question of how best to manage incidental health information, there is much conflicting advice about whether to seek, and how to manage, incidental and secondary findings.

Recent reports from other federal advisory groups show how unsettled the issue is. One report recommended early cancer screening for heavy smokers (3). Another suggested that early scans could cause more harm than good by detecting too many prob-

lems (4); their argument is that overdetection leads to overtreatment, arguably making the treatment worse than the potential disease.

Incidental findings, whether or not anticipatable, give rise to a wide range of practical and ethical challenges for recipients and practitioners. Clinicians might discover misattributed paternity when assessing a living organ donor and potential recipient who believe they are biologically related. This is anticipatable because it is known to be a possible finding associated with the procedure. An unanticipatable incidental finding could occur when a DTC genetic testing company identifies a health risk based on a newly discovered genetic association that was not knowable at the time the sample initially was submitted. The commission's report examines both kinds of situations because they call for distinct actions before and after an incidental discovery.

The context in which incidental findings occur makes a considerable difference in how they can and should be handled. Clinicians have a primary fiduciary duty to their patients to act in their interests. Research investigators have more limited duties to research participants. Obligations of DTC providers toward consumers, beyond honest dealings, are most uncertain and in flux. Even within one of these contexts, not all individuals will have the same preferences

Chair, Presidential Commission for the Study of Bioethical Issues, Washington, DC 20005, USA, and President, University of Pennsylvania, Philadelphia, PA 19104, USA. E-mail: info@bioethics.gov

with respect to disclosure, and that too makes an important difference in how incidental findings should be handled.

Communication and Shared Decisions

The presidential bioethics commission concluded that some ethical mandates span all three contexts. The commission's first recommendation is that all practitioners—clinicians, researchers, and DTC companies—should anticipate findings and describe (wherever feasible) what incidental findings are likely to arise from the tests and procedures before they are conducted. Practitioners should inform individuals about their plan for disclosing and managing incidental and secondary findings, specifying what findings will and will not be returned.

To improve the ability to anticipate findings across all contexts, another recommendation is that federal agencies and other interested parties continue to fund research that keeps abreast of the rapidly evolving nature and frequency of findings from various modalities, along with the potential costs, benefits, and harms of identifying, disclosing, and managing the full range of possible findings. A third recommendation is to enhance the education of all stakeholders, including practitioners, institutional review boards, and potential recipients on this increasingly important issue.

In addition, the commission emphasizes the need—based on justice and fairness—not just for a privileged few but for all individuals to have access to up-to-date information and the guidance needed to make informed choices about what tests to undergo, what kind of information to seek, and what to do with information once received. Equity (along with regulatory parsimony, which supports efficiency) is far better served by increasing access to health care information and guidance for everyone rather than by restricting access.

As expert practitioners look for more findings when using techniques such as large-scale genetic sequencing, and as guidelines develop with suggestions for how these findings should be managed, some anticipatable incidental findings will become secondary findings (actively sought, although not the primary reason for undertaking the technique). Rounding out recommendations that cross all three contexts, the commission recommends that professional groups develop guidelines that are tailored to each common procedure or test to inform practitioners about the anticipatable incidental findings likely to arise. The commission drew upon the work of many scholars, professional

groups, and others who addressed incidental and secondary findings in a variety of contexts, including 16 U.S. professional societies and working groups, and 16 international professional societies and working groups. For example, the American College of Medical Genetics and Genomics (ACMG) released recommendations earlier this year (5) regarding incidental and secondary findings that arise in one specific context—the clinic—and with one modality—large-scale genetic testing.

The commission and the ACMG both emphasize the importance of informed consent of patients and open communication between providers and patients. In addition, both the commission and the ACMG emphasize the need for better data regarding incidental and secondary findings, and both recognize the evolving nature of developing guidance as science and technology advance.

Notably, the ACMG recognized that genetic variants of unknown significance, or associated diseases that are not amenable to treatment, should not be reported to patients. As the commission explains, clinicians owe a duty of beneficence to their patients, which can include avoiding causing distress without any corresponding benefit. The ACMG also has embarked on what the commission recommends: contributing its professional expertise to determining which genetic variants are clinically significant and actionable and making a list of those secondary findings.

On one point, the commission offers a different path. The ACMG recommended and later clarified that “patients cannot opt out of the laboratory’s reporting of incidental findings to the ordering clinician” (6). The commission recommends that clinicians engage in shared decision-making with patients before testing about the scope of findings that will be sought and communicated and further steps to be taken. Shared decision-making is a process by which clinicians and patients engage in a dialogue to arrive at pathways forward that reflect the best interests of the patient. Clinicians, the commission recommends, should respect a patient’s preference not to actively seek or know about incidental or secondary findings to the extent consistent with their fiduciary duty to do no harm.

There are multiple points at which a clinician’s ability to communicate effectively about incidental and secondary findings is important. Before testing, clinicians should alert patients to the possibility of discovering incidental findings, as well as any sec-

ondary findings that will be actively sought, so that patients have the opportunity to express their preferences about disclosure and subsequent management. Many patients will want their practitioner to tell them about any information discovered. Others might not want to learn about incidental or secondary findings.

A patient who does not wish to learn about information related to the primary purpose of the test should not undergo the test. If a patient wishes to opt out of receiving incidental or secondary findings that are clinically significant and actionable, then clinicians should exercise their discretion regarding whether to proceed with testing. Clinicians should explain the potential benefits of receiving such information about clinically actionable findings. Clinicians should also respect the informed preferences of patients, which can vary due to life circumstances and perspectives.

Consider this hypothetical example, reflecting one among several possible ethical outcomes of shared decision-making. For years, a nonagenarian patient has undergone many rounds of treatment for multiple cancers now thought to be in remission. After close consultation with her doctors, as well as just before her doctors prescribe a body scan after an accidental fall, she tells them that she does not want to know about incidental, possibly cancerous, masses on a scan conducted for other purposes. She feels strongly that she has undergone enough biopsies and other cancer treatments. Her doctors, who would decide differently on their own, fully respect her decision.

Within certain limitations, if clinicians feel uncomfortable with patients’ decisions not to receive such findings, they may on ethical grounds decline to perform the test and elect to refer the patient elsewhere. If they understand and respect their patients’ decision, they may ethically agree to perform the test but not return incidental or secondary findings. To help ensure an ethically defensible outcome, they need to take time to proactively confer with their patients.

Once clinicians discover and disclose incidental and secondary findings, they also must communicate with patients about various options for further pursuit of the finding. Clinicians should clearly convey to patients the possible outcomes of investigating an incidental finding, the possibility of discovering additional incidental findings, and the potential benefits and risks of either pursuing or not pursuing the finding. Payment systems should not discourage clinicians from taking sufficient time to fully communicate

to each patient this necessary information.

Clinicians are ethically free to filter incidental findings that have so little clinical significance that they would not actively seek them as secondary findings. Here, too, in keeping with shared decision-making, clinicians live up to their highest calling when they discuss how they will handle incidental findings with their patients.

References and Notes

1. S. Hilgenberg, "Recipient of a finding incidental to research," Incidental Findings in Research, presentation to the Presidential Commission for the Study of Bioethical Issues, 30 April 2013; <http://bioethics.gov/node/1617>.
2. Presidential Commission for the Study of Bioethical Issues, *Anticipate and Communicate: Ethical Management of Incidental and Secondary Findings in the Clinical, Research, and Direct-to-Consumer Contexts* (Presidential Commission for the Study of Bioethical Issues, Washington, DC, 2013).
3. U.S. Preventive Services Task Force Screening for Lung Cancer, Draft Recommendation Statement (AHRQ Publication No. 13-05196-EF-3, USPSTF, Rockville, MD, 2013); www.uspreventiveservicestaskforce.org/uspstf13/lungcan/lungcandraftrec.htm.
4. L. J. Esserman, I. M. Thompson, Jr, B. Reid, *JAMA* **310**, 797 (2013).
5. R. C. Green et al., *Genet. Med.* **15**, 565 (2013).
6. *ACMG Genet. Med.* **15**, 664 (2013).

10.1126/science.1248764

CLIMATE CHANGE

What Role for Short-Lived Climate Pollutants in Mitigation Policy?

J. K. Shoemaker,¹ D. P. Schrag,^{1*} M. J. Molina,² V. Ramanathan^{3,4}

Short-lived climate pollutants (SLCPs) include methane (CH₄), black carbon (BC), tropospheric ozone, and hydrofluorocarbons (HFCs). They are important contributors to anthropogenic climate change, responsible for as much as one-third of the current total greenhouse forcing (1). An emerging strategy, which we refer to as hybrid climate mitigation (HCM), emphasizes reducing SLCPs in parallel with long-lived carbon dioxide (CO₂) so as to achieve climate goals, as well as health and food security benefits, associated with some of the SLCPs. Proponents of HCM argue that we should focus substantial effort on reducing SLCPs now, as we wait for sufficient political will to reduce CO₂ emissions (2–4). But others (5) worry that any strategy involving SLCPs risks delaying efforts to reduce CO₂, the main greenhouse gas most important for long-term warming if emissions continue as projected.

We attempt to clarify this emerging HCM strategy. Reducing emissions of SLCPs is an essential component of any comprehensive climate action plan for addressing both near-term and long-term climate change impacts (1, 3). There are real opportunities to reduce emissions of SLCPs without distracting from other mitigation efforts focused on CO₂. But the dangers of delaying efforts to reduce CO₂ emissions are serious and must be articulated clearly to the policy community. We believe that such a delay can be pre-

vented with appropriate policies, and that both short (decades) and long (century or longer) time scales must be considered.

Direct comparisons of the climate influence of SLCPs and CO₂ require making a judgment about the relative importance of short and long time scales. SLCPs have a powerful impact on climate, but they persist in the atmosphere for only a short time—days to weeks for BC, a decade for CH₄, and about 15 years for some HFCs. Thus, immediate reductions in SLCPs will result

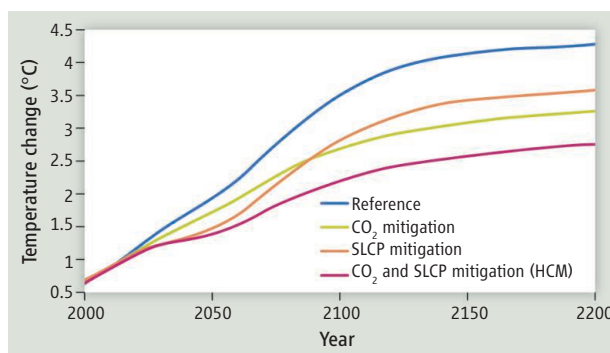
Parallel strategies must focus on long- and short-lived pollutants, but not at the cost of reducing pressure for action on CO₂.

in relatively immediate climate benefits, as the effects on climate depend largely on the emission rate, or flow, of SLCPs to the atmosphere. In contrast, CO₂ has a very long atmospheric lifetime; more than 20% will remain for thousands to tens of thousands of years (6). Thus, climate effects from CO₂ depend on the cumulative emissions, or stock, of CO₂ in the atmosphere (7).

In the next year, monthly mean CO₂ concentrations will reach 400 parts per million (ppm); annual mean CO₂ concentrations

have been rising more than 2 ppm per year because of emissions from fossil fuel use, and this will continue for at least the next several decades because of the dominance of fossil fuels in our world energy system. Because it is the most dominant greenhouse gas, near-complete reduction in CO₂ emissions is the only way to limit the rise of global temperatures and to avoid the risk of catastrophic impacts. But a partial reduction in CO₂ emissions over the next few decades will produce minimal relief from climate impacts until mid-century because of the long time scales of CO₂ in the atmosphere and the momentum of climate change due to the CO₂ already emitted.

One way to diminish climate impacts in the next few decades is to also reduce emissions of



Climate temperature response to reductions in emissions of CO₂, SLCPs, or both. Based on scenarios detailed in the supplemental material. Temperature change is shown relative to a pre-industrial baseline. In the Reference scenario, annual CO₂ emissions peak in 2080, after which they decline rapidly, while SLCP (CH₄, BC) emissions remain at or above current levels. In the "SLCP mitigation" scenario, deep cuts in BC (80%) and CH₄ (40%) emissions, relative to 2010 levels, are implemented linearly from 2010 to 2050. In the "CO₂ mitigation" scenario, CO₂ emissions are reduced by 20% relative to the reference scenario by 2050, followed by slowly decreasing emissions that intercept the reference scenario emissions at 2150. In this scenario, emissions of both BC and CH₄ are partially decreased relative to the reference scenario owing to those sources associated with fossil fuel consumption. The "HCM" scenario includes simultaneous mitigation of CO₂, CH₄, and BC, as described above. For simplicity, we ignore HFCs as well as different sulfate aerosol trajectories. Including these would slightly change the shape of the curves, but not the relative time scales between them.

¹Department of Earth and Planetary Sciences, Harvard University, Cambridge, MA 02138, USA. ²Division of Physical Chemistry, University of California, San Diego, La Jolla, CA 92093, USA. ³Scripps Institution of Oceanography, University of California San Diego, La Jolla, CA, 92093, USA. ⁴UNESCO Professor, TERI University, New Delhi, DL 110070, India. *Corresponding author: schrag@eps.harvard.edu

SLCPs. Some have argued that mitigating SLCPs to the maximum extent possible by using available technologies can reduce the projected warming by about a half, and sea level rise by about 25%, during this century, relative to a scenario in which only CO₂ emissions are reduced (8). Others have argued that the benefits would be smaller, because of the possibility that measures to mitigate CO₂ emissions will also mitigate emissions of SLCPs (9).

A key point is that the development of new, low-carbon technologies is driven by policies aimed at reducing CO₂ emissions. Removing political and economic pressure for their development can result in slower innovation, and lead to continued emissions and a warmer climate. In contrast, no new technological innovation is required for many cuts in SLCPs, such as sealing natural gas leaks or reducing biomass burning. Thus, if one delays societal pressure to reduce CO₂ emissions, one will end up with higher cumulative emissions and higher peak and long-term warming.

It is easy to understand why focusing on SLCPs is attractive. Reducing SLCPs achieves climate benefits on generational time scales. In contrast, a substantial reduction of CO₂ emissions requires a deep transformation of the world's fossil energy dependence. Some have argued that reducing emissions of SLCPs will help to avoid "tipping points" in the climate system, irreversible thresholds with drastic consequences. Exactly how to define a tipping point and when we might cross one remain controversial (10), but if such thresholds do exist, it is clear that reducing SLCPs alone can only delay by a few decades our reaching them (1, 11), as long as the concentration of atmospheric CO₂ continues to rise.

Another proposal is that an initial focus on SLCPs will slow the rate of warming by as much as 50% by 2050, allowing for easier adaptation by both human society and natural ecosystems (12), while we wait for political will to address CO₂ emissions. But if the focus on SLCPs inhibits actions to slow the growth of fossil CO₂ emissions, it will result in a higher peak temperature overall, and we will trade a slower rate of warming in the first half of this century for a steeper rise in temperature imposed thereafter (see the graph).

It is also important to recognize that CO₂ and SLCP emissions are not independent. Some of the steps to reduce CO₂ emissions will drive down emissions of SLCPs, as some of the largest sources of BC and methane are associated with fossil fuel pro-

duction and combustion. There is also the complicated case of sulfur emissions, which produce sulfate aerosols that are short-lived, like BC, but reflect sunlight and cool the climate, partially compensating for greenhouse warming. Reducing some types of fossil fuel use, especially sulfur-rich coal and ship fuel, will also reduce the concentration of sulfate aerosols, which may amplify warming in the near-term, but reduce the peak warming over the long term.

A common metric for valuation of different greenhouse gases, the 100-year global warming potential (GWP) (13, 14), compares the average radiative forcing of a greenhouse gas relative to CO₂ over the next 100 years. Some have argued that the 100-year GWP undervalues SLCPs, as the formulation includes no discount rate to prioritize near-term impacts. Others have argued that the 100-year GWP overvalues SLCPs as the formulation completely ignores any impacts beyond 100 years. Efforts to improve the GWP metric have encountered criticism from both perspectives (15). Our view is that there is no scientifically correct answer, as it requires trading near-term benefits for avoidance of substantial costs passed down to future generations, essentially in perpetuity.

Policy discussions about SLCPs are happening now. For example, the U.S. State Department, along with five other countries, unveiled in early 2012 an initiative for reducing emissions of BC, HFCs, and CH₄, and many other nations have now joined the initiative. If successful, such an initiative could lead to important health, agriculture, and climate benefits in the near-term. At the same time, there is legitimate concern that this initiative could be used to shield some countries from international pressure to reduce CO₂ emissions. It is imperative that this does not happen. The only way to permanently slow warming is through lowering emissions of CO₂. The only way to minimize the peak warming this century is to reduce emissions of CO₂ and SLCPs.

We suggest that the best way to prevent the slowing of CO₂ mitigation efforts is to emphasize parallel strategies for reducing SLCP and CO₂ emissions. For example, efforts to reduce BC emissions can be undertaken through air pollution measures whose main focus is on public health, such as regulations on diesel exhaust or the promotion of cleaner cooking technologies. HFCs can be regulated through the Montreal protocol. Such strategies have already proven to be effective. In California, for example, new regulations of particle emissions from diesel

exhaust resulted in a reduction in ambient BC over all of the state by 50% within the last 25 years (16). Another example is the recent agreement at the G-20 Summit in St. Petersburg to reduce use of HFCs.

An implication of our proposal is that trading between CO₂ and SLCP emissions, CH₄ in particular, should be discouraged. If efforts to reduce greenhouse gas emissions, both SLCPs and CO₂, were at a mature state with a well-developed market, we would embrace a broader discussion of the time scales of climate change and encourage society to reach a consensus on how to value short-term and long-term climate change. But we do not believe that real decisions about health policies and climate policies are made through an interconnected market, so parallel efforts are essential. We recognize that compromises may be required to achieve political goals; in particular, giving developing countries some form of "credit" for reductions in SLCPs may be important to broaden participation in international climate agreements. But more widespread trading between different greenhouse gases, especially when it may affect markets for low-carbon technologies, risks committing our children and grandchildren to even greater climate impacts in the more distant future.

References and Notes

1. V. Ramanathan, Y. Xu, *Proc. Natl. Acad. Sci. U.S.A.* **107**, 8055 (2010).
2. J. S. Wallack, V. Ramanathan, *Foreign Aff.* **88**, 105 (2009).
3. M. Molina *et al.*, *Proc. Natl. Acad. Sci. U.S.A.* **106**, 20616 (2009).
4. D. Shindell *et al.*, *Science* **335**, 183 (2012).
5. R. Pierrehumbert, RealClimate.org (2010); www.realclimate.org/index.php/archives/2010/12/losing-time-not-buying-time/.
6. D. Archer, V. Brovkin, *Clim. Change* **90**, 283 (2008).
7. M. R. Allen *et al.*, *Nature* **458**, 1163 (2009).
8. A. Hu, Y. Xu *et al.*, *Nat. Clim. Change* **3**, 730 (2013).
9. S. J. Smith, A. Mizrahi, *Proc. Natl. Acad. Sci. U.S.A.* **110**, 14202 (2013).
10. E. Kriegler *et al.*, *Proc. Natl. Acad. Sci. U.S.A.* **106**, 5041 (2009).
11. United Nations Environment Programme and World Meteorological Organization, "Integrated assessment of black carbon and tropospheric ozone" (UNEP, Nairobi, 2011).
12. D. Shindell, *Milken Inst. Rev.* **2013**, 36 (2013).
13. D. A. Lashof, D. R. Ahuja, *Nature* **344**, 529 (1990).
14. P. Forster *et al.*, in *Climate Change 2007: The Physical Science Basis. Contribution of Working Group I to the Fourth Assessment Report of the Intergovernmental Panel on Climate Change*, S. Solomon *et al.*, Eds. (Cambridge Univ. Press, New York, 2007), pp. 131–234.
15. J. S. Fuglestad *et al.*, *Clim. Change* **58**, 267 (2003).
16. V. Ramanathan *et al.*, "Black carbon and the regional climate of California" (for the California Air Resources Board, Univ. of California, San Diego, 2013); www.arb.ca.gov/research/rsc/3-8-13/item8dfr08-323.pdf.

Supplementary Materials

www.sciencemag.org/content/342/6164/1323/suppl/DC1

10.1126/science.1240162

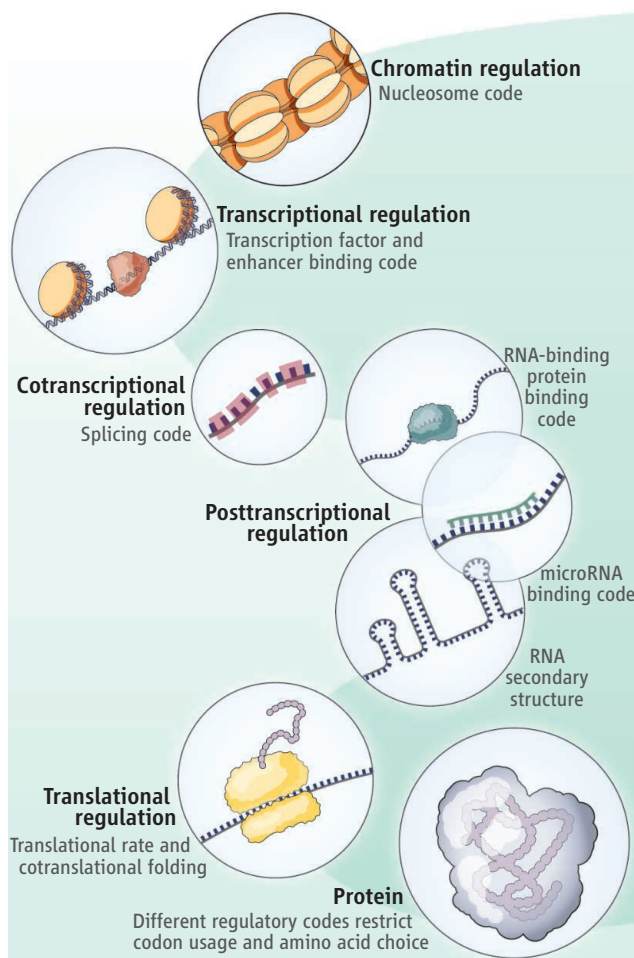
EVOLUTION

The Hidden Codes That Shape Protein Evolution

Robert J. Weatheritt and M. Madan Babu

Despite redundancy in the genetic code (1), the choice of codons used is highly biased in some proteins, suggesting that additional constraints operate in certain protein-coding regions of the genome. This suggests that the preference for particular codons, and therefore amino acids in specific regions of the protein, is often determined by factors unrelated to protein structure or function (2, 3). On page 1367 in this issue, Stergachis *et al.* (4) reveal that transcription factors bind within protein-coding regions (in addition to nearby noncoding regions) in a large number of human genes. Thus, a transcription factor “binding code” may influence codon choice and, consequently, protein evolution. This “binding” code joins other “regulatory” codes that govern chromatin organization (3), enhancers (5, 6), mRNA structure (7), mRNA splicing (3), microRNA target sites (6, 8), translational efficiency (9), and cotranslational folding (10), all of which have been proposed to constrain codon choice, and thus protein evolution (see the figure).

How widespread is the phenomenon of “regulatory” codes that overlap the genetic code, and how do they constrain the evolution of protein sequences? Stergachis *et al.* address these questions for the transcription factor–binding regulatory code. They use deoxyribonuclease I (DNase I) footprinting to map transcription factor occupancy (a protein bound to DNA can protect that region from enzymatic cleavage) at nucleotide resolution across the human genome in 81 diverse cell types. The authors determined that ~14% of the codons within 86.9% of human genes are occupied by transcription factors. Such regions, called



Constraints due to transcription factor binding within protein-coding regions of the genome result in biased codon usage and amino acid choice.

Constraining codes. Regulatory elements within protein-coding regions (such as transcription factor binding) can influence codon choice and amino acid preference that are independent of protein structure or function. Redundancy in the genetic code might facilitate the existence of multiple overlapping regulatory codes within protein-coding regions of the genome.

of DNA fragments protected from cleavage by DNase I in human cells, suggesting that such single-nucleotide variants affect transcription factor occupancy. They also determined that such variants are not biased toward whether they result in synonymous or non-synonymous changes in the protein sequence. Intriguingly, a large fraction of the variants that result in a nonsynonymous change are predicted not to alter protein function. This indicates that some variants within duons might primarily affect transcription factor binding instead. This supports the emerging idea that single-nucleotide variants within protein-coding regions can lead to disease without affecting protein structure or function (11, 12). Thus, the whole spectrum of “regulatory” codes within

“duons,” therefore encode two types of information: one that is interpreted by the genetic code to make proteins and the other, by the transcription factor–binding regulatory code to influence gene expression. This requirement for transcription factors to bind within protein-coding regions of the genome has led to a considerable bias in codon usage and choice of amino acids, in a manner that is constrained by the binding motif of each transcription factor.

To investigate whether single-nucleotide variants within duons affect transcription factor binding, Stergachis *et al.* mapped the known variants that are associated with a disease or a trait onto duons. Of those, 17.4% quantitatively skew the allelic origins

protein-coding regions should be considered when assessing the impact of single-nucleotide variants and interpreting disease mutation data from exome sequencing (only the protein-coding regions of the genome) and cancer genome studies.

Do the regulatory codes harmoniously coexist? Evidence is emerging that there can be conflicts. For example, in the fruit fly *Drosophila melanogaster*, there is a striking decrease in the use of codons that are optimal for translation, but a rise in codons that enhance RNA splicing, toward the end of exons (13). This may indicate that the requirement for accurate RNA splicing has superseded that for optimal translation. Likewise, Stergachis *et al.* observed that the binding

MRC Laboratory of Molecular Biology, Francis Crick Avenue, Cambridge CB2 0QH, UK. E-mail: rweather@mrc-lmb.cam.ac.uk; madanm@mrc-lmb.cam.ac.uk

motifs of transcription factors within protein-coding genomic regions are selectively devoid of sequences that contain a stop codon.

What features might permit synergistic coexistence of the regulatory and genetic codes? One major constraint of protein-coding genes is the requirement for the encoded polypeptide segment to fold into a defined tertiary structure. It is possible that in regions where folding constraints are not present, such as in intrinsically disordered regions (14), there might be increased tolerance for protein-coding genomic regions to harbor more regulatory elements that can be interpreted by different regulatory codes.

Stergachis *et al.* make a number of important genome-scale observations, but several mechanistic questions remain to be answered. For instance, although the authors report a weak tendency for transcription factors to preferentially bind to the protein-coding regions of highly expressed genes, it is unclear how the binding of a transcription factor within protein-coding regions mecha-

nistically influences the expression of a gene. Perhaps this type of binding might result in alternative promoters with different transcriptional start sites or affect the expression of neighboring genes (by acting as a distal enhancer element, for example). It is also unclear whether binding of a transcription factor within a protein-coding region may not directly affect gene expression but instead determine the formation and maintenance of higher-order chromatin structure.

Future research will need to determine the number of overlapping codes that can be tolerated by the genetic code. There is also the question of possible trade-offs, in terms of maintaining regulation and functionality, that have been made to accommodate coexistence of codes and whether this can lead to nonoptimal or deleterious consequences. For instance, protein-coding regions that cannot tolerate mutations due to multiple overlapping codes may be exploited by pathogens during host infection. The investigation of overlapping codes opens new vistas on the

functional interpretation of variation in coding regions and makes it clear that the story of the genetic code has not yet run its course.

References and Notes

1. M. Nirenberg, *Trends Biochem. Sci.* **29**, 46 (2004).
2. S. Itzkovitz, E. Hodis, E. Segal, *Genome Res.* **20**, 1582 (2010).
3. T. Warnecke, C. C. Weber, L. D. Hurst, *Biochem. Soc. Trans.* **37**, 756 (2009).
4. A. B. Stergachis *et al.*, *Science* **342**, 1367 (2013).
5. R. Y. Birnbaum *et al.*, *Genome Res.* **22**, 1059 (2012).
6. M. F. Lin *et al.*, *Genome Res.* **21**, 1916 (2011).
7. S. A. Shabalina, A. Y. Ogurtsov, N. A. Spiridonov, *Nucleic Acids Res.* **34**, 2428 (2006).
8. P. Brest *et al.*, *Nat. Genet.* **43**, 242 (2011).
9. K. Fredrick, M. Ibba, *Cell* **141**, 227 (2010).
10. S. Pechmann, J. Frydman, *Nat. Struct. Mol. Biol.* **20**, 237 (2013).
11. Z. E. Sauna, C. Kimchi-Sarfaty, *Nat. Rev. Genet.* **12**, 683 (2011).
12. J. B. Plotkin, G. Kudla, *Nat. Rev. Genet.* **12**, 32 (2011).
13. T. Warnecke, L. D. Hurst, *Mol. Biol. Evol.* **24**, 2755 (2007).
14. M. M. Babu, R. W. Kriwacki, R. V. Pappu, *Science* **337**, 1460 (2012).

Acknowledgments: We thank the UK Medical Research Council for support.

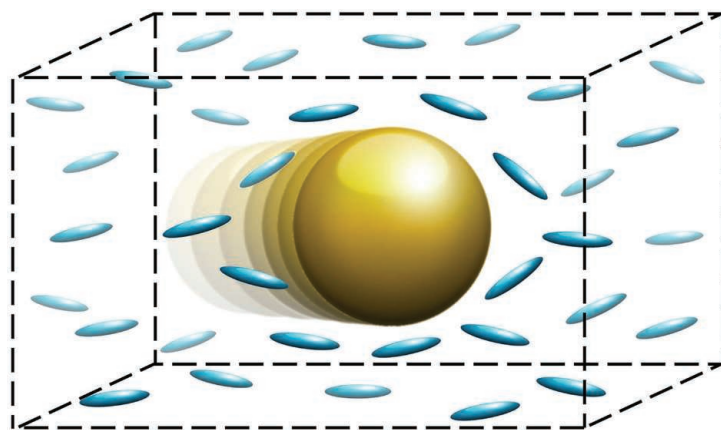
10.1126/science.1248425

APPLIED PHYSICS

Colloid Science Collides with Liquid Crystals

Nicholas L. Abbott

Brownian motion—the chaotic movement of colloidal particles that results from their collisions with solvent molecules—controls transport processes in systems as complex as the interior of living cells and as mundane as a film of drying paint. In a simple solvent, if you measure the distance the colloid travels (its displacement) for a sufficiently long time, the disorderly motion obeys a simple relation: The mean squared displacement (MSD) scales linearly with time. However, more recent studies of complex systems (e.g., concentrated solutions of proteins, polymers, or surfactants) revealed deviations from this classical behavior caused by local fluctuations in the composition and structure of the medium around the colloid (1–3). Now, in a strikingly elegant study described on page 1351 of this issue, Turiv *et al.* (4) unmask a



Taking timely directions.

The diffusion of a colloidal particle (gold) in a liquid crystalline solvent (blue) is depicted. The solvent molecules have a local average alignment. Turiv *et al.* show that dynamic fluctuations in the alignment direction can transfer momentum to the colloid and cause the time dependence of its diffusion to deviate from classical Brownian motion.

new example of “anomalous diffusion” of colloids that involves a liquid crystal (LC), a liquid-like phase that has long-range orientational ordering. Fluctuations in the solvent-molecule orientations cause MSDs of colloids to grow nonlinearly with time.

Research on LCs and colloidal diffusion was pioneered by Planer (5) and Smoluchowski (6), both of whom worked at the

University of Lviv, Ukraine, in the late 19th century. For many decades, the fields of colloid science and LCs evolved with only occasional exchanges of ideas. That situation has changed during the past 20 years. For example, LCs can mediate intercolloidal interactions with strengths, ranges, and symmetries that result in exotic colloidal assemblies (7, 8). Emulsions with internal structures can be

Chemical and Biological Engineering, University of Wisconsin, Madison, WI 53706, USA. E-mail: abbott@engr.wisc.edu

formed with LCs that are remarkably sensitive to the presence of specific biological adsorbates (9) and can serve as templates for the synthesis of spherical and nonspherical particles with chemical patches (10). These advances are leading to LC-based colloidal systems with functional properties and potential technological impact that go well beyond traditional applications of LCs in displays.

The LCs used in the study by Turiv *et al.* are low-molecular weight organic molecules that can be viewed as structured oils. The long-range orientational ordering of molecules in LCs, which gives rise to anisotropic viscosities and mechanical properties not found in simple isotropic solvents (11), is dynamic and patchy; local domains form, consisting of molecules with similar alignment. The alignment can be described theoretically with a director, a vector that represents the local average of the molecular orientations. In the late 1990s, it was shown that colloidal species dispersed in nematic LCs (the simplest type of LC that has no additional positional ordering) could locally strain the director of LCs, as well as introduce so-called topological defects. These defects are nanoscopic regions in which the LC orientational order differs substantially from the bulk (7).

The presence of these strains and defects, in combination with the anisotropic viscosities of LCs, were shown to give rise to anisotropic diffusion of colloidal particles in LCs (12, 13). However, in these earlier studies the MSDs followed the classical linear time dependence, and the measurements could be explained by construing the strain in the LC around the colloids as being static. Turiv *et al.* now demonstrate that fluctuations in the orientation of the LC director can influence the transfer of momentum from the LC to a colloid, such that the diffusion of the colloid departs from that predicted using the “static view” of the director (see the figure).

By focusing on a class of LCs with sufficiently slow fluctuations of the director, Turiv *et al.* imaged the displacements of colloids on time scales that lead to diffusive behaviors of the colloids that are faster or slower than classical Brownian motion. The measurements are striking examples of anomalous diffusion arising from purely orientational fluctuations in a solvent, and they define new questions and directions of inquiry. For example, whereas the measurements of anomalous diffusion reported by Turiv *et al.* occur on time scales consistent with the orientational fluctuations of the director in the LC, a detailed description of the dynamic coupling between the colloids and the LC is yet to be elucidated. Furthermore, the role of surface chemistry

(and, for example, colloid shape) in regulating near-particle fluctuations of the director is yet to be fully understood.

What is clear, however, is that the observations and ideas presented by Turiv *et al.* hint at new principles for manipulating colloidal transport processes. For example, one can envisage the application of time-dependent external fields (electrical, magnetic, or optical) to drive fluctuations in the director on relevant time scales and thus influence the exchange of momentum between colloids and LCs that gives rise to the anomalous diffusion. Alternatively, internally generated fields, such as those that are being explored in the context of designs of active matter (14, 15), might plausibly be harnessed to drive orientational fluctuations in LCs and thus regulate the transport of colloids.

References and Notes

1. A. Ott, J. P. Bouchaud, D. Langevin, W. Urbach, *Phys. Rev. Lett.* **65**, 2201 (1990).
2. D. S. Banks, C. Fradin, *Biophys. J.* **89**, 2960 (2005).

3. F. Höfling, T. Franosch, *Rep. Prog. Phys.* **76**, 046602 (2013).
4. T. Turiv *et al.*, *Science* **342**, 1351 (2013).
5. J. Planer, *Ann. Chem. Pharm.* **118**, 25 (1861).
6. M. von Smoluchowski, *Ann. Phys.* **21**, 756 (1906).
7. P. Poulin, H. Stark, T. C. Lubensky, D. A. Weitz, *Science* **275**, 1770 (1997).
8. I. Musevic, M. Skarabot, U. Tkalec, M. Ravnik, S. Zumer, *Science* **313**, 954 (2006).
9. I. H. Lin *et al.*, *Science* **332**, 1297 (2011).
10. F. Mondiot, X. Wang, J. J. de Pablo, N. L. Abbott, *J. Am. Chem. Soc.* **135**, 9972 (2013).
11. P. G. de Gennes, J. Prost, *The Physics of Liquid Crystals* (Clarendon, Oxford, ed. 2, 1993).
12. H. Stark, D. Venzki, *Phys. Rev. E* **64**, 031711 (2001).
13. J. C. Loudet, P. Hanusse, P. Poulin, *Science* **306**, 1525 (2004).
14. T. Sanchez, D. T. N. Chen, S. J. DeCamp, M. Heymann, Z. Dogic, *Nature* **491**, 431 (2012).
15. W. F. Paxton, S. Sundararajan, T. E. Mallouk, A. Sen, *Angew. Chem. Int. Ed.* **45**, 5420 (2006).

Acknowledgments: I thank X. Wang and D. Miller for preparing the figure. Supported by NSF grant DMR-1121288, Army Research Office grant W911NF-10-1-0181, and U.S. Department of Energy grant DE-SC0004025.

10.1126/science.1244987

GENETICS

My Oldest Sister Is a Sea Walnut?

Antonis Rokas

Decoding of the ctenophore genome prompts reevaluation of the complexity of the metazoan ancestor.

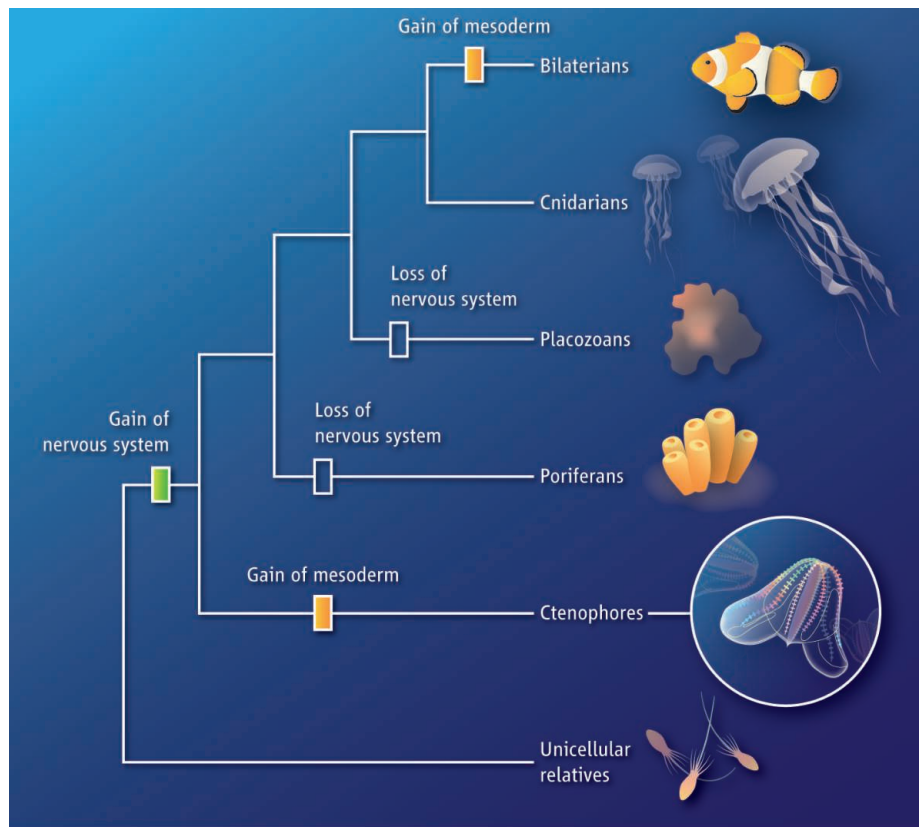
With common names such as “sea walnut,” “sea gooseberry,” and “Venus’ girdle” that reflect their morphological diversity, the jelly-like creatures belonging to the phylum Ctenophora that bear distinctive “combs” of cilia are not only breathtakingly beautiful (1) but are also key to understanding early animal evolution. On page 1336 of this issue, Ryan *et al.* (2) decode the genome of the sea walnut *Mnemiopsis leidyi*, the first member of this phylum to be sequenced, and propose that ctenophores might be the earliest branch of the animal tree and the sister lineage to that of all other animals. This paints a picture of early animal evolution full of cell type complexity, as well as its loss.

The ~200 ctenophore species discovered so far live in a wide variety of marine environments and at all latitudes (3). They get their name from the eight rows of linked tiny hairs known as “ctenes” (Greek for combs) that run

alongside their body and propel the animals through water. Although superficially similar to jellyfish (cnidarians), ctenophore morphology is quite distinct from that of the other three early-branching animal phyla, the poriferans (sponges), the largely enigmatic placozoans (known solely from organisms belonging to the phylum’s single genus, *Trichoplax*), and the cnidarians (jellyfish, sea anemones, and their kin). Unlike the radially symmetrical jellyfish, ctenophores are biradially symmetrical—their main body axis is defined by a mouth at one end and a gravity-sensing apical organ at the other end. Unlike sponges and placozoans, but like jellyfish, ctenophores contain both muscle and nerve cells. The latter are organized as a diffuse net that appears to be centralized at the apical organ (4).

With the exception of poriferans, whose bodies lack tissue organization, the tissues of the other three early-branching animal phyla are thought to develop from two distinct embryonic germ layers—the ectoderm (from which the nervous system develops) and the endoderm (the layer that gives rise to the gut). By contrast, the tissues of all bilaterians—

Department of Biological Sciences, Vanderbilt University, Nashville, TN 37235, USA. E-mail: antonis.rokas@vanderbilt.edu



Early branches in the animal tree. Major events of loss and gain in the evolution of early animal tissue complexity are suggested by the analysis of the first representative genome from the ctenophore phylum.

animals such as fruit flies, fish, and humans that have bilateral symmetry—can also be derived from a third germ layer called the mesoderm (the origin of muscle). Although ctenophore bodies are composed of an outer ectodermal layer of skin and nerve cells and an inner endodermal layer of gut cells, the presence of muscle cells and migratory cells in between these two cell layers, both of which originate from mesoderm, has raised the question of whether they share a three-cell-layer architecture with bilaterians (4).

The decoding of the ctenophore genome means that at least one genome sequence is now available from each member of the quartet of early-branching metazoan phyla, opening new vistas in both reconstructing early animal evolution and interpreting the somewhat disparate body plans and cell type diversity of ctenophores, cnidarians, poriferans, and placozoans in the context of their phylogeny. Although early embryologists thought ctenophores shared a close affinity with jellyfish, Ryan *et al.*'s phylogenetic analysis of an impressive amount of linear sequence data and gene content from diverse

animal proteomes rejects that notion (see the figure). Intriguingly, the analysis also recovers strong support for the placement of ctenophores as the sister group to all other animals (5).



Sea walnut (*Mnemiopsis leidyi*) at the New England Aquarium, Boston, MA.

Other recent studies have reached opposite conclusions, most notably grouping ctenophores and jellyfish together and placing poriferans as the earliest-branching lineage, which would mean that the oldest relative to the rest of animals is a sponge, not a sea walnut (6). However, this lack of consensus on the relative placement of early-branching phyla (7) is hardly surprising. The radiation that eventually gave rise to the body plans of the four early-branching phyla took place in a very narrow window of time more than 550 million years ago (8). Because the phylogenetic trees of such radiations have very short internal branches at their base, the historical signal present in gene sequences is often very weak to resolve such short branches and is frequently thwarted by various biases in the ways that genes evolve, muddling efforts to retrace ancient divergences (9). Following the lead of Ryan *et al.*, sequencing additional genomes from early-branching animals will be critical for better understanding not only the precise arrangement of the precise sequence of branchings at the base of the animal tree but also the variation in the rate of evolution between lineages over time and the underlying mechanisms that drove these varying rates—the “tempo and mode” of early animal life.

The lack of consensus on the exact branching pattern of the early offshoots of the animal phylogeny notwithstanding, comparison of the ~16,500 genes of the ctenophore genome to those of other early-branching animals, bilaterians, and to animals' closest unicellular relatives, the unicellular and colonial protists known as choanoflagellates (10), reveals two remarkable findings that challenge the standard view of early animal evolution. The first surprise is that patterns of coinheritance—the shared presence or shared absence of genes in two or more lineages—of transcription factors, axon guidance genes, and genes thought to be key for nervous system development and function, appear similar in the ctenophore and sponge genomes, even though sponges lack a nervous system. This coinheritance suggests that the genetic machinery required for nervous system development might have been present in the pan-animal ancestor and, more controversially, that this ancestor might have had a not-so-simple nervous system. By contrast, genes involved in mesoderm develop-

CREDITS (TOP TO BOTTOM): H. McDONALD/SCIENCE S. JOHNSON/WIKIMEDIA

ment in bilaterians lack homologous counterparts in the ctenophore genome (the second surprise), suggesting that the genetic machinery required for ctenophore mesoderm development may have originated independently from that found in bilaterians.

With the findings of Ryan *et al.*, we can finally dispense with the teleology-imbued notion that early animal evolution resembled a linear march of evolutionary forms from the

“simple” to the “complex.” The advent of the ctenophore genome suggests that simplification and loss of genes, pathways, and even cell types, and perhaps also their independent evolution, are an integral part of the fabric of animal origins.

References

1. R. Dawkins, *The Ancestor's Tale: A Pilgrimage to the Dawn of Evolution*. (Houghton Mifflin, Boston, 2004).
2. J. F. Ryan *et al.*, *Science* **342**, 1242592 (2013).

3. K. Pang, M. Q. Martindale, *CSH Protocols* **2008**, pdb.emo106 (2008); 10.1101/pdb.emo106.
4. M. Q. Martindale, *Nat. Rev. Genet.* **6**, 917 (2005).
5. C. W. Dunn *et al.*, *Nature* **452**, 745 (2008).
6. H. Philippe *et al.*, *Curr. Biol.* **19**, 706 (2009).
7. M. Dohrmann, G. Wörheide, *Integr. Comp. Biol.* **53**, 503 (2013).
8. A. Rokas, D. Krüger, S. B. Carroll, *Science* **310**, 1933 (2005).
9. L. Salichos, A. Rokas, *Nature* **497**, 327 (2013).
10. N. King *et al.*, *Nature* **451**, 783 (2008).

10.1126/science.1248424

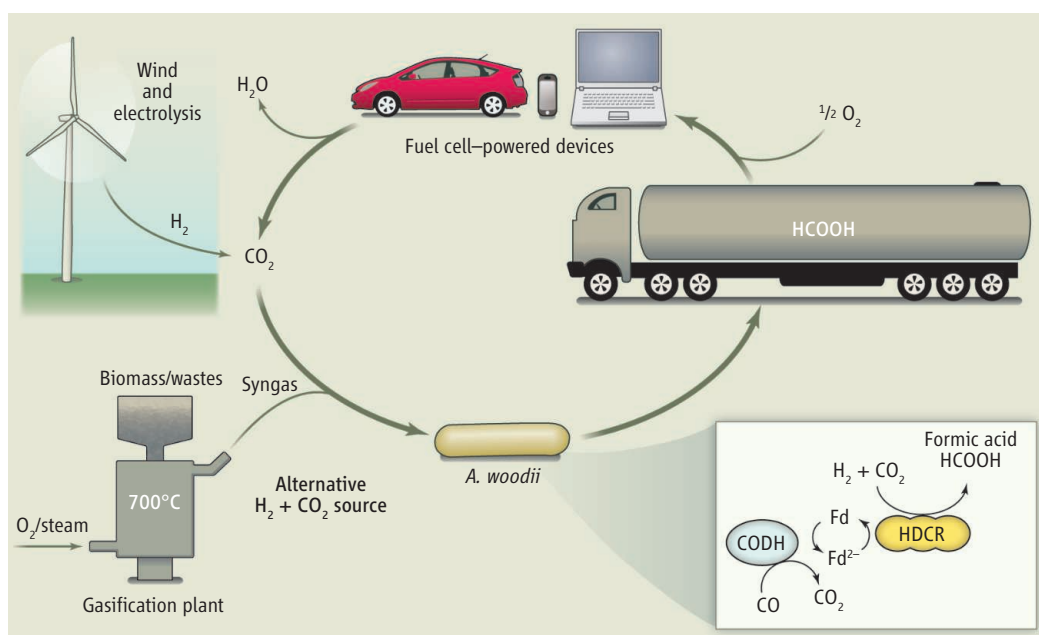
MICROBIOLOGY

An Enzymatic Route to H₂ Storage

Inês A. C. Pereira

Electricity is increasingly produced from renewable sources, but it remains difficult to store electric power at a large scale. Hydrogen is a strong candidate for energy storage, but there is still no safe, economically viable, and reasonably sized solution to store and transport it. The use of a liquid chemical hydrogen carrier with a high H₂ content per unit of mass and a good safety profile may solve this problem (1). For example, hydrogen may be safely stored by reducing carbon dioxide (CO₂) to formic acid (2), a liquid with a much higher energy density than H₂. Biological systems also use formate as a chemical equivalent of H₂ (3, 4). On page 1382 of this issue, Schuchmann and Müller (5) report a single-enzyme system that efficiently hydrogenates CO₂ without the need of cofactors.

Chemical catalysts for the interconversion of CO₂ and formic acid require noble metals and/or extreme conditions that are not economically viable (2, 6, 7). In biological systems, CO₂ is reversibly reduced to formate by formate dehydrogenases (4). These enzymes are abundant in anaerobic microbes that grow by reduction of CO₂ with H₂—acetogens (which produce acetate) and methanogens (which produce methane). Both groups are thought to descend from some of the earliest life forms on Earth (8). In acetogens, the



Storing hydrogen with enzymes. Schuchmann and Müller show that whole-cell biocatalysis of CO₂ hydrogenation by *A. woodii*, using HDCR, produces formic acid, a storage fuel that is a chemical equivalent of H₂ and can be used directly in fuel cells. Fd, ferredoxin.

first step of energy metabolism is the conversion of CO₂ to formate with H₂ as the physiological reductant. The best known formate dehydrogenases from acetogens are NADPH (reduced nicotinamide adenine dinucleotide phosphate)-dependent enzymes, which require the presence of additional proteins to produce this reduced cofactor.

The enzyme described by Schuchmann and Müller, a hydrogen-dependent carbon dioxide reductase (HDCR), was isolated from the model acetogen *Acetobacterium woodii* and is strikingly simple. It contains only two catalytic subunits—a hydrogenase and a formate dehydrogenase—and two electron transfer subunits. It directly reduces

An enzyme efficiently hydrogenates carbon dioxide to produce formate, a liquid that has a high energy density and can be safely transported.

CO₂ with H₂ to produce formate, without the need for NADPH or additional proteins, making it a very attractive target for practical applications. The activity is fully reversible and is controlled only by the substrate concentrations. Most important, its independence of other proteins or cofactors means that it can be decoupled from bacterial growth.

Schuchmann and Müller elegantly exploit the latter property to turn *A. woodii* into a whole-cell catalyst for CO₂ hydrogenation by inhibiting CO₂ consumption for energy metabolism either through the use of ionophores or by omitting Na⁺ ions. This is an ingenious way to redirect the metabolic

Bacterial Energy Metabolism Laboratory, ITQB António Xavier, Universidade Nova de Lisboa, Av. da República, 2780-157 Oeiras, Portugal. E-mail: ipereira@itqb.unl.pt

flux of reducing equivalents from respiration to formate production, because the *A. woodii* energy metabolism is strictly Na⁺-dependent. HDCR can also use ferredoxin [a small protein that serves as energy currency in anaerobes (9)] as an electron donor, and ferredoxin can be reduced by carbon monoxide dehydrogenase (CODH), also present in *A. woodii*. By exploring this property, the authors observed CO₂ reduction from syngas either by coupling the two enzymes or using the whole-cell system. Syngas (which contains varying concentrations of H₂, CO, and CO₂) can be produced from gasification of wastes or biomass and is thus considered a renewable energy source. HDCR thus efficiently transforms H₂ and CO₂ (or syngas) into formic acid/formate, which can be used to generate energy by means of direct formic acid fuel cells (see the figure). These fuel cells operate at low temperature and are not far from commercial application for small mobile devices.

The HDCR enzyme also helps to elucidate the physiology of acetogens. Like other anaerobes, acetogens and methanogens live close to the thermodynamic limit of life, and their metabolism entails several thermodynamically unfavorable reac-

tions. The most prominent of these is the reduction of ferredoxin by H₂ or NADH. A recent discovery transformed our understanding of the mechanisms used by these organisms to operate such difficult reactions (9). Buckel, Thauer, and co-workers have shown that an endergonic reaction (such as the reduction of ferredoxin by H₂) can be coupled to an exergonic reaction (such as the reduction of NAD⁺ by H₂) through the splitting of the H₂ electron pair at a flavin cofactor (9). This electron bifurcation mechanism seems to be widespread in anaerobic microorganisms and is essential to both acetogens (10, 11) and methanogens (12, 13).

As Schuchmann and Müller show, HDCR is the single enzyme responsible for CO₂ reduction in *A. woodii*. Although it also interacts with ferredoxin, no electron bifurcation is involved, indicating that the organism usually encounters H₂ at partial pressures high enough to allow direct reduction of CO₂. This is in contrast to the hydrogenase-formate dehydrogenase complex from the Na⁺-independent acetogen *Clostridium autoethanogenum*, which uses both NADPH and ferredoxin to reduce CO₂ in an electron confurcation process (the reverse mechanism of bifurcation, in which two electron

donors are coupled to reduce one substrate) (14). Clearly, different energy conservation strategies are used by each organism. These exciting advances in anaerobic microbiology will go a long way toward helping to develop a sustainable H₂ economy that exploits microbial metabolic diversity for H₂ storage and production.

References

1. H. L. Jiang, S. K. Singh, J. M. Yan, X. B. Zhang, Q. Xu, *ChemSusChem* **3**, 541 (2010).
2. S. Enthaler, J. von Langermann, T. Schmidt, *Energy Environ. Sci.* **3**, 1207 (2010).
3. S. M. da Silva et al., *Microbiology* **159**, 1760 (2013).
4. B. R. Crable, C. M. Plugge, M. J. McInerney, A. J. Stams, *Enzyme Res.* **2011**, 532536 (2011).
5. K. Schuchmann, V. Müller, *Science* **342**, 1382 (2013).
6. J. F. Hull et al., *Nat. Chem.* **4**, 383 (2012).
7. A. M. Appel et al., *Chem. Rev.* **113**, 6621 (2013).
8. F. L. Sousa et al., *Philos. Trans. R. Soc. London Ser. B* **368**, 20130088 (2013).
9. W. Buckel, R. K. Thauer, *Biochim. Biophys. Acta* **1827**, 94 (2013).
10. K. Schuchmann, V. Müller, *J. Biol. Chem.* **287**, 31165 (2012).
11. S. Wang, H. Huang, J. Kahnt, R. K. Thauer, *J. Bacteriol.* **195**, 1267 (2013).
12. K. C. Costa et al., *Proc. Natl. Acad. Sci. U.S.A.* **107**, 11050 (2010).
13. A. K. Kaster, J. Moll, K. Parey, R. K. Thauer, *Proc. Natl. Acad. Sci. U.S.A.* **108**, 2981 (2011).
14. S. Wang et al., *J. Bacteriol.* **195**, 4373 (2013).

10.1126/science.1247698

EPIDEMIOLOGY

Coming to an Airport Near You

Angela R. McLean

Faced with the complexity of the global spread of new infections, a common approach has been to create enormous computer simulations (1, 2). Most of these studies have yielded only tenuous insights, and scientific understanding has been slow to accrue. On page 1337 of this issue, Brockmann and Helbing (3) identify a useful metric—the effective distance—that helps to understand the spread of contagion across a travel network. Once this measure is specified, the global spread of infection can be understood as a simple reaction-diffusion process across the defined transportation network.

When a novel emerging infection appears, people ask themselves whether it will come to where they live and how long it will take to get there (4). Infectious diseases have long spread with travel and trade (5). Today, as the

spread of SARS in 2003 and H1N1 influenza in 2009 illustrate, the global aviation network has become a potent disseminator of infections (6, 7). However, geographical distance cannot explain the global spread of infection, because there are too many long-distance jumps across the air travel network. To overcome this problem, Brockmann and Helbing define an effective distance D_{eff} for any pair of airports in the global transportation network. For both simulated and past real epidemics, D_{eff} is a strong predictor of when a novel emerging infection will reach any given place from a specified starting point.

D_{eff} is driven by the proportion of people who leave one airport to go to another. Suppose you live in Busytown (8) and that 1% of people departing Busytown's airport arrive in Busytown, but only 0.01% of people who fly out of Faraway's airport land in Busytown. All other things being equal, a novel emerging infectious disease at Nearbytown poses a much greater threat to you than would the

Definition of an effective distance between airports helps to explain the spread of epidemics across the global aviation network.

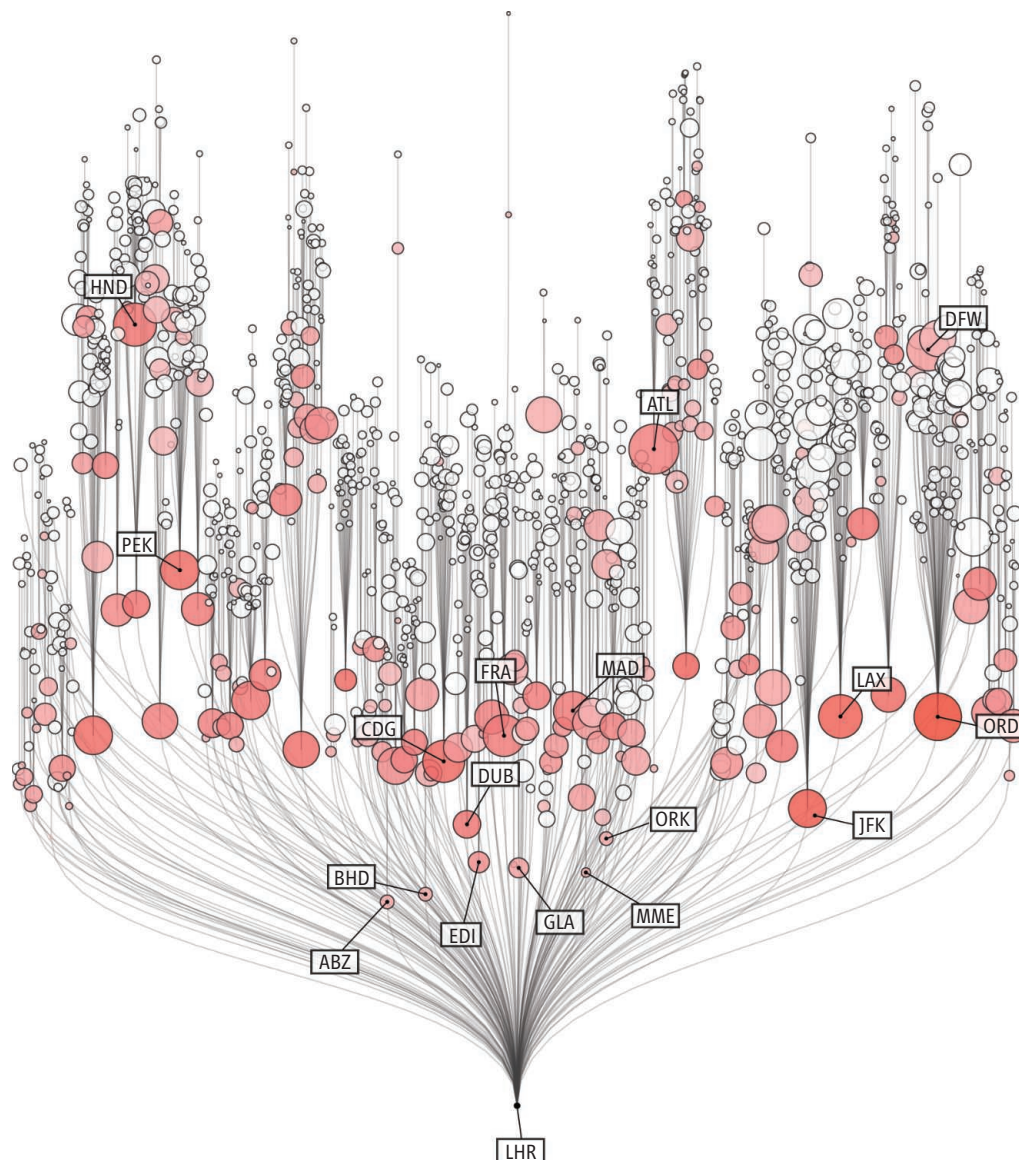
same disease at Faraway. This is the central idea of Brockmann and Helbing's D_{eff} , augmented with carefully crafted rules that define "shortest paths" for indirect journeys and formal models of the local spread of infection in the community served by each airport.

Once the effective distances between airports have been defined, the spread of infection across the global aviation network reduces to a simple reaction-diffusion process, with waves of infection propagating through a set of paths from one city to another. The new definition of distance explains quite precisely the speed at which SARS and H1N1 influenza spread to different countries around the world. Above all, from a plethora of detail and complexity of known facts about global travel, D_{eff} extracts the few things you need to know to answer the question "How long will 'it' take to get here?"

One of the powerful insights of this analysis is that the time to arrival of a new infection from one place to another is the prod-

Zoology Department, Oxford University, Oxford OX1 3PS, UK. E-mail: angela.mclean@zoo.ox.ac.uk

Who is coming to London? Brockmann and Helbing use the effective distance D_{eff} to illustrate where an infection might travel from a given location. A related (but different) version of D_{eff} measures how quickly a new emerging infection would arrive at an airport from another airport. As an example, the figure shows the shortest paths and effective distances from airports around the world to London Heathrow (LHR). Larger symbols have more traffic; darker symbols have more offspring branches in the tree. A small number of local UK airports such as Aberdeen (ABZ) and Glasgow (GLA) send a very large proportion of their passengers to London and are thus “close” according to this metric. Because Heathrow is a major hub in international travel, large airports such as those in New York (JFK), Los Angeles (LAX), and Beijing (PEK) are also “close” despite being geographically very distant. Other labeled airports are Atlanta (ATL), Belfast (BHD), Paris (CDG), Dallas (DFW), Dublin (DUB), Edinburgh (EDI), Frankfurt (FRA), Tokyo (HND), Madrid (MAD), Durham (MME), Chicago (ORD), and Cork (ORK).



uct of two components: the effective distance between them and the velocity of the wavefront. The first of these depends only on the static underlying travel network; it is not altered by the particular parameters that define how fast a particular disease might spread. In contrast, the propagation speed depends only on disease-specific epidemiological parameters. This separation into the travel network and a particular epidemic spreading on that network creates a ranking of all airports in terms of the risk each one poses to any given location as an imminent source of new infection. If you sit in London and are responsible for monitoring the risks posed by new emerging infections, D_{eff} tells you years in advance which locations to watch with particular vigilance, because it defines the locations that would be the fastest to send you any novel infection (see the figure). D_{eff} (and the resulting risk ranking) changes on the relatively slow time scales at which the global aviation network evolves, not on the harried time scales of an unfolding international health emergency.

This elegant treatment of a complex problem does involve some simplifying assumptions. The modeling assumes that the number of passengers flying out of an airport is

proportional to the size of the population served by that airport. Although this is a plausible assumption, it is not backed up by any data in Brockmann and Helbing's paper. This assumption needs testing with specific data on passenger traffic at various airports and the sizes of the populations they serve.

In recent years, network theories have been widely applied to explain the spread of epidemics (9). Such studies frequently assume (as do Brockmann and Helbing) that the underlying transmission network is fixed. For many networks, such as social interactions between individuals, that assumption is grossly restrictive. Perhaps one reason why Brockmann and Helbing's application of networks for epidemics seems to work so well is that it is reasonable to assume that the global aviation network is fixed, at least on the time scale of the spread of a pandemic. Given the projected growth of passenger numbers over

the coming decades, this theory may be able to illuminate how much faster the next SARS or H1N1 will spread as more and more people take to the sky (10).

References

1. S. Eubank et al., *Nature* **429**, 180 (2004).
2. N. M. Ferguson et al., *Nature* **442**, 448 (2006).
3. D. Brockmann, D. Helbing, *Science* **342**, 1337 (2013).
4. A. R. McLean, R. M. May, J. Pattison, R. A. Weiss, *Philos. Trans. R. Soc. London Ser. B* **359**, 1047 (2004).
5. A. D. Cliff et al., *Emergence and Re-Emergence: Infectious Diseases: A Geographical Analysis* (Oxford Univ. Press, Oxford, 2009).
6. L. Hufnagel, D. Brockmann, T. Geisel, *Proc. Natl. Acad. Sci. U.S.A.* **101**, 15124 (2004).
7. P. Bajardi et al., *PLOS ONE* **6**, e16591 (2011).
8. R. Scarry, *What Do People Do All Day?* (Random House, London, 1968).
9. L. Danon et al., *Interdiscip. Perspect. Infect. Dis.* **2011**, 284909 (2011).
10. Airline Industry Forecast; www.iata.org/publications/Pages/airline-industry-forecast.aspx.

10.1126/science.1247830

CHEMISTRY

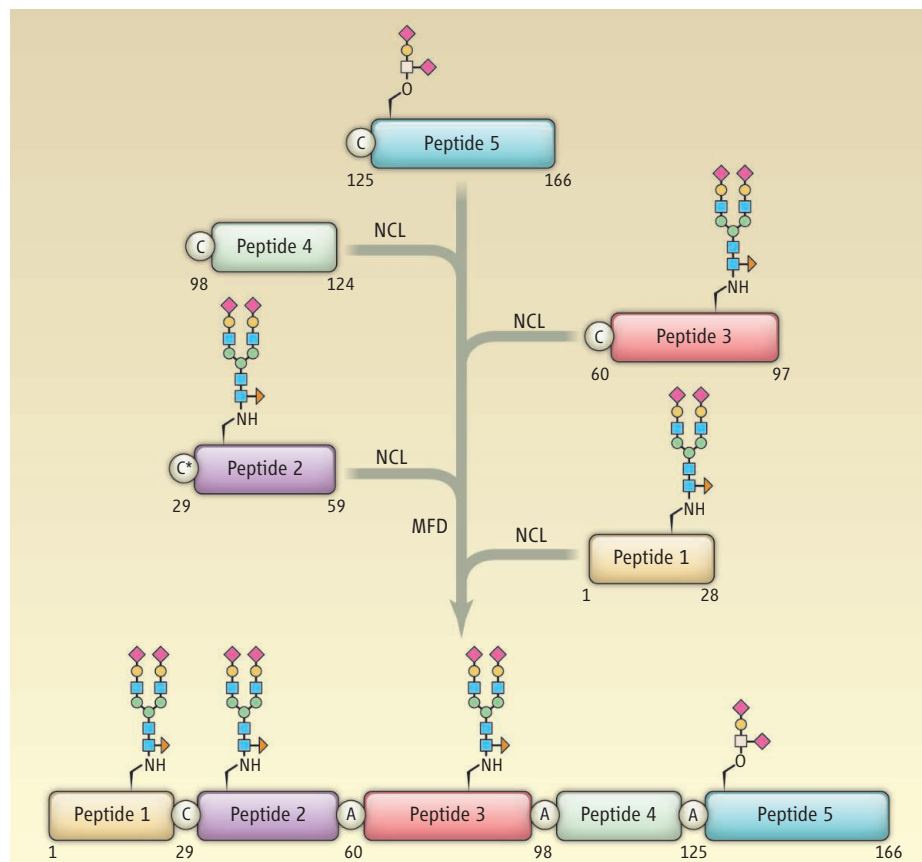
Improving Biologic Drugs via Total Chemical Synthesis

The chemical synthesis of a single glycosylated form of erythropoietin may help elucidate the functions of its sugars and tailor its properties.

Linda C. Hsieh-Wilson and Matthew E. Griffin

Most biologic therapeutics are large, complex molecules or heterogeneous mixtures of molecules that are manufactured in a living system (e.g., microorganism, plant cell, or animal cell) through recombinant DNA technology. Biologics are now being used to treat a wide range of diseases, including cancer, autoimmune disorders, and diabetes. It is estimated that half of the top 100 best-selling medications will soon be biologics, with Roche's anticancer biologic Avastin and AbbVie's anti-inflammatory antibody Humira rivaling the success of Pfizer's small-molecule drug Lipitor (1). Biologics differ fundamentally from small-molecule drugs in terms of purity, composition, and production. Small-molecule drugs typically have homogeneous, well-defined structures that have been finely tuned with atomic-level precision via chemical synthesis. On page 1357 of this issue, Wang *et al.* (2) bridge the gap between biologics and small-molecule drugs by accomplishing the total chemical synthesis of the biologic erythropoietin (EPO) in a single, pure form.

Erythropoietin is a 166-amino acid glycoprotein hormone that regulates the production of red blood cells (3). A major challenge in obtaining pure, homogeneous EPO is that cells produce the protein as a mixture of glycosylated forms (glycoforms). The protein undergoes extensive and variable glycosylation (the attachment of complex sugars) at four distinct sites (serine 126 and asparagine 24, 38, and 83). The commercial analogs of EPO, Procrit (Janssen), Epogen (Amgen), and Aranesp (Amgen), are sold as a mixture of glycoforms and are therapeutically used to treat anemia resulting from cancer, chemotherapy, or kidney failure. Studies suggest that the specific sugar modifications affect the stability and erythropoietic activity of EPO (4–6). Thus, systematic investigations into the structure-activity relations of the sugars and targeted production of the most active glycoform could improve the efficacy of EPO, as well as many other biologics. However, the individual therapeutic contributions of each



A homogeneous glycosylated erythropoietin. Wang *et al.* used native chemical ligation (NCL) to connect five separate peptides and form a single glycoform of the biologic drug EPO. An improved method for metal-free desulfurization (MFD) of unprotected cysteine residues (C) allows for ligation at more common alanine (A) junction sites between peptides. The application of convergent aspartylation to append complex *N*-glycans to these peptides before NCL permits the substitution of specific glycan structures to generate homogeneous glycoforms and study their individual activities.

glycoform are presently unknown because of an inability to precisely alter the sugar structures and isolate pure EPO glycoforms.

Wang *et al.* tackle this problem by constructing a single, complex glycoform of EPO via chemical synthesis (see the figure). This tour-de-force effort was made possible by several recent advances in chemical protein synthesis. Early work by Kent and colleagues paved the way with the development of native chemical ligation (NCL), a mild, selective reaction that enables two unprotected polypeptide chains to be joined (7). Long polypeptides beyond the reach of solid-phase peptide synthesis (which is generally limited to ~50 residues) can be synthesized

by NCL, but the process traditionally requires a cysteine residue at the ligation site between the peptides, and like many proteins, EPO lacks suitable cysteine residues at the desired junctions. To circumvent this problem, Wang *et al.* expanded on desulfurization methods to convert cysteine residues to alanine (8) and developed a mild, radical-based desulfurization procedure (9). This advance greatly increased the number of potential ligation sites, as alanine is far more prevalent than cysteine in proteins.

Still, these improvements only addressed half of the problem—the construction and attachment of glycans also posed a formidable challenge. The synthesis of complex

Division of Chemistry and Chemical Engineering and Howard Hughes Medical Institute, California Institute of Technology, Pasadena, CA 91125, USA. E-mail: lhw@caltech.edu

glycans is notoriously difficult because of the presence of multiple hydroxyl groups of comparable chemical reactivity and the stereospecific connections between the sugar units. Unlike the synthesis of peptides and oligonucleotides, there are no universal building blocks or methods for the synthesis of all glycans; thus, each synthesis requires meticulous design and experimentation to produce the exact desired structure. *N*-Glycans like those found in EPO may contain multiple branches of up to 20 sugar units and are some of the most complex oligosaccharide structures known (10).

Once synthesized, the glycan must then be attached to the peptide, which is again no small feat. However, a technique known as convergent aspartylation elegantly accomplishes this task (11, 12). This reaction combines the carboxylic acid of an aspartate residue and an amine-terminated oligosaccharide to attach the glycan to the peptide and simultaneously convert the aspartate to the native asparagine. To generate a single EPO glycoform of physiologically relevant complexity, Wang *et al.* synthesized and appended a “consensus” dodecasaccharide for the three

N-glycans and a glycophorin tetrasaccharide for the single *O*-glycan found on EPO.

However, their synthetic route was not without pitfalls. When the researchers attempted to join peptides containing the full consensus *N*-glycans using a ligation strategy previously shown to work with smaller glycans, one of the ligation steps was not successful, presumably because of the greater steric bulk of the larger *N*-glycan. Fortunately, reconfiguration of the synthesis with a different junction site distant from the problematic *N*-glycan allowed for smooth ligation, and assembly of the remaining peptide fragments produced the desired EPO structure. The fully synthetic EPO glycoform exhibited enhanced stability relative to its counterpart with smaller glycans and, upon folding, displayed *in vivo* erythropoietic activity comparable to that of the clinical drug Procrit.

Further advances are still required for chemical synthesis to be able to compete with biologic methods in terms of speed, scalability, and production. Nonetheless, the chemical synthesis of such a complex molecule represents an impressive culmination of more than a decade of synthetic efforts by

the Danishefsky laboratory. Their studies set the stage for generating “synthetic biologics” whose structures are controlled with the same atomic-level precision as small-molecule drugs. An understanding of how various, defined glycan structures affect the pharmacological properties of EPO and other biologics may ultimately contribute to the development of better and safer drugs.

References

1. B. Huggett, *Nat. Biotechnol.* **31**, 697 (2013).
2. P. Wang *et al.*, *Science* **342**, 1357 (2013).
3. A. J. Sytkowski, *Erythropoietin: Blood, Brain and Beyond* (Wiley-VCH, Weinheim, Germany, 2004).
4. L. O. Narhi *et al.*, *J. Biol. Chem.* **266**, 23022 (1991).
5. M. Mattio *et al.*, *Biotechnol. Prog.* **27**, 1018 (2011).
6. M. Higuchi *et al.*, *J. Biol. Chem.* **267**, 7703 (1992).
7. P. E. Dawson, T. W. Muir, I. Clark-Lewis, S. B. Kent, *Science* **266**, 776 (1994).
8. L. Z. Yan, P. E. Dawson, *J. Am. Chem. Soc.* **123**, 526 (2001).
9. Q. Wan, S. J. Danishefsky, *Angew. Chem. Int. Ed.* **46**, 9248 (2007).
10. P. H. Jensen, N. G. Karlsson, D. Kolarich, N. H. Packer, *Nat. Protoc.* **7**, 1299 (2012).
11. S. T. Cohen-Anisfeld, P. T. Lansbury Jr., *J. Am. Chem. Soc.* **115**, 10531 (1993).
12. P. Wang, B. Aussedat, Y. Vohra, S. J. Danishefsky, *Angew. Chem. Int. Ed.* **51**, 11571 (2012).

10.1126/science.1247615

MOLECULAR BIOLOGY

Finding the Right Partner in a 3D Genome

Pedro P. Rocha, Julie Chaumeil, Jane A. Skok

DNA integrity is frequently compromised as a result of exposure to cytotoxic agents, as well as the normal wear and tear of cellular processes like transcription and replication. DNA double-strand breaks (DSBs) are arguably the most dangerous type of DNA damage as they can lead to chromosomal translocations when their repair joins noncontiguous genomic regions together. Indeed, numerous malignancies have been associated with signature translocations in which an oncogene becomes deregulated through joining with another gene that exerts control over its expression.

By definition, illegitimate joining of broken DNA ends requires that the two partner genes are physically brought together, and in this context, frequent exchange partners have

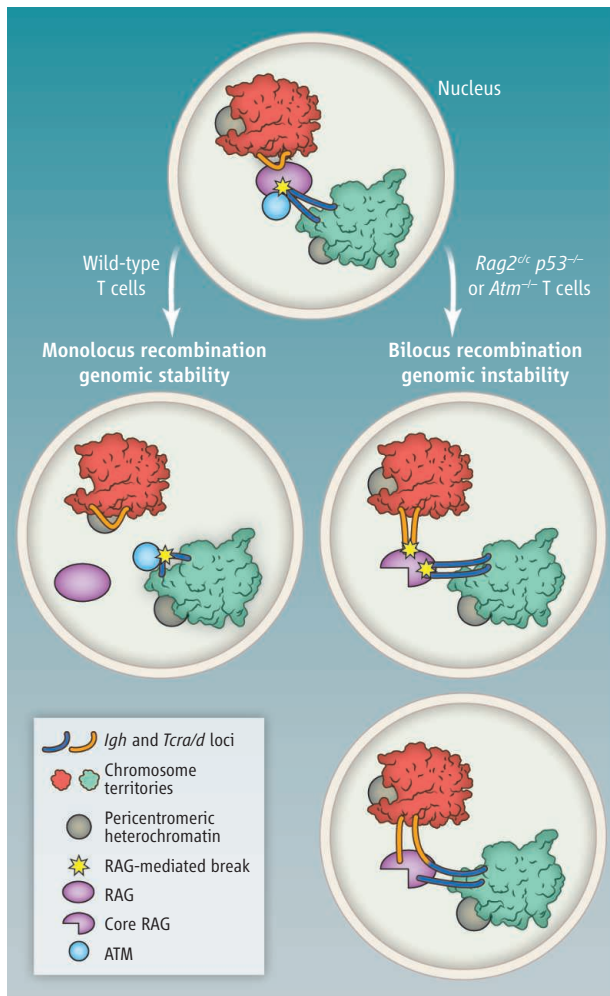
been found in closer spatial proximity in the nucleus than rare exchange partners (1), and to occupy the same polymerase II–enriched transcription factories (2). More recently, translocation capture data sets, combined with chromosome conformation capture (3C) (3), have further confirmed that nuclear organization has a major impact on the choice of translocation partners and that within a population of cells, most translocations occur between sites that are found most frequently in the same neighborhood (4). These conclusions are nonetheless limited to an end product that is the sum of the data from a population of formaldehyde-fixed cells.

Researchers are now starting to look at the architecture of the nucleus in real time. Using high-throughput time-lapse imaging in live cells containing DNA breaks in defined chromosomal locations marked by binding sites for fluorescent reporter proteins, Roukos *et al.* were able to track the formation of

The three-dimensional organization of the genome plays a role in controlling legitimate and illegitimate DNA recombination.

translocations after DSB induction (5). They found that translocations form within hours of a break after transitioning through three phases: DSB partner search, transient pairing, and persistent pairing. Breaks that result in a permanent fusion between two distant parts of the genome are more mobile than nontranslocating breaks. Curiously, the two ends of the same break move in unison during the break partner search and separate only after completion of a translocation. Ostensibly, this provides a mechanism to promote the correct rejoining of the two broken ends as opposed to illegitimate joining with a noncontiguous partner. The orchestrated movement of the two ends of a break also explains how reciprocal translocations can arise when unfaithful repair occurs between loci on different chromosomes. By tracking the cells over time, Roukos *et al.* could determine that most translocations arise from breaks in close proximity at the time of formation, but

Department of Pathology, New York University School of Medicine, 550 First Avenue, MSB 599, New York, NY 10016, USA. E-mail: jane.skok@nyumc.org



Promoting the right (and repressing the wrong) recombination pathways in immune cells. The DNA-repair protein ATM and the carboxyl terminus of the RAG2 protein recombinase help prevent genomic instability and translocations leading to leukemia and lymphomas. Figure derived from (11).

a small subset of translocations can also be generated by DSBs that undergo long-range motion, although joining of these takes longer.

Nuclear proximity also plays a role in minimizing the risks associated with DSBs introduced during V(D)J recombination (6). These programmed DNA rearrangements in B and T lymphocytes, mediated by the RAG1/2 recombinase, generate receptor diversity for antigen recognition as part of the adaptive immune response. Rearrangement is generally tightly controlled by developmental stage and cell lineage; however, in thymocytes, T cell receptor $\alpha\delta$ (*Tcra/d*) recombination temporally overlaps with a low level of promiscuous immunoglobulin heavy chain (*Igh*) rearrangement (*Igh* is normally rearranged in B cells), thereby providing an opportunity for illegitimate interlocus rearrangements. Under normal circumstances, the risks asso-

ciated with such an outcome are alleviated by trans regulation, which prevents simultaneous cleavage occurring on the two loci in the same cell (see the figure). Feedback control involves the DNA damage-sensing factor ataxia telangiectasia-mutated (ATM) that is recruited to the site of the break and the carboxyl terminus of the RAG2 protein (6). Recombining *Tcra/d* and *Igh* are brought into close nuclear proximity by the RAG recombinase. Pairing of the two loci (which are located on different chromosomes) occurs through RAG-dependent induction of higher-order monolocus loops that separate the RAG-bound loci from their respective chromosome territory. Targeted RAG breaks are then introduced in the looped out locus, while further cleavage events on the second locus are inhibited during repair of the first break. Both ATM and the carboxyl terminus of RAG2 control cleavage on the second locus by repositioning the uncleaved locus to repressive pericentromeric heterochromatin, inhibiting the formation of higher-order loops, and decreasing

the frequency of pairing. In the absence of the RAG2 carboxyl terminus ("core RAG2") or ATM, the two loci remain euchromatic, loops can form on both, and the loci stay paired at high frequency. This results in the introduction of bilocus breaks and damage on closely associated loci, providing a direct mechanism for the generation of interlocus *Tcra/d-Igh* translocations that are a hallmark of T cell tumors in ATM-deficient (7) and core RAG2 p53 (*Rag2^{Δc} p53^{-/-}*) double-mutant mice (see the figure) (8).

Nuclear organization is also important for DSB repair by homologous recombination, which in yeast is the predominant repair pathway. Current models postulate that the search for a matched template sequence occurs throughout the nucleus. Renkawitz *et al.* used time-resolved chromatin immunoprecipitations of repair proteins to test this notion (9). They instead discovered that the successful

search for homologous sequences in yeast is a function of either linear distance separation on the broken chromosome, or close proximity that results from chromosome architecture mediated by looping, centromere positioning, or other elements. In short, the closer the donor sequence, the more efficient the repair. In agreement with these findings, Agmon *et al.* demonstrate that efficient recombination occurs with sequences located in overlapping nuclear territories rather than those that are spatially separated (10). Furthermore, their studies suggest that the local search for homologous sequences could rely on DSB-induced mobility within a fixed territory.

Chromosome mobility is linked to both faithful and illegitimate DSB repair. In recombining lymphocytes, chromosome mobility that facilitates antigen receptor gene pairing and higher-order loop formation promotes regulated targeted cleavage on one locus, while persistent pairing and looping is linked to the introduction of bilocus breaks, which in turn can lead to undesirable interlocus rearrangements and genome instability.

Clearly, chromosome movement needs to be carefully controlled. In particular, regulated mobility is essential to prevent persistent DSBs from recombining with distant genomic sites, leading to an increased incidence of translocations. In the future, it will be important to identify the factors that promote chromosome movement by tracking the activities of wild-type and mutant repair proteins and remodeling factors over a period of time after the introduction of a break. It will also be necessary to generate systems that better define the contribution of transcription, replication, accessibility, and so on in creating abnormal DNA rearrangements. This is particularly relevant for the design of cancer therapies that do not promote translocations, which further contribute to oncogenic relapse. Undoubtedly, it is imperative to minimize these risks

References

1. J. J. Roix, P. G. McQueen, P. J. Munson, L. A. Parada, T. Misteli, *Nat. Genet.* **34**, 287 (2003).
2. C. S. Osborne *et al.*, *PLoS Biol.* **5**, e192 (2007).
3. P. P. Rocha, J. A. Skok, *Curr. Opin. Cell Biol.* **25**, 365 (2013).
4. P. P. Rocha *et al.*, *Mol. Cell* **47**, 873 (2012).
5. V. Roukos *et al.*, *Science* **341**, 660 (2013).
6. J. Chaumeil *et al.*, *Nat. Commun.* **4**, 2231 (2013).
7. M. Liyanage *et al.*, *Blood* **96**, 1940 (2000).
8. L. Deriano *et al.*, *Nature* **471**, 119 (2011).
9. J. Renkawitz, C. A. Lademann, M. Kalocsay, S. Jentsch, *Mol. Cell* **50**, 261 (2013).
10. N. Agmon, B. Liefshitz, C. Zimmer, E. Fabre, M. Kupiec, *Nat. Cell Biol.* **15**, 694 (2013).
11. J. Chaumeil, J. A. Skok, *Front. Immunol.* **10**, 3389/fimmu.2013.00423 (2013).

10.1126/science.1246106

CREDIT: P. HUEY/SCIENCE

RETROSPECTIVE

Michael Neuberger (1953–2013)

Julian E. Sale,¹ Ketan J. Patel,¹ Facundo D. Batista²

A sharp immunologist who unraveled the mechanisms of antibody diversification helped to launch a biomedical engineering revolution.

Michael Samuel Neuberger, the brilliant molecular biologist whose work stimulated the development of therapeutic antibodies and transformed our understanding of antibody diversification, died in Cambridge, UK, on 26 October from myeloma (a cancer of antibody-producing B cells), a week before his 60th birthday. Michael was the first to recognize this irony, writing after his diagnosis, “So after 35 years of tormenting antibodies in the lab, they are now getting their own back on me in the clinic.”

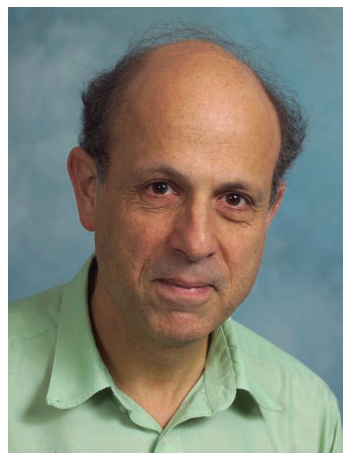
Michael was born in London on 2 November 1953. He attended Westminster School before going to Trinity College, Cambridge, to read Natural Sciences. In 1974, he undertook graduate work with Brian Hartley at Imperial College London, studying gene amplification in bacteria. During his thesis work, Michael visited the Laboratory of Molecular Biology (LMB) to collect bacterial strains from Nobel laureate Sydney Brenner. Michael made his way to Brenner's office, which he shared with fellow Nobel laureate Francis Crick. The door was closed, with loud animated voices emanating from behind it. Michael dared not interrupt and searched out the strains in the adjoining lab. Moments later, Brenner confronted the young intruder. The ensuing 2-hour discussion on Michael's Ph.D. left a deep impression on him scientifically and because of the generosity shown by Brenner in spending so much time with an unknown graduate student on a Saturday afternoon.

Michael was awarded a research fellowship at Trinity College in 1977 and was drawn back to LMB to work with the Nobel laureate César Milstein on antibodies. Following Brenner and Milstein's suggestion, he spent a year in the lab of immunologist Klaus Rajewsky at the University of Cologne. With this grounding, Michael returned to LMB in 1980. His early success in transfecting lymphocytes with antibody genes set the stage for understanding the control of antibody gene expression, for manipulating antibodies for therapeutic pur-

poses, and for defining the molecular architecture of the B cell receptor and how it extracts antigen to activate T cells.

Michael was among the first to produce chimeric antibodies, in which part of the molecule is derived from the mouse and part from human, thereby making the molecule less likely to be recognized as foreign by the body. His work paved the way for complementarity-determining region grafting (developed by his friend Greg Winter), in which only a very small part of a potential therapeutic antibody molecule is derived from the mouse in which the antibody was originally generated. Michael was also instrumental in engineering mice to produce fully humanized antibodies, work that together with that of Winter, laid the foundation of a multibillion-dollar industry and generated substantial royalties for the UK Medical Research Council.

Michael was preoccupied by the unresolved question of what drives the evolution of highly specific antibodies directed toward particular pathogens. He helped to develop transgenic mice and cell lines that defined the intrinsic features of this focused mutational process, known as somatic hypermutation. After the discovery of the enzyme responsible for this mutagenesis, activation-induced cytidine deaminase (AID), by the groups of Tasuku Honjo and Anne Durandy, Michael's group unraveled the mechanism by which AID acts in a series of papers published during 2002. Michael reasoned that AID acts on DNA, not RNA (as had been initially proposed). This work led to the simple but elegant model of immunoglobulin diversification in which enzymatic deamination of cytidine within the immunoglobulin variable regions leads to the formation of uracil. The direct replication or recognition and processing of uracil in DNA gives rise to the high levels of mutations seen in antibody genes. This concept of programmed deamination has since been extended beyond the confines of B cell immunology, and a family



of cytidine deaminases has been implicated in diverse processes including the restriction of retroviral proliferation and the generation of high levels of mutation in many cancers.

Michael was a deeply modest and selfless individual who possessed unique leadership skills. In 2002, he became joint head of the Division of Protein and Nucleic Acid Chemistry of LMB and in 2011, was made deputy director of LMB. All this he did quietly and with minimal fuss, driven by a deep sense of duty. During this last period, he codirected his lab with his long-term collaborator Cristina Rada.

His integrity and approach to science had a profound impact on those of us who were fortunate to come under his direct influence (we were students or postdoctoral fellows in his lab at LMB in the 1990s). We have unforgettable memories of entering his tiny, untidy, and cramped office with a pile of seemingly contradictory data and cluttered thoughts. Within a short time, he would engage his formidable intellect and power of deep concentration. The result would be a profound critical analysis, completely new insight, and several assignments to begin immediately.

Michael was elected a Fellow of the Royal Society before he was 40 and was one of the very few who was a Fellow contemporaneously with his father, Albert, a noted biochemist (and Ph.D. supervisor of twice Nobel laureate Fred Sanger). Just this year, Michael was elected to the U.S. National Academy of Sciences, a rare honor for a non-U.S. citizen and a mark of his huge influence on the field. Michael came from a remarkable family and had a wonderful and joyful family life with his wife Gill, an Australian doctor, and his two daughters and two sons. They, the extended scientific family that he spawned across the world, and his numerous friends and colleagues will miss his powerful presence in their lives.

10.1126/science.1248808

¹MRC Laboratory of Molecular Biology, Cambridge, UK.
²London Research Institute, Cancer Research UK, London, UK. E-mail: jes@mrc-lmb.cam.ac.uk; kjp@mrc-lmb.cam.ac.uk; facundo.batista@cancer.org.uk

The Genome of the Ctenophore *Mnemiopsis leidyi* and Its Implications for Cell Type Evolution

Joseph F. Ryan, Kevin Pang, Christine E. Schnitzler, Anh-Dao Nguyen, R. Travis Moreland, David K. Simmons, Bernard J. Koch, Warren R. Francis, Paul Havlak, NISC Comparative Sequencing Program, Stephen A. Smith, Nicholas H. Putnam, Steven H. D. Haddock, Casey W. Dunn, Tyra G. Wolfsberg, James C. Mullikin, Mark Q. Martindale, Andreas D. Baxeavanis*

Introduction: An understanding of ctenophore biology is critical for reconstructing events that occurred early in animal evolution. The phylogenetic relationship of ctenophores (comb jellies) to other animals has been a source of long-standing debate. Until recently, it was thought that Porifera (sponges) was the earliest diverging animal lineage, but recent reports have instead suggested Ctenophora as the earliest diverging animal lineage. Because ctenophores share some of the same complex cell types with bilaterians (such as neural and mesodermal cells), the phylogenetic position of ctenophores affects how we think about the early evolution of these cell types.

Methods: We have sequenced, annotated, and analyzed the 150-megabase genome of the ctenophore *Mnemiopsis leidyi*. We have performed detailed phylogenetic analyses on these new data using both sequence matrices and information on gene content. We conducted extensive genomic inventories on signaling pathway components and genes known to be critical to neural and mesodermal cell types, among others.

Results: Our phylogenetic analyses suggest that ctenophores are the sister group to the rest of the extant animals. We find that the sets of neural components present in the genomes of *Mnemiopsis* and the sponge *Amphimedon queenslandica* are quite similar, suggesting that sponges have the necessary genetic machinery for a functioning nervous system but may have lost these cell types. We also find that, although *Mnemiopsis* has most of the genes coding for structural components of mesodermal cells, they lack many of the genes involved in bilaterian mesodermal specification and, therefore, may have independently evolved these cell types.

Discussion: These results present a newly supported view of early animal evolution that accounts for major losses and/or gains of sophisticated cell types, including nerve and muscle cells. This evolutionary framework, along with the comprehensive genomic resources made available through this study, will yield myriad discoveries about our most distant animal relatives, many of which will shed light not only on the biology of these extant organisms but also on the evolutionary history of all animal species, including our own.

READ THE FULL ARTICLE ONLINE

<http://dx.doi.org/10.1126/science.1242592>



Cite this article as J. F. Ryan *et al.*, *Science* **342**, 1242592 (2013). DOI: 10.1126/science.1242592

FIGURES IN THE FULL ARTICLE

Fig. 1. *M. leidyi* life history and anatomy.

Fig. 2. Previously proposed relationships of the five deep clades of animals.

Fig. 3. Tree produced by maximum-likelihood analysis of the EST set.

Fig. 4. Tree produced by maximum-likelihood analysis of gene content.

Fig. 5. The origin of postsynaptic genes.

Fig. 6. Inventory of myogenic components in *M. leidyi*.

SUPPLEMENTARY MATERIALS

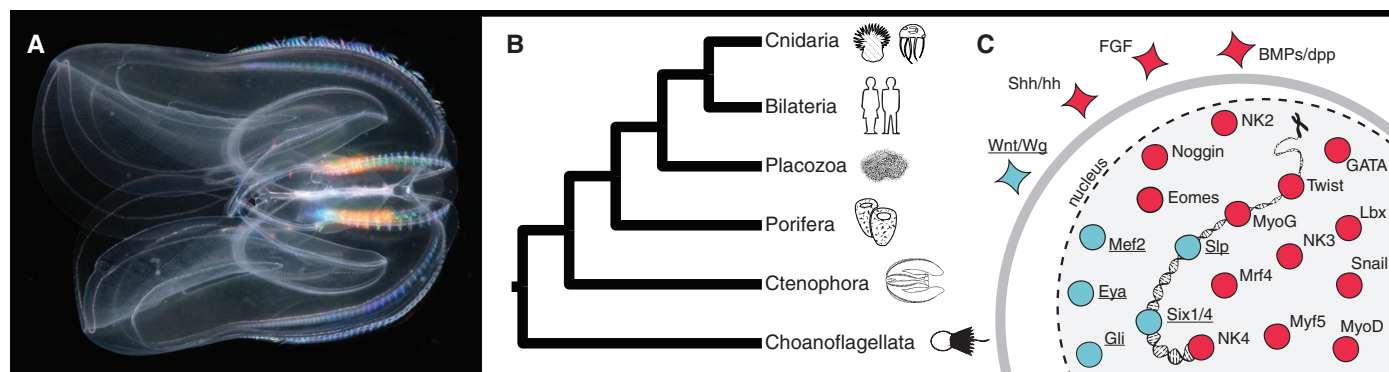
Materials and Methods

Figs. S1 to S10

Tables S1 to S31

References

The phylogenetic position of the ctenophore *Mnemiopsis leidyi* and its implications regarding the origin of mesodermal cell types. (A) Adult *M. leidyi*. (B) Summary of the relationships of the five main branches of animals and the outgroup Choanoflagellata. (C) Inventory of myogenic specification genes in *Mnemiopsis*. Components present in the *Mnemiopsis* genome are in blue, and names are underlined. Absent components are in red. The lack of many of these factors in *Mnemiopsis* indicates that ctenophore mesodermal cell types are specified differently than in bilaterians, suggesting that they perhaps evolved independently in these two lineages.



The list of author affiliations is available in the full article online.

*Corresponding author. E-mail: andy@mail.nih.gov

The Genome of the Ctenophore *Mnemiopsis leidyi* and Its Implications for Cell Type Evolution

Joseph F. Ryan,^{1,2} Kevin Pang,² Christine E. Schnitzler,¹ Anh-Dao Nguyen,¹ R. Travis Moreland,¹ David K. Simmons,³ Bernard J. Koch,¹ Warren R. Francis,⁴ Paul Havlak,⁵ NISC Comparative Sequencing Program,⁶ Stephen A. Smith,^{7,8} Nicholas H. Putnam,⁵ Steven H. D. Haddock,⁴ Casey W. Dunn,⁷ Tyra G. Wolfsberg,¹ James C. Mullikin,^{1,6} Mark Q. Martindale,³ Andreas D. Baxevanis^{1*}

An understanding of ctenophore biology is critical for reconstructing events that occurred early in animal evolution. Toward this goal, we have sequenced, assembled, and annotated the genome of the ctenophore *Mnemiopsis leidyi*. Our phylogenomic analyses of both amino acid positions and gene content suggest that ctenophores rather than sponges are the sister lineage to all other animals. *Mnemiopsis* lacks many of the genes found in bilaterian mesodermal cell types, suggesting that these cell types evolved independently. The set of neural genes in *Mnemiopsis* is similar to that of sponges, indicating that sponges may have lost a nervous system. These results present a newly supported view of early animal evolution that accounts for major losses and/or gains of sophisticated cell types, including nerve and muscle cells.

The phylogenetic position of ctenophores presents a challenge to our understanding of early animal evolution, especially as it relates to complex features such as cell types. The stark difference between the body plans of ctenophores and that of all other animals makes comparisons inherently difficult. Genomic sequencing of animals (1–4) and their closest relatives (5) provides invaluable insight into the molecular innovations contributing to the morphological diversity exhibited among modern-day animals. The vast majority of sequenced animal genomes are from Bilateria, the clade that includes most animal species (including humans and traditional model systems). Three of the four nonbilaterian metazoan lineages—Porifera (sponges), Placozoa, and Cnidaria (for example, sea anemones, corals, hydroids, and jellyfish)—have at least one species with a sequenced genome. The absence of a complete genome sequence from the fourth nonbilaterian metazoan lineage, Ctenophora (or comb jellies), has made it difficult to resolve the earliest evolutionary events in the animal tree of life and reconstruct the likely

gene inventory of the most recent common ancestor of animals.

Ctenophores are gelatinous marine animals characterized by eight longitudinal rows of ciliated comb plates that run along their oral-aboral axis (Fig. 1, A to C). Their bodies consist of an inner gastrodermal layer and an outer epidermal layer separated by a mesoglea. The muscular system, deployed in discrete regions of the body (for example, in the body wall, pharynx, and tentacles), is composed almost exclusively of smooth muscle cells; however, sarcomeric muscles have been reported in a single ctenophoran species (6). The ctenophore nervous system includes the apical sensory organ, a peripheral subepithelial nerve net, neurons that run through the mesoglea, and nerves associated with the tentacles. Most ctenophores, unlike all other animals, have specialized adhesive cells called colloblasts that are involved in prey capture. Most species are hermaphroditic and capable of self-fertilization. Fertilized eggs undergo a highly stereotyped ctenophore-specific cleavage program (Fig. 1, D to M), with embryogenesis in most species leading to a free-swimming cydippid stage that displays most of the features of the adult body plan (that is, development is direct).

Mnemiopsis leidyi is a lobate ctenophore native to the coastal waters of the western Atlantic Ocean. This species has recently invaded the Black, Caspian, and North Seas, causing major economic and ecological impact to native species in those areas. *M. leidyi* has been used effectively to study regeneration (7), axial patterning (8, 9), and bioluminescence (10–12). In addition, a cell lineage fate map (13–15), as well as resources for collecting and spawning, has been established (16), promoting *M. leidyi* as a leading model for evolutionary and developmental studies.

The phylogenetic relationship of ctenophores to other animals has been a source of long-standing

debate. The group lacks a reliable fossil record, and, on the basis of morphological features, ctenophores have been assigned various positions in animal phylogeny, including as sister to cnidarians in a clade called Coelenterata (sometimes called Radiata) (Fig. 2A) and as sister to Bilateria (Fig. 2B). Phylogenetic analyses of ribosomal RNA show little or no support uniting ctenophores with cnidarians or bilaterians and have tended to place ctenophores sister to a clade that includes all animals besides Porifera (Fig. 2C). Phylogenomic studies have also produced conflicting results, with a series of multigene analyses placing ctenophores sister to all other metazoans (Fig. 2D) (17, 18), and another, based primarily on ribosomal proteins, supporting the Coelenterata hypothesis (Fig. 2A) (19). Yet another study, also based primarily on ribosomal characters but with expanded taxon sampling, upheld the relationship of ctenophores as sister to all metazoans except Porifera (similar to Fig. 2C) (20). On the basis of its simple morphology, it has been suggested that Placozoa is the sister group to all animals (Fig. 2E) (21). Ctenophores have also been placed in a clade of nonbilaterian animals called “Diploblastica,” on the basis of a curated set of nuclear and mitochondrial proteins and a small morphological matrix (Fig. 2F) (22). The most recent analyses of the placement of sponges and ctenophores indicated that supermatrix analyses of the publicly available data are sensitive to gene selection, taxon sampling, model selection, and other factors (23). The inconsistency of reports about the phylogenetic position of ctenophores (table S1) has made it difficult to evaluate morphological, developmental, and experimental data involving these animals in an evolutionary context, complicating efforts to understand the early evolution of animals.

Genome Sequencing and Assembly

Genomic DNA was isolated from the embryos of two self-fertilized adult *M. leidyi* collected in Woods Hole, Massachusetts. DNA from one embryo pool was used to construct a library for Roche 454 sequencing. We generated 7.3 million raw reads, which yielded 2.5 Gb of sequence. Using the Phusion assembler (24), we assembled these data into 24,884 contigs, constituting 150 Mb of sequence and providing roughly 12-fold coverage of the genome. DNA from the other embryo pool was used to create two mate-pair libraries for Illumina GA-II sequencing, one with a 3-kb insert and the other with a 4-kb insert. After duplicate read-pairs were removed, 4.2 million and 2.6 million pairs remained for the 3- and 4-kb insert libraries, respectively. These reads were used to construct scaffolds of the original set of Roche 454 contigs. The final assembly consists of 5100 scaffolds, resulting in 160-fold physical coverage and an N50 of 187 kb (supplementary materials). To test the accuracy and completeness of our assembly, we aligned 99.4% of 15,752 public expressed sequence tags (ESTs) to our assembly. The average coverage of each alignable EST,

¹Genome Technology Branch, Division of Intramural Research, National Human Genome Research Institute, National Institutes of Health, Bethesda, MD 20892, USA. ²Sars International Centre for Marine Molecular Biology, University of Bergen, 5008 Bergen, Norway. ³Whitney Laboratory for Marine Bioscience, University of Florida, St. Augustine, FL 32080, USA. ⁴Monterey Bay Aquarium Research Institute, Moss Landing, CA 95039, USA. ⁵Department of Ecology and Evolutionary Biology, Rice University, Houston, TX 77098, USA. ⁶NIH Intramural Sequencing Center, National Human Genome Research Institute, National Institutes of Health, Rockville, MD 20852, USA. ⁷Department of Ecology and Evolutionary Biology, Brown University, Providence, RI 02912, USA. ⁸Department of Ecology and Evolutionary Biology, University of Michigan, Ann Arbor, MI 48109, USA.

*Corresponding author. E-mail: andy@mail.nih.gov

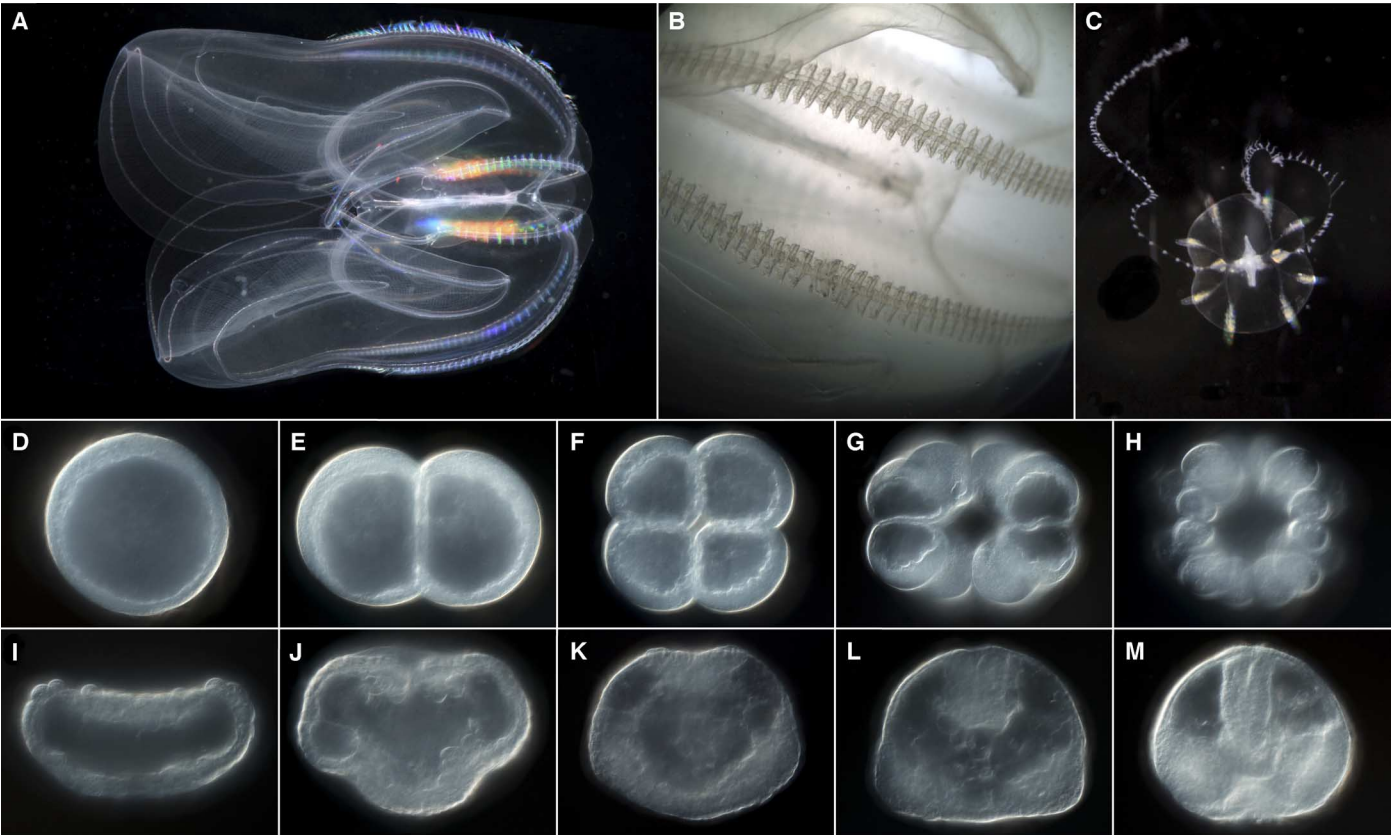


Fig. 1. *M. leidy* life history and anatomy. (A) Adult *M. leidy* (about 10 cm long). (B) Close-up view of comb rows. (C) Aboral view of cydippid stage. (D) One-celled fertilized embryo. (E to H) Early cleavage stages. (I) Gastrula stage. (J to M) Later development of *M. leidy* embryo shown oral side down. Embryos are about 200 μm. See the supplementary materials for a more detailed description of the ctenophore body plan. [Photo credit for (A): courtesy of Bruno Vellutini]

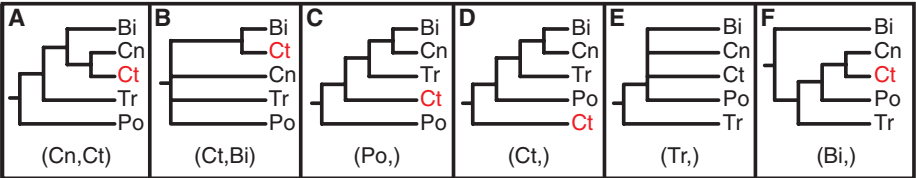


Fig. 2. Previously proposed relationships of the five deep clades of animals. The label at the bottom of each pane corresponds to the header of Table 1. (A) Coelenterata hypothesis. (B) Ctenophora as sister to Bilateria. (C) Porifera as sister group to the rest of Metazoa. (D) Ctenophora as sister group to the rest of Metazoa. (E) Placozoa as sister group to the rest of Metazoa. (F) Diploblastica hypothesis. We see no support in any of our analyses for the hypotheses in (A), (E), and (F) and very little support for (B) (see Table 1). Ct, Ctenophora; Po, Porifera; Tr, Placozoa; Cn, Cnidaria; Bi, Bilateria.

as determined by baa.pl (25), was 98.2%. In 94.8% of cases, a single EST mapped completely to a single scaffold. These numbers suggest that the assembly is both complete and accurately assembled.

Characteristics of the *M. leidy* Genome

The *M. leidy* genome is among the smallest 7% of genomes when compared with those cataloged in the Animal Genome Size Database (26) and is densely packed with gene sequences. It encodes 16,548 predicted protein-coding loci, which make up 58% of the genome, and we conservatively assign 44% of these gene predictions into homology


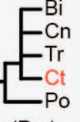

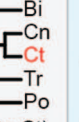
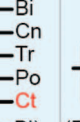
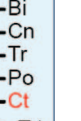
groups with non-ctenophores. The average length of an unspliced *M. leidy* transcript is 5.8 kb. Eight percent of predicted genes are embedded within other genes. This number of nested intronic genes is high compared to other genomes (table S2), but may be inflated owing to a subset of these being alternatively expressed exons. The level of repetitive sequence in the *M. leidy* genome is low to moderate, as compared to other metazoans (tables S3 and S4); this has made it possible to produce a high-quality genome assembly based on paired-end and mate-pair sequencing alone. Additional characteristics of this genome are presented in tables S5 to S10.

Phylogenetic Position of *M. leidy*

The availability of the complete genome of *M. leidy* has allowed us to improve on the ctenophore sampling used in previous phylogenomic analyses of gene sequence evolution. We assessed two data matrices that differ in breadth of taxon sampling and fraction of missing data: a “Genome Set” that includes only data from complete genomes (13 animals, 19.6% missing data) and an “EST Set” that includes partial genomic data from many taxa (58 animals, 64.9% missing data). We analyzed both matrices by using maximum-likelihood [with the GTR+Γ model as implemented in RAXML (27)] and Bayesian [with the CAT model as implemented in PhyloBayes (28)] methods. To understand the effect of outgroup selection on our ingroup topology, we included four different sets of nonmetazoan outgroups (table S11) in each combination of method and matrix. This multifactorial strategy yielded a total of 16 analyses (Table 1).

We found no support in any of these analyses for Coelenterata (Cn,Ct), Diploblastica (Bi.), or Placozoa being the sister lineage to the rest of animals (Tr.) (Table 1 and fig. S1). We recovered broad support for a sister relationship between Cnidaria and Bilateria (Cn,Bi) and for a clade of Placozoa, Cnidaria, and Bilateria (Tr,Cn,Bi). Maximum-likelihood analyses support the placement of Ctenophora as sister group to all other

Table 1. Support for various hypotheses across 16 phylogenetic analyses. Two amino acid matrices (Genome Set and EST Set) were analyzed with two different method/model combinations [ML indicates maximum-likelihood with the GTR+ Γ model using RAxML (27) and Bayes is Bayesian with the CAT model using PhyloBayes (28)], using four different sets of nonmetazoan outgroups for each analysis (Opisthokonta are fungi, amoeboids, and choanoflagellates; Holozoa, amoeboids and choanoflagellates; Choanimalia, choanoflagellates; and Animalia, no outgroups). Columns represent support for tested hypotheses, and most hypotheses are represented as trees in Fig. 2. In the absence of nonanimal outgroups, *(Ct,) and (Po,) are concordant with all possible topologies and ***(Ct,Po) is the same as (Bi,Cn,Tr). ***Despite an average run time of 205 days per run, none of the Bayesian analyses on the EST data set converged; convergence was monitored by using the maxdiff statistic generated by the bpcmp program within PhyloBayes (>0.3).

			Position of Ctenophora				Robustness of Cnidaria + Bilateria and Parahoxozoa	
								
			(Ct,)	(Po,)	(Ct,Po)	(Cn,Ct)	(Cn,Bi)	(Bi,Cn,Tr)
GENOME SET 104,840 cols 13 animals 80.4% occup.	ML	Opisthokonta	47	0	53	0	18	90
		Holozoa	31	0	69	0	27	90
		Choanimalia	100	0	0	0	41	100
		Animalia	*	*	**	0	92	100
	Bayes	Opisthokonta	0	0	100	0	100	100
		Holozoa	0	0	100	0	100	100
		Choanimalia	0	7	93	0	100	100
		Animalia	*	*	**	0	100	100
EST SET 88,384 cols 58 animals 35.1% occup.	ML	Opisthokonta	96	0	0	0	100	82
		Holozoa	96	0	0	0	100	83
		Choanimalia	93	0	0	0	100	62
		Animalia	*	*	**	0	100	35
	Bayes***	Opisthokonta	71	29	0	0	73	72
		Holozoa	13	64	0	0	33	30
		Choanimalia	2	98	0	0	100	99
		Animalia	*	*	**	0	100	97

Metazoa (Ct,) regardless of data matrix used (Fig. 3). The Bayesian analysis of the genome data set strongly supports a clade of Ctenophora and Porifera (Ct,Po) as the sister group to all other Metazoa. This relationship also receives some support in our maximum likelihood trees, and we suspect that the result is due to poor taxon sampling in the Genome Set. However, until there are more complete genomes available to test this hypothesis, this relationship cannot be completely dismissed. Despite an average run time of 205 days per run, none of the Bayesian analyses on the EST data set converged (maxdiff > 0.3). The lack of convergence in these analyses suggests that the application of this method to this data set is insufficient to resolve this relationship.

The analyses run without nonmetazoan outgroups show strong support for a monophyletic clade of Cnidaria and Bilateria (Table 1). This evidence contradicts the idea that long-branch attraction between ctenophores and the outgroup is masking a close relationship between ctenophores and cnidarians (19). Another common misconception, based on the extremely high evolutionary rates in the mitochondrial genomes of ctenophores (29, 30), is that the phylogenetic placement of these animals is essentially random because of

equally extreme rates of evolution in the nuclear genomes of ctenophores. We have found instead that the branch lengths in the phylogenetic analyses of our concatenated protein matrices show *M. leidyi* branches to be of similar length to those of *Drosophila melanogaster*, therefore exhibiting high (but not extreme) amino acid replacement rates (tables S12 and S13).

The conflict between the maximum-likelihood and Bayesian analyses of the amino acid matrix makes it difficult to determine from these analyses whether Ctenophora or Porifera is the sister group to the rest of the Metazoa, but there is substantial support for ctenophore as the sister group to the rest of animals (Table 1). Furthermore, our results strongly show that Placozoa, Cnidaria, and Bilateria (that is, Parahoxozoa) are monophyletic. Given the sensitivity of the molecular sequence evolution analyses to taxon sampling and inference method, consistent with other recent analyses (23), we also examined the evolution of gene content.

We clustered genes by using default parameters in OrthoMCL (31) and used these clusters to construct a gene presence/absence matrix. By using RAxML with a GTR+ Γ model, we conducted a weighted likelihood-based analysis on

this matrix. We then calibrated sites on the basis of the congruence of columns to known bilaterian relationships with the “-f” parameter in RAxML. The result of this analysis was a tree supporting Ctenophora as the sister group to all other animals (Ct,) (Fig. 4) and the rejection of all other alternative topologies (in Fig. 2) at the 5% confidence level by likelihood-based statistical hypothesis testing (table S14). The pattern of presence and absence of gene families and signaling pathway components seen in previous studies is consistent with these results (32–36). Our reanalysis of an expanded set of near intron pairs (37) was also consistent with these results (fig. S2).

Cell Signaling Components in *M. leidyi*

Across Bilateria, there are seven major cell signaling pathways that play important roles during embryological development: Wnt, transforming growth factor- β (TGF- β), receptor tyrosine kinase (RTK), Notch, nuclear receptor, Hedgehog, and Janus kinase (JAK)/signal transducers and activators of transcription (STAT) (38). Comparisons of nonbilaterian (2–4) and nonmetazoan genomes (5, 39) show that some of these signaling pathways evolved before the evolution of animal multicellularity, others are specific to metazoan evolution, and some were lineage-specific innovations. The cell signaling components present in the *M. leidyi* genome include the RTK family, which predates the origin of Metazoa (40); the TGF- β signaling pathway (33), thought to have evolved in the metazoan common ancestor (39); and the canonical Wnt signaling pathway (34). Notably absent from both the TGF- β and Wnt pathways are the major bilaterian antagonists; members of the Wnt/PCP (planar cell polarity) pathway, such as Flamingo and Strabismus, are not present. Relatively few components of the Notch pathway (tables S15 and S16) are present, and many of those lack key diagnostic domains. *M. leidyi* also lacks most of the major genes necessary for Hedgehog signaling [for example, the Hedgehog ligand, the smoothened receptor, and SUFU (suppressor of fused)]. Last, the JAK/STAT pathway is most likely a bilaterian innovation because there are no true JAK orthologs in *M. leidyi* or any other nonbilaterians reported to date.

Neural Components in *M. leidyi*

Ctenophores have a nervous system consisting of a nerve net, mesogleal fibers, and tentacular nerves (41). In contrast to the cnidarian nervous system, which contains an ectodermal and endodermal nerve net, the nerve nets of ctenophores consist of polygonal nerve cords spread under the ectodermal epithelium; these nerve nets show high levels of regional specialization and concentrations associated with the apical sensory organ/polar fields and tentacle bulbs, structures without clear homologs in any other animal groups (42). Unlike in cnidarians and bilaterians, immunological investigations have failed to detect the presence of serotonin in ctenophores (43). Ctenophore nervous systems are also unique in their abundance

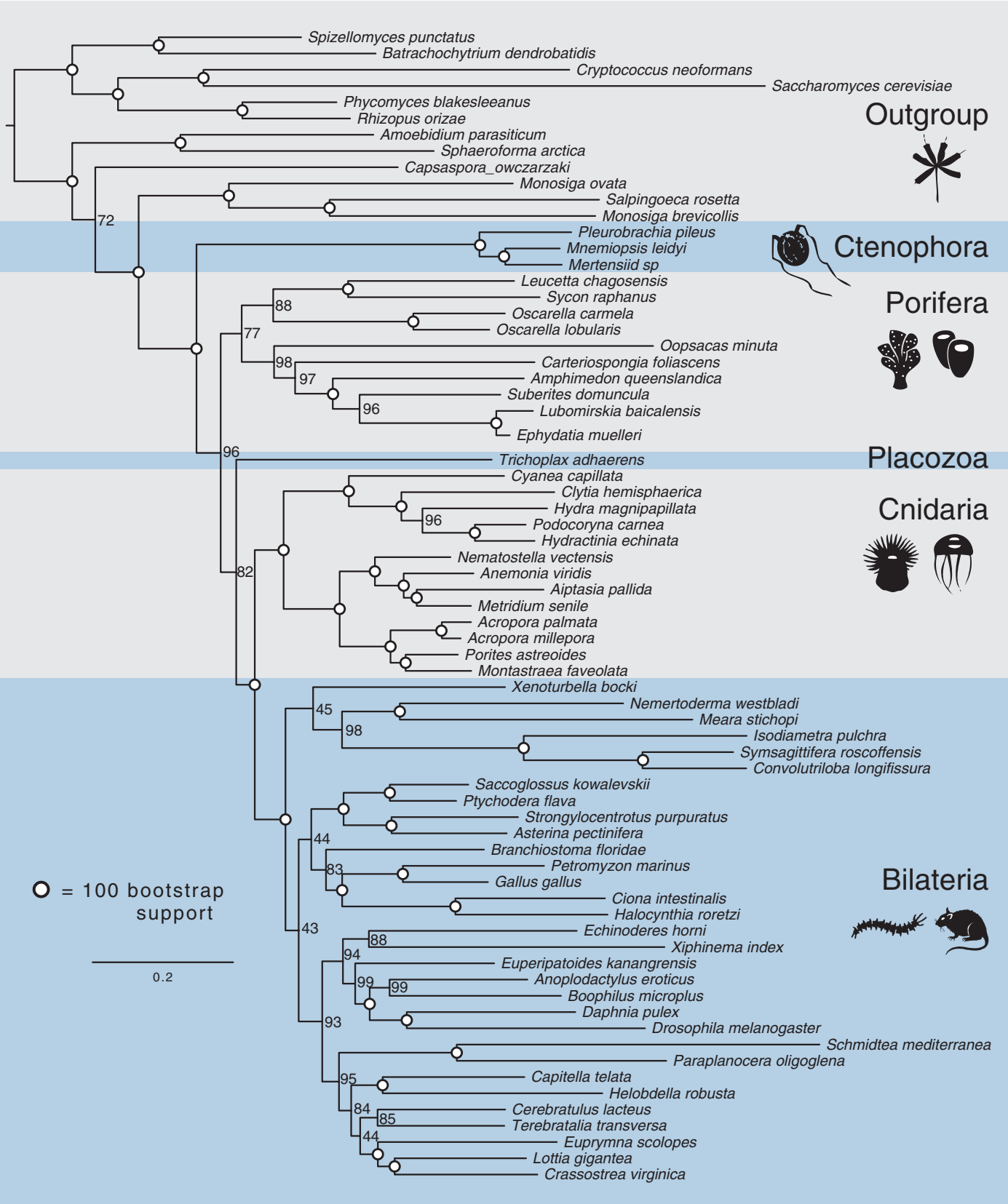


Fig. 3. Tree produced by maximum-likelihood analysis of the EST Set. The tree was produced from a matrix consisting of 242 genes and 104,840 amino acid characters. Circles on nodes indicate 100% bootstrap support. Support placing ctenophores as sister to the rest of Metazoa is 96% of 100 bootstrap replicates.

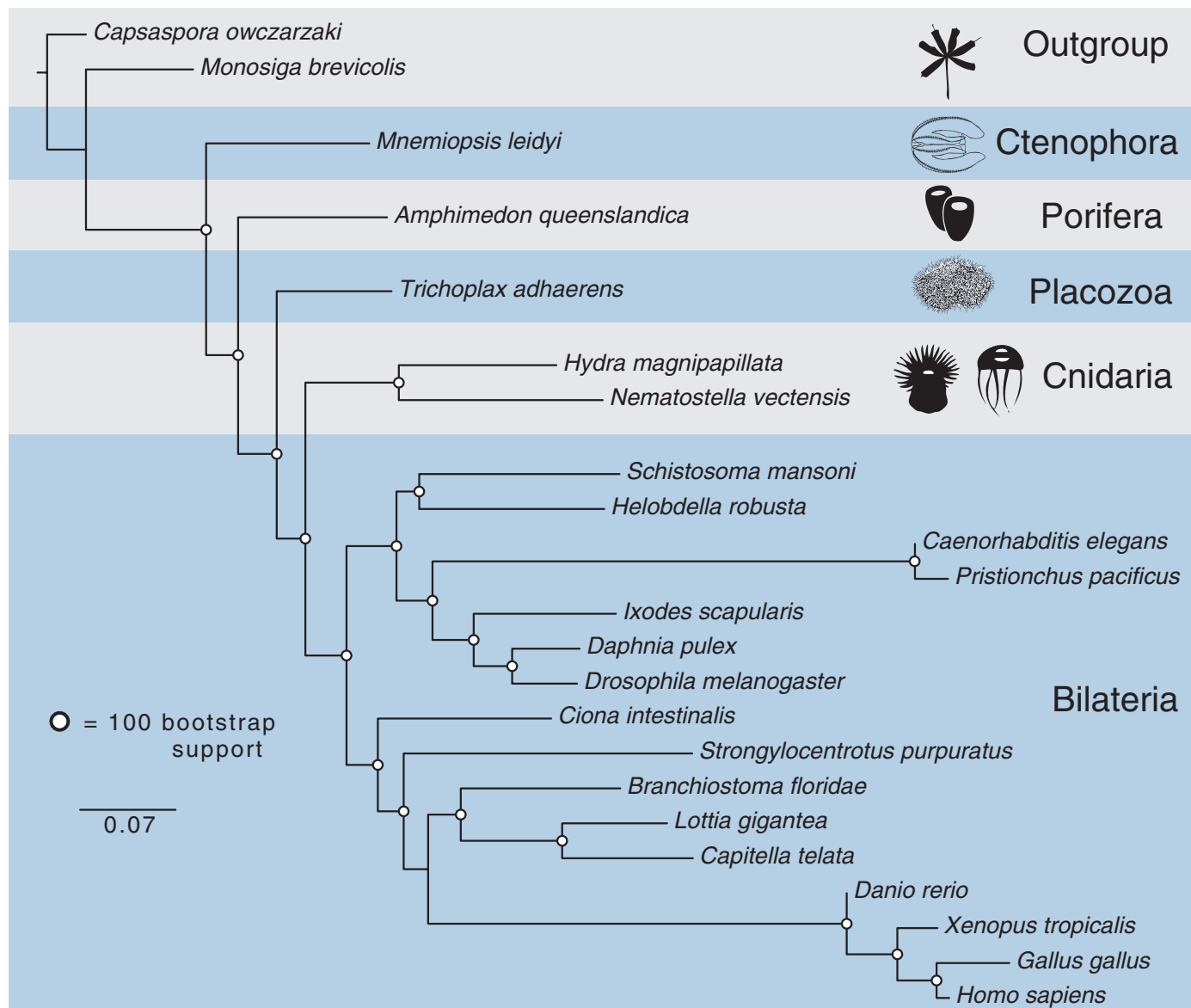


Fig. 4. Tree produced by maximum-likelihood analysis of gene content. The tree was produced from a matrix consisting of 23,910 binary characters indicating the presence or absence of a particular species within a cluster of genes. Clusters were produced with default settings of OrthoMCL. Columns consistent with known re-

lationships within Bilateria were up-weighted, whereas conflicting characters were down-weighted. The matrix was analyzed with RAxML under the GTR- Γ model of rate heterogeneity. All nodes received 100% bootstrap support. Constraining known relationships did not affect the position of Ctenophora (fig. S4).

of synaptic connections and their presynaptic morphology (44).

Many of the genes known to be critical to the nervous system of bilaterians and cnidarians are present in the sponge *Amphimedon queenslandica*, an animal without a nervous system. It has been hypothesized that the origin of the nervous system in nonsponges coincided with the origin of a few neural components that are absent from *A. queenslandica* (4, 45), but our phylogenetic results and the absence of these same components in *M. leidyi* challenge this hypothesis. Both *A. queenslandica* and *M. leidyi* contain orthologs of transcription factors involved in bilaterian and cnidarian neural development, including *lhx* (46), *bHLH* (basic helix-loop-helix), *six*, *gli*, and *sox* (classes B, C, E, and F) genes. The neural differ-

entiation RNA binding genes *ELAV* and *Musashi*, as well as the axon guidance genes *neurexin*, *semaphorin*, *plexin*, and an *ephrin* receptor, are all present in both *A. queenslandica* and *M. leidyi*. However, *netrin*, *slit*, and *unc-5*, involved in axon guidance, are absent from both genomes.

Many of the genes involved in the formation of bilaterian synapses and neural differentiation are present in both *A. queenslandica* and *M. leidyi*—but again, sponges and ctenophores lack a similar set of synaptic scaffolding genes (tables S17 and S18), all of which are present in cnidarians and bilaterians (Fig. 5). The pattern of presence and absence of these scaffolding genes is consistent with these genes being primitively absent in sponges and ctenophores. Almost all of the enzymes involved in the biosynthesis of dopamine and other catechol-

amine neurotransmitters are also absent in both *A. queenslandica* and *M. leidyi* (table S19). An exception to this shared pattern with sponges is the presence of two definitive opsin genes in *M. leidyi*, but not *A. queenslandica*, that are expressed in photocytes (light-producing cells), as well as in putative photosensory cells in the apical sense organ (12).

Mesoderm Components in *M. leidyi*

Ctenophores have several cell types (such as distinct muscle cells and mesenchymal cells) that, in bilaterians, are characteristically derived from mesodermal tissues. Cell lineage studies (14) have indicated that these cells are derived from a true endomesoderm because mesodermal cells are generated from precursors that also give rise to the endodermal portions of the gut; this is similar to the

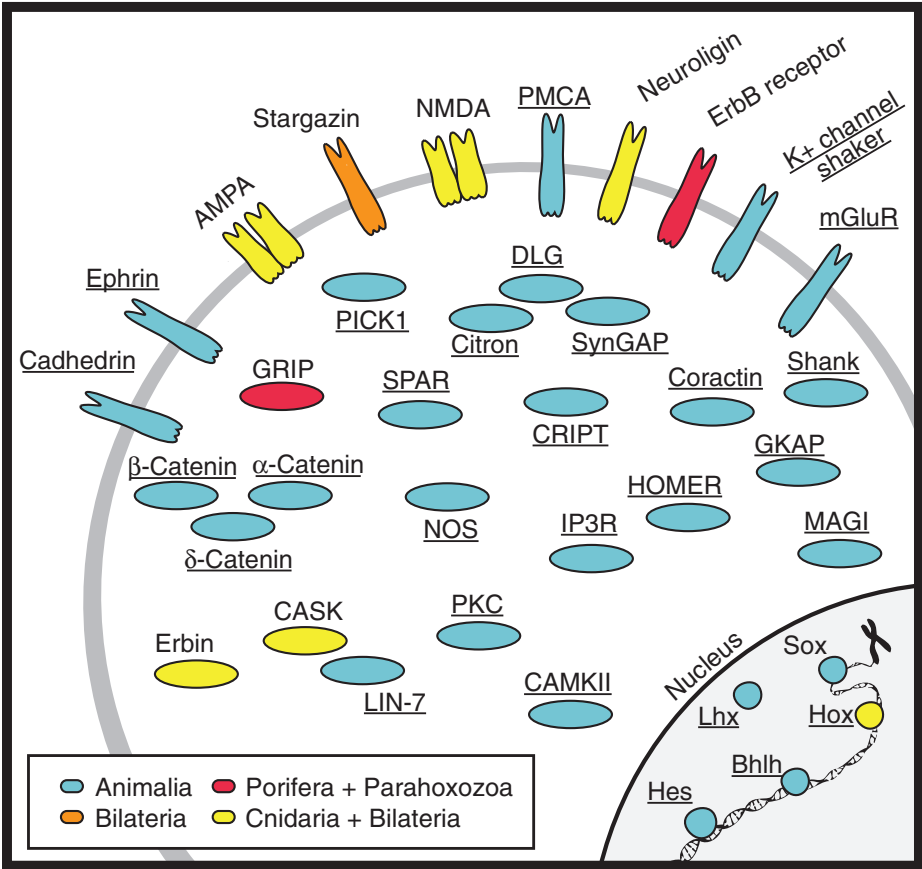


Fig. 5. Origin of postsynaptic genes. A possible configuration for postsynaptic genes. Genes are colored by their node of origin (*inset*). Names of genes present in the *M. leidy* genome are underlined. Accession numbers of *M. leidy* genes are given in table S16.

endomesodermal origins of mesoderm in virtually all bilaterians. However, screening the *M. leidy* genome reveals a surprising result in that almost none of the genes involved in bilaterian mesoderm development can be found (Fig. 6 and tables S20 and S21). Functional components of the fibroblast growth factor, Notch, Hedgehog, and the nodal (TGF- β superfamily) pathways, all of which are important in the segregation of mesoderm in different bilaterian forms, are also not observed. Other genes known to be involved in bilaterian mesoderm development, such as *gli/glis* genes, are expressed in neural (but not mesodermal) cells in *M. leidy* (47).

Mesoderm and Neural Components Also Absent from Other Ctenophores

To test whether these absences from the *M. leidy* genome were true for other ctenophores, we searched the deeply sequenced transcriptomes of seven other ctenophore species (*Bathocyctena chuni*, *Beroe forskalii*, *Charistephane fugiens*, *Euplokamis dunlapae*, *Hormiphora californensis*, *Lamnea lactea*, and *Thalassocalyce inconstans*) for FGF (fibroblast growth factor), Hedgehog, nodal, twist, snail, Lbx, NK4, NK3, NK2, Myf5, Noggin, Mrf4, Myogenin, Eomesoderm, GATA, MyoD, and troponin. We were able to identify putative snail genes in *T. inconstans* and *E. dunlapae* and putative GATA genes in five of the seven species. We were unable to identify the other 15 missing genes in any of these ctenophore transcriptomes (tables S22 and S23). A phylogenetic analysis of ionotropic glutamate receptor sequences from *M. leidy* and these ctenophore transcriptomes suggests that the ctenophore receptors form a sister clade to the bilaterian glutamate receptors

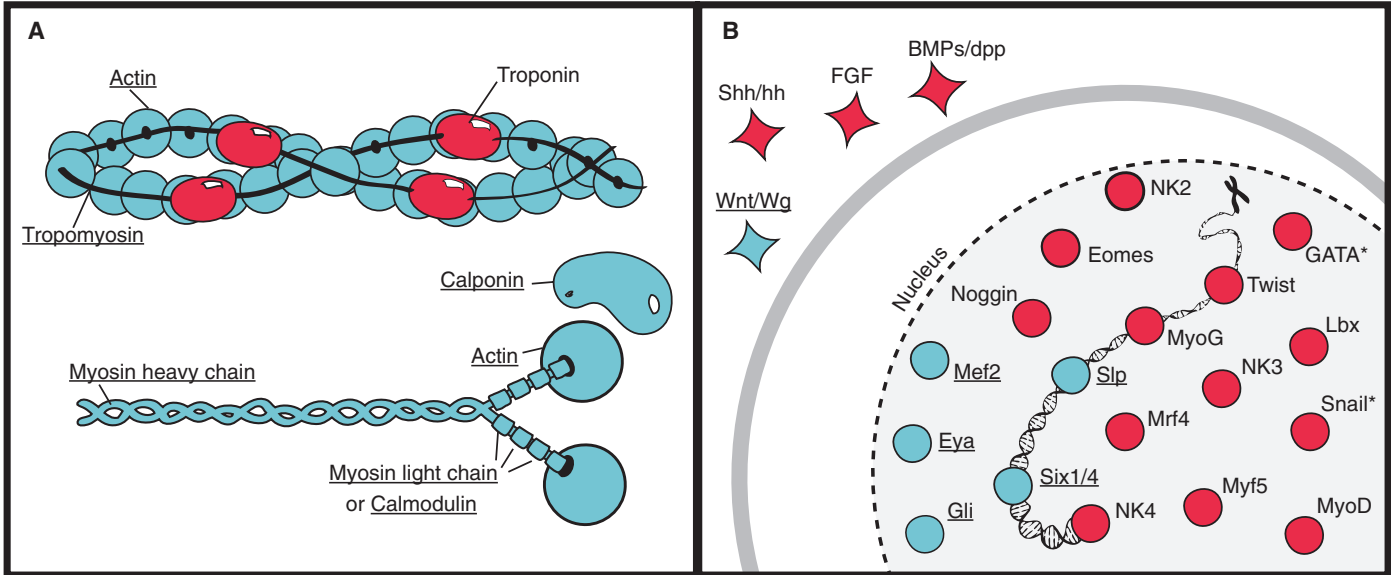


Fig. 6. Inventory of myogenic components in *M. leidy*. Components present in the *M. leidy* genome are in blue, and names are underlined. Absent components are in red. (A) The main structural components of smooth muscle are present in the *M. leidy* genome. All structural components are present except for troponin (in

red). (B) The majority of signaling molecules and transcription factors involved in specifying and differentiating the mesoderm of bilaterian animals are absent from the genome of *M. leidy*. The asterisks next to Snail and GATA indicate that these components have been identified in the transcriptomes of other ctenophores.

(fig. S3). Ionotropic glutamate receptors are absent from *A. queenslandica* but are present in the transcriptomes of eight other sponges (48). The tree topology suggests that the ctenophore sequences descended from an ancestral glutamate receptor that differentiated into AMPA, NMDA (*N*-methyl-D-aspartate), kainate-type, and delta-2-like glutamate receptors after ctenophores diverged from the rest of animals. These results indicate that, within ctenophores, the majority of absences are not specific to the *M. leidyi* lineage, but that there are some intriguing differences in gene content between ctenophores themselves.

Discussion and Conclusion

The sequence of the *M. leidyi* genome has given rise to multiple categories of evidence that support the placement of ctenophores as the sister group to all other animals, a conclusion supported by phylogenetic analysis of amino acid matrices from concatenated protein sequences. However, these analyses are sensitive to taxon sampling and phylogenetic methods and, therefore, provide some support for alternative hypotheses. With a ctenophore genome in hand, we show that gene content data support Ctenophora as the sister group to all other animals and statistically reject competing hypotheses. It will be important to test this result once more genomic data are available from other ctenophores, sponges, and other relevant groups. Nevertheless, this result is congruent with the structure and inventory of a variety of gene families and signaling pathways, as well as genes essential to neural and mesodermal cell types.

It appears that much of the genetic machinery necessary for a nervous system was present in the ancestor of all extant animals. This pattern suggests that a less elaborate nervous system was present in the metazoan ancestor and was secondarily reduced in placozoans and sponges. The alternative is that neural cell types arose independently in both the ctenophore lineage and the lineage that led to cnidarians and bilaterians, which might explain some of the unique aspects of the ctenophore nervous system. Resolving these alternative hypotheses will require functionally characterizing the nervous system-related genes in ctenophores and sponges.

Like the nervous system, the mesoderm appears to have had a complex evolutionary history. Our results are consistent with several alternative hypotheses. One possibility is that the mesoderm was present in the most recent common ancestor of ctenophores and bilaterians but was lost in sponges, placozoans, and cnidarians. However, given the absence of the majority of genes involved in the specification and differentiation of the bilaterian mesoderm from the *M. leidyi* genome, it appears more likely that ctenophores independently evolved mesodermal cell types after they diverged from the rest of animals. This interpretation is compatible with a recent report that striated musculature evolved independently in bilaterians, cnidarians, and in the ctenophore *E. dunlapae* (49).

The implications of these findings go well beyond the rearrangement of the branches of the meta-

zoan tree of life, arguing for a new way of thinking regarding the emergence and/or conservation of what heretofore were considered to be unique and indispensable biological features. Likewise, theories on the evolution of animal multicellularity have to be reevaluated. This evolutionary framework, along with the comprehensive genomic resources made available through this study, will undoubtedly yield myriad new discoveries about our most distant animal relatives, many of which will shed new light not only on the biology of these extant organisms but also on the evolutionary history of all animal species, including our own.

Methods

Genome Sequencing and Assembly

We isolated genomic DNA from the embryos of a self-fertilized adult and sequenced this DNA with Roche 454 sequencing. We generated another pool of genomic DNA from the embryos of a second self-fertilized adult and sequenced this DNA using Illumina GA-II mate-pair sequencing. These data were assembled using the Phusion assembler (24). We have deposited the assembly at GenBank under the project accession AGCP00000000.

Transcript Sequencing and Assembly

We isolated RNA from mixed-stage *M. leidyi* embryos and sequenced this material using Illumina GA-II sequencing. We assembled these data into transcripts using Cufflinks (50) and Trinity (51). Assembled transcripts are available through the *Mnemiopsis* Genome Project Portal (<http://research.nhgri.nih.gov/mnemiopsis/>).

Gene Prediction

We generated gene model predictions using a range of gene prediction programs and then used EvidenceModeler (EVM) (52) to combine models, transcripts, and sequence similarity to other protein data sets into a final set of protein-coding gene predictions. These are available through the *Mnemiopsis* Genome Project Portal (<http://research.nhgri.nih.gov/mnemiopsis/>).

Phylogenetic Analysis of Concatenated Gene Matrices

We analyzed two matrices constructed from concatenated protein sequences. One consisted of *M. leidyi* amino acids added to a genome-based data matrix that was reported in the *A. queenslandica* genome paper (4). The second used a phenetic sequence clustering method as described previously (18). We generated maximum-likelihood trees with the GTR+ Γ model using RAXML (27) and Bayesian trees with the CAT model using PhyloBayes (28). All alignments and trees are available at http://research.nhgri.nih.gov/manuscripts/Baxeavanis/science2013_supplement/.

Phylogenetic Analysis of Gene Content

We assembled a presence/absence matrix of gene clusters and analyzed these data with RAXML under the GTR-gamma model of rate heteroge-

neity. We used known bilaterian relationships to generate a weight matrix in RAXML. We used per-site log likelihoods generated in RAXML as input to CONSEL (53) to generate *P* values for alternative hypotheses.

References and Notes

1. J. A. Chapman *et al.*, The dynamic genome of *Hydra*. *Nature* **464**, 592–596 (2010). doi: [10.1038/nature08830](https://doi.org/10.1038/nature08830); pmid: [20228792](https://pubmed.ncbi.nlm.nih.gov/20228792/)
2. N. H. Putnam *et al.*, Sea anemone genome reveals ancestral eumetazoan gene repertoire and genomic organization. *Science* **317**, 86–94 (2007). doi: [10.1126/science.1139158](https://doi.org/10.1126/science.1139158); pmid: [17615350](https://pubmed.ncbi.nlm.nih.gov/17615350/)
3. M. Srivastava *et al.*, The *Trichoplax* genome and the nature of placozoans. *Nature* **454**, 955–960 (2008). doi: [10.1038/nature07191](https://doi.org/10.1038/nature07191); pmid: [18719581](https://pubmed.ncbi.nlm.nih.gov/18719581/)
4. M. Srivastava *et al.*, The *Amphimedon queenslandica* genome and the evolution of animal complexity. *Nature* **466**, 720–726 (2010). doi: [10.1038/nature09201](https://doi.org/10.1038/nature09201); pmid: [20686567](https://pubmed.ncbi.nlm.nih.gov/20686567/)
5. N. King *et al.*, The genome of the choanoflagellate *Monosiga brevicollis* and the origin of metazoans. *Nature* **451**, 783–788 (2008). doi: [10.1038/nature06617](https://doi.org/10.1038/nature06617); pmid: [18273011](https://pubmed.ncbi.nlm.nih.gov/18273011/)
6. G. O. Mackie, C. E. Mills, C. L. Singla, Structure and function of the prehensile tentilla of *Euplokamis* (Ctenophora, Cydippida). *Zoomorphology* **107**, 319–337 (1988). doi: [10.1007/BF00312216](https://doi.org/10.1007/BF00312216)
7. J. Q. Henry, M. Q. Martindale, Regulation and regeneration in the ctenophore *Mnemiopsis leidyi*. *Dev. Biol.* **227**, 720–733 (2000). doi: [10.1006/dbio.2000.9903](https://doi.org/10.1006/dbio.2000.9903); pmid: [11071786](https://pubmed.ncbi.nlm.nih.gov/11071786/)
8. M. Q. Martindale, J. R. Finnerty, J. Q. Henry, The Radiata and the evolutionary origins of the bilaterian body plan. *Mol. Phylogenet. Evol.* **24**, 358–365 (2002). doi: [10.1016/S1055-7903\(02\)00208-7](https://doi.org/10.1016/S1055-7903(02)00208-7); pmid: [12220977](https://pubmed.ncbi.nlm.nih.gov/12220977/)
9. K. Pang, M. Q. Martindale, Developmental expression of homeobox genes in the ctenophore *Mnemiopsis leidyi*. *Dev. Genes Evol.* **218**, 307–319 (2008). doi: [10.1007/s00427-008-0222-3](https://doi.org/10.1007/s00427-008-0222-3); pmid: [18504608](https://pubmed.ncbi.nlm.nih.gov/18504608/)
10. M. Antcliff, Ultrastructure of the luminescent system of the ctenophore *Mnemiopsis leidyi*. *Cell Tissue Res.* **242**, 333–340 (1985). doi: [10.1007/BF00214545](https://doi.org/10.1007/BF00214545)
11. G. Freeman, G. T. Reynolds, The development of bioluminescence in the ctenophore *Mnemiopsis leidyi*. *Dev. Biol.* **31**, 61–100 (1973). doi: [10.1016/0012-1606\(73\)90321-7](https://doi.org/10.1016/0012-1606(73)90321-7); pmid: [4150750](https://pubmed.ncbi.nlm.nih.gov/4150750/)
12. C. E. Schnitzler *et al.*, Genomic organization, evolution, and expression of photoprotein and opsin genes in *Mnemiopsis leidyi*: A new view of ctenophore photocytes. *BMC Biol.* **10**, 107 (2012). doi: [10.1186/1741-7007-10-107](https://doi.org/10.1186/1741-7007-10-107); pmid: [23259493](https://pubmed.ncbi.nlm.nih.gov/23259493/)
13. M. Q. Martindale, J. Q. Henry, Reassessing embryogenesis in the Ctenophora: The inductive role of e_1 micromeres in organizing ctenophore row formation in the “mosaic” embryo, *Mnemiopsis leidyi*. *Development* **124**, 1999–2006 (1997). pmid: [9169846](https://pubmed.ncbi.nlm.nih.gov/9169846/)
14. M. Q. Martindale, J. Q. Henry, Intracellular fate mapping in a basal metazoan, the ctenophore *Mnemiopsis leidyi*, reveals the origins of mesoderm and the existence of indeterminate cell lineages. *Dev. Biol.* **214**, 243–257 (1999). doi: [10.1006/dbio.1999.9427](https://doi.org/10.1006/dbio.1999.9427); pmid: [10525332](https://pubmed.ncbi.nlm.nih.gov/10525332/)
15. G. Reverberi, G. Ortolani, On the origin of the ciliated plates and mesoderm in the Ctenophore. *Acta Embryol. Morphol. Exp.* **6**, 175–199 (1963).
16. K. Pang, M. Q. Martindale, *Mnemiopsis leidyi* spawning and embryo collection. *CSH Protoc.* **2008**, pdb.prot5085 (2008). pmid: [21356725](https://pubmed.ncbi.nlm.nih.gov/21356725/)
17. C. W. Dunn *et al.*, Broad phylogenomic sampling improves resolution of the animal tree of life. *Nature* **452**, 745–749 (2008). doi: [10.1038/nature06614](https://doi.org/10.1038/nature06614); pmid: [18322464](https://pubmed.ncbi.nlm.nih.gov/18322464/)
18. A. Hejnol *et al.*, Assessing the root of bilaterian animals with scalable phylogenomic methods. *Proc. Biol. Sci.* **276**, 4261–4270 (2009). doi: [10.1098/rspb.2009.0896](https://doi.org/10.1098/rspb.2009.0896); pmid: [19759036](https://pubmed.ncbi.nlm.nih.gov/19759036/)
19. H. Philippe *et al.*, Phylogenomics revives traditional views on deep animal relationships. *Curr. Biol.* **19**, 706–712 (2009). doi: [10.1016/j.cub.2009.02.052](https://doi.org/10.1016/j.cub.2009.02.052); pmid: [19345102](https://pubmed.ncbi.nlm.nih.gov/19345102/)

20. K. S. Pick *et al.*, Improved phylogenomic taxon sampling noticeably affects non-bilaterian relationships. *Mol. Biol. Evol.* **27**, 1983–1987 (2010). doi: [10.1093/molbev/msq089](https://doi.org/10.1093/molbev/msq089); pmid: [20378579](https://pubmed.ncbi.nlm.nih.gov/20378579/)
21. B. Schierwater, My favorite animal, *Trichoplax adhaerens*. *Bioessays* **27**, 1294–1302 (2005). doi: [10.1002/bies.20320](https://doi.org/10.1002/bies.20320); pmid: [16299758](https://pubmed.ncbi.nlm.nih.gov/16299758/)
22. B. Schierwater *et al.*, Concatenated analysis sheds light on early metazoan evolution and fuels a modern “urmetazoan” hypothesis. *PLOS Biol.* **7**, e20 (2009). doi: [10.1371/journal.pbio.1000020](https://doi.org/10.1371/journal.pbio.1000020); pmid: [19175291](https://pubmed.ncbi.nlm.nih.gov/19175291/)
23. T. Nosenko *et al.*, Deep metazoan phylogeny: When different genes tell different stories. *Mol. Phylogenet. Evol.* **67**, 223–233 (2013). doi: [10.1016/j.ympev.2013.01.010](https://doi.org/10.1016/j.ympev.2013.01.010); pmid: [23353073](https://pubmed.ncbi.nlm.nih.gov/23353073/)
24. J. C. Mullikin, Z. Ning, The phusion assembler. *Genome Res.* **13**, 81–90 (2003). doi: [10.1101/gr.731003](https://doi.org/10.1101/gr.731003); pmid: [12529309](https://pubmed.ncbi.nlm.nih.gov/12529309/)
25. J. F. Ryan, Baa.pl: A tool to evaluate de novo genome assemblies with RNA transcripts (2013), <http://arxiv.org/abs/1309.2087>.
26. T. R. Gregory, Animal Genome Size Database, www.genomesize.com.
27. A. Stamatakis, RAxML-VI-HPC: Maximum likelihood-based phylogenetic analyses with thousands of taxa and mixed models. *Bioinformatics* **22**, 2688–2690 (2006). doi: [10.1093/bioinformatics/btl446](https://doi.org/10.1093/bioinformatics/btl446); pmid: [16928733](https://pubmed.ncbi.nlm.nih.gov/16928733/)
28. N. Lartillot, T. Lepage, S. Blanquart, PhyloBayes 3: A Bayesian software package for phylogenetic reconstruction and molecular dating. *Bioinformatics* **25**, 2286–2288 (2009). doi: [10.1093/bioinformatics/btp368](https://doi.org/10.1093/bioinformatics/btp368); pmid: [19535536](https://pubmed.ncbi.nlm.nih.gov/19535536/)
29. A. B. Kohn *et al.*, Rapid evolution of the compact and unusual mitochondrial genome in the ctenophore, *Pleurobrachia bachei*. *Mol. Phylogenet. Evol.* **63**, 203–207 (2012). doi: [10.1016/j.ympev.2011.12.009](https://doi.org/10.1016/j.ympev.2011.12.009); pmid: [22201557](https://pubmed.ncbi.nlm.nih.gov/22201557/)
30. W. Pett *et al.*, Extreme mitochondrial evolution in the ctenophore *Mnemiopsis leidyi*: Insight from mtDNA and the nuclear genome. *Mitochondrial DNA* **22**, 130–142 (2011). doi: [10.3109/19401736.2011.624611](https://doi.org/10.3109/19401736.2011.624611); pmid: [21985407](https://pubmed.ncbi.nlm.nih.gov/21985407/)
31. L. Li, C. J. Stoeckert Jr., D. S. Roos, OrthoMCL: Identification of ortholog groups for eukaryotic genomes. *Genome Res.* **13**, 2178–2189 (2003). doi: [10.1101/gr.1224503](https://doi.org/10.1101/gr.1224503); pmid: [12952885](https://pubmed.ncbi.nlm.nih.gov/12952885/)
32. B. J. Liebeskind, D. M. Hillis, H. H. Zakon, Evolution of sodium channels predates the origin of nervous systems in animals. *Proc. Natl. Acad. Sci. U.S.A.* **108**, 9154–9159 (2011). doi: [10.1073/pnas.1106363108](https://doi.org/10.1073/pnas.1106363108); pmid: [21576472](https://pubmed.ncbi.nlm.nih.gov/21576472/)
33. K. Pang, J. F. Ryan, A. D. Baxeavanis, M. Q. Martindale, Evolution of the TGF- β signaling pathway and its potential role in the ctenophore, *Mnemiopsis leidyi*. *PLOS One* **6**, e24152 (2011). doi: [10.1371/journal.pone.0024152](https://doi.org/10.1371/journal.pone.0024152); pmid: [21931657](https://pubmed.ncbi.nlm.nih.gov/21931657/)
34. K. Pang, J. F. Ryan, NISC Comparative Sequencing Program, J. C. Mullikin, A. D. Baxeavanis, M. Q. Martindale, Genomic insights into Wnt signaling in an early diverging metazoan, the ctenophore *Mnemiopsis leidyi*. *Evodevo* **1**, 10 (2010). doi: [10.1186/2041-9139-1-10](https://doi.org/10.1186/2041-9139-1-10); pmid: [20920349](https://pubmed.ncbi.nlm.nih.gov/20920349/)
35. A. M. Reitzel *et al.*, Nuclear receptors from the ctenophore *Mnemiopsis leidyi* lack a zinc-finger DNA-binding domain: Lineage-specific loss or ancestral condition in the emergence of the nuclear receptor superfamily? *Evodevo* **2**, 3 (2011). doi: [10.1186/2041-9139-2-3](https://doi.org/10.1186/2041-9139-2-3); pmid: [21291545](https://pubmed.ncbi.nlm.nih.gov/21291545/)
36. J. F. Ryan, K. Pang, NISC Comparative Sequencing Program, J. C. Mullikin, M. Q. Martindale, A. D. Baxeavanis, The homeodomain complement of the ctenophore *Mnemiopsis leidyi* suggests that Ctenophora and Porifera diverged prior to the ParaHoxozoa. *Evodevo* **1**, 9 (2010). doi: [10.1186/2041-9139-1-9](https://doi.org/10.1186/2041-9139-1-9); pmid: [20920347](https://pubmed.ncbi.nlm.nih.gov/20920347/)
37. J. Lehmann, P. F. Stadler, V. Krauss, Near intron pairs and the metazoan tree. *Mol. Phylogenet. Evol.* **66**, 811–823 (2013). doi: [10.1016/j.ympev.2012.11.012](https://doi.org/10.1016/j.ympev.2012.11.012); pmid: [23201572](https://pubmed.ncbi.nlm.nih.gov/23201572/)
38. A. Pires-daSilva, R. J. Sommer, The evolution of signalling pathways in animal development. *Nat. Rev. Genet.* **4**, 39–49 (2003). doi: [10.1038/nrg977](https://doi.org/10.1038/nrg977); pmid: [12509752](https://pubmed.ncbi.nlm.nih.gov/12509752/)
39. A. Sebe-Pedros, A. J. Roger, F. B. Lang, N. King, I. Ruiz-Trillo, Ancient origin of the integrin-mediated adhesion and signaling machinery. *Proc. Natl. Acad. Sci. U.S.A.* **107**, 10142–10147 (2010). doi: [10.1073/pnas.1002257107](https://doi.org/10.1073/pnas.1002257107); pmid: [20479219](https://pubmed.ncbi.nlm.nih.gov/20479219/)
40. N. King, S. B. Carroll, A receptor tyrosine kinase from choanoflagellates: Molecular insights into early animal evolution. *Proc. Natl. Acad. Sci. U.S.A.* **98**, 15032–15037 (2001). doi: [10.1073/pnas.261477698](https://doi.org/10.1073/pnas.261477698); pmid: [11752452](https://pubmed.ncbi.nlm.nih.gov/11752452/)
41. M. Jäger *et al.*, New insights on ctenophore neural anatomy: Immunofluorescence study in *Pleurobrachia pileus* (Müller, 1776). *J. Exp. Zool. B Mol. Dev. Evol.* **316B**, 171–187 (2011). pmid: [21462312](https://pubmed.ncbi.nlm.nih.gov/21462312/)
42. G. R. Harbison, On the classification and evolution of the Ctenophora, in *The Origins and Relationships of Lower Invertebrates*, S. Conway Morris, J. D. George, R. Gibson, H. M. Platt, Eds. (Oxford Univ. Press, Oxford, 1985), pp. 78–100.
43. A. Hay-Schmidt, The evolution of the serotonergic nervous system. *Proc. Biol. Sci.* **267**, 1071–1079 (2000). doi: [10.1098/rspb.2000.1111](https://doi.org/10.1098/rspb.2000.1111); pmid: [10885511](https://pubmed.ncbi.nlm.nih.gov/10885511/)
44. M. L. Hernandez-Nicaise, The nervous system of ctenophores. III. Ultrastructure of synapses. *J. Neurocytol.* **2**, 249–263 (1973). doi: [10.1007/BF01104029](https://doi.org/10.1007/BF01104029); pmid: [9224490](https://pubmed.ncbi.nlm.nih.gov/9224490/)
45. O. Sakarya *et al.*, A post-synaptic scaffold at the origin of the animal kingdom. *PLOS One* **2**, e506 (2007). doi: [10.1371/journal.pone.0000506](https://doi.org/10.1371/journal.pone.0000506); pmid: [17551586](https://pubmed.ncbi.nlm.nih.gov/17551586/)
46. D. K. Simmons, K. Pang, M. Q. Martindale, Lim homeobox genes in the Ctenophore *Mnemiopsis leidyi*: The evolution of neural cell type specification. *Evodevo* **3**, 2 (2012). doi: [10.1186/2041-9139-3-2](https://doi.org/10.1186/2041-9139-3-2); pmid: [22239757](https://pubmed.ncbi.nlm.nih.gov/22239757/)
47. M. J. Layden, N. P. Meyer, K. Pang, E. C. Seaver, M. Q. Martindale, Expression and phylogenetic analysis of the *zic* gene family in the evolution and development of metazoans. *Evodevo* **1**, 12 (2010). doi: [10.1186/2041-9139-1-12](https://doi.org/10.1186/2041-9139-1-12); pmid: [21054859](https://pubmed.ncbi.nlm.nih.gov/21054859/)
48. N. Farrar, A. Riesgo, S. Leys, paper presented at the 2013 Society for Integrative and Comparative Biology Annual Meeting, San Francisco, CA, 3 to 7 January 2013.
49. P. R. H. Steinmetz *et al.*, Independent evolution of striated muscles in cnidarians and bilaterians. *Nature* **487**, 231–234 (2012). doi: [10.1038/nature11180](https://doi.org/10.1038/nature11180); pmid: [22763458](https://pubmed.ncbi.nlm.nih.gov/22763458/)
50. C. Trapnell *et al.*, Transcript assembly and quantification by RNA-Seq reveals unannotated transcripts and isoform switching during cell differentiation. *Nat. Biotechnol.* **28**, 511–515 (2010). doi: [10.1038/nbt.1621](https://doi.org/10.1038/nbt.1621); pmid: [20436464](https://pubmed.ncbi.nlm.nih.gov/20436464/)
51. M. G. Grabherr *et al.*, Full-length transcriptome assembly from RNA-Seq data without a reference genome. *Nat. Biotechnol.* **29**, 644–652 (2011). doi: [10.1038/nbt.1883](https://doi.org/10.1038/nbt.1883); pmid: [21572440](https://pubmed.ncbi.nlm.nih.gov/21572440/)
52. B. J. Haas *et al.*, Automated eukaryotic gene structure annotation using EvidenceModeler and the Program to Assemble Spliced Alignments. *Genome Biol.* **9**, R7 (2008). doi: [10.1186/gb-2008-9-1-r7](https://doi.org/10.1186/gb-2008-9-1-r7); pmid: [18190707](https://pubmed.ncbi.nlm.nih.gov/18190707/)
53. H. Shimodaira, M. Hasegawa, CONSEL: For assessing the confidence of phylogenetic tree selection. *Bioinformatics* **17**, 1246–1247 (2001). doi: [10.1093/bioinformatics/17.12.1246](https://doi.org/10.1093/bioinformatics/17.12.1246); pmid: [11751242](https://pubmed.ncbi.nlm.nih.gov/11751242/)

Acknowledgments: This research was supported by the Intramural Research Program of the National Human Genome Research Institute (NHGRI), NIH. This work was also supported in part by NASA and NSF grants to M.Q.M. J.F.R. received additional support from the Sars International Centre for Marine Molecular Biology and the University of Bergen. We thank A. Young, B. Schmidt, N. Gurson, R. Legaspi, B. Novotny, and R. Blakesley, who were responsible for the sequencing performed at the NIH Intramural Sequencing Center (NISC); A. Prasad, D. Gildea, N. Trivedi, A. Yun, K. Siewert, D. Leja, S. Bond, and G. Bouffard at NHGRI; A. Hejnol, D. Chourrout, L. Leclère, G. Richards, F. Rentzsch, C. Martin, H. Hausen, S. Henriët, S. Church, and S9 at Sars; B. Vellutini for the photo of *M. leidyi* used in Fig. 1A; W. Browne for access to additional RNA-seq data from early developmental stages of *M. leidyi*; J. Lehmann for supplying an updated near intron pair matrix; C. Trapnell for help with the Bowtie short-read aligner and Cufflinks transcript assembly program; M. Srivastava for phylogenetic data sets and advice; I. Ruiz-Trillo and the Origins of Multicellularity Sequencing Project, Broad Institute of Harvard and MIT for use of their genomic data; D. Rokhsar and the Joint Genome Institute for use of their genomic data; and other researchers whose publicly available sequence data were used in this study. The views expressed in this paper do not necessarily reflect the views of those acknowledged. We dedicate this manuscript to the pioneering work of the late Sebastian Beroe of the Stazione Zoologica in Naples. The authors declare no competing financial interests. The genome sequence data can be accessed from GenBank as project accession AGCP000000000 and from <http://research.nhgri.nih.gov/mnemiopsis/>. Contributions are as follows: genome and RNA-seq sequencing and assembly: NISC and J.C.M.; annotation: J.F.R., K.P., C.E.S., P.H., N.H.P., A.-D.N., R.T.M., B.J.K., and T.G.W.; analysis: J.F.R., K.P., C.E.S., D.K.S., B.J.K., P.H., N.H.P., M.Q.M., and A.D.B.; additional ctenophore data: S.H.D.H. and W.R.F.; phylogenetics: J.F.R., S.A.S., and C.W.D.; writing: J.F.R., K.P., C.E.S., D.K.S., R.T.M., C.W.D., M.Q.M., and A.D.B.; project design and coordination: J.F.R., M.Q.M., and A.D.B.

Supplementary Materials

www.sciencemag.org/content/342/6164/1242592/suppl/DC1
Materials and Methods
Figs. S1 to S10
Tables S1 to S31
References

1 July 2013; accepted 28 October 2013
[10.1126/science.1242592](https://doi.org/10.1126/science.1242592)

The Hidden Geometry of Complex, Network-Driven Contagion Phenomena

Dirk Brockmann^{1,2,3*} and Dirk Helbing^{4,5}

The global spread of epidemics, rumors, opinions, and innovations are complex, network-driven dynamic processes. The combined multiscale nature and intrinsic heterogeneity of the underlying networks make it difficult to develop an intuitive understanding of these processes, to distinguish relevant from peripheral factors, to predict their time course, and to locate their origin. However, we show that complex spatiotemporal patterns can be reduced to surprisingly simple, homogeneous wave propagation patterns, if conventional geographic distance is replaced by a probabilistically motivated effective distance. In the context of global, air-traffic-mediated epidemics, we show that effective distance reliably predicts disease arrival times. Even if epidemiological parameters are unknown, the method can still deliver relative arrival times. The approach can also identify the spatial origin of spreading processes and successfully be applied to data of the worldwide 2009 H1N1 influenza pandemic and 2003 SARS epidemic.

The geographic spread of emergent infectious diseases affects the lives of tens of thousands or even millions of people (1, 2). Recent examples of emergent diseases are the SARS epidemic of 2003, the 2009 H1N1 influenza pandemic, and most recently a new strain (H7N9) of avian influenza virus (3, 4). Progressing worldwide urbanization, combined with growing connectivity among metropolitan centers, has increased the risk that highly virulent emergent pathogens will spread (5–8). The complexity of global human mobility, particularly air traffic (Fig. 1A), makes it increasingly difficult to develop effective containment and mitigation strategies on the time scale imposed by the speed at which modern diseases can spread (9–11). Because timely, accurate, and focused action can potentially save the lives of many people and reduce the socioeconomic impact of infectious diseases (12, 13), understanding global disease dynamics has become a major 21st-century challenge. Unraveling the core mechanisms that underlie these phenomena and being able to distinguish key factors from peripheral ones are required to develop quantitative, efficient, and predictive models that public health authorities can employ to assess situations quickly, make informed decisions, and optimize vaccination and drug delivery plans. After the initial outbreak of an epidemic, the key questions are as follows: (i) Where did the novel pathogen emerge? (ii) Where are new cases to be expected? (iii) When is an epidemic going to arrive at distant locations? (iv) How many cases are to be expected?

Historically, for cases like the spread of the Black Death in Europe, reaction-diffusion mod-

els have been quite useful in addressing these questions (14, 15). Despite their high level of abstraction, these models provide a solid intuition and understanding of spreading processes. Their mathematical simplicity permits the assessment of key properties, e.g., spreading speed, arrival times, and how pattern geometry depends on system parameters (16). However, because of long-distance travel, simple reaction-diffusion models are inadequate for the description of today's complex, spatially incoherent spreading patterns that generically bear no metric regularity, that depend sensitively on model parameters and initial conditions (17–20) (Fig. 1, B to E, and fig. S2).

Consequently, scientists have been developing powerful, large-scale computational models and sophisticated, parameter-rich epidemic simulators that tackle the above key questions in detailed ways. These consider demographics, mobility, and epidemiological data, as well as disease-specific mechanisms, all of which are believed to play a role (21–23). Models range from high-level stochastic metapopulation models (5, 20, 24) to agent-based computer simulations that account for the behavior and interactions of millions of individuals in large populations (25). These approaches have become remarkably successful in reproducing observed patterns and predicting the temporal evolution of ongoing epidemics (26). Many such models reproduce similar dynamic features despite major differences in their underlying assumptions and data (27). The abundance of different, often mutually incompatible, models suggests that we still lack a fundamental understanding of the key factors that determine the observed spatiotemporal dynamics. It is unclear how the multitude of factors shape the dynamics and how much detail is required to achieve a certain level of predictive fidelity. Moreover, detailed computational models that incorporate all potentially relevant factors at initiation do not inform which factors are actually relevant and which ones are not (28). They are also hard to calibrate and of limited use when the knowledge of epidemiological parameters is uncertain.

Here, we propose an intuitive and efficient approach that remedies the situation by connecting the conceptual power of simple reaction-diffusion systems with the predictive power of high-level, computational models. Our approach is based on the idea of replacing conventional geographic distance by a measure of effective distance derived from the underlying mobility network. Based on this novel notion of distance, patterns that exhibit complex spatiotemporal structure in the conventional geographic perspective turn into regular, wavelike solutions reminiscent of simple reaction-diffusion systems. This permits the definition of effective epidemic wavefronts, propagation speeds, and the reliable estimation of epidemic arrival times, based on the knowledge of the underlying mobility network. The method, however, goes beyond remapping data. It provides two key insights. First, epidemiological parameters enter the spreading dynamics separately from the transport parameters, and second, the dynamics is dominated by only a small percentage of transport connections. Furthermore, our approach can quickly identify the geographic origin of emergent diseases, using temporal snapshots of the spatial disease distribution. This detection of the origin of complex, multiscale dynamical spreading patterns is important for three reasons: (i) to determine what has caused the disease, (ii) to develop timely mitigation strategies, and (iii) to predict its further spread (the arrival times in remote locations and the expected prevalence).

Modeling Network-Driven Contagion Phenomena

For illustration, we consider a complex network of coupled populations (a metapopulation) in which the local disease time course is described by a conventional susceptible-infected-recovered (SIR) dynamics (1):

$$\begin{aligned}\partial_t S_n &= -\alpha I_n S_n / N_n, \\ \partial_t I_n &= \alpha I_n S_n / N_n - \beta I_n \quad n = 1, \dots, M\end{aligned}\quad (1)$$

where N_n is the population size of population n , M is the number of populations, and S_n , I_n , $R_n = N_n - S_n - I_n$ are absolute numbers of susceptible, infected, and recovered individuals, respectively. Parameter β is the mean recovery rate of individuals (for influenza-like diseases $\beta^{-1} = 3$ to 5 days), and $R_0 = \alpha/\beta$ is the basic reproduction ratio (for which we assume typical values in the range 1.4 to 2.9). (The focus on SIR kinetics is not essential, as the following results are also valid for other types of local dynamics.) Each local population represents a node n in the global mobility network (GMN), depicted in Fig. 1A. In addition to the local dynamics, individuals travel between nodes according to the rate equation

$$\partial_t U_n = \sum_{m \neq n} w_{nm} U_m - w_{nn} U_n \quad (2)$$

where U_n is a placeholder for the classes S_n , I_n , and R_n . The quantities $w_{nm} = F_{nm}/N_m$ represent the per-capita traffic flux from location m to n .

¹Robert-Koch-Institute, Seestraße 10, 13353 Berlin, Germany.

²Institute for Theoretical Biology, Humboldt-University Berlin, Invalidenstrasse 42, 10115 Berlin, Germany. ³Department of Engineering Sciences and Applied Mathematics and Northwestern Institute on Complex Systems, Northwestern University, Evanston, IL 60208, USA. ⁴ETH Zurich, Swiss Federal Institute of Technology, CLU E1, Clausiusstrasse 50, 8092 Zurich, Switzerland. ⁵Risk Center, ETH Zurich, Scheuchzerstrasse 7, 8092 Zurich, Switzerland.

*Corresponding author. E-mail: dirk.brockmann@hu-berlin.de

Weighted links F_{mn} quantify direct air traffic (passengers per day) from node m to node n . The GMN is constructed from the worldwide air traffic between 4069 airports with 25,453 direct connections. Details on the data and network construction are provided in the supplementary materials (e.g., fig. S1 and table S1) (5, 13, 20, 29). The total network traffic is approximately $\Phi = 8.91 \times 10^6$ passengers per day. Assuming that the total traffic in and out of a node is proportional to its population size, Eqs. 1 and 2 can be rewritten as

$$\begin{aligned} \partial_t j_n &= \alpha s_n j_n \sigma(j_n/\varepsilon) - \beta j_n + \gamma \sum_{m \neq n} P_{mn} (j_m - j_n) \\ \partial_t s_n &= -\alpha s_n j_n \sigma(j_n/\varepsilon) + \gamma \sum_{m \neq n} P_{mn} (s_m - s_n) \end{aligned} \quad (3)$$

with $s_n = S_n/N_n$, $j_n = I_n/N_n$, and $r_n = 1 - s_n - j_n$. A detailed derivation is provided in the supplementary text. The mobility parameter γ is the average mobility rate, i.e., $\gamma = \Phi/\Omega$, where $\Omega = \sum_n N_n$ is the total population in the system. This yields numerical values in the range $\gamma = 0.0013 - 0.0178 \text{ day}^{-1}$. The matrix \mathbf{P} with $0 \leq P_{mn} \leq 1$ quantifies the fraction of the passenger flux with destination m

emanating from node n , i.e., $P_{mn} = F_{mn}/F_n$, where $F_n = \sum_m F_{mn}$. The additional sigmoid function $\sigma(x) = x^\eta/(1 + x^\eta)$ with gain parameter $\eta \gg 0$ accounts for the local invasion threshold ε and fluctuation effects for $j_n < \varepsilon$ (30–32). Typical parameter choices for ε and η are $\eta = 4, 8, \infty$ and $-\log_{10} \varepsilon = 4, \dots, 6$. Our results are robust with respect to changes in these parameters (e.g., figs. S5 and S13).

Figure 1B shows a temporal snapshot of the dynamical system defined by Eq. 3 for a hypothetical pandemic with initial outbreak location (OL) in Hong Kong (HKG) (see also Fig. 2B and fig. S2 for temporal sequences of the dynamical system for various other OLs). Generally, the metapopulation model above and related models used in the past generate solutions that are characterized by similar qualitative features. First, only during the early stage of the process does the prevalence $j_n(t)$ (i.e., the fraction of infected individuals) correlate significantly with geographic distance from the OL. Second, at in-

termediate and later stages, the multiscale structure of the GMN induces a spatial decoherence of the spreading pattern. Third, despite the global connectivity, the spatiotemporal patterns do not converge to the same pattern, i.e., spatiotemporal differences are not a transient effect (figs. S3 to S6 and movies S1 to S3). This type of complexity sharply contrasts the generic behavior of ordinary reaction-diffusion systems, which typically exhibit spatially coherent wavefronts.

Most Probable Paths and Effective Distance

The key idea we pursue here is that, despite the structural complexity of the underlying network, the redundancy of connections, and the multiplicity of paths a contagion phenomenon can take, the dynamic process is dominated by a set of most probable trajectories that can be derived from the connectivity matrix \mathbf{P} . This hypothesis is analogous to the dominance of the smallest resistor in a strongly heterogeneous electrical network with parallel conducting lines. Given the flux-fraction $0 \leq P_{mn} \leq 1$, i.e., the fraction of travelers that leave node n and

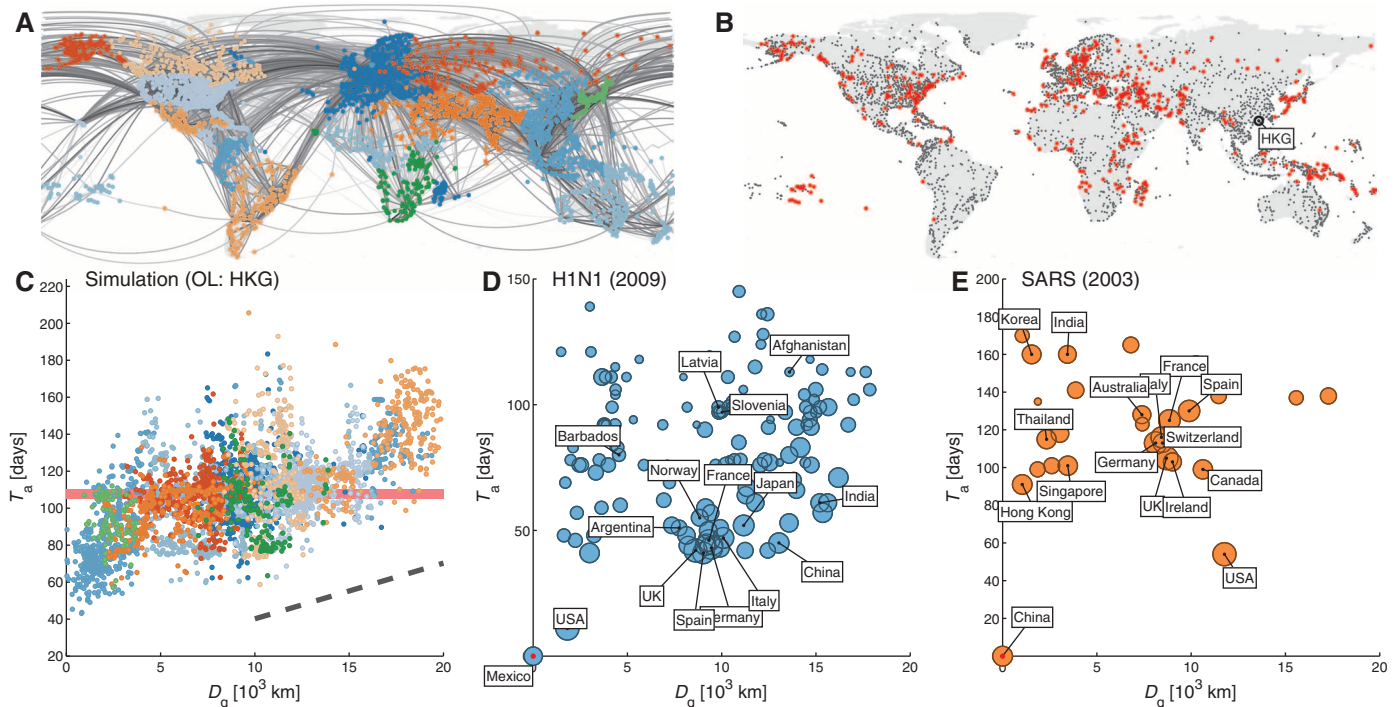


Fig. 1. Complexity in global, network-driven contagion phenomena. (A) The global mobility network (GMN). Gray lines represent passenger flows along direct connections between 4069 airports worldwide. Geographic regions are distinguished by color [classified according to network modularity maximization (39)]. (B) Temporal snapshot of a simulated global pandemic with initial outbreak location (OL) in Hong Kong (HKG). The simulation is based on the metapopulation model defined by Eq. 3 with parameters $R_0 = 1.5$, $\beta = 0.285 \text{ day}^{-1}$, $\gamma = 2.8 \times 10^{-3} \text{ day}^{-1}$, $\varepsilon = 10^{-6}$. Red symbols depict locations with epidemic arrival times in the time window $105 \text{ days} \leq T_a \leq 110 \text{ days}$. Because of the multiscale structure of the underlying network, the spatial distribution of disease prevalence (i.e., the fraction of infected individuals) lacks geometric coherence. No clear wavefront is visible, and based on this dynamic state, the OL cannot be easily deduced. (C) For the same simulation as in (B), the panel depicts arrival times T_a as a function of geographic distance D_g from the OL [nodes are colored according to geographic region as in (A)] for each of the 4069 nodes in the network. On a

global scale, T_a weakly correlates with geographic distance D_g ($R^2 = 0.34$). A linear fit yields an average global spreading speed of $v_g = 331 \text{ km/day}$ (see also fig. S7). Using D_g and v_g to estimate arrival times for specific locations, however, does not work well owing to the strong variability of the arrival times for a given geographic distance. The red horizontal bar corresponds to the arrival time window shown in (B). (D) Arrival times versus geographic distance from the source (Mexico) for the 2009 H1N1 pandemic. Symbols represent 140 affected countries, and symbol size quantifies total traffic per country. Arrival times are defined as the date of the first confirmed case in a given country after the initial outbreak on 17 March 2009. As in the simulated scenario, arrival time and geographic distance are only weakly correlated ($R^2 = 0.0394$). (E) In analogy to (D), the panel depicts the arrival times versus geographic distance from the source (China) of the 2003 SARS epidemic for 29 affected countries worldwide. Arrival times are taken from WHO published data (2). As in (C) and (D), arrival time correlates weakly with geographic distance.

arrive at node m , we define the effective distance d_{mn} from a node n to a connected node m as

$$d_{mn} = (1 - \log P_{mn}) \geq 1 \quad (4)$$

This concept of effective distance reflects the idea that a small fraction of traffic $n \rightarrow m$ is effectively equivalent to a large distance, and vice versa. As explained in more detail in the supplementary text, the logarithm is a consequence of the requirement that effective lengths are additive, whereas probabilities along multistep paths are multiplicative. Eq. 4 defines a quasi-distance, which is generally asymmetric, i.e., $d_{mn} \neq d_{nm}$. The lack of symmetry is analogous to a road network of one-way streets, where the shortest distance from A to B may differ from the one from B to A. This asymmetry captures the effect that a randomly seeded disease in a peripheral node of the network has a higher probability of being transmitted to a well-connected hub than vice versa (figs. S8 to S10). More properties of effective distance as defined by Eq. 4 are discussed in the supplementary text. On the basis of effective distance, we can define the directed length $\lambda(\Gamma)$ of an ordered path

$\Gamma = \{n_1, \dots, n_L\}$ as the sum of effective lengths along the legs of the path. Moreover, we define the effective distance D_{mn} from an arbitrary reference node n to another node m in the network by the length of the shortest path from n to m :

$$D_{mn} = \min_{\Gamma} \lambda(\Gamma) \quad (5)$$

Again, we typically have $D_{mn} \neq D_{nm}$. From the perspective of a chosen origin node n , the set of shortest paths to all other nodes constitutes a shortest path tree Ψ_n (Fig. 2A), illustrating the most probable sequence of paths from the root node n to the other nodes.

Effective Distance Perspective Reveals Hidden Pattern Geometry

The key question is how, compared to the conventional geographic representation, the same spreading process evolves on the shortest path tree. Figure 2B portrays this comparison. We see that the effective distance representation has notable advantages: It reveals simple coherent wave fronts, whereas spatiotemporal patterns in geographical space are complex, incoherent, and hard

to understand. This is a generic feature that is robust against variations in epidemic parameters and true for any choice of the OL (figs. S11 and S12). Using effective distance, one can thus calculate the spreading speed and arrival times of a disease, and determine functional relationships between epidemiological and mobility parameters. The dynamic simplicity in the new representation is much more than just a trivial visual rearrangement of the spatiotemporal pattern. Simple propagating waves in the new perspective imply that the contagion process is dominated by most probable paths, as this is the underlying assumption in the derivation of Eq. 5. Also, effective distance and the shortest path trees only depend on the static mobility matrix \mathbf{P} . This implies that, on a spatial scale described by the metapopulation model (Eq. 3), the complexity of the spatiotemporal pattern is largely determined by the structure of the mobility component in Eq. 3 and not by the nonlinearities or the disease-specific, epidemiological rate parameters of the model.

Figure 2C presents the correlation of arrival times T_a with effective distances D_{eff} for the

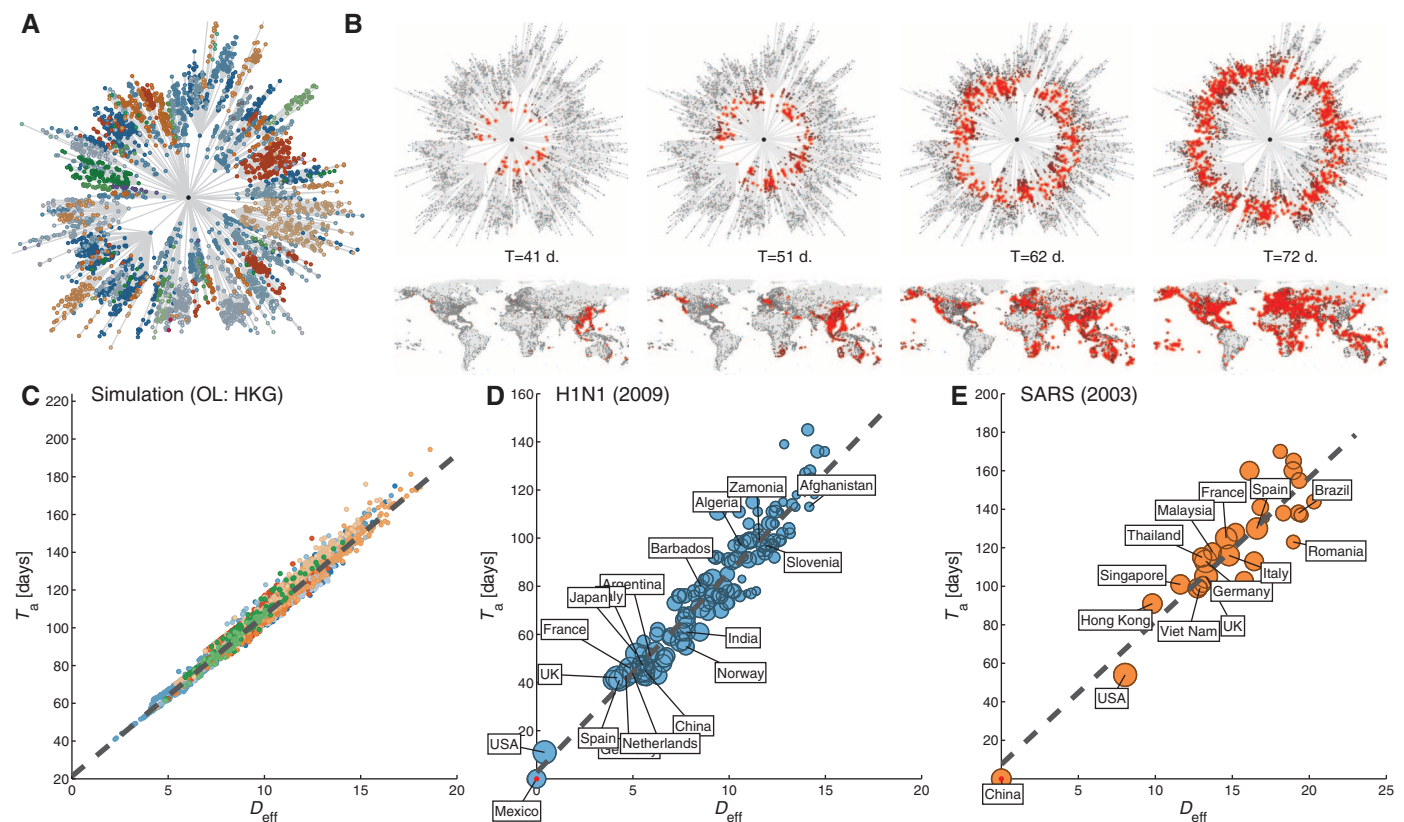


Fig. 2. Understanding global contagion phenomena using effective distance. (A) The structure of the shortest path tree (in gray) from Hong Kong (central node). Radial distance represents effective distance D_{eff} as defined by Eqs. 4 and 5. Nodes are colored according to the same scheme as in Fig. 1A. (B) The sequence (from left to right) of panels depicts the time course of a simulated model disease with initial outbreak in Hong Kong (HKG), for the same parameter set as used in Fig. 1B. Prevalence is reflected by the redness of the symbols. Each panel compares the state of the system in the conventional geographic representation (bottom) with the effective distance representation (top). The complex spatial pattern in the conventional view is equivalent to a homoge-

neous wave that propagates outwards at constant effective speed in the effective distance representation. (C) Epidemic arrival time T_a versus effective distance D_{eff} for the same simulated epidemic as in (B). In contrast to geographic distance (Fig. 1C), effective distance correlates strongly with arrival time ($R^2 = 0.973$), i.e., effective distance is an excellent predictor of arrival times. (D and E) Linear relationship between effective distance and arrival time for the 2009 H1N1 pandemic (D) and the 2003 SARS epidemic (E). The arrival time data are the same as in Fig. 1, D and E. The effective distance was computed from the projected global mobility network between countries. As in the model system, we observe a strong correlation between arrival time and effective distance.

simulation shown in Fig. 2B. Compared to Fig. 1C, this demonstrates that effective distance generates a much higher correlation than geographic distance ($R_{\text{eff}}^2 = 0.97$ compared to $R_{\text{geo}}^2 = 0.34$; see tables S2 and S3 and fig. S12 for more examples). Furthermore, the relationship of T_a and D_{eff} is linear, which means that the effective speed $v_{\text{eff}} = D_{\text{eff}}/T_a$ of the wavefront is a well-defined constant. To compare the regression quality, we computed the distribution of relative residuals $r = \delta T_a/T_a$, using effective or geographic distance as a regressor. The ratio of residual variances implies a more than 50-fold higher prediction quality (table S3 and fig. S13).

Although we have demonstrated the clear linear functional relationship for simulated, hypothetical scenarios of global disease spread, it is crucial to test the validity and usefulness of the effective distance approach on empirical data. Figure 2, D and E, depict arrival time versus effective distance on the basis of data for the 2009 H1N1 pandemic and the global 2003 SARS epidemic, respectively (figs. S14 to S16 and table S4). Arrival times are the same as in Fig. 1, D and E, but shown across effective rather than geographic distances. As the empirical data are available on a country resolution, we determined the traffic between countries by aggregation to specify a coarse-grained network (GMNc) (189 nodes, 5004 links) and effective distances from the origin location in each case (see supplementary text for details).

Both the H1N1 and SARS data exhibit a clear linear relationship between arrival time and effective distance from the source, even though additional factors complicate the spreading of real diseases. Fluctuations, effects due to coarse graining, and errors in arrival-time measurements can add noise to the system, which increases the scatter in the linear relationship. To address the general validity of the observed effects, we also analyzed data generated by the global epidemic and mobility model (GLEAM) (www.gleamviz.org), a sophisticated epidemic simulation framework (21). GLEAM incorporates air transportation and local commuter traffic on a global scale, is fully stochastic, and permits the simulation of infectious state-dependent mobility behavior, clinical states, antiviral treatment, and more. The results of this analysis are shown in figs. S17 to S19 and are consistent with our claims.

Relative Arrival Times Are Independent of Epidemic Parameters

Our results reveal an important, approximate relationship between the system parameters, which can be summarized as follows:

$$T_a = \underbrace{D_{\text{eff}}(\mathbf{P})}_{\text{eff. distance}} / \underbrace{v_{\text{eff}}(\alpha, R_0, \gamma, \varepsilon)}_{\text{eff. speed}} \quad (6)$$

This equation states that arrival times can be computed with high fidelity based on the ef-

fective distances D_{eff} and effective spreading speed v_{eff} , and that each factor depends on different parameters of the dynamical system. The epidemiological parameters determine the effective speed, whereas effective distance depends only on the topological features of the static underlying network, i.e., the matrix \mathbf{P} . When confronted with the outbreak of an emergent infectious disease, one of the key problems is that the disease-specific parameters are typically unknown in the beginning, and simulations based on plausible parameter ranges typically exhibit substantial variability in predicted outcomes. However, Eq. 6 allows us to compute relative arrival times without knowledge of these parameters. If, for example, the outbreak node is labeled k , while n and m are arbitrary nodes, then $T_a(n|k)/T_a(m|k) = D_{\text{eff}}(n|k)/D_{\text{eff}}(m|k)$. Equation 6 states that the effective speed v_{eff} is a global property, independent of the mobility network and the outbreak location. Thus, irrespective of mobility and OL, one can investigate how the effective speed depends on rate parameters of the system.

Origin of Outbreak Reconstruction Based on Effective Distance

The concept of effective distance is particularly valuable for solving the aforementioned inverse problem: Given a spatially distributed prevalence pattern that was generated by an

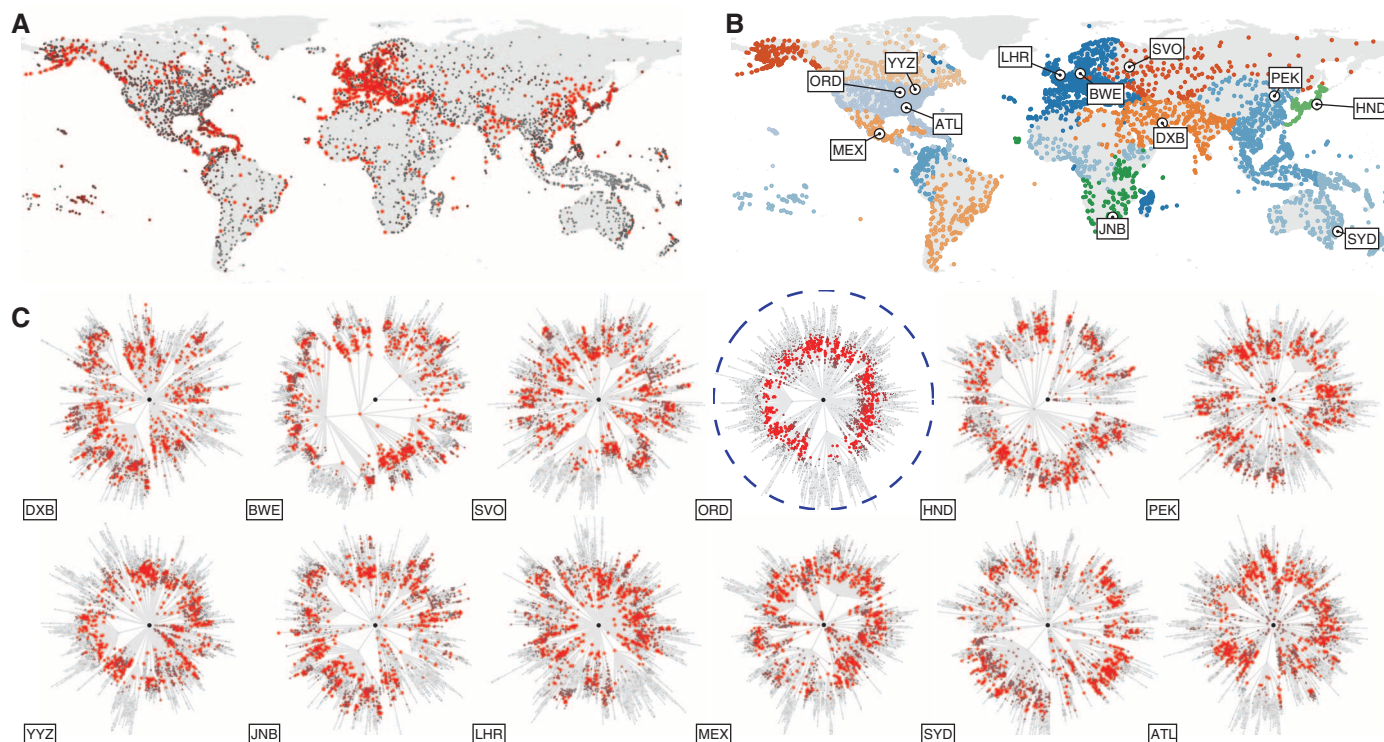


Fig. 3. Qualitative outbreak reconstruction based on effective distance. (A) Spatial distribution of prevalence $j_n(t)$ at time $T = 81$ days for OL Chicago (parameters $\beta = 0.28 \text{ day}^{-1}$, $R_0 = 1.9$, $\gamma = 2.8 \times 10^{-3} \text{ day}^{-1}$, and $\varepsilon = 10^{-6}$). After this time, it is difficult, if not impossible, to determine the correct OL from snapshots of the dynamics. (B) Candidate OLs chosen from different geographic regions. (C) Panels depict the state of the system shown in (A) from the

perspective of each candidate OL, using each OL's shortest path tree representation. Only the actual OL (ORD, circled in blue) produces a circular wavefront. Even for comparable North American airports [Atlanta (ATL), Toronto (YYZ), and Mexico City (MEX)], the wavefronts are not nearly as concentric. Effective distances thus permit the extraction of the correct OL, based on information on the mobility network and a single snapshot of the dynamics.

underlying, and potentially hidden, spreading mechanism, how can we determine the most likely initial outbreak location (33, 34)? A crucial property of the effective distance perspective is that spreading concentricity (Fig. 2B) is only observed from the perspective of the actual OL. Therefore, given a spatiotemporal snapshot of the spreading dynamics (Fig. 3A), we can represent the spreading process from the perspective of

candidate OLs (Fig. 3C) and determine the degree of concentricity of the pattern in effective distance. Compared to alternative OL candidates, the representation for the actual OL exhibits the most concentric shape, identifying this node as the correct outbreak location. This type of qualitative analysis can be made more systematic by introducing a measure for concentricity. We investigated two conceptually differ-

ent approaches. First, for every one of the 4069 potential outbreak locations n , we computed the shortest path tree Ψ_n , the effective distance to all other locations $D_{\text{eff}}(m|n)$, and arrival times $T_a(m|n)$. For each candidate node, we computed the correlation coefficient $c(T_a, D_{\text{eff}})$ of effective distance and arrival time for candidate location n . This approach should yield the highest correlation when n is the actual outbreak location.

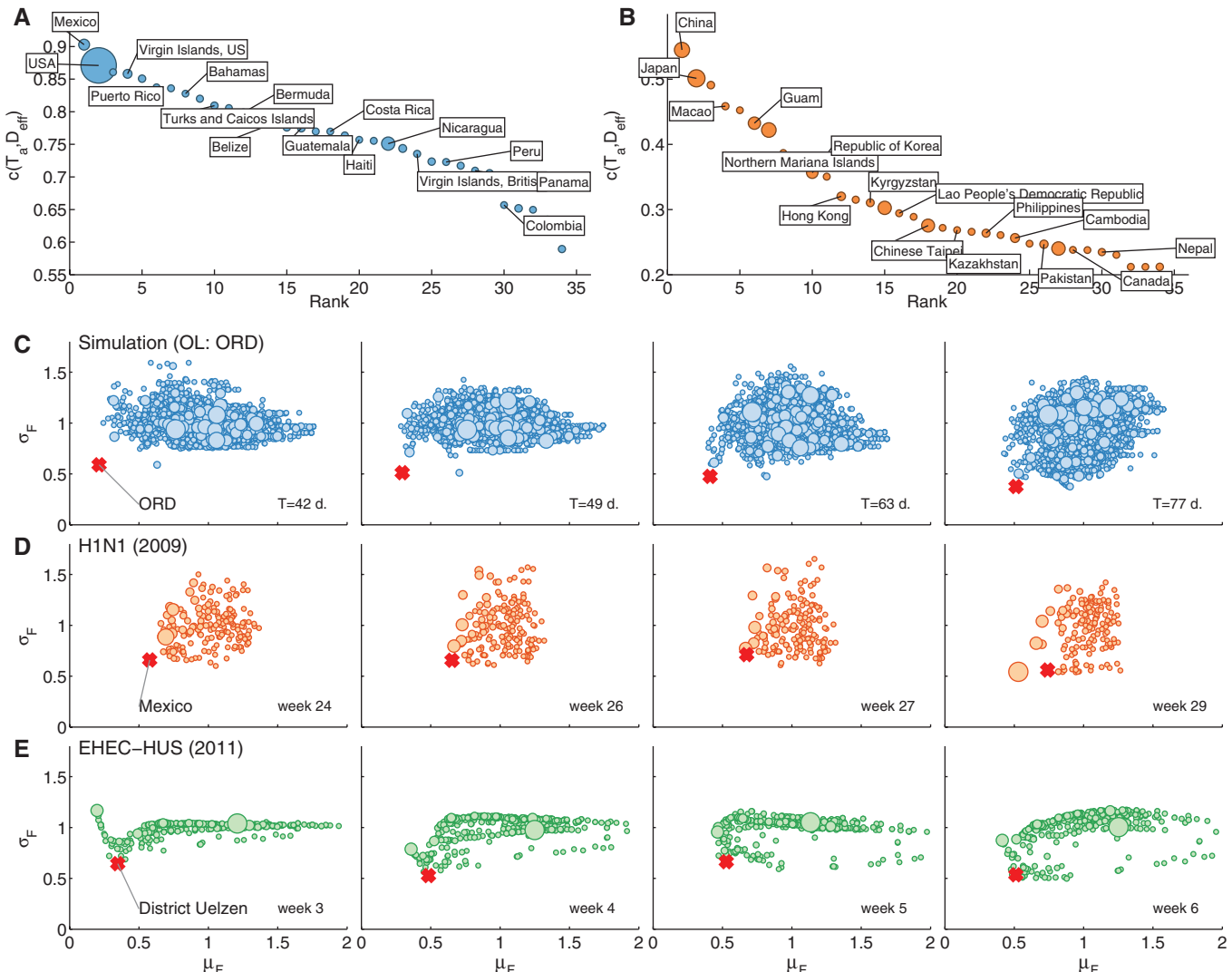


Fig. 4. Quantitative outbreak reconstruction based on effective distance. (A) Correlation-based outbreak reconstruction using arrival-time data for the 2009 H1N1 pandemic. For each country n as a potential source, we computed the correlation coefficient $c(T_a, D_{\text{eff}})$ of arrival time $T_a(m|n)$ and effective distance $D_{\text{eff}}(m|n)$. According to our analysis, high correlation implies a concentric pattern from the chosen node. The panel depicts $c(T_a, D_{\text{eff}})$ as a function of rank. Mexico (followed by the United States) exhibits the largest correlation, consistent with the known outbreak scenario. (B) Correlation rank diagram for the 2003 SARS epidemic analogous to (A). Here, China is correctly identified as the source. (C) Sequence of panels depicting an alternative outbreak reconstruction technique based on temporal snapshots in the scenario of a simulated pandemic with outbreak in Chicago (ORD) with parameters identical to those used in Fig. 3. At each time, we computed the mean μ_F and variance σ_F of effective distance (see text) from each potential OL to the wavefront. A combined low mean and variance are equivalent to a high degree of concentricity. The red symbol corresponds to the actual OL, which is clearly

separated from the point cloud. Symbol size quantifies total traffic per node. (D) Along the same lines as in (C), the panels depict data pairs (μ_F, σ_F) for all countries as outbreak candidates for the H1N1 pandemic during four different weeks of the pandemic. As described in the text, we used a coarse-grained, country-resolution global mobility network (GMNc). Although the actual outbreak location does not separate from the main point cloud as much as in the simulated scenario, the actual outbreak location is nevertheless identified as the point with minimum combined (μ_F, σ_F) , except for the last time frame where the approach would identify the United States as the source. (E) Outbreak reconstruction for the 2011 EHEC-HUS outbreak, using a model and data for food distribution among 412 districts in Germany as the underlying network. The actual district Uelzen is correctly identified in all but the last time windows. For all times, however, some other locations possess comparatively low values of (μ_F, σ_F) as well. Although this makes definite source identification difficult, it substantially reduces the number of potential outbreak locations.

As expected, this is the case for the H1N1 and SARS data sets (Fig. 4, A and B). However, this approach requires knowledge of the entire time course of the epidemic, e.g., arrival times at all locations, which is typically not available in real situations. Therefore, we used an alternative approach, mathematically similar to surface roughness characterization (35), that only requires dynamic information in a small time window, e.g., one snapshot of the spreading pattern. For each of the potential candidate outbreak locations, we computed the effective distance to the subset of nodes with prevalence above a certain threshold, e.g., the red symbols in the patterns of Fig. 3A or Fig. 1B. On the basis of this set of effective distances (denoted by F), we compute the mean $\mu_F(D_{\text{eff}})$ and standard deviation $\sigma_F(D_{\text{eff}})$. Concentricity increases with a combined minimization of mean and standard deviation (supplementary text). Figure 4C depicts the distribution of ensemble-normalized pairs $[\mu_F(D_{\text{eff}}), \sigma_F(D_{\text{eff}})]$ for a simulated scenario at four different times. For all time points, the actual outbreak location is well separated from the remaining point cloud and closest to the origin. This shows that the effective distance perspective is unique from the actual outbreak location and that knowledge of a temporal snapshot of the spreading state combined with knowledge of the underlying mobility network is a powerful tool for outbreak reconstruction.

Although our method works well for simulation-generated data (i.e., disease dynamics generated by Eq. 3), real data pose additional challenges: (i) Data are subject to inaccuracies and incompleteness in prevalence counts; (ii) fluctuations, not captured explicitly by our model, may play a particular role during the onset of an epidemic; and (iii) response and mitigation measures that can change the time course of disease dynamics are not accounted for by our model. Therefore, to assess the applicability of our approach in a realistic context, we validated the effective distance method using data on the 2009 H1N1 pandemic and the 2011 outbreak of food-borne enterohemorrhagic *Escherichia coli* (EHEC) O104:H4/HUS in Germany with ~4000 cases and 53 deaths. Although the application to the H1N1 pandemic is a proof-of-concept application, as finding the spatial origin on a country resolution was actually not the problem that we investigated here, reconstructing the spatial outbreak origin during the EHEC-HUS epidemic (district Uelzen in Northern Germany) was notoriously difficult because of the spatial incoherence of reported cases. For the application to H1N1, we used data of the worldwide prevalence count by country in weeks 14 to 30 of 2009 (36). For EHEC-HUS, we constructed a network of food distribution in Germany using a gravity model for transportation networks (37). For the spatial prevalence, we used data on case counts per district in Germany (38).

Figure 4D illustrates the results for H1N1. In analogy to Fig. 4C, we use four distinct time windows (weeks 24, 26, 27, and 29). The method

successfully identifies Mexico as the source of this event, even though the time windows cover a 2-month period when the pandemic's peak prevalence had already reached a broad geographical distribution (fig. S16). Only as late as week 29, another country (the United States) is incorrectly identified as the likely outbreak location.

Figure 4E depicts the analogous results for the 2011 EHEC-HUS epidemic, where disease spreading was promoted not by air transportation, but by food transport. The nodes in the network are 412 administrative districts in Germany, coupled by the food supply network of the country. As time windows, we chose weeks 3 to 6 after onset. For this epidemic, a local farm in Bienenbüttel, district Uelzen, was later identified as the source of contaminated sprouts (38). On the basis of prevalence distribution in the entire country, the effective distance method correctly identifies district Uelzen as the most likely geographic source. However, in this case, the separation in the mean/standard deviation diagram is not as pronounced as for disease spread by air passenger flows. Nevertheless, although the method cannot identify the OL with full reliability here, it dramatically reduces the set of potential origin locations.

In both real-world scenarios—the 2011 EHEC/HUS epidemic and the 2009 H1N1 pandemic—the OL reconstruction works surprisingly well, despite the intrinsic fluctuations and the low-incidence regime. The unexpected degree of predictability indicates that the set of links in the network contributing the shortest paths accumulates a substantial fraction of the overall transmission probability (and that this set is almost identical from the perspective of all nodes; fig. S20).

Discussion

In summary, the analysis of global disease dynamics in the framework of effective distances enables researchers to understand complex contagion dynamics in multiscale networks with simple reaction-diffusion models. Given fixed values for epidemic parameters, our analysis shows that network and flux information are sufficient to predict the dynamics and arrival times. The method is a promising starting point for more detailed investigations, including the functional dependencies of key epidemic variables such as the spreading speed and related macroscopic quantities on epidemiological parameters. The successful application to real epidemic data suggests that our method is also of practical use. Finally, it seems promising to generalize the effective distance method to other contagion phenomena, such as human-mediated bioinvasion and the spread of rumors or violence, a subject of ever-more importance in an increasingly connected society.

References and Notes

1. R. M. Anderson, R. M. May, *Infectious Diseases of Humans: Dynamics and Control* (Oxford Univ. Press, Oxford and New York, 1991).
2. World Health Organization, Global Alert and Response; www.who.int/csr/en/.

3. A. R. McLean, R. M. May, J. Pattison, R. A. Weiss, *SARS: A Case Study in Emerging Infections* (Oxford Univ. Press, 2005).
4. C. Fraser et al., *Science* **324**, 1557–1561 (2009).
5. L. Hufnagel, D. Brockmann, T. Geisel, *Proc. Natl. Acad. Sci. U.S.A.* **101**, 15124–15129 (2004).
6. D. Brockmann, L. Hufnagel, T. Geisel, *Nature* **439**, 462–465 (2006).
7. M. Moore, P. Gould, B. S. Keary, *Int. J. Hyg. Environ. Health* **206**, 269–278 (2003).
8. A. Vespignani, *Science* **325**, 425–428 (2009).
9. V. Colizza, A. Barrat, M. Barthélemy, A. Vespignani, *Proc. Natl. Acad. Sci. U.S.A.* **103**, 2015–2020 (2006).
10. B. S. Cooper, R. J. Pitman, W. J. Edmunds, N. J. Gay, *PLOS Med.* **3**, e212 (2006).
11. T. D. Hollingsworth, N. M. Ferguson, R. M. Anderson, *Emerg. Infect. Dis.* **13**, 1288–1294 (2007).
12. J. M. Epstein et al., *PLOS ONE* **2**, e401 (2007).
13. V. Colizza, A. Barrat, M. Barthélemy, A.-J. Valleron, A. Vespignani, *PLOS Med.* **e13**, 95 (2007).
14. R. Fisher, *Ann. Eugen.* **7**, 355–369 (1937).
15. J. V. Noble, *Nature* **250**, 726–729 (1974).
16. J. D. Murray, *Mathematical Biology* (Springer, Berlin, 2005).
17. D. Brockmann, T. Geisel, *Phys. Rev. Lett.* **90**, 170601 (2003).
18. D. Brockmann, L. Hufnagel, *Phys. Rev. Lett.* **98**, 178301 (2007).
19. D. Balcan et al., *Proc. Natl. Acad. Sci. U.S.A.* **106**, 21484–21489 (2009).
20. V. Colizza, R. Pastor-Satorras, A. Vespignani, *Nat. Phys.* **3**, 276–282 (2007).
21. W. Van den Broeck et al., *BMC Infect. Dis.* **11**, 37 (2011).
22. D. Balcan et al., *J. Comput. Sci.* **1**, 132–145 (2010).
23. N. M. Ferguson et al., *Nature* **442**, 448–452 (2006).
24. L. A. Rvachev, I. M. Longini Jr., *Math. Biosci.* **75**, 3 (1985).
25. S. Eubank et al., *Nature* **429**, 180–184 (2004).
26. M. Tizzoni et al., *BMC Med.* **10**, 165 (2012).
27. M. Ajelli et al., *BMC Infect. Dis.* **10**, 190 (2010).
28. R. M. May, *Science* **303**, 790–793 (2004).
29. D. Grady, C. Thiemann, D. Brockmann, *Nat. Commun.* **3**, 864 (2012).
30. V. Colizza, A. Vespignani, *Phys. Rev. Lett.* **99**, 148701 (2007).
31. V. Belik, T. Geisel, D. Brockmann, *Physical Review X* **1**, 011001 (2011).
32. E. Brunet, B. Derrida, *Phys. Rev. E Stat. Phys. Plasmas Fluids Relat. Interdiscip. Topics* **56**, 2597–2604 (1997).
33. A. Y. Likhov, M. Mézard, H. Ohta, L. Zdeborová, Inferring the origin of an epidemic with dynamic message-passing algorithm; <http://arxiv.org/abs/1303.5315> (2013).
34. P. C. Pinto, P. Thiran, M. Vetterli, *Phys. Rev. Lett.* **109**, 068702 (2012).
35. E. J. Abbott, F. A. Firestone, *Mech. Eng.* **55**, 569–572 (1933).
36. World Health Organization, FluNet (2013).
37. J. Anderson, *Am. Econ. Rev.* **69**, 106–116 (1979).
38. Robert-Koch-Institute, Survstat (2012).
39. O. Woolley-Meza et al., *Eur. Phys. J. B* **84**, 589–600 (2011).

Acknowledgments: D.B. thanks W. Kath, D. Grady, W. H. Grund, O. Woolley-Meza, and A. Bentley for fruitful discussions and comments and W. Moers, B. May, and FutuRiCT for inspiration. We thank R. Brune for contributions during the early phase of the project and for work on the origin reconstruction and C. Thiemann for the development of the SPaTo network visualization tool (www.spato.net). Global mobility data was provided by OAG (www.oag.com), prevalence data of H1N1 and SARS by the WHO (www.who.int), and EHEC data by the RKI-Survstat (www3.rki.de/SurvStat/). This work was supported by the Volkswagen Foundation (project: “Bioinvasion and epidemic spread in complex transportation networks”) and partially supported by the ETH project “Systemic Risks, Systemic Solutions” (CHIRP II project ETH 48 12-1).

Supplementary Materials

www.sciencemag.org/content/342/6164/1337/suppl/DC1
Supplementary Text
Figs. S1 to S20
Tables S1 to S4
Movies S1 to S3
References (40–45)

27 August 2013; accepted 25 October 2013
10.1126/science.1245200

Detection of a Noble Gas Molecular Ion, $^{36}\text{ArH}^+$, in the Crab Nebula

M. J. Barlow,^{1*} B. M. Swinyard,^{1,2} P. J. Owen,¹ J. Cernicharo,³ H. L. Gomez,⁴ R. J. Ivison,⁵ O. Krause,⁶ T. L. Lim,² M. Matsuura,¹ S. Miller,¹ G. Olofsson,⁷ E. T. Polehampton^{2,8}

Noble gas molecules have not hitherto been detected in space. From spectra obtained with the Herschel Space Observatory, we report the detection of emission in the 617.5- and 1234.6-gigahertz $J = 1-0$ and $2-1$ rotational lines of $^{36}\text{ArH}^+$ at several positions in the Crab Nebula, a supernova remnant known to contain both molecular hydrogen and regions of enhanced ionized argon emission. Argon-36 is believed to have originated from explosive nucleosynthesis in massive stars during core-collapse supernova events. Its detection in the Crab Nebula, the product of such a supernova event, confirms this expectation. The likely excitation mechanism for the observed $^{36}\text{ArH}^+$ emission lines is electron collisions in partially ionized regions with electron densities of a few hundred per centimeter cubed.

Noble gas compounds have not yet been found in space, despite some examples, such as ionized hydrides, being relatively stable (1). Astronomical searches for the near-infrared and far-infrared lines of HeH^+ , whose dissociation energy is 1.8 eV (2), have not been successful (3, 4). The Crab Nebula is the product of the supernova of 1054 AD and is thought to have originated from the core-collapse explosion of a star 8 to 16 times as massive as the Sun (5). We have obtained far-infrared-to-submillimeter spectra of the Crab Nebula using the Herschel Space Observatory (6). We report here the detection of emission lines from the ionized hydride of argon, an element predicted to form by explosive nucleosynthesis in core-collapse supernovae (7).

The Crab Nebula was observed with the Fourier Transform Spectrometer (FTS) of the Spectral and Photometric Imaging Receiver (SPIRE) (8, 9) on operational day 466 of the Herschel mission, as part of the Mass-loss of Evolved Stars (MESS) Guaranteed Time Key Project (10). The 19 SPIRE Long Wavelength (SLW) detectors, each with a beamwidth of ~ 37 arc sec, covered the 447- to 989-GHz frequency range (303 to 671 μm), while 35 SPIRE Short Wavelength (SSW) detectors, each with a beamwidth of ~ 18 arc sec, covered the 959- to 1544-GHz frequency range (194 to

313 μm) (Fig. 1). The full width at half maximum spectral resolution was 1.44 GHz at all frequencies, corresponding to a resolving power of 690 in the middle of the frequency range. The observation consisted of 48 FTS scans, for a total on-source exposure time of 3197 s. The data were processed using the extended source calibration in version 11 of the Herschel Interactive Processing Environment (11). The $J = 2-1$, $F = 5/2-3/2$ line of OH^+ at 971.8038 GHz (12), which falls in the SLW and SSW spectral overlap region, is present in emission in many of the spectra (Fig. 2). This line has been observed from a range of astrophysical environments by the Herschel Space

Observatory, both in absorption (13) and emission (14, 15). In addition, two unidentified emission lines were found to be present in some of the Crab spectra, one in the SLW range at ~ 618 GHz and the other in the SSW range at ~ 1235 GHz.

The knots and filaments of the Crab Nebula are known to exhibit expansion velocities ranging between 700 and 1800 km s^{-1} (16); in different detectors we measured radial velocities for the OH^+ 971.8038 GHz line that ranged between -603 and $+1037$ km s^{-1} . Several spectra showed multiple OH^+ velocity components, some blended, but in most spectra the OH^+ velocity components were unresolved, exhibiting very different radial velocities from detector to detector, consistent with an origin from differing knots or filaments in the nebula, each with its own discrete velocity. Because OH^+ was the only identified species in the spectra initially, we used the measured radial velocities of the 971.8038 GHz OH^+ line, whose centroid frequency could typically be measured to an accuracy of $\pm(25$ to $40)$ km s^{-1} , as a reference to correct to a “rest” frequency the observed frequencies of the 618- or 1235-GHz line falling in the same spectrum. There were four SLW spectra, those from detectors B3, C3, D3 and D4, in which the OH^+ line and the 618-GHz line were both present, with emission line surface brightnesses exceeding 2×10^{-10} $\text{W m}^{-2} \text{sr}^{-1}$. These four spectra yielded a mean “rest” frequency for the 618-GHz line of 617.554 ± 0.209 GHz. The 1235-GHz line was detected in five SSW spectra (A2, B1, B2, B3, and D4), but only in

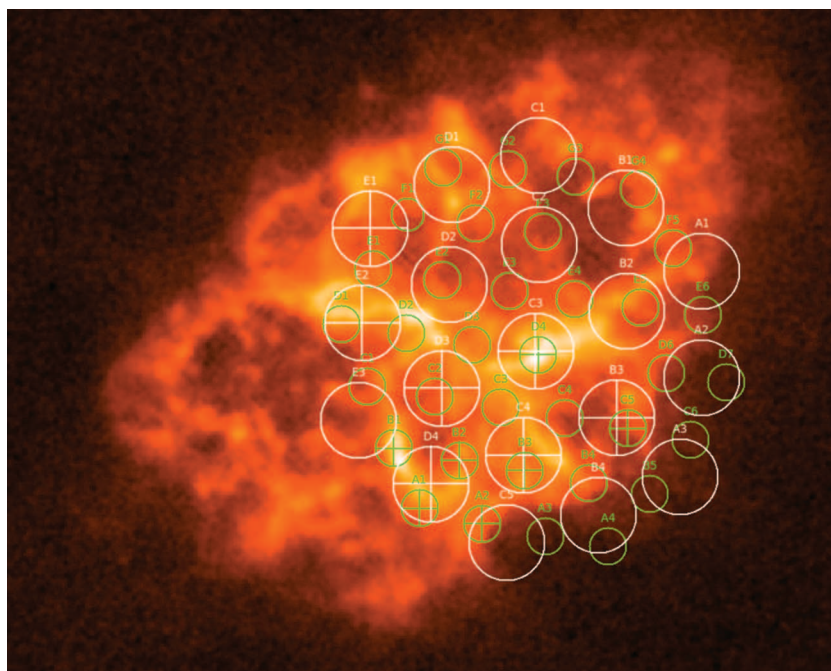
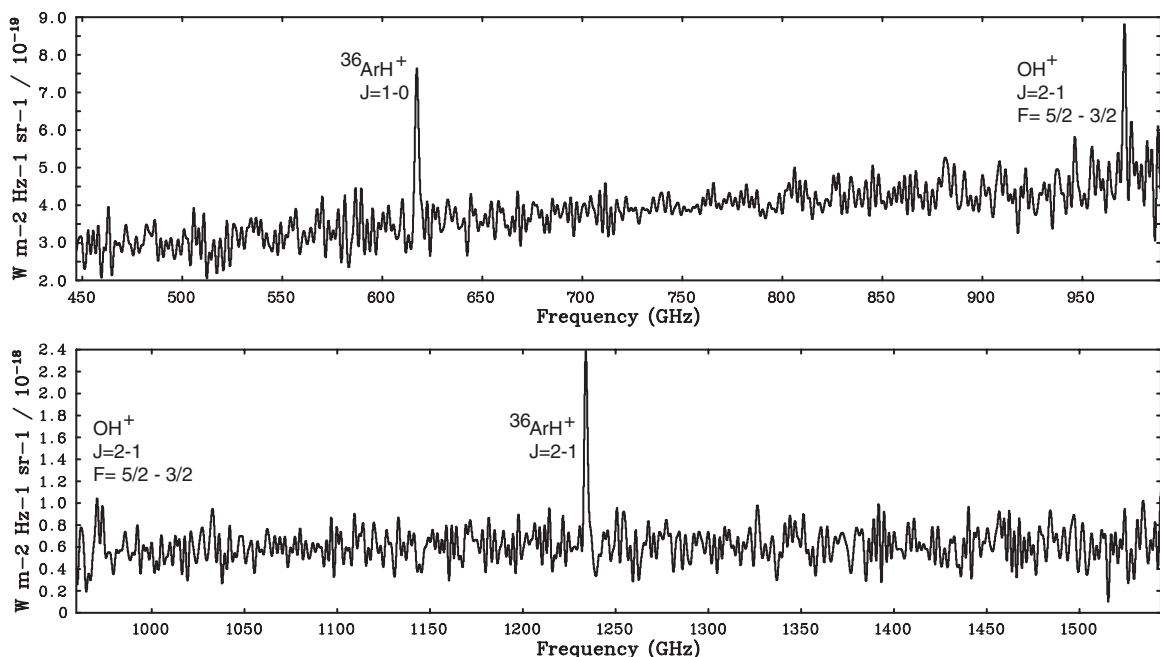


Fig. 1. A broadband Herschel-Photodetector Array Camera and Spectrometer image mapping the 70- μm dust emission from the Crab Nebula. North is up and east is to the left. The positions on the nebula of the 19 SLW and 35 SSW detectors of the SPIRE FTS are marked with circles whose angular diameters of 37 and 18 arc sec correspond to the SLW and SSW beam sizes. The positions of detectors in whose spectra the $J = 1-0$ or $2-1$ rotational lines of $^{36}\text{ArH}^+$ were detected are marked with crosses.

¹Department of Physics and Astronomy, University College London, Gower Street, London WC1E 6BT, UK. ²Space Science and Technology Department, Rutherford Appleton Laboratory, Didcot OX11 0QX, UK. ³Laboratory of Molecular Astrophysics, Department of Astrophysics, Centro de Astrobiología, Instituto Nacional de Técnicas Aeroespaciales-Consejo Superior de Investigaciones Científicas, Ctra de Ajalvir, km 4, 28850 Torrejón de Ardoz, Madrid, Spain. ⁴School of Physics and Astronomy, Cardiff University, The Parade, Cardiff CF24 3AA, UK. ⁵UK Astronomy Technology Centre, Royal Observatory Edinburgh, Blackford Hill, Edinburgh EH9 3HJ, UK. ⁶Max-Planck-Institut für Astronomie, Königstuhl 17, D-69117 Heidelberg, Germany. ⁷Department of Astronomy, Stockholm University, AlbaNova University Center, Roslagstullsbacken 21, 10691 Stockholm, Sweden. ⁸Institute for Space Imaging Science, Department of Physics and Astronomy, University of Lethbridge, Lethbridge, Alberta T1K 3M4, Canada.

*Corresponding author. E-mail: mjb@star.ucl.ac.uk

Fig. 2. SPIRE FTS spectra of the Crab Nebula, plotting surface brightness (in $\text{W m}^{-2} \text{Hz}^{-1} \text{sr}^{-1}$) against frequency (in GHz). Several emission lines are superposed on a continuum attributed to thermal dust emission (32). Upper plot: the spectrum from the SLW D4 detector, whose position on the nebula is marked in Fig. 1. Emission line velocity components attributed to the $J = 2-1$, $F = 5/2-3/2$ 971.8038 GHz rotational line of OH^+ and the $J = 1-0$ 617.525 GHz rotational line of $^{36}\text{ArH}^+$ are visible. Lower plot: the SSW B1 spectrum. In addition to OH^+ 971.8038 GHz velocity components, emission in the $J = 2-1$ 1234.603 GHz line of $^{36}\text{ArH}^+$ is visible. The radial velocities and surface brightnesses of the $^{36}\text{ArH}^+$ emission lines that are present in the spectra obtained from these and other FTS detectors are listed in Table 1.



the B1 (Fig. 2) and B3 spectra were both it and the 971.8038 GHz OH^+ line present with a single unresolved component. The $J = 1-1$, $F = 1/2-1/2$ line of OH^+ at 1032.998 GHz was also detected in emission in the SSW B1 spectrum, enabling a third estimate of the rest frequency of the 1235-GHz line. The mean frequency derived from these three estimates was 1234.786 ± 0.643 GHz.

The ratio of the derived rest frequencies of 1234.786 ± 0.643 GHz and 617.554 ± 0.209 GHz is 1.9995 ± 0.0012 , which suggests that the lines correspond to the 2-1 and 1-0 rotational transitions of a simple diatomic molecule (we can rule out their being 4-3 and 2-1 transitions, with a frequency ratio of 4:2, because of the lack of a corresponding 3-2 transition at ~926 GHz). A search using the Cologne Database for Molecular Spectroscopy (12) and the madex code (17) found the only candidate to be $^{36}\text{ArH}^+$, whose 1-0 and 2-1 rotational transitions lie at 617.52523 ± 0.00015 GHz and 1234.60275 ± 0.00030 GHz, respectively, agreeing with the derived frequencies for the Crab Nebula lines within the uncertainties. The 1-0 and 2-1 rotational transitions of $^{40}\text{ArH}^+$ are at 615.85813 ± 0.00005 GHz and 1231.27100 ± 0.00009 GHz, while the corresponding transitions of $^{38}\text{ArH}^+$ are at 616.64871 ± 0.00004 GHz and 1232.85100 ± 0.00004 GHz, ruling out these two isotopic variants as identifications. Argon is the third most abundant species in Earth's atmosphere, 0.93% by number, with $^{40}\text{Ar}/^{38}\text{Ar}/^{36}\text{Ar}$ isotopic ratios of 1584/1.00/5.30 (18). However, ^{40}Ar in Earth's atmosphere is a product of the decay, mainly in rocks, of ^{40}K , whose half-life is 1.25×10^9 years. For the solar wind, the $^{40}\text{Ar}/^{38}\text{Ar}/^{36}\text{Ar}$ isotopic ratios have been measured to be 0.00/1.00/5.50 (19). ^{36}Ar is expected to be the

dominant isotope of argon in stars, being an explosive nucleosynthesis product of the α -particle capture chain that takes place in massive-star core-collapse supernovae (7). Regions of enhanced emission from optical forbidden lines of ionized argon have previously been mapped in the Crab Nebula (20–22), almost certainly corresponding to enriched argon abundances. Strongly enhanced infrared forbidden lines of Ar^+ and Ar^{2+} have been detected from the southern filament (22) where we find $^{36}\text{ArH}^+$ line emission to be strongest (SSW detector B1; Fig. 1 and Table 1). The enhanced lines of ionized argon and $^{36}\text{ArH}^+$ strongly indicate the presence there of pockets of ^{36}Ar produced by explosive nucleosynthesis during the supernova event.

The ^{38}Ar isotope of argon is also predicted to be synthesized in core-collapse supernova events (7). We used Crab Nebula SPIRE-FTS spectra in which the $^{36}\text{ArH}^+$ velocity components are strong and narrow to put limits on the isotopic ratios of ^{40}Ar and ^{38}Ar relative to ^{36}Ar in the emitting regions. Because the frequency separation between the isotopic variants of ArH^+ is a factor of 2 larger for the $J = 2-1$ lines than for the 1-0 lines, whereas the SPIRE-FTS frequency resolution is constant, the 2-1 lines are better suited for placing limits on the isotopic ratios of argon. Relative to the $^{36}\text{ArH}^+$ 2-1 line, the separation of the $^{40}\text{ArH}^+$ 2-1 line is -3.33175 GHz, while that of the $^{38}\text{ArH}^+$ 2-1 line is -1.75175 GHz. To estimate upper limits to the abundances of these species, we added synthetic lines to the spectra having the appropriate frequency offset and the same line width as the $^{36}\text{ArH}^+$ 2-1 line, changing the strength of the synthetic lines until the signal-to-noise ratio estimated by the line-fitting routine reached 3σ . The SSW B1 (Fig. 2) and SSW B3 spectra both yielded 3σ

lower limits to the abundance ratio of $^{36}\text{ArH}^+ / ^{38}\text{ArH}^+$ of >2 , along with $^{36}\text{ArH}^+ / ^{40}\text{ArH}^+$ lower limits of >5 and >4 , respectively.

ArH^+ is a stable molecular ion [dissociation energy $D_0 = 3.9 \pm 0.1$ eV (1)] that has been studied extensively in the laboratory. The Crab Nebula consists predominantly of ionized gas, photo-ionized by synchrotron radiation from the pulsar wind nebula (5, 16). It also contains many H_2 -emitting neutral clumps (23, 24). Transition zones between fully ionized and molecular gas will exist, where ArH^+ can be formed by the exothermic reaction $\text{Ar}^+ + \text{H}_2 \rightarrow \text{ArH}^+ + \text{H}$, releasing 1.49 eV (25). If the elemental species created by the supernova explosion were still largely unmixed in the remnant, then it is possible that ArH^+ molecules would be found only at interfaces between H-rich gas and Ar-rich gas where mixing has occurred. Four of the seven FTS SSW detectors in whose spectra $J = 2-1$ $^{36}\text{ArH}^+$ emission was detected (SSW B1, B2, A1, and A2) are situated on a bright filament south of the center of the nebula (Fig. 1), as is the SLW D4 detector in which the strongest $J = 1-0$ emission was detected. A cluster of seven near-infrared H_2 -emitting knots, with a wide range of radial velocities, is coincident with the same bright filament (24). Detectors SLW C3 and SSW D4 also show $^{36}\text{ArH}^+$ emission and are coincident with an H_2 -emitting knot. The lack of ArH^+ emission in the northwest quadrant of the nebula is mirrored by a relative lack of H_2 emission knots in that region. However, there are many H_2 knots in the northeast quadrant, whereas ArH^+ emission is only detected there in two FTS detectors (SLW E1 and E2).

The reaction rate for the formation of ArH^+ via $\text{Ar}^+ + \text{H}_2 \rightarrow \text{ArH}^+ + \text{H}$ is $8.9 \times 10^{-10} \text{ cm}^3 \text{ s}^{-1}$ at 300 K (25). Reaction rates are known for the

Table 1. SPIRE-FTS radial velocity and line surface brightness measurements for the $J = 1-0$ and $2-1$ rotational lines of $^{36}\text{ArH}^+$ from the Crab Nebula.

$J = 1-0$ 617.525 GHz			$J = 2-1$ 1234.603 GHz		
SLW detector	Radial velocity (km s^{-1})	Surface brightness ($10^{-10} \text{ W m}^{-2} \text{ sr}^{-1}$)	SSW detector	Radial velocity (km s^{-1})	Surface brightness ($10^{-10} \text{ W m}^{-2} \text{ sr}^{-1}$)
B3	$+317 \pm 67$	2.23 ± 0.41	C5	-1354 ± 26	8.2 ± 1.2
C3	$+933 \pm 33$	4.63 ± 0.40	D4	$+743 \pm 26$	11.7 ± 1.6
C4	-58 ± 50	8.65 ± 0.55	B3	-101 ± 20	17.5 ± 1.4
D3	$+826 \pm 32$	3.13 ± 0.34			
D3	-709 ± 42	2.30 ± 0.34	A1	-51 ± 52	13.9 ± 2.0
D4	$+101 \pm 27$	9.89 ± 0.52	B2	-572 ± 25	10.8 ± 1.7
			B1	$+140 \pm 34$	38.4 ± 1.6
			A2	$+61 \pm 28$	10.1 ± 1.4
E1	$+278 \pm 46$	5.69 ± 0.62			
E2	-594 ± 37	4.25 ± 0.46			

ArH^+ destruction reaction with H_2 [to yield $\text{Ar} + \text{H}_3^+$, with a reaction rate of $6.3 \times 10^{-10} \text{ cm}^3 \text{ s}^{-1}$ at 300 K (26)] and for its dissociative recombination with electrons [$\text{ArH}^+ + \text{e}^- \rightarrow \text{Ar} + \text{H}^*$, with a rate of $\leq 5 \times 10^{-10} \text{ cm}^3 \text{ s}^{-1}$ at low electron energies (27)]. However, because the Crab Nebula is photoionized by its pulsar wind nebula (5, 16), photodissociation could be the main ArH^+ destruction mechanism.

The main excitation mechanism for the observed ArH^+ emission lines is likely to be collisions with either electrons or H_2 molecules, but rate calculations or measurements do not yet exist. The $J = 1$ and 2 levels of $^{36}\text{ArH}^+$ are situated 29.6 and 88.9 K above the ground state, respectively, which is negligible compared to the electron temperatures of 7500 to 15,000 K measured for the ionized gas in the Crab Nebula (5), or even compared to the H_2 excitation temperatures of 2000 to 3000 K that have been measured (28). If the electron or H_2 densities in the transition zones where ArH^+ is hypothesized to be located should exceed the “critical densities” of the emitting levels (where the sum of the collisional excitation and deexcitation rates from a level exceed the radiative decay rate from the level), then the level populations will be in Boltzmann equilibrium. Using the known molecular parameters of ArH^+ (12, 17), the 2-1/1-0 line emission ratios should then be on the order of 30, for excitation temperatures appreciably exceeding 100 K. The SSW D4 and SLW C3 detectors are centered on the same bright knot (Fig. 1) and yield a 2-1/1-0 line surface brightness ratio of 2.5, while the spectra from the approximately colocated SSW B3 and SLW C4 detectors yield a line surface brightness ratio of 2.0 (Table 1), well below the ratio for Boltzmann equilibrium. The densities of the collision partners in the emitting regions must therefore be well below the corresponding critical densities of the ArH^+ rotational levels. We used the MADEX code (17) with the molecular parameters of ArH^+ , together with $\text{SiH}^+ + \text{He}$ collisional deexcitation rates (29) in place of those of $\text{ArH}^+ + \text{H}_2$, and $\text{CH}^+ + \text{e}^-$ collisional de-

excitation rates (30) in place of those for $\text{ArH}^+ + \text{e}^-$ (with upward rates calculated using detailed balance and the correct values of the energies for the levels of ArH^+) to estimate corresponding H_2 and electron critical densities of $\sim 10^8$ and $\sim 10^4 \text{ cm}^{-3}$, respectively. The observed 2-1/1-0 line ratios of 2.5 and 2.0 indicate H_2 densities of a few $\times 10^6 \text{ cm}^{-3}$ or electron densities of a few $\times 10^2 \text{ cm}^{-3}$. The calculations take into account opacity effects, although the line center optical depths are estimated to be appreciably less than unity for line widths larger than 1 km s^{-1} . For H_2 collisions at temperatures between 100 and 3000 K and densities of $\sim 10^6 \text{ cm}^{-3}$, or electron collisions at temperatures of $\sim 3000 \text{ K}$ and densities of a few $\times 10^2 \text{ cm}^{-3}$, we estimate $^{36}\text{ArH}^+$ column densities of 10^{12} to 10^{13} cm^{-2} .

Given that likely electron collisional excitation rates are $\sim 10^4$ larger than those of H_2 and that the parent Ar^+ ion must exist in a region that is at least partially ionized, electron collisions are expected to dominate the excitation of ArH^+ . A density of $\sim 10^4 \text{ cm}^{-3}$ has been estimated for the Crab H_2 knots (28), a factor of 100 below that required for H_2 collisions to be the excitation mechanism for the ArH^+ lines. This lends further support to electron collisions in partially ionized transition regions being the main ArH^+ excitation mechanism.

Our detection of $^{36}\text{ArH}^+$ in the Crab Nebula suggests that an unidentified multicomponent broad absorption feature seen between 617 and 618 GHz in a Herschel HIFI spectrum of Sgr B2(M) (toward the center of our galaxy) (31) can potentially be identified with ground-state absorption in the $J = 0-1$ 617.525 GHz line of $^{36}\text{ArH}^+$ along the interstellar sightline.

References and Notes

1. J. R. Wyatt *et al.*, *J. Chem. Phys.* **62**, 2555 (1975).
2. S. G. Lias, J. F. Liebman, R. D. Levin, *J. Phys. Chem. Ref. Data* **13**, 695 (1984).
3. J. M. Moorhead, R. P. Lowe, W. H. Wehlau, J.-P. Maillard, P. F. Bernath, *Astrophys. J.* **326**, 899 (1988).
4. X.-W. Liu *et al.*, *Mon. Not. R. Astron. Soc.* **290**, L71–L75 (1997).

5. K. Davidson, R. A. Fesen, *Annu. Rev. Astron. Astrophys.* **23**, 119–146 (1985).
6. G. L. Pilbratt *et al.*, *Astron. Astrophys.* **518**, L1 (2010).
7. D. Arnett, *Supernovae and Nucleosynthesis* (Princeton Univ. Press, Princeton, NJ, 1996).
8. M. J. Griffin *et al.*, *Astron. Astrophys.* **518**, L3 (2010).
9. B. M. Swinyard *et al.*, *Astron. Astrophys.* **518**, L4 (2010).
10. M. Groenewegen *et al.*, *Astron. Astrophys.* **526**, A162 (2011).
11. S. Ott, *Astron. Soc. Pacific Conf. Ser.* **434**, 139 (2010).
12. H. S. P. Müller, F. Schlöder, J. Stutzki, G. Winnewisser, *J. Mol. Struct.* **742**, 215–227 (2005).
13. D. A. Neufeld *et al.*, *Astron. Astrophys.* **521**, L10 (2010).
14. P. P. van der Werf *et al.*, *Astron. Astrophys.* **518**, L42 (2010).
15. L. Spinoglio *et al.*, *Astrophys. J.* **758**, 108 (2012).
16. J. J. Hester, *Annu. Rev. Astron. Astrophys.* **46**, 127–155 (2008).
17. J. Cernicharo, *EAS Publ. Ser.* **58**, 251–261 (2012).
18. J.-Y. Lee *et al.*, *Geochim. Cosmochim. Acta* **70**, 4507–4512 (2006).
19. A. Meshik *et al.*, *Science* **318**, 433–435 (2007).
20. G. M. MacAlpine *et al.*, *Astrophys. J.* **432**, L131 (1994).
21. E. L. Schaller, R. A. Fesen, *Astron. J.* **123**, 941–947 (2002).
22. T. Temim *et al.*, *Astrophys. J.* **753**, 72 (2012).
23. J. R. Graham, G. S. Wright, A. J. Longmore, *Astrophys. J.* **352**, 172 (1990).
24. E. F. Loh *et al.*, *Astrophys. J. Suppl. Ser.* **194**, 30 (2011).
25. A. C. Roach, P. J. Kuntz, *Chem. Commun.*, 1336 (1970).
26. V. G. Anich, *NASA JPL Publ.* 03-19 (2003).
27. J. B. A. Mitchell *et al.*, *J. Phys. B* **38**, L175–L181 (2005).
28. E. D. Loh *et al.*, *Mon. Not. R. Astron. Soc.* **421**, 789 (2012).
29. C. Nkem *et al.*, *J. Mol. Struct. THEOCHEM* **901**, 220–225 (2009).
30. A. J. Lim, I. Rabadán, J. Tennyson, *Mon. Not. R. Astron. Soc.* **306**, 473–478 (1999).
31. P. Schilke, HEXOS Team, in *Proceedings of the Herschel First Results Symposium* (2010); http://herschel.esac.esa.int/FirstResultsSymposium/presentations/A34_SchilkeP_SgrB2.pdf.
32. H. L. Gomez *et al.*, *Astrophys. J.* **760**, 96 (2012).

Acknowledgments: We thank the anonymous referees for their constructive reports. We thank E. Bergin for drawing our attention to the 2010 HEXOS Herschel HIFI spectrum of Sgr B2 (M) that shows an unidentified broad absorption feature below 618 GHz. Herschel is a European Space Agency (ESA) space observatory with science instruments provided by European-led Principal Investigator consortia and with important participation from NASA. SPIRE has been developed by a consortium of institutes led by Cardiff University (UK) and including University of Lethbridge (Canada); National Astronomical Observatories, Chinese Academy of Sciences Commissariat à l'énergie atomique et aux énergies alternatives Laboratoire d'Astrophysique de Marseille (France); Istituto di fisica dello Spazio Interplanetario University of Padua (Italy); Instituto de Astrofísica de Canarias (Spain); Stockholm Observatory (Sweden); Imperial College London, Rutherford Appleton Laboratory, University College London–Mullard Space Science Laboratory, United Kingdom Astronomy Technology Centre, University of Sussex (UK); and California Institute of Technology, Jet Propulsion Laboratory, NASA Herschel Science Center, University of Colorado (USA). This development has been supported by national funding agencies: Canadian Space Agency (Canada); NAOJ (China); CEA, Centre national d'études spatiales, Centre national de la recherche scientifique (France); Agenzia Spaziale Italiana (Italy); Ministerio de Economía (Spain); Swedish National Space Board (Sweden); Science Technology and Facilities Council and United Kingdom Space Agency (UK); and NASA (USA). J.C. thanks MINECO for financial support under projects AYA2009-07304, AYA2012-32032, and Consolider program ASTROMOL CSD2009-00038.

22 July 2013; accepted 5 November 2013
10.1126/science.1243582

Nondestructive Detection of an Optical Photon

Andreas Reiserer, Stephan Ritter,* Gerhard Rempe

All optical detectors to date annihilate photons upon detection, thus excluding repeated measurements. Here, we demonstrate a robust photon detection scheme that does not rely on absorption. Instead, an incoming photon is reflected from an optical resonator containing a single atom prepared in a superposition of two states. The reflection toggles the superposition phase, which is then measured to trace the photon. Characterizing the device with faint laser pulses, a single-photon detection efficiency of 74% and a survival probability of 66% are achieved. The efficiency can be further increased by observing the photon repeatedly. The large single-photon nonlinearity of the experiment should enable the development of photonic quantum gates and the preparation of exotic quantum states of light.

More than a century ago, Planck's idea of a quantized energy exchange between light and matter and Einstein's conclusion that a light beam consists of a stream of particles have revolutionized our view of the world. The explanation of the photoelectric effect in terms of a photon-absorption process is the basis of the theoretical description of light with normally ordered photon creation and annihilation operators (1, 2). The picture of photon detection as a destructive process has been confirmed experimentally ever since. Nondestructive detection (3)—namely, the ability to watch individual photons fly by—has until now been an unaccomplished “ultimate goal” (4) of optical measurements.

Nondestructive detection has two major implications. First, a single photon can be detected more than once. Thus, concatenating several devices improves the detection efficiency of single photons. Second, nondestructive detection can serve as a herald that signals the presence of a photon without affecting its other degrees of freedom, such as its temporal shape or its polarization. This is in stark contrast to absorbing detectors, in which the quantum state of the photon is projected and therefore lost. Both implications are of great importance for rapidly evolving research fields such as quantum measurement (5), optical quantum computing (6), and quantum communication and networking (7, 8).

The interaction mechanism (9) we implement is based on the principles of cavity quantum electrodynamics, remarkably robust, and applicable to many different physical systems. It allows one to nondestructively detect propagating optical photons and thus to complement experiments with microwave fields trapped in superconducting resonators (10–12). To this end, a faint laser pulse is reflected off a resonant cavity in which a trapped atom has been prepared in a superposition of two internal states. The cavity induces strong coupling between the light pulse and the atom in one of the atomic states, but not the other. This leads

to a phase flip of the atomic superposition state upon reflection of a photon. Subsequent readout of the atomic phase thus makes it possible to detect a photon without absorbing it.

A detailed theoretical treatment of the atom-photon interaction mechanism is given in (9, 13). For an intuitive explanation, consider a three-level atom in a single-sided cavity (Fig. 1A) in which one of the mirrors is perfectly reflecting and the small transmission of the other mirror allows for in- and outcoupling of light. The cavity is thus overcoupled and resonant with the transition between the atomic states $|2\rangle_a$ and $|3\rangle_a$. A photon, resonant with the empty cavity, is impinging onto the transmitting mirror. If the atom is in the state $|1\rangle_a$, it will not interact with the photon because any transition is far detuned. Thus, the photon

will enter the cavity before being reflected. If, however, the atom is in $|2\rangle_a$ (Fig. 1B), the strong atom-photon coupling leads to a normal-mode splitting, so that the photon is reflected without entering the cavity. In this case, atom and photon were never in the same place. Nevertheless, the photon has left a trace in the state of the atom: When light is reflected from a resonant cavity, it experiences a phase shift of π , whereas there is no phase shift in the strongly coupled case. When the impinging photon is denoted by the state $|1\rangle_p$, we thus find $|2\rangle_a|1\rangle_p \rightarrow |2\rangle_a|1\rangle_p$, whereas $|1\rangle_a|1\rangle_p \rightarrow e^{i\pi}|1\rangle_a|1\rangle_p = -|1\rangle_a|1\rangle_p$.

To use this conditional phase shift for nondestructive photon detection, the atom is prepared in the superposition state $\frac{1}{\sqrt{2}}(|1\rangle_a + |2\rangle_a)$ (Fig. 1C). If there is no impinging photon, the atomic state remains unchanged (Fig. 1D, solid green circle). If, however, a photon is reflected, the atomic state becomes (omitting a global phase) $\frac{1}{\sqrt{2}}(|1\rangle_a + |2\rangle_a)|1\rangle_p \rightarrow \frac{1}{\sqrt{2}}(|1\rangle_a - |2\rangle_a)|1\rangle_p$ (Fig. 1D, red arrow and solid red circle). To measure this phase flip, a $\pi/2$ rotation maps the atomic state $\frac{1}{\sqrt{2}}(|1\rangle_a + |2\rangle_a)$ onto $|1\rangle_a$, whereas $\frac{1}{\sqrt{2}}(|1\rangle_a - |2\rangle_a)$ is rotated to $|2\rangle_a$ (Fig. 1E). Subsequently, cavity-enhanced fluorescence state detection (14) is used to discriminate between the atomic states $|1\rangle_a$ and $|2\rangle_a$ (Fig. 1F) (15). Two photons in the input pulse lead to a phase shift of $e^{i2\pi} = 1$. The used sequence therefore measures the odd-even parity of the photon number. As long as the average photon number per measurement interval is much smaller than one, only zero or one photon events are present, and the detection result is unambiguous.

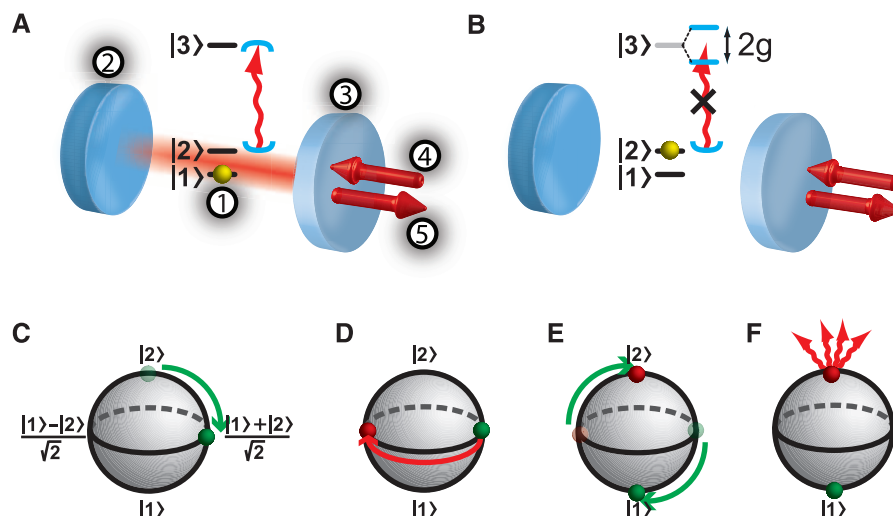


Fig. 1. Nondestructive photon detection. (A and B) Sketch of the setup and atomic level scheme. A single atom, (1), is trapped in an optical cavity that consists of a high-reflector, (2), and a coupling mirror, (3). A resonant photon is impinging on, (4), and reflected off, (5), the cavity. (A) If the atom is in state $|1\rangle_a$, the photon (red wavy arrow) enters the cavity (blue semicircles) before being reflected. In this process, the combined atom-photon state acquires a phase shift of π . (B) If the atom is in $|2\rangle_a$, the strong coupling on the $|2\rangle_a \leftrightarrow |3\rangle_a$ transition leads to a normal-mode splitting of $2g$, so that the photon cannot enter the cavity and is directly reflected without a phase shift. (C to F) Procedure to measure whether a photon has been reflected. (C) The atomic state, visualized on the Bloch sphere, is prepared in the superposition state $\frac{1}{\sqrt{2}}(|1\rangle_a + |2\rangle_a)$. (D) If a photon impinges, the atomic state is flipped to $\frac{1}{\sqrt{2}}(|1\rangle_a - |2\rangle_a)$. (E) The atomic state is rotated by $\frac{\pi}{2}$. (F) Fluorescence detection is used to discriminate between the states $|1\rangle_a$ and $|2\rangle_a$.

Max-Planck-Institut für Quantenoptik, Hans-Kopfermann-Strasse 1, 85748 Garching, Germany.

*Corresponding author. E-mail: stephan.ritter@mpq.mpg.de

In our setup (16), a single ^{87}Rb atom is trapped in a three-dimensional optical lattice at the center of a Fabry-Perot resonator. The coupling mirror has a transmission of 95 parts per million (ppm), which is large compared with the transmission of the high-reflector and the scattering and absorption losses (8 ppm). The cavity field decay rate is $\kappa = 2\pi \times 2.5$ MHz, the atomic dipole decay rate is $\gamma = 2\pi \times 3$ MHz, and the measured atom-cavity coupling constant on the $|2\rangle_a \leftrightarrow |3\rangle_a$ transition is $g = 2\pi \times 6.7$ MHz (16). Thus, the system operates in the strong-coupling regime of cavity quantum electrodynamics.

We first demonstrate that we can accurately prepare, control, and readout the atomic state. The atom is initialized in the state $|2\rangle_a$ by optical pumping, and the levels $|2\rangle_a$ and $|1\rangle_a$ are coupled by using a pair of Raman lasers (15). To characterize this coupling, the Raman beams were applied for a variable duration, and the population in $|2\rangle_a$ was measured (14, 15). Observing Rabi oscillations (Fig. 2A) with a visibility of 97% represents an upper bound for the quality of our state preparation, rotation, and readout process.

Strong coupling between the atom and impinging light is demonstrated by measuring the reflection of the system with the atom prepared in $|2\rangle_a$ as a function of the probe light frequency (Fig. 2B, red data). The observed normal-mode splitting testifies to the strong coupling. On resonance, 62(2)% of the impinging photons are reflected (with the number in parentheses being the statistical SE). With increasing coupling strength, this value is expected to approach unity. When the atom is prepared in the uncoupled state $|1\rangle_a$, 70(2)% of the incoming light is reflected on resonance (Fig. 2B, black data). The missing 30% are either transmitted through the high reflector or lost via scattering or absorption, which is in good agreement with input-output theory calculations (17) when using the independently measured mirror parameters.

Having characterized the individual steps of the protocol, they are now combined to detect photons in a nondestructive way. The atom is prepared in the superposition state $\frac{1}{\sqrt{2}}(|1\rangle_a + |2\rangle_a)$. Within a 2.5- μs -long trigger interval, we sent in a weak coherent laser pulse with an average photon number of $\bar{n} = 0.115(11)$ and monitor its reflection with conventional single-photon counting modules (SPCMs). A typical experimental run is shown in Fig. 3A, in which a photon was subsequently detected (red line in the blue trigger interval). Therefore, after $\pi/2$ rotation of the atomic state many fluorescence photons are observed (14) in the 25- μs -long readout interval (gray), unambiguously signaling the atomic state change induced by the detected photon. Thus, in the case shown in Fig. 3A a photon is detected twice: by the nondestructive detector and with a conventional, absorptive SPCM. The depicted trace also indicates that the setup works as an all-optical switch (18) that does not destroy the impinging trigger photon and also does not affect its temporal envelope. The latter can be seen in Fig. 3B,

in which the arrival-time histogram of the photons detected with the SPCM after reflection from the setup is shown. The data taken during the nondestructive photon measurement (Fig. 3B, black squares) do not show a clear deviation from the reference curve recorded without atom (Fig. 3B, red points)—except for a small reduction in amplitude, which is consistent with the results of Fig. 2B.

When the input pulse is blocked, no photons are observed, neither in the blue nor in the gray interval of Fig. 3A, in 97.1(4)% of all runs. In the remaining 2.9%, many fluorescence photons are observed during the atomic state readout, corresponding to a “dark count” of the nondestructive photon detector. This is caused by imperfections in the atomic state preparation, rotation, and readout and might be improved by magnetic shielding of the setup and by using more complex state-rotation techniques, such as composite pulses (19).

We then investigated the photon detection efficiency of our nondestructive device. The probability of detecting a photon in the input pulse is given in Fig. 3C. The results obtained with calibrated conventional SPCM, without and with correction for their limited quantum efficiency of 55(5)%, are shown as yellow and gray bars, respectively. The red bars are obtained from the atomic-state readout. Comparison of the gray and red bars shows good agreement but does not reveal information about potential systematic errors. Therefore, we also analyzed correlations be-

tween the detection of a reflected photon by the SPCM and by our nondestructive detector. The blue bars show the probability of finding the atom in $|2\rangle_a$, conditioned on the detection of a photon by the SPCM. We obtained 82.1(1.7)%. Correcting for the influence of two-photon components in the input laser field (and SPCM dark counts) (15), the conditional detection efficiency of our device for single photons is 87%.

There are two major experimental imperfections (15) that contribute to the deviation of the conditional detection efficiency from unity. First, the spatial mode matching of the input photons and the cavity mode [92(2)%; corresponding reduction 12(3)%], and second, the fidelity of the atomic state preparation, rotation, and readout (estimated reduction 3%) (15). None of the imperfections has a fundamental limit. Therefore, it should be possible to further increase the ef-

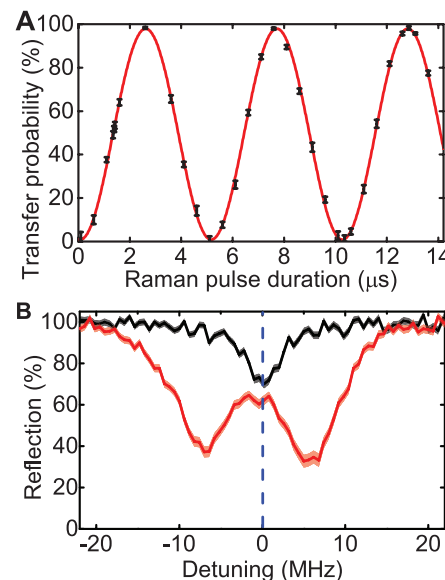


Fig. 2. Atomic state manipulation and cavity reflection spectrum. (A) Rabi oscillations of the atomic population when the atom is prepared in $|2\rangle_a$, and two Raman laser beams are applied for a variable duration. The red fit curve gives a visibility of 97%. (B) Reflection off the atom-cavity system as a function of probe laser frequency, with the atom in the strongly coupled state $|2\rangle_a$ (red) or in the uncoupled state $|1\rangle_a$ (black). The statistical SE is given by the thickness of the lines.

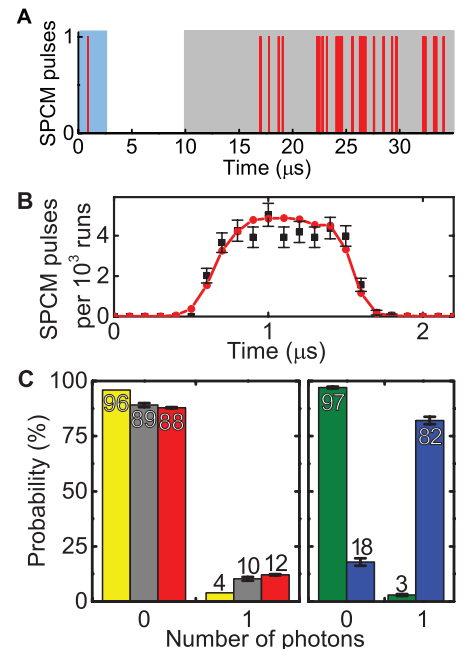


Fig. 3. Experimental results. (A) Typical trace of an experimental run. A photon (red bar) impinging in the trigger interval (blue area) leads to the emission of many photons in the readout interval (gray area). When the input pulse is blocked, no photons are detected in both intervals. (B) Temporal envelope of the reflected photon pulse when an atom is present (black squares) compared with a reference run without atom (red points). Within the errors, no deviation in the pulse shape is observable, except for a small amplitude change stemming from the slightly different reflectivities (Fig. 2B). (C) Nondestructive detection of a single photon. The probability of detecting zero or one photon is plotted. Yellow, result of the SPCM detection; gray, calculated input pulse, taking into account the SPCM detection efficiency; red, result of the atomic state readout; green, atomic state readout without impinging light; blue, atomic state, conditioned on the SPCM detection of a reflected photon in the trigger interval.

efficiency achieved in our first proof-of-principle experiment, which already compares well with state-of-the-art absorbing single-photon detectors (20–22).

The probability that an impinging photon is reflected is on average 66(2)%. If a photon is absorbed, the atomic state is projected, and the detection process gives the wrong result with a probability of 50%. Therefore, the probability to detect a single input photon without postselection on its reflection from the cavity is calculated to be 74% (15).

In contrast to all absorbing detectors, the efficiency of our detector can be further improved by attempting more measurements. Concatenating two of our devices is expected to increase the detection efficiency to 87%, whereas three or more devices should yield 89% (15). The achieved value is currently limited by absorption and scattering losses of both the atom and the cavity mirrors. To further improve, a decrease in cavity loss or an increase in atom-cavity coupling strength would be required. Both can be achieved either in Fabry-Perot (23) or other (24–26) resonators.

The atom-photon interaction mechanism that has been presented in this work lays the ground work for numerous experiments. A first step is the repeated nondestructive measurement of a single optical photon. Next, with a higher number of photons in the impinging laser pulse, the odd-even parity measurement allows one to generate new quantum states of optical light fields, such as Schrödinger-cat states (27). Measuring the phase

of the reflected light could be used to entangle two atoms in the cavity (28). Moreover, using the polarization degree of freedom as a qubit should facilitate a deterministic quantum gate between a single photon and a single atom (9, 13). This can be further extended to an entangling gate between several successively impinging photons (9) or between several atoms trapped in the same or even in remote cavities, thus efficiently generating atomic cluster states (13, 29, 30). Implementing this gate operation would also allow for a deterministic photonic Bell-state measurement, which would increase the efficiency of measurement-based quantum networks with remote single atoms (31, 32) close to unity.

References and Notes

- R. J. Glauber, *Phys. Rev.* **130**, 2529–2539 (1963).
- L. Mandel, E. Wolf, *Optical Coherence and Quantum Optics* (Cambridge Univ. Press, Cambridge, 1995).
- V. B. Braginsky, F. Y. Khalili, *Rev. Mod. Phys.* **68**, 1–11 (1996).
- P. Grangier, J. A. Levenson, J.-P. Poizat, *Nature* **396**, 537–542 (1998).
- H. M. Wiseman, G. J. Milburn, *Quantum Measurement and Control* (Cambridge Univ. Press, Cambridge, 2009).
- J. L. O'Brien, *Science* **318**, 1567–1570 (2007).
- N. Gisin, R. Thew, *Nat. Photonics* **1**, 165–171 (2007).
- H. J. Kimble, *Nature* **453**, 1023–1030 (2008).
- L.-M. Duan, H. J. Kimble, *Phys. Rev. Lett.* **92**, 127902 (2004).
- G. Nogues *et al.*, *Nature* **400**, 239–242 (1999).
- C. Guerlin *et al.*, *Nature* **448**, 889–893 (2007).
- B. R. Johnson *et al.*, *Nat. Phys.* **6**, 663–667 (2010).
- J. Cho, H.-W. Lee, *Phys. Rev. Lett.* **95**, 160501 (2005).
- J. Bochmann *et al.*, *Phys. Rev. Lett.* **104**, 203601 (2010).

- Materials and methods are available as supplementary materials on Science Online.
- A. Reiserer, C. Nölleke, S. Ritter, G. Rempe, *Phys. Rev. Lett.* **110**, 223003 (2013).
- D. F. Walls, G. J. Milburn, *Quantum Optics* (Springer, 2008).
- W. Chen *et al.*, *Science* **341**, 768–770 (2013).
- L. M. K. Vandersypen, I. L. Chuang, *Rev. Mod. Phys.* **76**, 1037–1069 (2005).
- R. H. Hadfield, *Nat. Photonics* **3**, 696–705 (2009).
- M. D. Eisaman, J. Fan, A. Migdall, S. V. Polyakov, *Rev. Sci. Instrum.* **82**, 071101 (2011).
- F. Marsili *et al.*, *Nat. Photonics* **7**, 210–214 (2013).
- Y. Colombe *et al.*, *Nature* **450**, 272–276 (2007).
- B. Dayan *et al.*, *Science* **319**, 1062–1065 (2008).
- C. Junge, D. O'Shea, J. Volz, A. Rauschenbeutel, *Phys. Rev. Lett.* **110**, 213604 (2013).
- J. D. Thompson *et al.*, *Science* **340**, 1202–1205 (2013).
- B. Wang, L.-M. Duan, *Phys. Rev. A* **72**, 022320 (2005).
- A. S. Sørensen, K. Mølmer, *Phys. Rev. Lett.* **91**, 097905 (2003).
- Y.-F. Xiao *et al.*, *Phys. Rev. A* **70**, 042314 (2004).
- L.-M. Duan, B. Wang, H. J. Kimble, *Phys. Rev. A* **72**, 032333 (2005).
- D. L. Moehring *et al.*, *Nature* **449**, 68–71 (2007).
- C. Nölleke *et al.*, *Phys. Rev. Lett.* **110**, 140403 (2013).

Acknowledgments: We thank N. Kalb for experimental assistance. This work was supported by the European Union (Collaborative Project SIQS) and the Bundesministerium für Bildung und Forschung via IKT 2020 (QK_QuORep).

Supplementary Materials

www.sciencemag.org/content/342/6164/1349/suppl/DC1
Materials and Methods
Fig. S1

18 September 2013; accepted 5 November 2013

Published online 14 November 2013;

10.1126/science.1246164

Effect of Collective Molecular Reorientations on Brownian Motion of Colloids in Nematic Liquid Crystal

T. Turiv,^{1,2} I. Lazo,² A. Brodin,^{1,3} B. I. Lev,⁴ V. Reiffenrath,⁵
V. G. Nazarenko,¹ O. D. Lavrentovich^{2*}

In the simplest realization of Brownian motion, a colloidal sphere moves randomly in an isotropic fluid; its mean squared displacement (MSD) grows linearly with time τ . Brownian motion in an orientationally ordered fluid—a nematic—is anisotropic, with the MSD being larger along the axis of molecular orientation, called the director. We found that at short time scales, the anisotropic diffusion in a nematic becomes anomalous, with the MSD growing slower or faster than τ ; these states are respectively termed subdiffusion and superdiffusion. The anomalous diffusion occurs at time scales that correspond to the relaxation times of director deformations around the sphere. Once the nematic melts, the diffusion becomes normal and isotropic. Our experiment shows that the deformations and fluctuations of long-range orientational order profoundly influence diffusive regimes.

Random displacements of a small particle in a fluid are controlled by kinetic energy dissipation (1). The mean displacement is zero but the average mean squared displacement (MSD) is finite, growing linearly with time lag τ (2): $\langle \Delta r^2(\tau) \rangle = 6D\tau$, where D is the translational diffusion coefficient. Brownian particles in complex fluids may exhibit an anomalous behavior,

$\langle \Delta r^2(\tau) \rangle \propto \tau^\alpha$, with the exponent α either smaller than 1 (subdiffusion) or larger than 1 (superdiffusion). Subdiffusion is observed in polymer (3) and F-actin networks (4) and in surfactant dispersions (5); superdiffusion occurs in concentrated suspensions of swimming bacteria (6) and dispersions of polymer-like micelles (7–10). The diffusion regimes should reflect the properties of the host medium

(11), one of which is often a local or long-range orientational order of molecules.

The simplest orientationally ordered fluid is a uniaxial nematic, in which the average orientation of molecules is described by a unit director \hat{n} . Because of different effective viscosities $\eta_{\parallel} \neq \eta_{\perp}$ for motion parallel and perpendicular to \hat{n} , Brownian motion becomes anisotropic, with two coefficients D_{\parallel} and D_{\perp} (12–19). The anisotropic diffusion characterized experimentally to date for nematics at relatively long time lags τ remains “normal,” with $\alpha = 1$ (14–19). In some cases, anomalous diffusion has also been observed, but it was attributed to features other than the orientational order, such as bacterial activity (6), size distribution of building units (7), spatial modulation of hydrophobic and hydrophilic regions (8), bending rigidity of the molecular aggregates (8), fluctuations of concentration (9), or director distortions around the dye molecules (20). Here, we show that the nematic orientational order and its

¹Institute of Physics NASU, Prospect Nauky 46, Kyiv 03039, Ukraine. ²Liquid Crystal Institute, Kent State University, Kent, OH 44242, USA. ³National Technical University of Ukraine “KPI,” Prospect Peremogy 37, Kyiv 03056, Ukraine. ⁴Bogolyubov Institute for Theoretical Physics NASU, 14-b Metrolohichna Street, Kyiv 03680, Ukraine. ⁵Liquid Crystals Division, Merck KGaA, 64271 Darmstadt, Germany.

*Corresponding author. E-mail: olavrent@kent.edu

Phosphorus in the Young Supernova Remnant Cassiopeia A

Bon-Chul Koo,^{1*} Yong-Hyun Lee,¹ Dae-Sik Moon,^{2,3,4} Sung-Chul Yoon,¹ John C. Raymond⁵

Phosphorus (^{31}P), which is essential for life, is thought to be synthesized in massive stars and dispersed into interstellar space when these stars explode as supernovae (SNe). Here, we report on near-infrared spectroscopic observations of the young SN remnant Cassiopeia A, which show that the abundance ratio of phosphorus to the major nucleosynthetic product iron (^{56}Fe) in SN material is up to 100 times the average ratio of the Milky Way, confirming that phosphorus is produced in SNe. The observed range is compatible with predictions from SN nucleosynthetic models but not with the scenario in which the chemical elements in the inner SN layers are completely mixed by hydrodynamic instabilities during the explosion.

Phosphorus (P) is an indispensable ingredient for life together with carbon, hydrogen, nitrogen, oxygen, and sulfur (S). In our solar system, its abundance relative to hydrogen is 2.8×10^{-7} by number, which is 50 to 1900 times less than those of the other life-keeping α elements (1). The abundance of P in the diffuse interstellar medium and stars in our galaxy's disk is comparable with that of the solar system or the cosmic abundance, with some dependence on metallicity (2, 3). P is believed to be mainly formed in massive [≥ 8 solar mass (M_{\odot})] stars by neutron capture on silicon (Si) in hydrostatic neon-burning shells in the pre-SN stage and also in explosive carbon- and neon-burning layers during SN explosion (4, 5).

Freshly synthesized P should thus be found in young core-collapse SN remnants (SNRs) resulting from the explosion of massive stars. Cassiopeia A (Cas A) is the youngest confirmed core-collapse SNR in our galaxy; it has been extensively studied in all wavebands (Fig. 1). It is located at a distance of 3.4 kpc (6) and thought to be the remnant of a SN event in C.E. 1681 ± 19 (7). The spectrum of the light echo from the SN event indicated a SN of Type IIb that had a small hydrogen envelope at the time of explosion (8). The total estimated mass of the SN ejecta is 2 to 4 M_{\odot} , and the inferred initial mass of the progenitor star ranges from 15 to 25 M_{\odot} (9, 10). Emission from P II was previously detected from Cas A (11), but no analysis of the emission line has been done.

We conducted near-infrared (NIR) spectroscopic observations of the main SN ejecta shell using the TripleSpec spectrograph mounted on the Palomar 5-m Hale telescope in 2008 (Fig. 1) (12). TripleSpec provides continuous wavelength

coverage from 0.94 to 2.46 μm at medium spectral resolving power of ~ 2700 . By analyzing the spectra, we identified 63 knots of emission and, for each knot, measured the radial velocities and fluxes of emission lines, including [P II] lines (12).

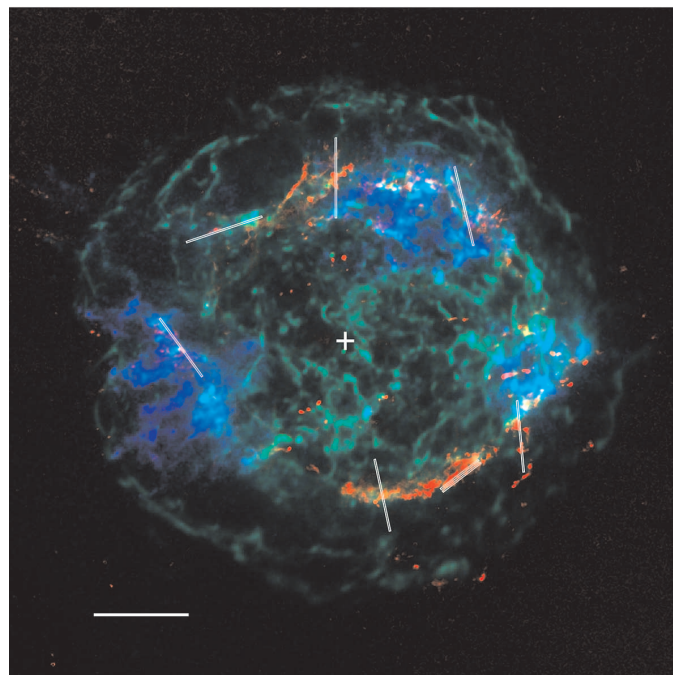
The knots show distinct spectroscopic and kinematic properties depending on their origins (Fig. 2). The knots with strong [S II] lines (Fig. 2, red symbols) have high ($\geq 100 \text{ km s}^{-1}$) radial velocities, and most of them have strong [P II] lines too, suggesting that the production of P is tightly correlated with the production of S. Some knots without apparent [S II] lines have low radial velocities ($\leq 100 \text{ km s}^{-1}$) and strong He I lines (Fig. 2, green symbols). Their properties match those of “quasi-stationary flocculi,” the material lost from the hydrogen envelope of the progenitor during its red-supergiant phase

as slow wind (13, 14). The rest of the knots without [S II] lines (Fig. 2, blue symbols) have little He I emission, and most of them have high radial velocities. They have [Fe II] lines as strong as those from the other knots. These knots are probably pure iron (Fe) material from complete Si-burning in the innermost region of the SN, corresponding to the pure Fe ejecta detected in x-rays (9). They are found mainly in the southern bright [Fe II] filament, where the x-ray-emitting Fe ejecta is not prominent (Fig. 1).

The P/Fe abundance ratio of the knots can be derived from the flux ratio of [P II] 1.189 μm and [Fe II] 1.257 μm lines ($F_{[\text{P II}]1.189}/F_{[\text{Fe II}]1.257}$). These two lines have comparable excitation energies and critical densities, which together with the fact that the ionization energies of P and Fe are comparable (10.49 and 7.90 eV) greatly simplifies the abundance analysis (15). (This is not the case for [S II] lines that have considerably higher excitation energies.) We assume that the line-emitting region is at $T_e = 10,000 \text{ K}$ and has a uniform density, with equal fractions of singly ionized ions. This simple model yields P/Fe abundances accurate to within $\sim 30\%$ mostly for both SN and circumstellar knots (12). The observed $F_{[\text{P II}]1.189}/F_{[\text{Fe II}]1.257}$ ratios (Fig. 3) imply that the P-to-Fe abundance ratio by number, $X(\text{P/Fe})$, of the SN ejecta knots is up to 100 times higher than the cosmic abundance $X_{\odot}(\text{P/Fe}) = 8.1 \times 10^{-3}$ (1), whereas the knots of the circumstellar medium have ratios close to the cosmic abundance. The enhanced P abundance over Fe in these SN ejecta knots is direct evidence for the in situ production of P in Cas A.

The observed range of $X(\text{P/Fe})$ is compatible with the local nucleosynthetic yield of P in SN

Fig. 1. Three-color composite image of the young SN remnant Cas A. Red is a Palomar [Fe II] 1.644- μm image representing SN material at $\sim 10^4 \text{ K}$, green is a *Chandra* x-ray continuum (4.20 to 6.40 keV) image representing hot gas and relativistic particles that are heated by SNR blast wave, and blue is a *Chandra* Fe K (6.52 to 6.94 keV) image representing SN material at $\sim 2 \times 10^7 \text{ K}$, respectively. The slit positions in our NIR spectroscopic observations are marked by thin white bars. The central white plus symbol represents the position of the SN explosion center determined from proper motions (28). The scale bar in the lower left represents an angular scale of $1'$, which corresponds to $\sim 1 \text{ pc}$ at the distance (3.4 kpc) of the SNR.



¹Department of Physics and Astronomy, Seoul National University, Seoul 151-747, Korea. ²Department of Astronomy and Astrophysics, University of Toronto, Toronto, Ontario M5S 3H4, Canada. ³Space Radiation Laboratory, California Institute of Technology, Pasadena, CA 91125, USA. ⁴Visiting Brain Pool Scholar, Korea Astronomy and Space Science Institute, Daejeon 305-348, Korea. ⁵Harvard-Smithsonian Center for Astrophysics, 60 Garden Street, Cambridge, MA 02138, USA.

*Corresponding author. E-mail: koo@astro.snu.ac.kr

Fig. 2. NIR line fluxes of the Cas A's knots as a function of their radial velocities. NIR line fluxes are in erg per square centimeter per second. Shown are He I 1.083 μm ($^3P \rightarrow ^3S_1$), [P II] 1.189 μm ($^1D_2 \rightarrow ^3P_2$), [S II] 1.032 μm ($^2P_{3/2} \rightarrow ^2D_{5/2}$), and [Fe II] 1.257 μm ($a^4D_{7/2} \rightarrow a^6D_{9/2}$) lines, from top to bottom. The knots not detected in the line emission are marked by open, upside-down triangles representing 3σ upper limits. The fluxes are corrected for extinction. The different colors represent knots of different characteristics: red symbols, knots with strong [S II] lines; green symbols, knots without [S II] lines but with strong He I lines at low radial velocities ($< 100 \text{ km s}^{-1}$); blue symbols, knots without [S II] lines and with little He I emission.

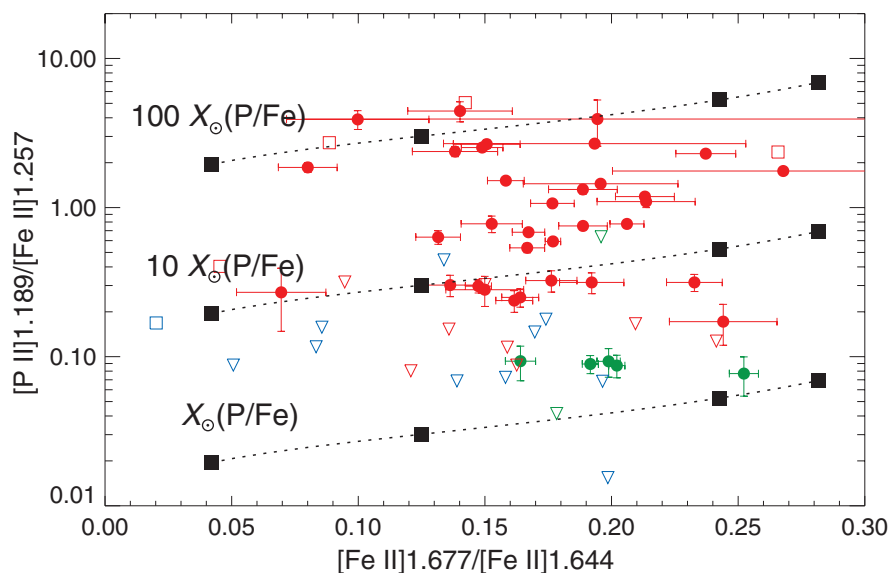
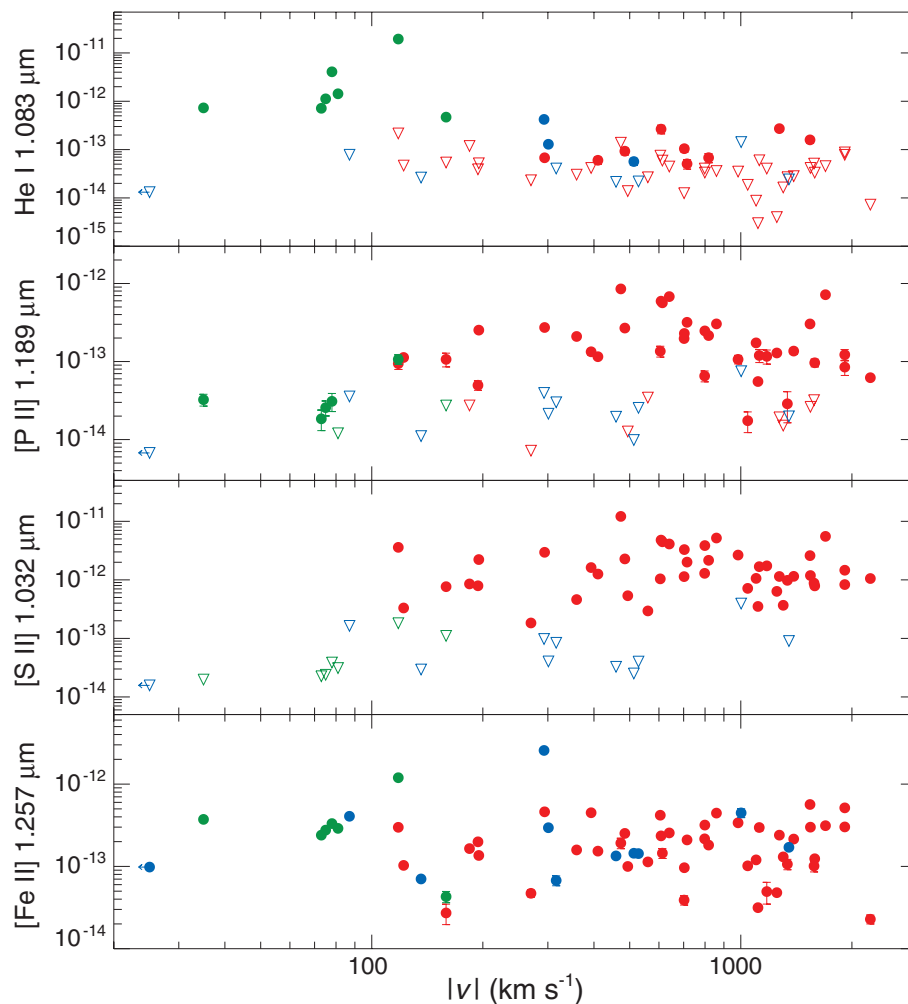


Fig. 3. [P II] 1.189/[Fe II] 1.257 versus density-sensitive [Fe II] line ratios of the Cas A's knots. The knots are marked in the same colors as in Fig. 2. The open, upside-down triangles represent the knots undetected in the [P II] line emission, whereas the open squares represent the knots undetected in [Fe II] 1.677 μm line emission, including the one undetected in either line emission at (0.020, 0.17). The dotted lines show theoretical line ratios for $X(\text{P}/\text{Fe}) = 1, 10$, and 100 times the cosmic abundance. The solid squares along the lines represent the ratios at $n_e = 10^3, 10^4, 10^5$, and 10^6 cm^{-3} , from left to right. The [Fe II] line ratio in the abscissa is essentially given by a function of n_e , and the observed ratios indicate that $n_e = 3 \times 10^3$ to $2 \times 10^5 \text{ cm}^{-3}$.

models. The internal chemical composition and the resulting $X(\text{P}/\text{Fe})$ profile of a spherically symmetric SN model for progenitor mass of $15 M_\odot$ is shown in Fig. 4 (16). In the oxygen-rich layer, P is enhanced, whereas Fe is slightly depleted because of neutron capture. (^{56}Fe and ^{58}Fe are the two major Fe isotopes in the oxygen-rich layer.) This makes $X(\text{P}/\text{Fe})$ higher by two orders of magnitude than that of the outer He-rich layer, which is essentially equal to the cosmic abundance. The extended P enhancement in $M_r/M_{\text{core}} = 0.55$ to 0.73 is the result of hydrostatic burning in pre-SN, whereas the bump at $M_r/M_{\text{core}} \sim 0.5$ is due to explosive burning during the explosion. The knots that we observed are probably from somewhere in the oxygen-rich layer. It is, however, difficult to precisely determine the knots' original positions in the progenitor star from the comparison of the measured P/Fe ratio with the model prediction because the local $X(\text{P}/\text{Fe})$ are very much model-dependent (Fig. 4B) and subject to further modifications owing to the Rayleigh-Taylor instability during the explosion (17). We instead assumed that the knots have been expanding freely, with an expansion rate of 2800 km s^{-1} (18 pc^{-1}) (18). We then converted the obtained space velocities to mass coordinates using the ejecta

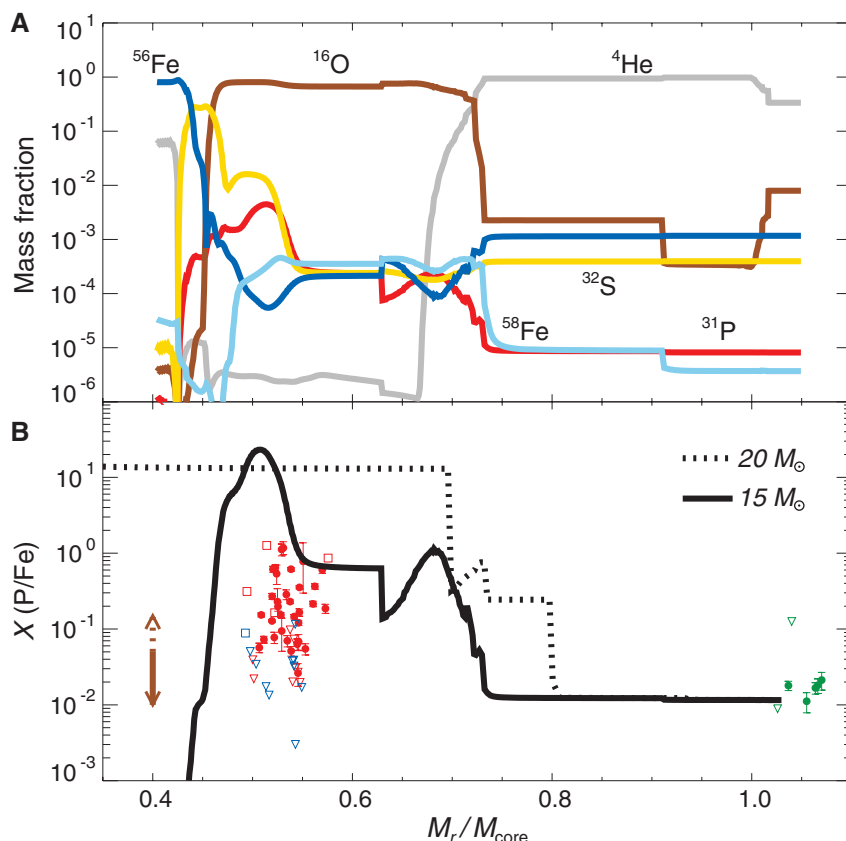


Fig. 4. Comparison of the abundance ratio $X(\text{P}/\text{Fe})$ of the Cas A's knots with predictions from SN nucleosynthetic models. (A) Internal, post-SN chemical composition of a $15 M_{\odot}$ SN model (16). The abscissa is the mass inside a radius r from the explosion center normalized by the mass of the SN core, which is $4.163 M_{\odot}$. The mass inside the “mass cut” ($1.683 M_{\odot}$ or $M_r/M_{\text{core}} = 0.40$) becomes a stellar remnant, whereas the rest is ejected with the explosion. Most of the mass outside the core would have been lost as a stellar wind for SN Type IIb, such as Cas A. In a real SN, the profile will be smoother because of the hydrodynamic mixing of material. **(B)** Profile of the abundance ratio $X(\text{P}/\text{Fe})$ of the $15 M_{\odot}$ SN (solid line). The Fe abundance includes all stable Fe isotopes. The observed $X(\text{P}/\text{Fe})$ ratios of the Cas A SN ejecta knots are marked in the same colors and symbols as in Fig. 3. The knots of circumstellar medium (green symbols) are marked at $M_r/M_{\text{core}} > 1$. For comparison, the dotted line shows $X(\text{P}/\text{Fe})$ profile of a $20 M_{\odot}$ SN (16) with a very high P yield because of unusual convection mixing the Si and oxygen layers before the explosion. The other typical SN models of 15 to $25 M_{\odot}$ in the literature have chemical structures similar to that of the $15 M_{\odot}$ SN model here. The brown arrow to the left represents the expected range of $X(\text{P}/\text{Fe})$ for a complete mixing of the core below the He-rich layer.

velocity profile of a $15 M_{\odot}$ SN IIb model (19) scaled to the chemical structure of the model in Fig. 4 (16). The resulting mass coordinates have considerable uncertainties because of model-dependency but provide rough locations of the knots (Fig. 4B).

$X(\text{P}/\text{Fe})$ of the [P II] line-emitting ejecta knots fall into the $X(\text{P}/\text{Fe})$ range of the oxygen-rich layer in the model, whereas the $X(\text{P}/\text{Fe})$ of the “pure” Fe knots are often less than the cosmic abundance (Fig. 4B). The fact that the circumstellar knots have $X(\text{P}/\text{Fe})$ close to the cosmic abundance— $X(\text{P}/\text{Fe}) \sim 2 X_{\odot}(\text{P}/\text{Fe})$ —gives confidence in the derived $X(\text{P}/\text{Fe})$ in the core. The extended $X(\text{P}/\text{Fe})$ range over nearly two orders of magnitude may be explained by the hydrodynamic chemical mixing during the SN explosion. But, our result does not support a complete mixing of the core below the He-rich layer be-

cause in such a case, $X(\text{P}/\text{Fe})$ will be much lower as marked by the brown arrow in Fig. 4B; the available yields in the literature imply $X(\text{P}/\text{Fe}) = 0.01$ to 0.05 for a SN of 15 to $25 M_{\odot}$ (4, 16, 20, 21), which is represented by the solid part of the arrow, or 0.01 to 0.15 when the unusually high P yield of the $20 M_{\odot}$ model of (16) is included. The detection of P-depleted, pure Fe material probably produced in the innermost, complete Si-burning layer also indicates that these dense SN ejecta materials largely retain their original abundance.

The high $X(\text{P}/\text{Fe})$ ratio, in principle, could also result from the depletion of Fe in the gas phase if Fe atoms are locked in dust grains. In Cas A, a substantial amount ($\sim 0.1 M_{\odot}$) of newly formed dust grains in the SN ejecta has been indeed detected (22–24). But, they are most likely silicate dust, with only 1% of Fe in the form of FeS (25). Also, the fact that [P II] lines in the SN ejecta

are much stronger than in the circumstellar knots (Fig. 2) is best explained by the enhanced abundance of P rather than by the depletion of Fe onto dust.

References and Notes

1. M. Asplund, N. Grevesse, A. J. Sauval, P. Scott, *Annu. Rev. Astron. Astrophys.* **47**, 481–522 (2009).
2. V. Leboutteiller, *Astron. Astrophys.* **443**, 509 (2005).
3. E. Caffau, P. Bonifacio, R. Faraggiana, M. Steffen, *Astron. Astrophys.* **532**, A98 (2011).
4. S. E. Woosley, T. A. Weaver, *Astrophys. J. Suppl. Ser.* **101**, 181 (1995).
5. Another type of stellar explosions (Type Ia supernovae) are also thought to contribute, but to a much lesser extent (26, 27).
6. J. E. Reed, J. J. Hester, A. C. Fabian, P. F. Winkler, *Astrophys. J.* **440**, 706 (1995).
7. R. A. Fesen et al., *Astrophys. J.* **645**, 283–292 (2006).
8. O. Krause et al., *Science* **320**, 1195–1197 (2008).
9. U. Hwang, J. M. Laming, *Astrophys. J.* **746**, 130 (2012).
10. P. A. Young et al., *Astrophys. J.* **640**, 891–900 (2006).
11. C. L. Gerardy, R. A. Fesen, *Astron. J.* **121**, 2781–2791 (2001).
12. Materials and methods are available as supplementary materials on Science Online.
13. S. van den Bergh, *Astrophys. J.* **165**, 457 (1971).
14. J.-J. Lee, S. Park, J. P. Hughes, P. O. Slane, arXiv:1304.3973 (2013).
15. E. Oliva et al., *Astron. Astrophys.* **369**, L5–L8 (2001).
16. T. Rauscher, A. Heger, R. D. Hoffman, S. E. Woosley, *Astrophys. J.* **576**, 323–348 (2002).
17. K. Kifonidis, T. Plewa, H.-T. Janka, E. Müller, *Astron. Astrophys.* **408**, 621 (2003).
18. T. DeLaney et al., *Astrophys. J.* **725**, 2038–2058 (2010).
19. S. E. Woosley, R. G. Eastman, T. A. Weaver, P. A. Pinto, *Astrophys. J.* **429**, 300 (1994).
20. C. Kobayashi, H. Umeda, K. Nomoto, N. Tominaga, T. Ohkubo, *Astrophys. J.* **653**, 1145–1171 (2006).
21. A. Chieffi, M. Limongi, *Astrophys. J.* **764**, 21 (2013).
22. J. Rho et al., *Astrophys. J.* **673**, 271–282 (2008).
23. B. Sibthorpe et al., *Astrophys. J.* **719**, 1553–1564 (2010).
24. M. J. Barlow et al., *Astron. Astrophys.* **518**, L138 (2010).
25. T. Nozawa et al., *Astrophys. J.* **713**, 356–373 (2010).
26. G. Cescutti, F. Matteucci, E. Caffau, P. François, *Astron. Astrophys.* **540**, A33 (2012).
27. C. West, A. Heger, *Astrophys. J.* **774**, 75 (2013).
28. J. R. Thorstensen, R. A. Fesen, S. van den Bergh, *Astron. J.* **122**, 297–307 (2001).

Acknowledgments: This work was supported by Basic Science Research (NRF-2011-0007223) and International Cooperation in Science and Technology (NRF-2010-616-C00020) programs through the National Research Foundation of Korea (NRF) funded by the Ministry of Education, Science and Technology, and also by the Korean Federation of Science and Technology Societies (KOFST). D.-S.M. acknowledges support from the the Natural Science and Engineering Research Council of Canada. We thank M. Munro for his help in observations and J.-J. Lee for providing the *Chandra* 1Ms x-ray images.

Supplementary Materials

www.sciencemag.org/content/342/6164/1346/suppl/DC1
Materials and Methods
Figs. S1 to S4
Tables S1 and S2
References (29–49)

26 July 2013; accepted 7 November 2013
10.1126/science.1243823

fluctuations alone can cause the diffusion to be both anisotropic and anomalous.

We used silica spheres of diameter $d = 1.6$ to $10\ \mu\text{m}$ with two types of surface alignment (21) that set either perpendicular (Fig. 1A) or tangential (Fig. 1B) orientation of $\hat{\mathbf{n}}$. The spheres are placed in a cell with uniform director alignment $\hat{\mathbf{n}}_0$ set by unidirectionally treated bounding plates (21). The director distortions around the particle (22) cause repulsion from the bounding substrates, so that the colloids levitate in the nematic bulk (fig. S1) (23). To minimize experimental errors caused by birefringence, we use the nematic IS-8200 with ultralow birefringence $\Delta n = 0.0015$ (fig. S2) (24).

The typical measured MSD versus τ dependencies are presented in Fig. 2 for perpendicular anchoring and in fig. S5 for tangential anchoring. In the isotropic phase, at $T = 60^\circ\text{C}$, diffusion is normal with $D = 9.2 \times 10^{-16}\ \text{m}^2/\text{s}$. In the nematic, at $T = 50^\circ\text{C}$, diffusion becomes anisotropic. At relatively long time scales ($\tau > 20$ to $40\ \text{s}$), this anisotropic diffusion is normal because both MSD components, measured for displacements parallel and perpendicular to $\hat{\mathbf{n}}_0$, grow linearly with τ . We find $D_{\parallel} = 1.9 \times 10^{-16}\ \text{m}^2/\text{s}$ and $D_{\perp} = 1.4 \times 10^{-16}\ \text{m}^2/\text{s}$ for the normally anchored spheres, and $D_{\parallel} = 2.2 \times 10^{-16}\ \text{m}^2/\text{s}$ and $D_{\perp} = 1.3 \times 10^{-16}\ \text{m}^2/\text{s}$ for tangential anchoring. In all these cases, $\alpha = 1.0 \pm 0.03$. At the times shorter than 20 to 40 s, the MSD versus τ relation becomes nonlinear (Fig. 2A and fig. S5A), signaling anomalous regimes.

To obtain better insight into the different diffusion regimes, we calculated the velocity autocorrelation function (VACF) $C_{v_{ij}}(\tau) = \langle v_x(\tau)v_x(0) \rangle$ (25, 26), where v_x is the velocity of the particle along the x axis, and a similar quantity $C_{v_{\perp}}(\tau) = \langle v_y(\tau)v_y(0) \rangle$ for the y direction. For the isotropic melt (Fig. 2D and fig. S5D) and for the long time scales in the nematic, $C_{v_{ij}}(\tau)$ and $C_{v_{\perp}}(\tau)$ are close to zero (Fig. 2, B and C, and fig. S5, B and C), as should be the case when $\alpha = 1$. However, when the time steps for the nematic are within a certain interval $\tau_{\text{sup}} < \tau < \tau_{\text{sub}}$, both $C_{v_{ij}}(\tau)$ and $C_{v_{\perp}}(\tau)$ become negative, indicating subdiffusion. At yet shorter times $\tau < \tau_{\text{sub}}$, $C_{v_{ij}}(\tau)$ and $C_{v_{\perp}}(\tau)$ are positive, reflecting superdiffusion.

Experimentally, one determines τ_{sup} as the time point at which the VACF changes its sign, and $\tau_{\text{sub}}^{\text{min}}$ as the time point at which the function reaches its minimum; τ_{sub} is determined approximately when the deviation from zero exceeds $10^{-17}\ \text{m}^2/\text{s}^2$ (a typical scatter of VACF data is shown in Fig. 2, B and C). We find that τ_{sup} and $\tau_{\text{sub}}^{\text{min}}$ increase quadratically with the sphere's diameter (Fig. 3).

The dynamic complexity of the director environment around the Brownian particles and finite span (in terms of time lags) make each of the anomalous regimes unlikely to follow a single power law with a fixed value of α . Qualitatively, the existence of slopes in the MSD versus τ dependencies that are smaller than 1 (for $\tau_{\text{sup}} < \tau < \tau_{\text{sub}}$) and larger than 1 (for $\tau < \tau_{\text{sup}}$) is seen in the log-log plot shown in figs. S13D, S14, and

S15 (21). If we oversimplify the situation and assume a single power law, $\text{MSD} \propto \tau^\alpha$, for the τ limits identified above, then the best fit for the subdiffusive domain $\tau_{\text{sup}} < \tau < \tau_{\text{sub}}$ in IS-8200 is achieved for $\alpha_{\parallel} = 0.35 \pm 0.01$ and $\alpha_{\perp} = 0.30 \pm 0.01$; for $\tau < \tau_{\text{sup}}$, one obtains $\alpha_{\parallel} = 1.32 \pm 0.01$ and $\alpha_{\perp} = 1.20 \pm 0.01$.

Anomalous diffusion is also featured in the probability distribution of particle displacements. We calculate the probability distribution function $G(\Delta x, \tau)$ for displacements parallel to $\hat{\mathbf{n}}_0$ (Fig. 4) and $G(\Delta y, \tau)$ for the perpendicular component (fig. S16). Both functions show a distinct behavior within different time scales. For the longest time lags, $\tau = 40\ \text{s}$, $G(\Delta x, \tau)$ coincides with the Gaussian fitting $G_G(\Delta x)$. Such a behavior is characteristic of normal diffusion (14, 18). For the intermediate time lags, $\tau = 10\ \text{s}$, only the central part of $G(\Delta x, \tau)$ (small displacements) is approximately Gaussian. The probability of finding a large displacement at these time lags is noticeably lower than for the Gaussian distribution. This behavior correlates with the idea of subdiffusion, as the particle remains close to its original position. Finally, for the shortest time lags, $\tau = 1\ \text{s}$ (Fig. 4), large displacements are more probable than with the normal diffusion; this behavior is indicative of superdiffusion.

The nematic IS-8200 is not unique in terms of the observed effects. In an appropriate range of time scales, subdiffusion is also observed in the thermotropic 4'-penty-4-cyanobiphenyl (5CB) (figs. S11 and S14) and in the lyotropic chromonic liquid crystal disodium cromoglycate (figs. S12 and S15).

The experiments demonstrate that the effect of orientationally ordered environment on

Brownian motion is profound, causing, in addition to anisotropy, anomalous super- and subdiffusion. These two regimes are observed at relatively short time scales that vary with the material, type of anchoring at the particle's surface, size, and displacement direction with respect to $\hat{\mathbf{n}}_0$. Beyond these short time scales, the diffusion becomes normal (but still anisotropic).

The current models of Brownian motion in a nematic (12–14, 18) consider the director field around the particle as stationary. The predicted diffusion is normal, albeit anisotropic (12–18). We attribute the observed anomalous diffusion to the coupling of the sphere's displacements to the director field and its fluctuations—that is, to an intrinsic memory (27) of the system associated with the orientational order, as discussed below.

The director field $\hat{\mathbf{n}}(\mathbf{r}, t)$ is coupled to the velocity field $\mathbf{v}(\mathbf{r}, t)$ of the nematic. Both $\hat{\mathbf{n}}(\mathbf{r}, t)$ and $\mathbf{v}(\mathbf{r}, t)$ are perturbed by the particle and by the director fluctuations. A perturbation of the director around a colloid of diameter d relaxes within a characteristic time (28) $\tau_d \approx \beta^2 \eta_{\text{eff}} d^2 / K$, where β is a numerical coefficient on the order of 1 that describes the length scale $\sim \beta d$ of deformations (29), η_{eff} is the effective viscosity, and K is the elastic constant. For IS-8200, $\eta_{\text{eff}}/K \approx 10^{11}\ \text{s/m}^2$ (figs. S7 to S10) (21) and thus τ_d is in the range (depending on d) $\tau_d = 0.1$ to $10\ \text{s}$; this is much longer than the time $\rho d^2 / \eta \approx 1\ \mu\text{s}$ needed by the perturbed fluid of density ρ and viscosity $\eta \approx 0.1\ \text{Pa}\cdot\text{s}$ to flow over the distance d (28). It means that the isotropic hydrodynamic memory is not the reason for anomalous diffusion, consistent with data for the isotropic melt (Fig. 2, A and D, and fig. S5, A and D).

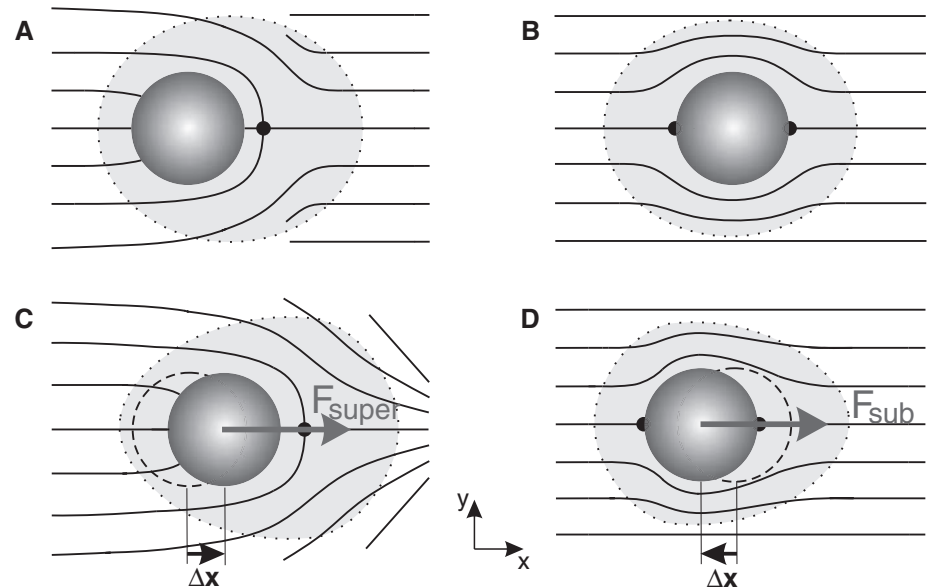


Fig. 1. Director deformations around a sphere and mechanisms of super- and subdiffusion in nematic. (A and B) Equilibrium director for normal (A) and tangential (B) surface anchoring. (C) Elastic force $\mathbf{F}_{\text{super}}$ caused by a fluctuative splay on the right side moves the sphere toward the splay. (D) Restoring force \mathbf{F}_{sub} responds to displacement $\Delta \mathbf{x}$ that creates stronger director gradients on the left side.

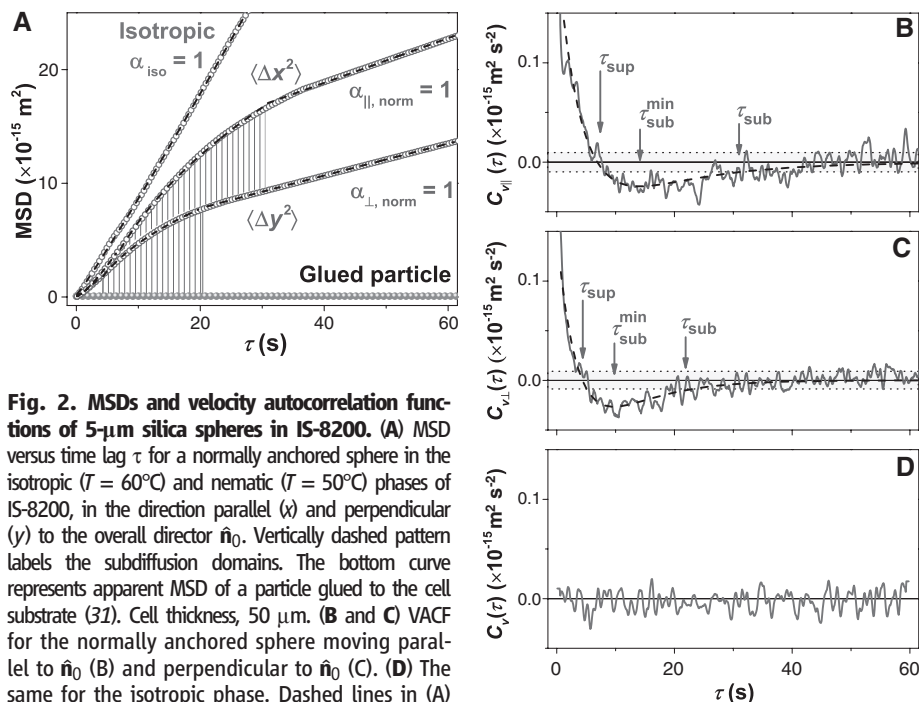


Fig. 2. MSDs and velocity autocorrelation functions of 5- μm silica spheres in IS-8200. (A) MSD versus time lag τ for a normally anchored sphere in the isotropic ($T = 60^\circ\text{C}$) and nematic ($T = 50^\circ\text{C}$) phases of IS-8200, in the direction parallel (x) and perpendicular (y) to the overall director \hat{n}_0 . Vertically dashed pattern labels the subdiffusion domains. The bottom curve represents apparent MSD of a particle glued to the cell substrate (31). Cell thickness, 50 μm . **(B and C)** VACF for the normally anchored sphere moving parallel to \hat{n}_0 (B) and perpendicular to \hat{n}_0 (C). **(D)** The same for the isotropic phase. Dashed lines in (A) to (C) are least-squares fits. Levels of noise in the VACF data for the linear domain are shown in (B) and (C) as dotted horizontal lines.

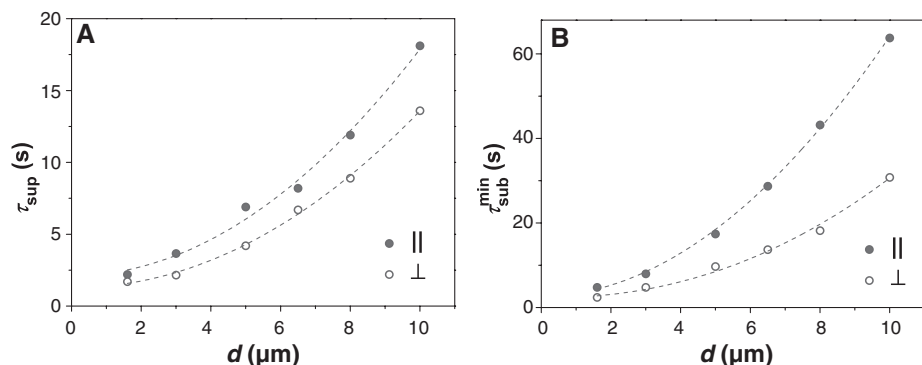


Fig. 3. Characteristic times of anomalous diffusion versus sphere diameter d . (A and B) Measurements of τ_{sup} (A) and $\tau_{\text{sub}}^{\text{min}}$ (B) for normally anchored spheres in the nematic IS-8200 parallel and perpendicular to \hat{n}_0 . Cell thickness, 50 μm ; $T = 50^\circ\text{C}$. Dashed lines are quadratic fits.

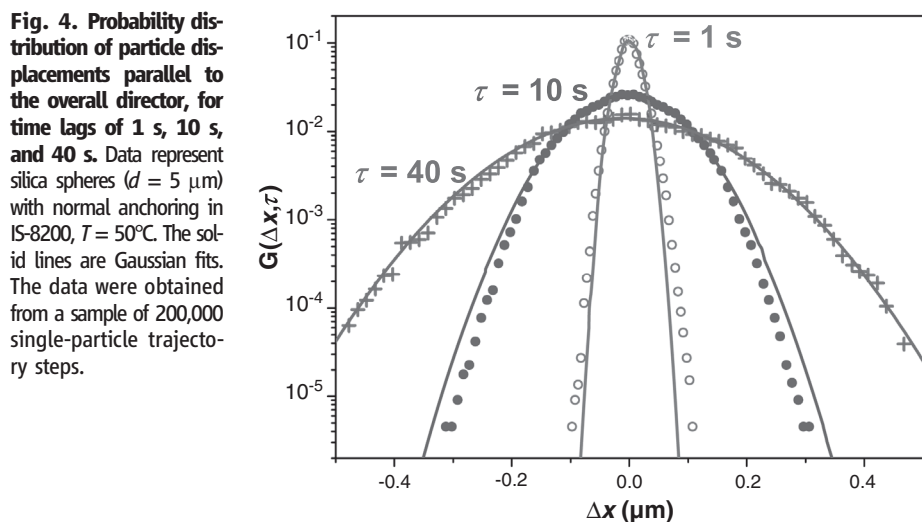


Fig. 4. Probability distribution of particle displacements parallel to the overall director, for time lags of 1 s, 10 s, and 40 s. Data represent silica spheres ($d = 5 \mu\text{m}$) with normal anchoring in IS-8200, $T = 50^\circ\text{C}$. The solid lines are Gaussian fits. The data were obtained from a sample of 200,000 single-particle trajectory steps.

The coupling of director and displacements that leads to subdiffusion at the time scales $\tau_{\text{sub}}, \tau_{\text{sub}}^{\text{min}} \approx \tau_d$ can be illustrated with a tangentially anchored sphere (Fig. 1B). A fluctuative displacement of the sphere, say, to its left by a distance Δx (Fig. 1D) temporarily increases the elastic energy density on the left side and decreases it on the right side. The difference creates a restoring elastic force $\mathbf{F}_{\text{sub}} \approx -K\Delta x/d$ that slows down the diffusive motion.

The case of superdiffusion is sketched in Fig. 1C for a normally anchored sphere that finds itself near a fluctuative splay of the director. The particle experiences an attractive or repulsive force toward the splay, $\mathbf{F}_{\text{super}} = -\nabla U$, where $U = -4\pi K[\mathbf{P} \cdot \mathbf{n}(\nabla \cdot \mathbf{n})dV]$ and \mathbf{P} is the elastic dipole of the sphere, $P \propto d^2$ (29). This force leads to superdiffusive motion during the lifetime of splay fluctuation.

The memory span in the examples above is determined mostly by τ_d . For $\tau \ll \tau_d$, the influence of perturbations with wavelength much shorter than d averages to zero. The life span of fluctuations is also limited from above by the cell thickness h , $\tau_h \approx \eta_{\text{eff}} h^2 / \pi^2 K$. For $h \gg d$, the thickness dependence is expected to be weak and dependent on how far from the boundary the sphere levitates (23); the latter is determined not only by h but also by densities and by elastic and surface anchoring parameters.

For a sphere with $d = 5 \mu\text{m}$ in an IS-8200 cell of thickness 50 μm , we estimate $\tau_d \approx 2.5 \text{ s}$ (assuming $\beta = 1$ and $\eta_{\text{eff}}/K = 10^{11} \text{ s/m}^2$) and $\tau_h \approx 30 \text{ s}$. These values correlate well with the experimentally found $\tau_{\text{sup}} = 4$ to 10 s and $\tau_{\text{sub}} = 20$ to 42 s (Fig. 2 and table S2). The quadratic dependence of τ_{sup} and $\tau_{\text{sub}}^{\text{min}}$ on d (Fig. 3) is another strong indication of the director relaxation mechanism.

The considerations above are not restricted to the specific examples in Fig. 1, C and D. For example, a tangentially anchored particle might be attracted by fluctuative deformation in its neighborhood, whereas displacements of a normally anchored sphere would lead to asymmetric director distortions and a subdiffusive slowing. The universality of director distortions (in terms of attraction or repulsion of colloids) is already known for stationary director fields (30).

Our work demonstrates that the orientational order in a nematic liquid crystal causes a profound effect on Brownian motion of a small spherical particle and results in anisotropic subdiffusion and superdiffusion. These two phenomena are different from the normal diffusion observed in simple isotropic fluids and from the anisotropic but linear behavior of MSD established for long time scales in liquid crystals. We observe that as the time scale τ decreases, the normal diffusion is replaced by subdiffusion and then by superdiffusion. All three regimes are anisotropic, with different MSDs in the direction parallel to the overall director and perpendicular to it. The characteristic times at which the anomalous regimes are observed are within the range of relaxation times of the director distortions around the particle and director fluctuations.

Although this study dealt with standard liquid crystals, the observed anomalous diffusion is expected to arise in any dispersive environment with orientational order.

References and Notes

- W. T. Coffey, Y. P. Kalmykov, J. T. Waldron, *The Langevin Equation: With Applications in Physics, Chemistry and Electrical Engineering* (World Scientific, Singapore, 1996).
- A. Einstein, *Ann. Phys.* **17**, 549 (1905).
- J. Sprakel, J. van der Gucht, M. A. Cohen Stuart, N. A. M. Besseling, *Phys. Rev. E* **77**, 061502 (2008).
- I. Y. Wong *et al.*, *Phys. Rev. Lett.* **92**, 178101 (2004).
- M. M. Alam, R. Mezzenga, *Langmuir* **27**, 6171–6178 (2011).
- X. L. Wu, A. Libchaber, *Phys. Rev. Lett.* **86**, 557 (2001).
- A. Ott, J. P. Bouchaud, D. Langevin, W. Urbach, *Phys. Rev. Lett.* **65**, 2201–2204 (1990).
- Y. Gambin, G. Massiera, L. Ramos, C. Ligoure, W. Urbach, *Phys. Rev. Lett.* **94**, 110602 (2005).
- R. Ganapathy, A. K. Sood, S. Ramaswamy, *Europhys. Lett.* **77**, 18007 (2007).
- R. Angelico, A. Ceglie, U. Olsson, G. Palazzo, L. Ambrosone, *Phys. Rev. E* **74**, 031403 (2006).
- T. G. Mason, D. A. Weitz, *Phys. Rev. Lett.* **74**, 1250–1253 (1995).
- R. W. Ruhwandl, E. M. Terentjev, *Phys. Rev. E* **54**, 5204–5210 (1996).
- H. Stark, D. Ventzki, M. Reichert, *J. Phys. Condens. Matter* **15**, S191–S196 (2003).
- J. C. Loudet, P. Hanusse, P. Poulin, *Science* **306**, 1525 (2004).
- G. M. Koenig Jr. *et al.*, *Nano Lett.* **9**, 2794–2801 (2009).
- M. Škarabot, I. Mušević, *Soft Matter* **6**, 5476–5481 (2010).
- J. A. Moreno-Razo *et al.*, *Soft Matter* **7**, 6828–6835 (2011).
- F. Mondiot *et al.*, *Phys. Rev. E* **86**, 010401 (2012).
- D. Abras, G. Pranami, N. L. Abbott, *Soft Matter* **8**, 2026–2035 (2012).
- M. Pumpa, F. Cichos, *J. Phys. Chem. B* **116**, 14487–14493 (2012).
- See supplementary materials on Science Online.
- P. Poulin, H. Stark, T. C. Lubensky, D. A. Weitz, *Science* **275**, 1770–1773 (1997).
- O. P. Pishnyak, S. Tang, J. R. Kelly, S. V. Shiyankovskii, O. D. Lavrentovich, *Phys. Rev. Lett.* **99**, 127802 (2007).
- V. Reiffenrath, M. Bremer, *Anisotropic Organic Materials* (American Chemical Society, Washington, DC, 2001), pp. 195–205.
- V. M. Kenkre, R. Kühne, P. Reineker, *Z. Phys. B* **41**, 177–180 (1981).
- H. Scher, M. Lax, *Phys. Rev. B* **7**, 4491–4502 (1973).
- N. Kumar, U. Harbola, K. Lindenberg, *Phys. Rev. E* **82**, 021101 (2010).
- P. G. de Gennes, J. Prost, *The Physics of Liquid Crystals* (Clarendon, Oxford, 1993).
- T. C. Lubensky, D. Pettay, N. Currier, H. Stark, *Phys. Rev. E* **57**, 610–625 (1998).
- D. Voloshchenko, O. P. Pishnyak, S. V. Shiyankovskii, O. D. Lavrentovich, *Phys. Rev. E* **65**, 060701 (2002).
- D. S. Martin, M. B. Forstner, J. A. Käs, *Biophys. J.* **83**, 2109–2117 (2002).

Acknowledgments: We thank R. Kamien, E. I. Kats, T. C. Lubensky, and E. Weeks for fruitful discussions, and O. Boiko, U. Ognysta, and A. Nych for help in the experiments. Supported by NSF grants DMR 1104850 and 1121288, Science & Technology Center in Ukraine project no. 5258, DFFD F35/534-2011, and NASU 1.4.1B/10. See supplementary materials for further details on data.

Supplementary Materials

www.sciencemag.org/content/342/6164/1351/suppl/DC1
Materials and Methods
Supplementary Text
Figs. S1 to S16
Tables S1 and S2
References (32–39)

16 May 2013; accepted 7 November 2013
10.1126/science.1240591

Detection and Structure of HOON: Microwave Spectroscopy Reveals an O–O Bond Exceeding 1.9 Å

Kyle N. Crabtree,¹ Marat R. Talipov,² Oscar Martinez Jr.,¹ Gerard D. O'Connor,^{1*} Sergey L. Khursan,³ Michael C. McCarthy^{1†}

Nitric oxide (NO) reacts with hydroxyl radicals (OH) in the gas phase to produce nitrous acid, HONO, but essentially nothing is known about the isomeric nitrosyl-*O*-hydroxide (HOON), owing to its perceived instability. We report the detection of gas-phase HOON in a supersonic molecular beam by Fourier transform microwave spectroscopy and a precise determination of its molecular structure by further spectroscopic analysis of its ²H, ¹⁵N, and ¹⁸O isotopologs. HOON contains the longest O–O bond in any known molecule (1.9149 ± 0.0005 Å) and appears surprisingly stable, with an abundance roughly 3% that of HONO in our experiments.

Gaseous nitric oxide (NO) is known to undergo association with hydroxyl radicals to generate nitrous acid (OH + •NO → HONO) (1). This elementary step is part of a detailed nitrous acid reaction scheme in the atmosphere, involving soil chemistry, photochemistry, gas-phase reactions, and other heterogeneous processes (2–4); in particular, during the daytime, OH and NO are also regenerated from photolysis of HONO, leading to an association-dissociation cycle. Whereas the aforementioned reaction involves attachment at the nitrogen position of NO,

photolysis studies in ice matrices with other radicals have also yielded the isomeric isonitrosyl species: X + •ON → XON (X = H, Br, Cl, or CN) (5). For the nitrous acid system, such a reaction would generate the isomer nitrosyl-*O*-hydroxide: HOON.

Although this isomer may be formed in the OH + NO reaction, and the higher-energy imine peroxide (HNOO) isomer has been previously observed in ice matrices (6, 7), HOON has never been detected experimentally and has received relatively little attention from theoretical chemists. Perhaps this can be attributed to the results of early calculations, which suggested that HOON is not likely to be stable (8), with one study explicitly stating, “[HOON] should be extremely unstable; it is liable to be decomposed to NO + OH with virtually no activation barrier” (9). Until very recently, it was only considered as a short-lived, unstable intermediate in the NH + O₂ → OH + NO reaction (9–11) and as a possible dynamical intermediate in highly excited O–H stretching overtones

of HONO (12). High-level ab initio calculations, however, suggest that the dissociation energy of the O–O bond in HOON is ~8 kcal mol^{–1}, and therefore HOON might be a candidate for matrix isolation studies (13).

A striking feature of HOON is its central O–O bond, which calculations have predicted to lie anywhere from 1.5 to 2.0 Å. Uncertainty in both the O–O bond length and stability against dissociation are reminiscent of HO₃, a radical that has received much recent experimental and theoretical attention (14–17). For HO₃, the central O–O bond length was found to be 1.684 ± 0.003 Å (15), considerably longer than a standard O–O single bond—for example, for H₂O₂, *r*(O–O) = 1.452 Å (18)—and its dissociation energy was recently measured to be 2.97 ± 0.07 kcal mol^{–1} (19). Despite a calculated dissociation energy nearly three times as high as that of HO₃, HOON was most recently predicted to have an O–O bond substantially longer still: 1.89 Å for *trans*-HOON, and 1.91 Å for *cis*-HOON, which lies ~2 kcal mol^{–1} higher in energy (13).

Here, we report the detection of the rotational spectrum of *trans*-HOON in the gas phase by means of Fourier-transform microwave (FTM) spectroscopy and double resonance (DR) techniques, as well as a precise determination of its molecular structure by extensive isotopic substitution. The O–O bond length is found to be 1.9149 ± 0.0005 Å, and HOON is formed at roughly 3% of the abundance of HONO under the same conditions, suggesting that this isomer is more stable than previously thought.

HOON was generated in a pulsed supersonic expansion discharge nozzle fed by a gas mixture of NO and water vapor heavily diluted in Ne, a combination known to produce rotationally cold (~2 K) HONO in high abundance (20). Both *cis*- and *trans*-HOON are asymmetric rotors close

¹Harvard-Smithsonian Center for Astrophysics, 60 Garden Street, Cambridge, MA 02138, USA. ²Department of Chemistry, Marquette University, 535 North 14th Street, Milwaukee, WI 53201, USA. ³Institute of Organic Chemistry, Ufa Scientific Centre, Russian Academy of Sciences pr. Oktyabrya 71, Ufa, 450054 Russian Federation.

*Present address: School of Chemistry, The University of Sydney, New South Wales 2006, Australia.

†Corresponding author. E-mail: mccarthy@cfa.harvard.edu

to the prolate limit with modest dipole moments along the *a* and *b* inertial axes (13, 21, 22). As such, both possess *a*-type rotational spectra in which successive lines are nearly harmonically related in frequency; the lowest two of these are expected to fall in the 5 to 43 GHz range of our FTM spectrometer. The fundamental *a*-type transitions of the two isomers differ by only ~4% in frequency (600 MHz at $B + C \sim 16.5$ GHz), and each is expected to display closely spaced (on the order of 1 MHz) hyperfine structure from nitrogen quadrupole splitting, which is readily observed at the high spectral resolution (~0.1 parts per million) of the measurement. Because of the simplicity of the line pattern, a search for these

transitions was conducted from 15.2 to 17.0 GHz, using experimental conditions that optimize production of *cis*-HONO (1–0 line at 24,533 MHz). Three tightly spaced lines with the characteristic 3:5:1 intensity ratio of nitrogen quadrupole hyperfine splitting were found at 16,306 MHz (Fig. 1). These lines were only observed in the presence of an electric discharge, and their intensities were not altered by application of a magnetic field, implying that the carrier is a closed-shell neutral molecule. No other lines with similar behavior were found in the search.

A second rotational transition with apparent nitrogen quadrupole splitting was then found at 32,605 MHz and linked to the 16,306 MHz tran-

sition by microwave-microwave DR (see supplementary text). These observations are consistent with the predicted *a*-type spectrum of either *cis*- or *trans*-HOON, but it is not possible to distinguish between the two from this information alone; spectroscopy of isotopologs is required. By empirically scaling rotational constants derived from the predicted structures of the *cis* and *trans* isomers, we estimated frequency shifts of the fundamental *a*-type transition for various isotopologs relative to the normal isotopic species (see Table 1). Using H_2^{18}O in place of normal water, transitions corresponding to H^{18}OON and HO^{18}ON were soon found at 15,367 and 16,167 MHz, respectively; with D_2O , a DOON transition was observed at 15,459 MHz, and with $^{15}\text{NO} + \text{H}_2\text{O}$, a HOO^{15}N transition was found at 15,913 MHz. The observed shifts are in excellent agreement with those predicted for the *trans* isomer (DOON in particular) (Table 1). As with HO_3 , no evidence for *cis*-HOON was found in any of our spectral surveys (14–16).

Because the strongest low-*J* *b*-type rotational transitions of *trans*-HOON lie well above the 43 GHz frequency limit of the FTM spectrometer, DR spectroscopy was used to determine the three rotational constants to high precision. Owing to the relatively large uncertainty of the *A* rotational constant, searches spanning several GHz were initially required, but ultimately, a strong line was observed by this method (Fig. 1), enabling the frequencies of additional *b*-type transitions to be calculated with much greater accuracy. A total of 39 hyperfine components from nine rotational transitions of *trans*-HOON were recorded (Fig. 1), as well as *a*- and *b*-type transitions of several other isotopologs. Frequencies of all observed transitions are listed in tables S1 and S2, and full sets of spectroscopic constants derived from a fit to a standard asymmetric top effective Hamiltonian are given in table S3.

The structure of *trans*-HOON was determined by fitting the five structural parameters to the moments of inertia for the five observed isotopologs, yielding a ground state (r_0) structure (23). A semi-empirical equilibrium structure (r_e^{emp}) (Fig. 2) has been derived from a combination of the experimentally measured isotopic data and vibration-rotation constants (table S5) calculated theoretically (24). In contrast to HOOO , this combined approach works extremely well; it yields a highly precise, planar structure, implying in general terms that this molecule is rigidly bound, with little large amplitude motion. Inertial defects ($\Delta \propto C^{-1} - B^{-1} - A^{-1}$) for all species are less than 0.005 atomic mass units (amu) \AA^2 (Table 2), although they are systematically positive, possibly suggesting the need for zero-point corrections at still higher levels of theory.

The most prominent feature of the semi-empirical structure is the O–O bond: 1.9149 ± 0.0005 \AA , about 14% longer than the analogous bond in the HO_3 radical and 32% longer than the typical O–O single bond in hydrogen peroxide.

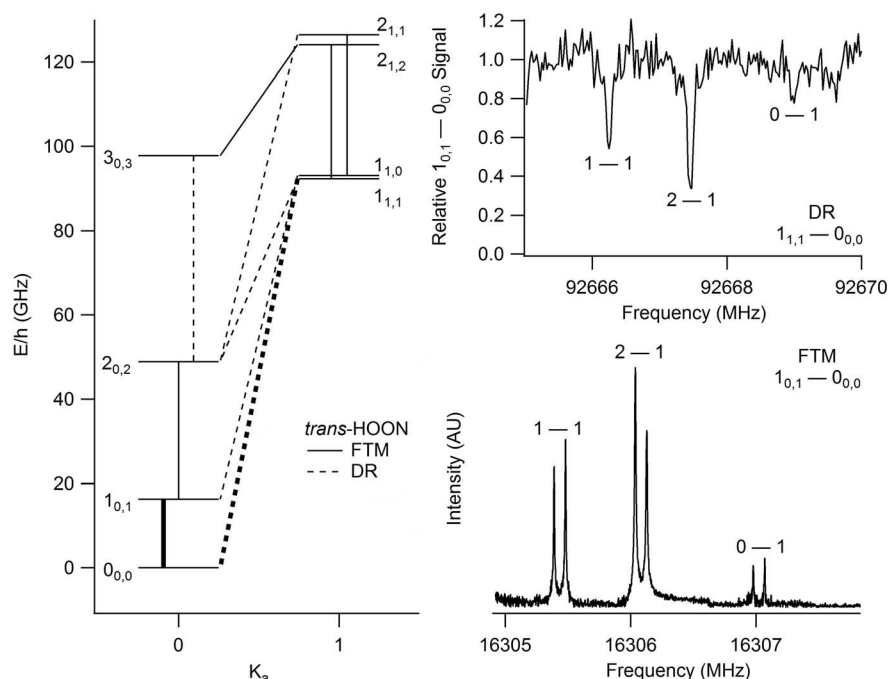


Fig. 1. Observed transitions of *trans*-HOON. In the energy level diagram at left, solid lines indicate transitions measured with FTM spectroscopy, and dotted lines transitions measured with DR spectroscopy. The fundamental *a*- and *b*-type transitions (marked with bold lines) are shown in the spectra on the right. The FTM spectrum of the $1_{0,1} - 0_{0,0}$ transition (right, bottom) is stitched together from six partially overlapping scans, each the coverage of 200 gas pulses and 1 MHz in bandwidth, and represents a total of just over 3 min of integration. Each hyperfine component, labeled by its $F' - F$ quantum numbers, shows the characteristic Doppler doubling arising from the coaxial alignment of the supersonic molecular beam with respect to the Fabry-Perot cavity. The DR spectrum of the $1_{1,1} - 0_{0,0}$ transition (right, top) is plotted as the relative intensity of the $1_{0,1} - 0_{0,0}$ $F = 2 - 1$ FTM signal as a function of DR frequency. At each 25-kHz frequency step, the free induction decays of 20 gas pulses were averaged; the total integration time was 11 min.

Table 1. Calculated frequency shifts from the fundamental *a*-type transition (at 16,306.1 MHz) upon isotopic substitution of *cis*- and *trans*-HOON compared with observed shifts (all in MHz). Calculated shifts are empirically scaled by the ratio of the observed transition frequency to that predicted from the CCSD(T)/aug-cc-pV5Z structure for each isomer (13, 22), i.e., by $(B + C)_{\text{obs}}/(B + C)_{\text{calc}, \text{cis}}$ and $(B + C)_{\text{obs}}/(B + C)_{\text{calc}, \text{trans}}$.

Species	δ obs.	δ <i>cis</i> calc.	δ <i>trans</i> calc.
H^{18}OON	−939	−983	−939
HO^{18}ON	−139	−133	−141
DOON	−848	−516	−905
HOO^{15}N	−393	−405	−399

Also noteworthy are the O–H bond length of 0.9698 ± 0.0010 Å, nearly the same as free OH (0.9697 Å) (25), and the N–O length of 1.1264 ± 0.0005 Å, between that of NO (1.1508 Å) and NO^+ (1.0632 Å) (26). Despite such a long O–O bond, detection of gaseous HOON provides unambiguous proof of its existence and stability. Taking into account differences in dipole moment and partition functions, we estimate that HOON is present at roughly 3% of the abundance of HONO, a stable gas-phase isomer lying much lower in energy (~ 45 kcal mol $^{-1}$). Such a large abundance relative to its lower-energy isomer suggests that HOON is more stable than previously thought.

Further evidence for the rigidity and stability of *trans*-HOON (i.e., the strength of its O–O bond) is provided by the value of its quartic centrifugal distortion constant D_J , which in the present context represents the extent of deviation from a rigid rotor due to stretching of bonds along the a inertial axis. A molecule containing two groups linked by a weak central bond oriented nearly coincident to the a axis can be approximated as an effective diatomic species with $D_J = 4B_{\text{eff}}^3/\omega^2$, where B_{eff} is $(B + C)/2$ and ω is the effective diatomic stretching frequency, related to the force constant of the central bond. Table S4 shows the effective stretching frequencies of HOON, HOOO, $(\text{H}_2\text{O})_2$, and Ar- H_2O using this model. By this metric, the central O–O bond in HOON is estimated to be more rigid than that in HOOO and much more rigid than either the central H–O hydrogen bond in $(\text{H}_2\text{O})_2$ or the van der Waals bond in Ar- H_2O . The effective harmonic stretching frequency for HOON (311 cm $^{-1}$) inferred from this simple model is in excellent agreement with the calculated CCSD(T)/aug-cc-

pVTZ harmonic frequency of 305 cm $^{-1}$, lending additional support to the idea that HOON is more strongly bound than HOOO despite its much longer O–O bond.

The formation mechanism of HOON in our plasma is likely three-body association: $\text{OH} + \text{NO} \rightarrow (\text{HOON})^* + \text{Ne} \rightarrow \text{HOON} + \text{Ne}$. When H_2^{18}O is used as a OH source with NO, lines of H^{18}OON are found to be ~ 4 times as strong as those of HO^{18}ON , suggesting that the OH bond from water is largely preserved in molecule formation but that some scrambling of oxygen does take place. Hydrogen migration from one oxygen to the other is known to be facile in *cis*-HONO (10). On the $[\text{H}, \text{N}, \text{O}_2]$ potential energy surface, the barrier for *trans*-HOON \rightarrow *cis*-HONO isomerization is comparable to the O–O dissociation energy of 8 kcal mol $^{-1}$ (13). Oxygen scrambling could therefore plausibly be effected by the pathway (27): $\text{H}^{18}\text{O} + \text{NO} \rightarrow (\text{cis-}\text{H}^{18}\text{ONO})^* \rightarrow (\text{cis-}\text{H}^{18}\text{ONOH})^* \rightarrow (\text{trans-}\text{HO}^{18}\text{ON})^* \rightarrow (\text{trans-}\text{HO}^{18}\text{ON})^* + \text{Ne} \rightarrow \text{trans-}\text{HO}^{18}\text{ON} + \text{Ne}$. The observed oxygen scrambling suggests that some fraction of HOON observed in the molecular beam is formed through a pathway that involves *cis*-HONO, consistent with isomerization through an activated collision complex.

The apparent stability of gaseous HOON as evidenced by its gas-phase detection suggests that this isomer might be formed as a part of the HONO photochemical cycle in the troposphere, which has not been considered in chemical models. By contrast, the involvement of peroxyxynitrous acid (HOONO , an isomer of nitric acid) in the $\text{OH} + \text{NO}_2$ radical termination reaction had been previously anticipated from kinetics studies even before its gas phase identification (28, 29), which in turn has enabled further studies of its par-

ticipation in the nitric acid system (30, 31). Analogously, the $\text{OH} + \text{NO}$ association reaction is barrierless, and some fraction of three-body $\text{OH} + \text{NO}$ collisions will likely result in the formation of stable HOON, possibly approaching or exceeding the level (3%) measured in our supersonic expansion. Once HOON is formed, it may dissociate, isomerize to HONO, or, most interestingly, participate in further chemical reactions with other atmospheric species if its lifetime is sufficiently long. Considering the O–O bond length derived from these microwave measurements, HOON should be a highly reactive species. The present study provides essential spectroscopic information to facilitate detection of this species in other regions of the electromagnetic spectrum and to enable measurements to be made under conditions simulating Earth's troposphere. Further investigations to assess the reactivity of HOON with other atmospheric constituents, its lifetime, and its role in the larger chemistry of $[\text{H}, \text{N}, \text{O}]$ -containing species are needed.

References and Notes

- F. Stuhl, H. Niki, *J. Chem. Phys.* **57**, 3677 (1972).
- N. Zhang *et al.*, *Geophys. Res. Lett.* **36**, L15820 (2009).
- H. Su *et al.*, *Science* **333**, 1616–1618 (2011).
- X. Li *et al.*, *Atmos. Chem. Phys.* **12**, 1497–1513 (2012).
- G. Maier, H. P. Reisenauer, M. D. Marco, *Chemistry* **6**, 800–808 (2000).
- S. L. Laursen, J. E. Grace, R. L. DeKock, S. Spronk, *J. Am. Chem. Soc.* **120**, 12583–12594 (1998).
- R. L. DeKock *et al.*, *J. Phys. Chem. A* **108**, 2893–2903 (2004).
- S. Nakamura, M. Takahashi, R. Okazaki, K. Morokuma, *J. Am. Chem. Soc.* **109**, 4142–4148 (1987).
- T. Fueno, K. Yokoyama, S.-Y. Takane, *Theor. Chim. Acta* **82**, 299–308 (1992).
- R. Asatryan, J. W. Bozzelli, J. M. Simmie, *Int. J. Chem. Kinet.* **39**, 378–398 (2007).
- M. R. Talipov, S. L. Khursan, R. L. Safiullin, *J. Phys. Chem. A* **113**, 6468–6476 (2009).
- Y. Miller, G. M. Chaban, B. J. Finlayson-Pitts, R. B. Gerber, *J. Phys. Chem. A* **110**, 5342–5354 (2006).
- M. R. Talipov, Q. K. Timerghazin, R. L. Safiullin, S. L. Khursan, *J. Phys. Chem. A* **117**, 679–685 (2013).
- K. Suma, Y. Sumiyoshi, Y. Endo, *Science* **308**, 1885–1886 (2005).
- M. C. McCarthy, V. Lattanzi, D. Kokkin, O. Martinez Jr., J. F. Stanton, *J. Chem. Phys.* **136**, 034303 (2012).
- P. L. Raston, T. Liang, G. E. Doublerly, *J. Chem. Phys.* **137**, 184302 (2012).
- A. J. C. Varandas, *J. Chem. Theory Comput.* **8**, 428–441 (2012).
- J. Koput, *Chem. Phys. Lett.* **236**, 516–520 (1995).
- S. D. Le Picard, M. Tizniti, A. Canosa, I. R. Sims, I. W. M. Smith, *Science* **328**, 1258–1262 (2010).
- Materials and methods are available as supplementary materials on Science Online.
- At the CCSD(T)/aug-cc-pVTZ level of theory, $\mu_a = 1.46$ D and $\mu_b = 1.71$ D for *trans*-HOON, and $\mu_a = 2.23$ D and $\mu_b = 1.01$ D for *cis*-HOON.
- Equilibrium rotational constants at CCSD(T)/aug-cc-pV5Z (13): *trans*-HOON, $A = 84859$ MHz, $B = 8976$ MHz, and $C = 8118$ MHz; *cis*-HOON, $A = 88403$ MHz, $B = 8637$ MHz, and $C = 7869$ MHz.
- The fully experimental r_0 structure is given in table S6 and the principal atomic coordinates in table S7.
- J. F. Stanton, J. Gauss, *Int. Rev. Phys. Chem.* **19**, 61–95 (2000).

Fig. 2. Semiempirical equilibrium structure of *trans*-HOON. Zero-point corrections to the rotational constants were calculated at the CCSD(T)/aug-cc-pVTZ level of theory. Bold numbers are the semiempirical values, numbers in italics are from the CCSD(T)/aug-cc-pV5Z structure, and numbers in normal type are from the multi-

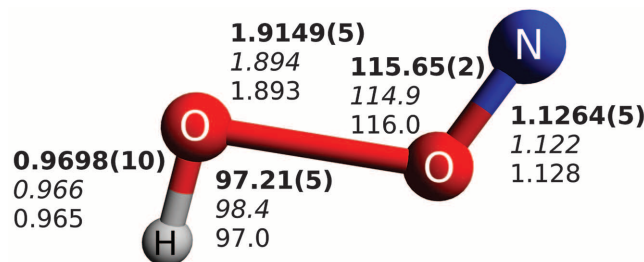


Table 2. Semiempirical equilibrium rotational constants and inertial defects of *trans*-HOON and its isotopologs. Zero-point corrections to the rotational constants for each species were calculated at the CCSD(T)/aug-cc-pVTZ level of theory.

Species	A_e (MHz)	B_e (MHz)	C_e (MHz)	Δ (amu Å 2)
HOON	85,170.50	8768.14	7949.54	0.00163
H^{18}OON	84,276.27	8242.88	7508.34	0.00146
HO^{18}ON	79,998.74	8715.46	7858.95	0.00233
DOON	79,453.51	8296.86	7512.20	0.00405
HOO^{15}N	83,557.31	8551.30	7757.06	0.00167

25. K. P. Huber, G. Herzberg, *Molecular Spectra and Molecular Structure. IV. Constants of Diatomic Molecules* (Van Nostrand Reinhold, New York, 1979).
26. R. Polák, J. Fiser, *Chem. Phys.* **303**, 73–83 (2004).
27. Other pathways, including dissociation of *cis*-HON¹⁸O, followed by recombination with OH to form *trans*-HO¹⁸ON, might also be feasible.
28. J. Troe, *Int. J. Chem. Kinet.* **33**, 878–889 (2001).
29. S. Nizkorodov, P. O. Wennberg, *J. Phys. Chem. A* **106**, 855–859 (2002).
30. B. D. Bean *et al.*, *J. Phys. Chem. A* **107**, 6974–6985 (2003).

31. J. Zhang, N. M. Donahue, *J. Phys. Chem. A* **110**, 6898–6911 (2006).

Acknowledgments: K.N.C. has been supported by a Cfa Postdoctoral Fellowship from the Smithsonian Astrophysical Observatory. The work in Cambridge is supported by NSF grant CHE-1058063. Calculations were funded by National Science Foundation awards OCI-0923037, MRI: Acquisition of a Parallel Computing Cluster and Storage for the Marquette University Grid (MUGrid), and CBET-0521602, Acquisition of a Linux Cluster to Support College-Wide

Research and Teaching Activities. We thank C. A. Gottlieb for helpful discussions and E. S. Palmer for technical assistance.

Supplementary Materials

www.sciencemag.org/content/342/6164/1354/suppl/DC1
Materials and Methods
Tables S1 to S8
References (32–47)

2 August 2013; accepted 1 November 2013
10.1126/science.1244180

Erythropoietin Derived by Chemical Synthesis

Ping Wang,^{1*} Suwei Dong,^{1*} Jae-Hung Shieh,² Elizabeth Peguero,² Ronald Hendrickson,³ Malcolm A. S. Moore,² Samuel J. Danishefsky^{1,4†}

Erythropoietin is a signaling glycoprotein that controls the fundamental process of erythropoiesis, orchestrating the production and maintenance of red blood cells. As administered clinically, erythropoietin has a polypeptide backbone with complex dishomogeneity in its carbohydrate domains. Here we describe the total synthesis of homogeneous erythropoietin with consensus carbohydrate domains incorporated at all of the native glycosylation sites. The oligosaccharide sectors were built by total synthesis and attached stereospecifically to peptidyl fragments of the wild-type primary sequence, themselves obtained by solid-phase peptide synthesis. The glycopeptidyl constructs were joined by chemical ligation, followed by metal-free dethylation, and subsequently folded. This homogeneous erythropoietin glycosylated at the three wild-type aspartates with N-linked high-mannose sialic acid-containing oligosaccharides and O-linked glycoporphin exhibits Procrit-level *in vivo* activity in mice.

Erythropoietin (EPO) is functionally a hormone that plays a key role in erythropoiesis, which is central to the orchestration and production of erythrocytes (1, 2). EPO is a glycoprotein with both a highly conserved polypeptide domain and four tightly conserved sites of glycosylation. However, the actual carbohydrate ensembles, particularly at the N linkages, are strikingly variable (3). Before our earlier work (4, 5), there were no reports of a naturally isolated or synthetically derived structurally defined, homogeneously glycosylated, EPO sample of wild-type primary structure—bearing glycosyl domains at the conserved sites.

The defining goal that we undertook in 2002 was to prepare, by total synthesis, a “wild-type” EPO polypeptide homogeneously glycosylated at the three conserved N-linked sites, as well as at the single O-linked center, by oligosaccharides of biolevel complexity (Fig. 1) (6). All of the carbohydrate domains would also be prepared through total synthesis (7–10). Given the widespread appearance of glycoporphin (fig. S1, structure S1) in O linkages in complex EPO-type

glycoproteins, we chose to install this motif at Ser¹²⁶ in our envisioned synthetic EPO (11). As for the three asparagine-linked domains, we designed what was perceived to be a consensus sequence of realistic EPO-level complexity (12–14). The N-linked glycan domain would display a char-

acteristic chitobiose disaccharide at its reducing end, which would bear a signature branching β -linkage to L-fucose and a core branched trimannosyl ensemble. The latter would in turn be linked at C2 and C2' of its “wing” mannose residues to two identical trisaccharide sialyllactose domains. The sense of sialylation (α -2,3) of the lactosamine would correspond to the wild-type recombinant motif (15, 16). This thinking led us to propose structure S2 as the consensus dodecasaccharide (fig. S1).

To undertake this program, four synthetic methodology entries were crucial to our endeavors, including native chemical ligation (NCL), metal-free desulfurization (MFD), o-mercaptoparyl ester rearrangement (OMER)-mediated ligation, and one-flask aspartylation (fig. S2). Developed by Kent and co-workers (17), NCL serves as a key technology in complex peptide synthesis. However, we could take advantage of only one NCL to affix an N-terminal cysteine to a suitable C-terminal thioester donor. Our contribution for extending the range of NCL logic to enable ligations at ultimately noncysteine N termini was that of MFD (18), which has allowed for the implementation of an earlier recognition by Dawson

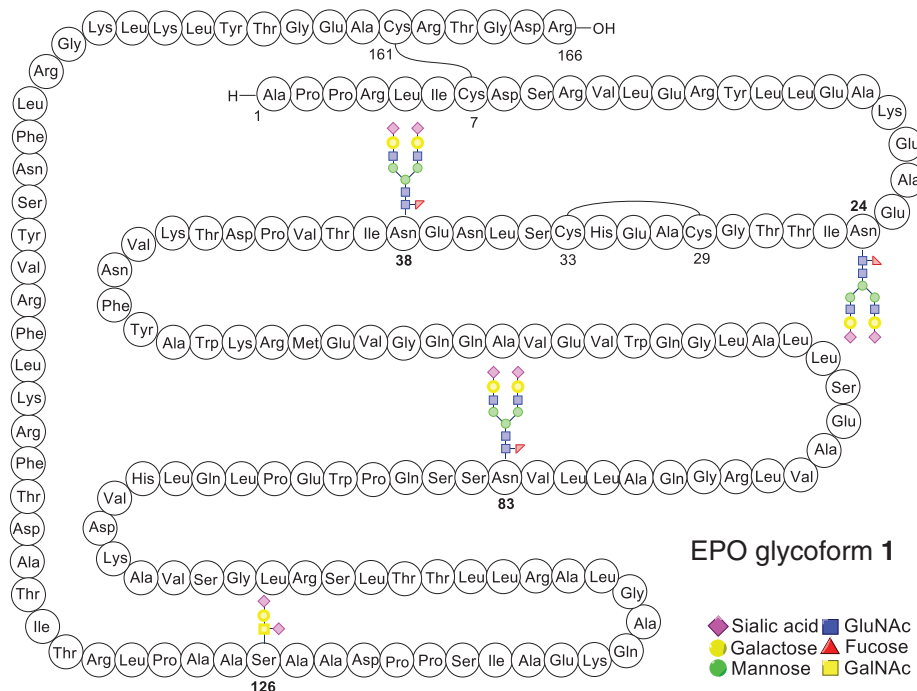


Fig. 1. Schematic representation of the target homogeneous EPO glycoform 1.

¹Laboratory for Bioorganic Chemistry, Sloan-Kettering Institute for Cancer Research, 1275 York Avenue, New York, NY 10065, USA. ²Cell Biology Program, Sloan-Kettering Institute for Cancer Research, 1275 York Avenue, New York, NY 10065, USA. ³Department of Pharmacology and Chemistry, Sloan-Kettering Institute for Cancer Research, 1275 York Avenue, New York, NY 10065, USA. ⁴Department of Chemistry, Columbia University, Havemeyer Hall, 3000 Broadway, New York, NY 10027, USA.

*These authors contributed equally to this work.

†Corresponding author. E-mail: s-danishefsky@ski.mskcc.org

that MFD of a cysteine can lead to an alanine (19). Despite a dearth of useful cysteine ligation sites, the primary structure of target EPO glycoform **1** offers a variety of alanine centers, thereby inviting a range of retrosynthetic options for reaching our goal. OMER-mediated ligation served as a device for in situ generation of the activated thioesters (20, 21) and proved to be particularly useful in the synthesis of fragment **S7** (fig. S4)

(22). Finally, and critical to our mission, was the capacity to realize maximally convergent amidation of highly complex oligosaccharide glycosylamines with suitably differentiated aspartates, even in substantially sized polypeptides (23, 24).

For programmatic expediency, we first field-tested our methodological capabilities and the implementability of our retrosynthetic logic in the context of a simpler target, where the three

N linkages serve to join chitobiose disaccharides to the conserved asparagines of the wild-type 166-oligomer (4, 5). Naively, we thought at the time that the pathway to **S3**, if followed faithfully (with the highly challenging provision that the N-linked oligosaccharides corresponding to **S2** would be in place), would soon lead us to our long-term, noncompromisable target, **1**. We were able to synthesize the N-linked fragments **S4**, **S5**,

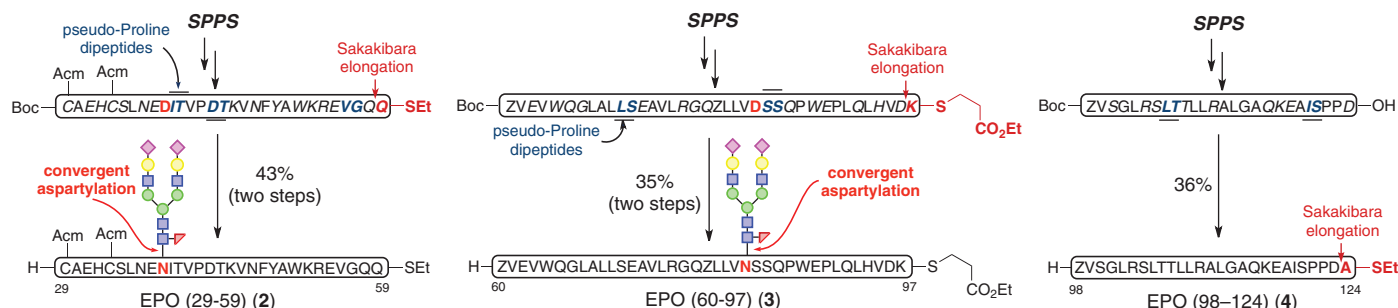


Fig. 2. Synthesis of revised glycopeptide fragments. Reaction conditions for Sakakibara elongation (26): Peptidyl acid, amino acid thioester, EDC free base, HOOBt, CHCl_3/TFE , room temperature (rt). Reaction conditions for aspartylation: (i) Peptidyl thioester, **S2**, HATU, DIEA, DMSO, rt. (ii) TFA/TIS/ H_2O /phenol, rt. EDC = *N*-(3-

Dimethylaminopropyl)-*N*-ethylcarbodiimide; HOOBt = 3-Hydroxy-1,2,3-benzotriazin-4(3*H*)-one; HATU = 1-[Bis(dimethylamino)methylene]-1*H*-1,2,3-triazolo[4,5-*b*]pyridinium 3-oxid hexafluorophosphate; TFE = trifluoroethanol; DIEA = *N,N*-Diisopropylethylamine; DMSO = dimethyl sulfoxide; TFA = trifluoroacetic acid; TIS = triisopropylsilane.

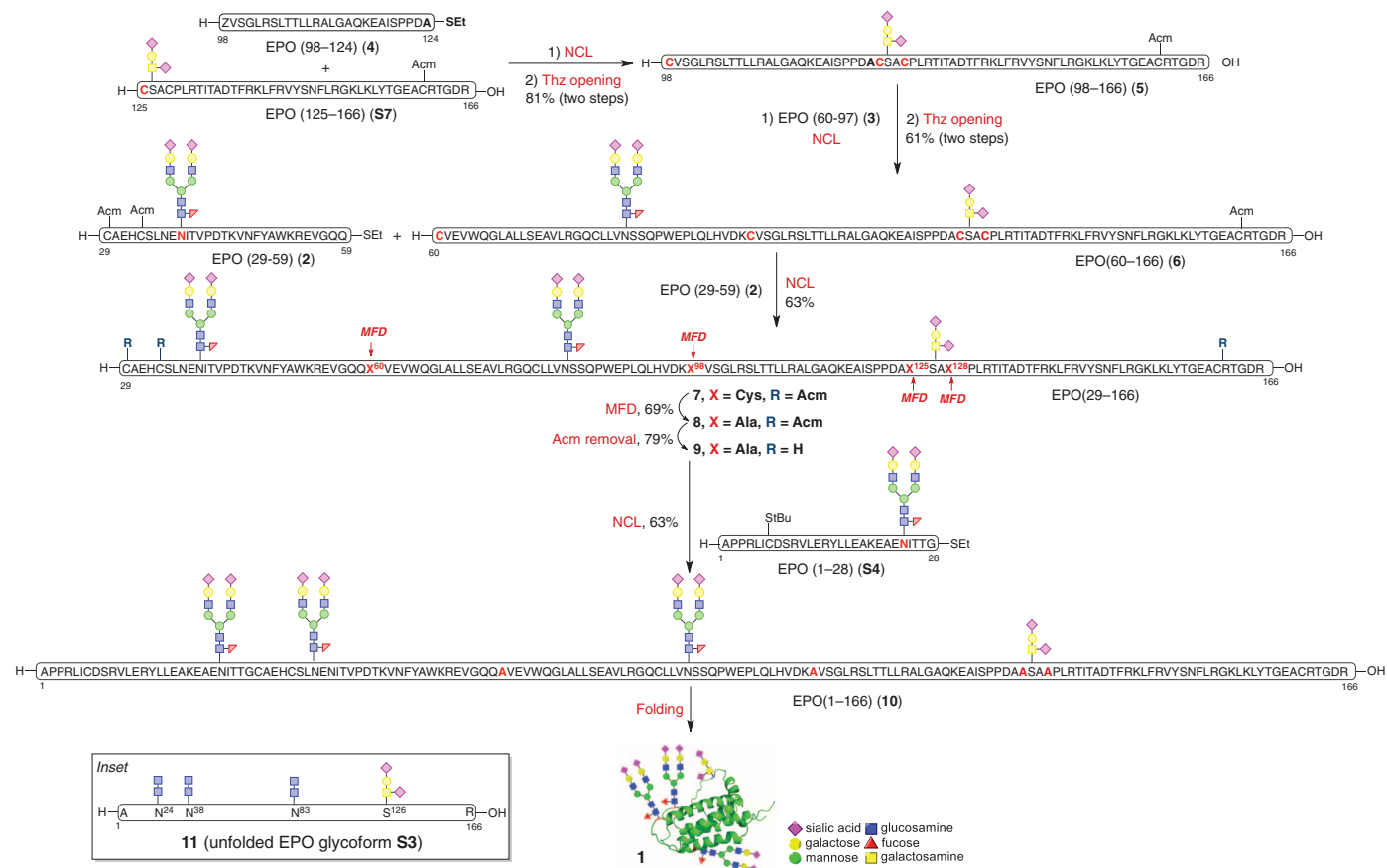


Fig. 3. Synthesis of homogeneous EPO glycoform 1. SPPS, solid-phase peptide synthesis. Reaction conditions for NCL: 6 M GND•HCl, 300 mM Na_2HPO_4 , 20 mM TCEP•HCl, 200 mM MPAA, pH 7.2, rt. Reaction conditions for Thz opening: MeONH_2 •HCl, rt. Reaction conditions for MFD: 5.7 M GND•HCl, 200 mM Na_2HPO_4 , 300 mM TCEP (Bond-Breaker), *t*-BuSH, VA-044,

pH 6.8, 37°C. Reaction conditions for AcM removal: AgOAc, AcOH/ H_2O , rt. Reaction conditions for folding: cysteine/cystine (8:1). GND = guanidine; TCEP = tris(2-carboxyethyl)phosphine; MPAA = 4-Mercaptophenylacetic acid; Thz = thiazolidine; VA-044 = 2,2'-Azobis[2-(2-imidazolin-2-yl)propane]dihydrochloride.

and **S6** (fig. S4A) containing the fully synthetic dodecamer polysaccharide moieties.

With the required fragments in hand, we proceeded toward **1** (Fig. 1). The coupling of glycopeptides **S6** and **S7** under NCL conditions followed by deprotection of the thiazolidine (Thz) (25) afforded a prospective EPO (79-166) domain (**S8**) in good yield (fig. S4B). Unfortunately, the coupling of **S8** to prospective EPO fragment **S5**, intended to produce the prospective EPO (29-166) domain (**S9**), was not successful (at best, 10%). After numerous investigations, it was surmised that the breakdown in the attempted merger of **S8** and **S5** arose from the large consensus carbohydrate domain at position 83 in fragment **S8**.

Accordingly, we had to reconfigure the erstwhile fragments **S5** and **S6**, generating in their wake more manageable NCL-worthy prealanine coupling domains for filling in the space between amino acids 29 to 124. We reorganized the domain associated with pre-EPO (29-124) into three fragments, shown in Fig. 2 as building blocks **2**, **3**, and **4** (26). Thus, following the one-flask convergent aspartylation protocol, glycopeptide fragments EPO (29-59) (**2**) and EPO (60-97) (**3**) were prepared in good overall yields. In this manner, the previously troublesome Asn⁸³-glycosylated fragment was reengineered so that the consensus carbohydrate domain was placed at a distance from the terminus involved in the required ligations.

Having accomplished the syntheses of pre-EPO (29-124) fragments **2** to **4**, we proceeded toward their assembly. We began by extending glycopeptide **S7** to create the EPO (98-166) domain, which upon Thz deprotection afforded N-terminal ligation partner **5** (Fig. 3). Subsequent ligation between **5** and **3** (bearing a C-terminal lysine thioester donor at position 97) proceeded smoothly. This coupling was followed again by

Thz deprotection to provide **6**, encompassing amino acids 60-166 of our projected EPO glycoprotein. Glycopeptide **6** showed much-improved reactivity in the ligation with EPO (29-59) domain (**2**) and afforded the corresponding ligation product **7** in excellent conversion (85%). These observations indicate that the large carbohydrate domain may block ligation because of sheer steric bulk. Alternatively, it may alter the conformation in the N-terminal region of **S8** in such a fashion as to hide its crucial Cys⁷⁹ ligation machinery. These results further underscore the synthetic challenges associated with the preparation of glycopeptides incorporating multiple complex-type oligosaccharides and suggest opportunities in retrosynthetic analysis for building multifaceted biologics in the laboratory.

What we perceived as the final step in the synthesis would be the only NCL that would actually result in a surviving cysteine residue. For this to be possible, it was first necessary to achieve four concurrent MFD transformations to reveal the required alanines (from their erstwhile cysteine precursors) before exposing the prospective surviving cysteines at positions 29, 33, and 161 in the large 29-166 subunit. This task was accomplished as shown in Fig. 3 (8). After smooth cleavage of the Ac₂O-protecting groups at cysteines 29, 33, and 161 using silver acetate (AgOAc) (**9**) (27), the stage for the final ligation was in place. Fortunately, the projected NCL was smoothly accomplished (~80 to 85% conversion), thereby providing **10**, the tetrahydro (unfolded) precursor of **1** (28, 29).

Compound **10** exhibited enhanced stability relative to its glycotruncated counterpart **11** (the unfolded tetrahydro version of **S3**; Fig. 3, inset). For instance, NCL-generated **10** survived lyophilization of solvent, whereas under comparable treatment, at least in our hands, **11** suffered con-

siderable aggregation during the lyophilization and thus required resolubilization before folding. However, even in the case of **10**, storage caused attrition of the material. Hence we proceeded rapidly to its twofold oxidation/folding in a dialysis cassette using cysteine/cystine as the redox shuffling agent (30). After gradual dilution of the folding buffer (25), **10** was successfully converted to the long-pursued **1**. That success had been achieved was first indicated by the circular dichroism (CD) criterion (Fig. 4A) (31, 32) and was further supported by the remarkable erythropoietic activity of **1** as judged by *in vitro* and *in vivo* assays. Formulated recombinant EPO (Procrit) was used as the standard in these experiments. This recombinant version of EPO has only 165 amino acids as compared with our synthesized human EPO, which has an additional C-terminal Arg known to be cleaved by the Golgi complex in recombinant EPO produced in mammalian cells (33).

As seen in Fig. 4C, the activities of **1** and Procrit track remarkably closely in their effects on the proliferation of TF-1 cells. The *in vivo* comparison of the effect on **1** and Procrit on the peripheral blood reticulocyte numbers in mice (Fig. 4D) was equally heartening. The initial burst of activity of fully synthetic **1** was ~70% that of Procrit when clinically relevant doses were used (supplementary materials). Further confidence that we indeed generated homogeneous polyglycopolypeptides arose from comparison of the electrophoretic mobility of commercial rhEPO- α (expressed in CHO cells), compound **1**, compound **S3**, and compound **9** under reducing conditions [SDS-polyacrylamide gel electrophoresis (SDS-PAGE); compare bandwidths in Fig. 4B].

At least for now, we propose the descriptor EPO(S)1 as a name for this homogeneous, wild-type, biocompetent EPO (**1**). We emphasize, however,

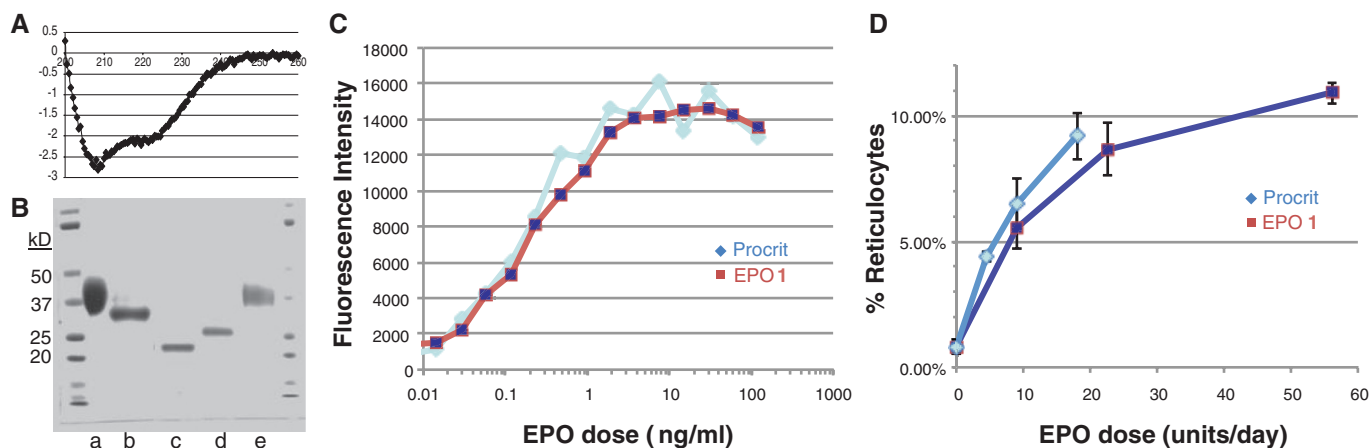


Fig. 4. Functional characterization of **1.** (A) CD spectrum of EPO(S)1 (**1**). (B) SDS-PAGE conducted on two separate gels (**1**, lanes a and b; **2**, lanes c, d, and e) both using rEPO α (EMD) as control (lanes a and e). Lane b: EPO(S)1 (**1**); Lane c: EPO glycoform **S3**; Lane d: EPO (29-166) (**9**). (C) *In vitro* assay of the effect of Procrit and EPO(S)1 (**1**) on the proliferation of TF-1 cells. The results are expressed as average relative fluorescent intensity \pm SD, run in triplicate. Relative fluorescent intensity = fluorescent intensity of EPO-treated TF-1 cells/maximal fluorescent intensity of 10 ng/ml Procrit-EPO-treated TF-1 cells.

(D) Effect of Procrit and EPO(S)1 (**1**) on peripheral blood reticulocyte numbers *in vivo*. C57 mice (three mice per group) were subcutaneously injected with 100 μ l of saline containing 1 mg/ml bovine serum albumin and various doses of EPO daily for 3 days. After 24 hours since the last injection, peripheral blood from each mouse was harvested and stained with reticulocyte stain reagent, and reticulocytes per 200 red blood cells were counted under a microscope with a 100 \times objective lens. The results are expressed as the average \pm SD, $n = 3$ mice.

that the particular rendering of folded EPO **1**, shown in Fig. 4, is provided for convenience solely by analogy with a reported structure of a tri-Lys24,38,83-mutated EPO aglycone bound to the EPO receptor (34).

The ability to reach a molecule of the complexity of **1** by entirely chemical means provides convincing testimony about the growing power of organic synthesis. As a result of synergistic contributions from many laboratories, the aspirations of synthesis may now include, with some degree of realism, structures hitherto referred to as “biologics”—a term used to suggest accessibility only by biological means (isolation from plants, fungi, soil samples, corals, or microorganisms, or by recombinant expression). Formidable as these methods are for the discovery, development, and manufacturing of biologics, one can foresee increasing needs and opportunities for chemical synthesis to provide the first samples of homogeneous biologics. As to production, the experiments described above must be seen as very early days. In no way do we mean to suggest that chemical synthesis is competitive with biologic-type methods to produce EPO, if product homogeneity is not of concern. However, one can well imagine that with continuing improvements in the practicality of solid-phase peptide synthesis (35, 36), new ligation methods, the operational handling of synthetic polypeptides, and enzymatic means of oligosaccharide assembly, synthesis is likely to be of growing value, even in terrains currently described as strictly biologic (39).

References and Notes

- S. Elliott, M. A. Foote, G. Molinieux, *Erythropoietins, Erythropoietic Factors, and Erythropoiesis* (Birkhäuser, Basel, Switzerland, ed. 2, 2009).
- A. J. Sytkowski, *Erythropoietin* (Wiley-VCH, Weinheim, Germany, 2004).
- R. S. Rush *et al.*, *Anal. Chem.* **67**, 1442–1452 (1995).
- P. Wang *et al.*, *Angew. Chem. Int. Ed.* **51**, 11576–11584 (2012).
- R. M. Wilson, S. Dong, P. Wang, S. J. Danishefsky, *Angew. Chem. Int. Ed.* **52**, 7646–7665 (2013).
- During the course of these investigations, ongoing studies from other laboratories provided striking results in reaching congeners of various sorts with promising erythropoietic activity. This work is summarized in (5) and includes references (31, 37, 38).
- B. Wu *et al.*, *Tetrahedron Lett.* **47**, 5577–5579 (2006).
- B. Wu *et al.*, *Tetrahedron Lett.* **47**, 8009–8011 (2006).
- S. J. Danishefsky, M. T. Bilodeau, *Angew. Chem. Int. Ed. Engl.* **35**, 1380–1419 (1996).
- S. J. Danishefsky, J. R. Allen, *Angew. Chem. Int. Ed.* **39**, 836–863 (2000).
- J. B. Schwarz *et al.*, *J. Am. Chem. Soc.* **121**, 2662–2673 (1999).
- There are over 50 glycoforms of recombinant EPO containing combinations of bi-, tri-, and tetraantennary carbohydrate domains, which have not been separated or fully characterized [see (13)].
- H. Sasaki, B. Bothner, A. Dell, M. Fukuda, *J. Biol. Chem.* **262**, 12059–12076 (1987).
- M. Takeuchi, A. Kobata, *Glycobiology* **1**, 337–346 (1991).
- S. R. Hamilton *et al.*, *Science* **313**, 1441–1443 (2006).
- J. H. Nett *et al.*, *J. Biotechnol.* **157**, 198–206 (2012).
- P. E. Dawson, T. W. Muir, I. Clark-Lewis, S. B. Kent, *Science* **266**, 776–779 (1994).
- Q. Wan, S. J. Danishefsky, *Angew. Chem. Int. Ed.* **46**, 9248–9252 (2007).
- L. Z. Yan, P. E. Dawson, *J. Am. Chem. Soc.* **123**, 526–533 (2001).
- J. D. Warren, J. S. Miller, S. J. Keding, S. J. Danishefsky, *J. Am. Chem. Soc.* **126**, 6576–6578 (2004).
- G. Chen *et al.*, *J. Am. Chem. Soc.* **128**, 7460–7462 (2006).
- S. Dong, S. Shang, Z. Tan, S. J. Danishefsky, *Isr. J. Chem.* **51**, 968–976 (2011).
- P. Wang, B. Aussedat, Y. Vohra, S. J. Danishefsky, *Angew. Chem. Int. Ed.* **51**, 11571–11575 (2012).
- V. Ullmann *et al.*, *Angew. Chem. Int. Ed.* **51**, 11566–11570 (2012).
- D. Bang, S. B. Kent, *Angew. Chem. Int. Ed.* **43**, 2534–2538 (2004).
- S. Sakakibara, *Biopolymers* **37**, 17–28 (1995).
- S. Liu, B. L. Pentelute, S. B. Kent, *Angew. Chem. Int. Ed.* **51**, 993–999 (2012).
- The mass spectrum of **10** (figs. S24 and S25) is supportive of the assignment. However, as is the case with previous attempts at obtaining high-quality readouts from extensively glycosylated polysialic acid-containing domains, this attempt has not been fully successful.
- E. Llop, R. Gutiérrez-Gallego, J. Segura, J. Mallorquí, J. A. Pascual, *Anal. Biochem.* **383**, 243–254 (2008).
- V. P. Saxena, D. B. Wetlaufer, *Biochemistry* **9**, 5015–5023 (1970).
- G. G. Kochendoerfer *et al.*, *Science* **299**, 884–887 (2003).
- L. O. Narhi *et al.*, *Protein Eng.* **14**, 135–140 (2001).
- M. A. Recny, H. A. Scoble, Y. Kim, *J. Biol. Chem.* **262**, 17156–17163 (1987).
- R. S. Syed *et al.*, *Nature* **395**, 511–516 (1998).
- R. B. Merrifield, *J. Am. Chem. Soc.* **85**, 2149–2154 (1963).
- T. Wang, S. J. Danishefsky, *Proc. Natl. Acad. Sci. U.S.A.* **110**, 11708–11713 (2013).
- K. Hirano, D. Macmillan, K. Tezuka, T. Tsuji, Y. Kajihara, *Angew. Chem. Int. Ed. Engl.* **48**, 9557–9560 (2009).
- M. Murakami, R. Okamoto, M. Izumi, Y. Kajihara, *Angew. Chem. Int. Ed. Engl.* **51**, 3567–3572 (2012).
- Information on materials and methods, including spectroscopic data of new compounds, is available on Science Online.

Acknowledgments: The authors are grateful for support from the National Institutes of Health (grant HL025848), for spectroscopic assistance from G. Sukenick and H. Fang of the Sloan-Kettering Institute’s nuclear magnetic resonance core facility, and to L. Wilson and L. Ambrosini Vadola for preparation of the manuscript. We also thank M. Luo and H. Guo for their assistance on gel electrophoresis and Y. Xia for helpful discussions regarding mass spectroscopy.

Supplementary Materials

www.sciencemag.org/content/342/6164/1357/suppl/DC1
Materials and Methods
Figs. S1 to S27
References (40–42)

23 August 2013; accepted 23 October 2013
10.1126/science.1245095

The Missing Mountain Water: Slower Westerlies Decrease Orographic Enhancement in the Pacific Northwest USA

C. H. Luce,^{1*} J. T. Abatzoglou,² Z. A. Holden³

Trends in streamflow timing and volume in the Pacific Northwest United States have been attributed to increased temperatures, because trends in precipitation at lower-elevation stations were negligible. We demonstrate that observed streamflow declines are probably associated with declines in mountain precipitation, revealing previously unexplored differential trends. Lower-troposphere winter (November to March) westerlies are strongly correlated with high-elevation precipitation but weakly correlated with low-elevation precipitation. Decreases in lower-tropospheric winter westerlies across the region from 1950 to 2012 are hypothesized to have reduced orographic precipitation enhancement, yielding differential trends in precipitation across elevations and contributing to the decline in annual streamflow. Climate projections show weakened lower-troposphere zonal flow across the region under enhanced greenhouse forcing, highlighting an additional stressor that is relevant for climate change impacts on hydrology.

Despite the importance of mountains as sources of water and the conservation of biodiversity, particularly in a changing climate, our understanding of climate change in

them is limited because of sparse observational data and difficult modeling conditions (1). Although the consequences of increased temperature for mountain snow are relatively well understood and

severe (2–4), poor information about both historical and projected changes in mountain precipitation may lead to substantial misjudgment of risks and maladaptation. In particular, ecosystems and water supplies may be more sensitive to declines in precipitation than to increases in temperature (5–7).

We synthesized across multiple data sources to infer substantial historical declines in precipitation in the Cascades and Northern Rockies of the Pacific Northwest (PNW) United States and linked them to observed changes in atmospheric circulation. These historical declines contradict published assessments that there have probably been no significant declines in PNW precipitation over the past 60 years (4, 8, 9). The information basis for the lack of historical decline is the estimation of trends from the U.S. Historical Climate Network (HCN) precipitation stations in the PNW

¹U.S. Forest Service Research and Development, 322 East Front Street, Boise, ID 83702, USA. ²Department of Geography, University of Idaho, 875 Perimeter Drive, Moscow, ID 83844, USA. ³U.S. Forest Service Region 1, 200 East Broadway Street, Missoula, MT 59807, USA.

*Corresponding author. E-mail: cluce@fs.fed.us

showing mostly nonsignificant declines in precipitation over the region from 1948 to 2006 (Fig. 1). In contrast, annual (by water year) streamflows from relatively undisturbed watersheds in the PNW have shown marked declines (10–12).

One hypothesis for the cause of declining trends in streamflow is increased evapotranspiration (ET). Because very few of the HCN precipitation stations fall within the watersheds where streamflow was measured (Fig. 1), direct assessment of the water balance through comparison of precipitation and streamflow in the basins would have substantial uncertainty. However, the energy balance provides an important limiting condition.

Closure of the energy balance in a warming environment requires that increases in ET not exceed increased external energy input (such as downwelling longwave radiation). This sets an upper limit on ET, forming a robust test of whether ET could explain flow trends. Trends in downwelling longwave and shortwave radiation from NCEP/NCAR (National Centers for Environmental Prediction/National Center for Atmospheric Research) Reanalysis 1 over the region do not have a significant trend, although the global average increase in radiative forcing over the late 20th century is $\sim 1.6 \text{ W/m}^2$ (confidence range 0.6 to 2.4 W/m^2) (1). The decline in flow per unit of area of watershed multiplied by the latent heat of vaporization gives an estimate of the energy cost if all streamflow losses are assumed to result from ET (averaged here across the entire year). In all but the driest basins, the energy requirement to explain the observed historical trend in the 25th-percentile flows exceeds the increase in downwelling long-

wave radiation (fig. S2), in some cases by an order of magnitude. We can further augment the available energy by considering increases in net radiation due to earlier snowmelt (earlier loss in albedo), but would still see only a marginal increase of $\sim 2.9 \text{ W/m}^2$ for the annual average per week of advance (supplementary materials), which would still not explain the magnitude of observed streamflow changes.

The disparity between declining streamflows that cannot be explained by ET and insignificant trends at precipitation stations presents an important but previously unrecognized paradox. Stream gauges integrate precipitation across elevation gradients in mountain basins, whereas HCN precipitation stations primarily sample low elevations (Fig. 1 and fig. S3). The substantial declines in annual flow thus imply differential trends in high- and low-elevation precipitation.

Orographic enhancement of precipitation is a primary driver of the geographic distribution of precipitation across the PNW and other mountainous regions (13). A majority of the precipitation received in the PNW occurs during October to April, when a progressive storm track and embedded cyclones advect moist and stably stratified air masses toward mountain barriers, thereby providing conditions conducive to upslope precipitation enhancement. To underscore the broad importance of orographic precipitation enhancement in the region, the average annual precipitation from the HCN is 712 mm, whereas the average annual streamflow at the 43 gauges (which do not account for ET) is 1063 mm.

A fundamental dynamic driver of orographic enhancement is the lower-tropospheric wind speed

normal to a mountain barrier (14–17), which has been shown to explain a substantial proportion of interstorm and interannual variability in orographic enhancement (18–22). Westerly lower-tropospheric flow is hypothesized to modulate orographic precipitation enhancement, because major mountain ranges of the PNW are broadly N-S oriented. Correlations between regionally averaged (42.5° to 47.5°N , 115° to 130°W) November–March lower-tropospheric westerly wind speeds at 700 hPa (u700) and November–March precipitation at higher-elevation Snowpack Telemetry (SNOTEL) stations was stronger than at lower-elevation HCN stations (Fig. 2 and fig. S6). Orographic precipitation enhancement is strongest on the windward sides of mountain barriers and a short distance leeward of the crest. Blocking, a phenomenon in which some air stagnates near the base of steep mountain barriers, can extend the mountain front influence upwind (23). These same patterns are visible in correlations between precipitation and u700 in transects across the region (Fig. 2). At a regional scale, orographic precipitation enhancement is not strictly elevation-related; rather, the effect is related to proximity to strong elevation gradients. Some stations of the HCN network sample “low-elevation” areas with orographic precipitation enhancement, although few have strong correlations (fig. S6), and the great majority of HCN stations are not in places that are usually associated with orographic enhancement. Correlations between annual streamflow and u700 are about the same strength as in the SNOTEL data (fig. S6).

u700 declined over the period from 1950 to 2012 (Fig. 3), with a more pronounced trend in lower extremes (0.3 m/s/decade , $P = 0.015$) than the mean (0.2 m/s/decade , $P = 0.034$), similar in pattern to streamflow trends. Others have also reported declines in u700 over this period in other regions (24, 25). A portion of the interannual variability in u700 is linearly correlated with large-scale modes of climate variability realized through the El Niño–Southern Oscillation [correlation coefficient (r^2) = 0.28, $P < 0.001$], the Pacific Decadal Oscillation ($r^2 = 0.33$, $P < 0.001$), and the Pacific North American pattern ($r^2 = 0.3$, $P < 0.001$). Together they explain some ($r^2 = 0.37$, $P < 0.001$) but not a majority of the interannual variability, and decreases in u700 persist when the influence of these climate modes is linearly removed (fig. S4). This supports an argument that factors exogenous to primary modes of internal climate variability may be associated with observed u700 decreases.

Changes in u700 might be expected with differential warming rates associated with latitude and land-ocean contrasts through their effect on midlatitude meridional thermal gradients (MTGs, the N-S gradient in temperature) (26). Historically, interannual variations in u700 over the PNW have been associated with the regional MTG ($r^2 = 0.73$, fig. S8). When 20th-century trends in the Coupled Model Intercomparison Project Phase 5 (CMIP5) were examined, 16 of the 24 models

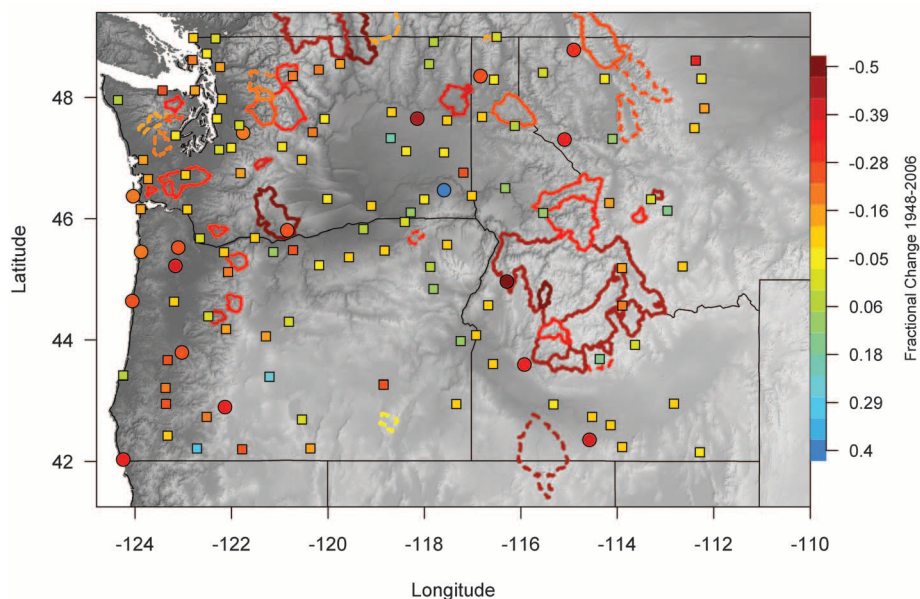


Fig. 1. Location and trends of lower-quartile annual (water-year) precipitation and streamflow at HCN precipitation stations (points) and Hydro-Climatic Data Network streamflow gauges (watershed outlines) from 1948 to 2006. Statistically significant trends are denoted with circles for precipitation and with solid boundaries for streamflow. Squares and dashed boundaries denote non-significant trends.

polled showed a negative trend in u_{700} , with historical radiative forcing having a median trend of -0.2 m/s over the 1950–2005 simulated period (20% of the trend in Fig. 3 and table S1), and comparison of future differences in u_{700} assessed from these models between 2071–2100 and 1950–2005 for experiment RCP8.5 show a small, yet systematic decline during the winter on the order of 0.65 m/s (6.5%) for the region addressed in this study (Fig. 4 and table S1). The regional slowing of the lower-tropospheric westerlies may be partially a consequence of a general relaxation of the regional MTG associated with differential rates of winter warming across the broader region (fig. S9). The average projected change in u_{700} over the 21st century is only slightly greater than the observed decrease, and both represent a substantial decline with respect to the 1950–2005 average (fig. S3). Both the past two decades and projected mean wind speed represent dry conditions for the PNW, with current streamflows being comparable to the 1930s, recognized regionally as one of the driest periods in the past few centuries [(27–29) and supplementary materials].

The slopes of the regressions between SNOTEL precipitation and u_{700} were on the order of 10 to 15% of precipitation per unit (1 m/s) of change in u_{700} (fig. S6) and broadly show the same geographic pattern as the correlations (fig. S5). Decline in the mean u_{700} over the period was about 1 m/s, and these slopes are comparable to the average decline in mean streamflow of 16% over the period (10). Some of the difference between observed and modeled decline may be due to changes in atmospheric moisture fluxes related to water vapor content changes that also contribute to orographic precipitation enhancement (30). Long-term changes in moisture availability and temperature are likely to modulate the influence of wind changes on orographic precipitation enhancement, but the mechanisms are varied and complex and rely on assumptions about upwind boundary conditions and cloud microphysics, making projections uncertain and requiring more complex modeling efforts (17, 31).

The topography used by global circulation models (GCMs) substantially flattens even the largest mountain ranges, minimizing their influence on air masses and precipitation. Although GCMs capture the effects of the broadening Hadley cell and poleward movement of midlatitude storm tracks, yielding general agreement on decreased precipitation and streamflow in the southwestern U.S. (32), the effects of decreased midlatitude westerly wind speeds on orographic precipitation have not been accounted for in mountainous regions. Regional climate models (RCMs) that better resolve mountain ranges could conceptually help frame expectations regarding orographic precipitation (33). However, parameterizations of fine-scale processes still require tuning to empirical observations, and information about high-elevation precipitation trends implicit in streamflow data may assist with calibration.

Better precipitation projections for mountainous areas are critical because of (i) their importance for the conservation of biodiversity in a changing climate, and (ii) their importance as a water supply for downstream agriculture, industry, energy, and municipal use. Although mountains may serve as refugia for cold-adapted species and reservoirs for late-season runoff, decreases in high-elevation precipitation combined with warming temperatures and shifts in precipitation phases could have profound consequences for the ecohydrology of mountain ecosystems. Decreases in precipitation, particularly in the driest years, increase the risk of forest fires and may pose a greater risk than temperature increases (5), although more broadly combined drying and warming are most detrimental (34). Cold-water aquatic species faced with warm-

ing stream temperatures will seek higher elevations and smaller tributary streams (35) but may find less habitat there as headwater streamflows decrease.

Previous studies have attributed changes in streamflow timing, spring onset, and snowpack to warming temperatures (2, 4, 36). Our findings suggest that an additional mechanism—decreased orographic precipitation enhancement associated with decreases in zonal winds—may also have contributed to observed trends. The lack of concordance between the traditionally used HCN network and either higher-elevation SNOTEL stations or streamflow measurements should place an important caveat on the assumption that circulation and precipitation have been unaffected in this region, particularly in the mountains, where most precipitation falls.

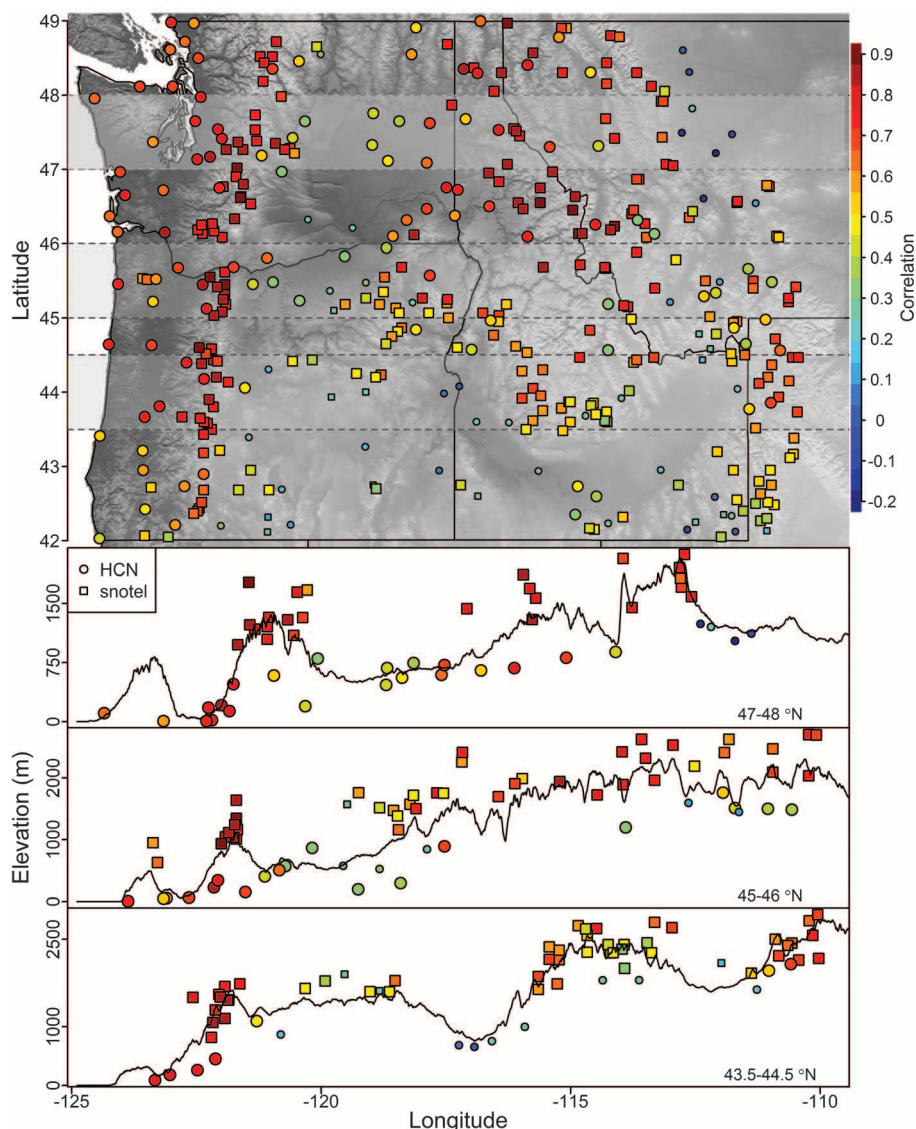


Fig. 2. Correlation of 1982–2012 November to March HCN (circles) and SNOTEL (squares) precipitation with November to March u_{700} zonal winds over 42.5° to 47.5° N and 115° to 130° W. Three longitudinal transects (lower panels) show examples of the pattern of correlations with elevation. The larger symbols indicate statistical significance ($P < 10\%$).

Improved understanding of the relative roles of temperature and precipitation on snowpack storage and runoff timing is critical for climate change adaptation. One of the recommendations for adaptation to earlier snowmelt is to increase the storage capacity in reservoirs to replace snowpack storage; however, in circumstances of declining precipitation, this could be maladaptive. For instance, reductions in snowpack storage driven by reduced precipitation would also result in earlier streamflow timing (5, 10). In such a case, a dam would represent another consumptive use of water, and the water rights necessary to fill the dam may not be available in the driest and consequently “earliest” years.

The lack of long-term precipitation data from mountains severely limits our understanding of historical trends and the empirical framework needed for understanding impacts of climate variability and change. The analyses here further highlight the importance of historical streamflow and wind data and suggest that they could be used to extend high-elevation precipitation records to earlier periods or enhance existing gridded historical climatological data sets. Interannual variability in orographic enhancement is partially captured by the SNOTEL network, dating to the 1980s. However, reliance on time-invariant orographic precipitation ratios for earlier

historical analyses may lead to errors in interpreting trends, because the differential changes in low-elevation and high-elevation precipitation are not reflected.

Prediction of orographic precipitation effects in a changing climate has been acknowledged as a difficult task that depends on a number of assumptions (17, 31, 37). The analysis of disparate streamflow and precipitation records in this region, encompassing much of the headwaters of the Snake and Columbia River basins, highlights a change of substantial magnitude with considerable ecological and economic consequences that has heretofore been ignored or dismissed. At the same time, we note new utility for streamflow data and a potential approach for the assessment of orographic precipitation changes related to increased radiative forcing using macroscale wind information.

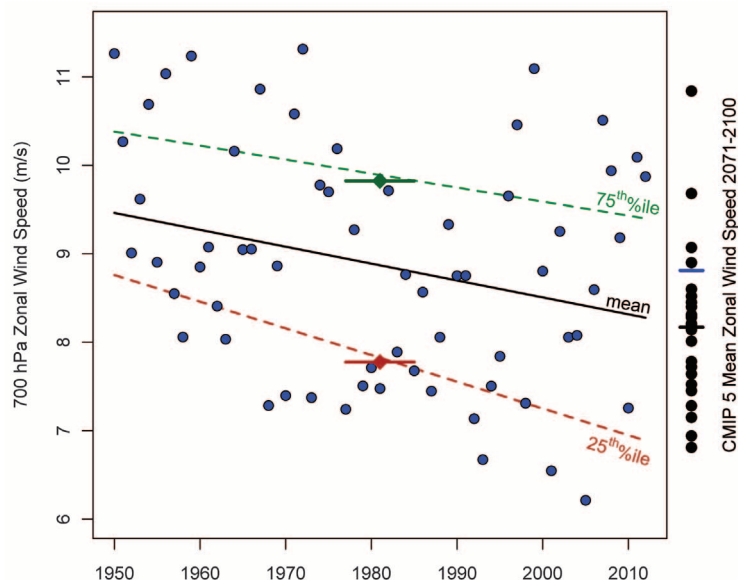
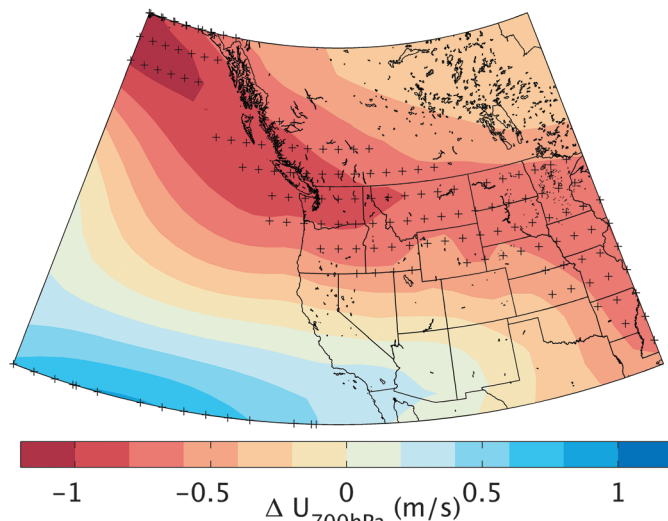


Fig. 3. Upper-quartile (green), lower-quartile (red), and mean (black) trends in November to March u700 zonal winds averaged over 42.5° to 47.5°N and 115° to 130°W. Only the mean and lower-quartile trends are significant ($P = 0.03$ and 0.02 , respectively). Also shown with a diamond and bar centered on 1981 are the unconditional quartiles. CMIP5 projections for future wind speeds were calculated from modeled changes between 1950–2005 and 2071–2100 added to the observed 1950–2005 mean (blue bar on right). Estimates for each model are shown as black dots on the right. The mean projection is shown with a black bar.

Fig. 4. Projected changes in November to March u700 zonal wind averaged across 24 CMIP5 models, 2071–2100 versus 1971–2000 RCP8.5. Plus signs denote areas where >80% of the models agree on the sign of the change. 20 of the 24 models predict a decrease in the PNW.



References and Notes

1. S. Solomon *et al.*, Eds., *Climate Change 2007: The Physical Science Basis. Contribution of Working Group I to the Fourth Assessment, Report of the Intergovernmental Panel on Climate Change* (Cambridge Univ. Press, Cambridge, 2007).
2. P. C. D. Milly *et al.*, *Science* **319**, 573–574 (2008).
3. R. F. Service, *Science* **303**, 1124–1127 (2004).
4. P. W. Mote, A. F. Hamlet, M. P. Clark, D. P. Lettenmaier, *Bull. Am. Meteorol. Soc.* **86**, 39–49 (2005).
5. Z. A. Holden, C. H. Luce, M. A. Crimmins, P. Morgan, *Ecohydrology* **5**, 677–684 (2012).
6. A. E. Cahill *et al.*, *Proc. Biol. Sci.* **280**, 20121890 (2013).
7. S. M. Crimmins, S. Z. Dobrowski, J. A. Greenberg, J. T. Abatzoglou, A. R. Mynsberge, *Science* **331**, 324–327 (2011).
8. T. P. Barnett *et al.*, *Science* **319**, 1080–1083 (2008).
9. S. Regonda, B. Rajagopalan, M. Clark, J. Pitlick, *J. Clim.* **18**, 372–384 (2005).
10. C. H. Luce, Z. A. Holden, *Geophys. Res. Lett.* **36**, L16401 (2009).
11. G. Fu, M. Barber, S. Chen, *Hydrol. Processes* **24**, 866–878 (2010).
12. G. M. Clark, *J. Am. Water Resour. Assoc.* **46**, 486–497 (2010).
13. C. Daly, R. P. Neilson, D. L. Phillips, *J. Appl. Meteorol.* **33**, 140–150 (1994).
14. R. B. Smith, I. Barstad, *J. Atmos. Sci.* **61**, 1377–1391 (2004).
15. B. A. Colle, *J. Atmos. Sci.* **61**, 588–606 (2004).
16. R. B. Smith, in *Advances in Geophysics*, B. Saltzman, Ed. (Academic Press, New York, 1979), vol. 21, pp. 87–230.
17. R. A. Houze Jr., *Rev. Geophys.* **50**, RG1001 (2012).
18. L. Panziera, U. Germann, *Q. J. R. Meteorol. Soc.* **136**, 222–238 (2010).
19. S. E. Yuter, D. A. Stark, J. A. Crouch, M. J. Payne, B. A. Colle, *J. Hydrometeorol.* **12**, 329–351 (2011).
20. M. D. Dettinger, K. T. Redmond, D. R. Cayan, *J. Hydrometeorol.* **5**, 1102–1116 (2004).
21. N. Siler, G. Roe, D. Durran, *J. Hydrometeorol.* **14**, 122–139 (2013).
22. T. P. Burt, N. J. K. Howden, *Water Resour. Res.* **49**, 3504–3515 (2013).
23. M. Hughes, A. Hall, R. G. Fovell, *J. Atmos. Sci.* **66**, 508–518 (2009).
24. Y. Jiang, Y. Luo, Z. Zhao, S. Tao, *Theor. Appl. Climatol.* **99**, 421–430 (2010).
25. T. R. McVicar *et al.*, *Geophys. Res. Lett.* **37**, L06402 (2010).
26. K. Braganza *et al.*, *Clim. Dyn.* **22**, 823–838 (2004).
27. E. R. Cook, C. A. Woodhouse, C. M. Eakin, D. M. Meko, D. W. Stahle, *Science* **306**, 1015–1018 (2004).

28. Z. Gedalof, D. L. Peterson, N. J. Mantua, *J. Am. Water Resour. Assoc.* **40**, 1579–1592 (2004).
29. E. R. Lutz, A. F. Hamlet, J. S. Littell, *Water Resour. Res.* **48**, W01525 (2012).
30. F. M. Ralph *et al.*, *Geophys. Res. Lett.* **33**, L13801 (2006).
31. P. A. O'Gorman, C. J. Muller, *Environ. Res. Lett.* **5**, 025207 (2010).
32. P. C. D. Milly, K. A. Dunne, A. V. Vecchia, *Nature* **438**, 347–350 (2005).
33. E. P. Salathé Jr., L. R. Leung, Y. Qian, Y. Zhang, *Clim. Change* **102**, 51–75 (2010).
34. D. D. Breshears *et al.*, *Proc. Natl. Acad. Sci. U.S.A.* **102**, 15144–15148 (2005).
35. S. J. Wenger *et al.*, *Proc. Natl. Acad. Sci. U.S.A.* **108**, 14175–14180 (2011).
36. G. T. Pederson, J. L. Betancourt, G. J. McCabe, *Geophys. Res. Lett.* **40**, 1811–1816 (2013).
37. J. R. Minder, *J. Clim.* **23**, 2634–2650 (2010).

Acknowledgments: We acknowledge the World Climate Research Programme's Working Group on Coupled Modelling, which is responsible for CMIP, and we thank the climate modeling groups (listed in table S1 of this paper) for producing and making available their model output. The U.S. Department of Energy's Program for Climate Model Diagnosis and Intercomparison provides coordinating support for CMIP and led the development of software infrastructure in partnership with the Global Organization for Earth System Science Portals. We thank the reviewers for their comments and insights, which substantially improved the paper. J.T.A.

was supported by NSF's Experimental Program to Stimulate Competitive Research (EPSCoR) (EPS-0814387). This work was partially supported by NASA through NNH11ZDA001N-FIRES.

Supplementary Materials

www.sciencemag.org/content/342/6164/1360/suppl/DC1
Materials and Methods
Supplementary Text
Figs. S1 to S9
Tables S1 and S2
References (38–60)

24 June 2013; accepted 8 November 2013
10.1126/science.1242335

Long-Term Dynamics of Adaptation in Asexual Populations

Michael J. Wiser,^{1,2} Noah Ribeck,^{1,3} Richard E. Lenski^{1,2,3*}

Experimental studies of evolution have increased greatly in number in recent years, stimulated by the growing power of genomic tools. However, organismal fitness remains the ultimate metric for interpreting these experiments, and the dynamics of fitness remain poorly understood over long time scales. Here, we examine fitness trajectories for 12 *Escherichia coli* populations during 50,000 generations. Mean fitness appears to increase without bound, consistent with a power law. We also derive this power-law relation theoretically by incorporating clonal interference and diminishing-returns epistasis into a dynamical model of changes in mean fitness over time.

The dynamics of evolving populations are often discussed in terms of movement on an adaptive landscape, where peaks and valleys are states of high and low fitness, respectively. There is considerable interest in the structure of these landscapes (1–7). Recent decades have seen tremendous growth in experiments using microbes to address fundamental questions about evolution (8), but most have been short in duration. The Long-Term Evolution Experiment (LTEE) with *Escherichia coli* provides the opportunity to characterize the dynamics of adaptive evolution over long periods under constant conditions (1, 9, 10). Twelve populations were founded from a common ancestor in 1988 and have been evolving for >50,000 generations, with samples frozen every 500 generations. The frozen bacteria remain viable, and we use this “fossil record” to assess whether fitness continues to increase and to characterize mean fitness trajectories (11).

We first performed 108 competitions, in the same conditions as the LTEE, between samples from nine populations at 40,000 and 50,000 generations against marked 40,000-generation clones (11). Three populations were excluded for technical reasons (11). Fitness was quantified as the dimensionless ratio of the competitors' realized

growth rates. Most populations experienced significant improvement (Fig. 1A), and the grand mean fitness increased by 3.0% (Fig. 1B).

To examine the shape of the fitness trajectory, we competed samples from all 12 populations and up to 41 time points against the ancestor (11). We compared the fit of two alternative models with the fitness trajectories. The hyperbolic model describes a decelerating trajectory with an asymptote. The power law also decelerates (provided the exponent is <1), but fitness has no upper limit.

Hyperbolic model

$$\bar{w} = 1 + at/(t + b)$$

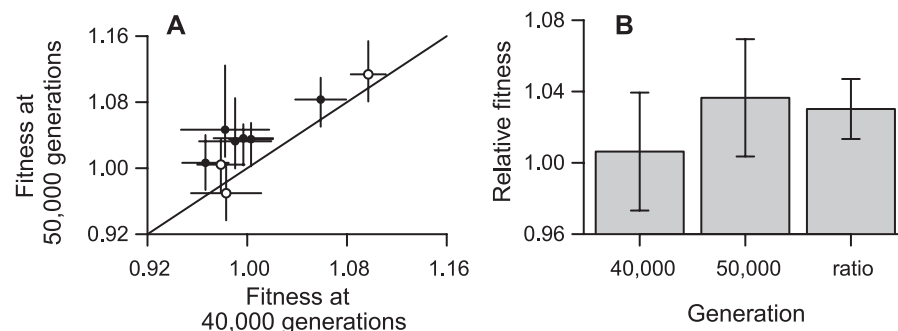


Fig. 1. Fitness changes in nine *E. coli* populations between 40,000 and 50,000 generations. (A) Filled symbols: six populations whose improvement was significant ($P < 0.05$); open symbols: three populations without significant improvement. **(B)** Grand-mean fitness at 40,000 and 50,000 generations relative to 40,000-generation competitor and the ratio of means showing overall gain. Error bars are 95% confidence limits based on replicate assays (A) or populations (B).

¹BEACON Center for the Study of Evolution in Action, Michigan State University, East Lansing, MI 48824, USA. ²Department of Zoology, Michigan State University, East Lansing, MI 48824, USA. ³Department of Microbiology and Molecular Genetics, Michigan State University, East Lansing, MI 48824, USA.

*Corresponding author. E-mail: lenski@msu.edu

only, the hyperbolic model badly underestimates later measurements, whereas the power-law trajectory predicts them accurately (Fig. 2B and fig. S3).

The power law describes the fitness trajectories well, but it is not explanatory. We have derived a dynamical model of asexual populations with clonal interference and diminishing-returns epistasis, which generates mean-fitness trajectories that agree well with the experimental data. Clonal interference refers to competition among organisms with different beneficial mutations, which impedes their spread in asexual populations (13–16). Diminishing-returns epistasis occurs when the marginal improvement from a beneficial mutation declines with increasing fitness (5, 6). We outline key points of the model below (11).

We used a coarse-grained approach that describes the magnitudes and time scales of fixation events (13). Beneficial mutations of advantage s are exponentially distributed with probability density $\alpha e^{-\alpha s}$, where $1/\alpha$ is the mean advantage. This distribution is for mathematical convenience; the theory of clonal interference is robust to the form of the distribution (13). We assume that deleterious mutations do not appreciably affect the dynamics; deleterious mutations occur at a higher rate than beneficial mutations, but the resulting

load is very small relative to the fitness increase measured over the course of the LTEE (17).

We assume the distribution of available benefits declines after a mutation with advantage $\langle s \rangle$ fixes, such that α increases by a factor linearly related to $\langle s \rangle$:

$$\alpha_{n+1} = \alpha_n(1 + g\langle s_{n+1} \rangle)$$

where $g > 0$ is the diminishing-returns parameter, $\langle s_n \rangle$ is beneficial effect of the n th fixed mutation, and α_n is α after n fixations. Then, the mean fitness of an asexual population adapting to a constant environment is approximated by (11):

$$\bar{w} \approx \left(2g\langle s_1 \rangle e^{g\langle s_1 \rangle} \frac{t}{\langle t_1 \rangle} + 1 \right)^{1/2g}$$

where $\langle s_1 \rangle$ and $\langle t_1 \rangle$ are the beneficial effect and fixation time, respectively, for the first fixed mutation.

Comparing this formula with the power law, $g = 1/2a$. The value of g estimated for the six populations that retained the low ancestral mutation rate throughout 50,000 generations is 6.0 (95% confidence interval 5.3 to 6.9). In the LTEE, the beneficial effect of the first fixation, $\langle s_1 \rangle$, is typically ~ 0.1 (1, 9, 10). It follows that the dis-

tribution of beneficial effects immediately after the first fixation is shifted such that the mean advantage is $1/(1 + g\langle s_1 \rangle) \approx 63\%$ of its initial value (11). This estimate of g also accords well with epistasis observed for early mutations in one of the populations (fig. S4). In principle, g might vary among populations if some fixed mutations lead to regions of the fitness landscape with different epistatic tendencies (18). However, an analysis of variance shows no significant heterogeneity in g among the six populations that maintained the ancestral mutation rate ($P = 0.3478$) (table S3). The g values tend to be lower for several populations that evolved hypermutability (table S4). However, these fits are confounded by the change in mutation rate; we show below that it is not necessary to invoke a difference in diminishing-returns epistasis between the hypermutable populations and those that retained the low ancestral mutation rate.

Diminishing-returns epistasis generates the power-law dynamics through the relation between a and g . Clonal interference affects the dynamics through the parameter b , which depends on $\langle s_1 \rangle$ and $\langle t_1 \rangle$, which in turn are functions of the population size N , beneficial mutation rate μ , and initial mean beneficial effect $1/\alpha_0$ (11). For the LTEE, $N = 3.3 \times 10^7$, which takes into account the daily dilutions and regrowth (1). However, μ and α_0 are unknown. Pairs of values that all match the best fit to the populations that retained the low mutation rate are shown in Fig. 3A. The expected values for beneficial effects and fixation times across a range of pairs are shown in Fig. 3B. The dynamics are similar among pairs with high beneficial mutation rates ($\mu > 10^{-8}$), giving $\langle s_1 \rangle \approx 0.1$ and $\langle t_1 \rangle \approx 300$ generations for the first fixation, which agree well with observations from the LTEE (1, 9, 10). At lower values of μ , adaptation becomes limited by the supply of beneficial mutations, and fixation times are inconsistent with the LTEE. This model also predicts that the rate of adaptation decelerates more sharply than the rate of genomic evolution (fig. S5), which is qualitatively consistent with observations (10, 11). The model assumes that individual beneficial mutations sweep sequentially, although “cohorts” of beneficial mutations may co-occur, especially at high μ (11, 15, 16, 19). However, the inferred role of diminishing returns in generating population mean-fitness dynamics is unaffected by this complication, because the power-law exponent is independent of μ . Moreover, we have verified by numerical simulations that co-occurring beneficial mutations have no appreciable effect on long-term fitness trajectories over the range of parameters considered here (fig. S6).

Six populations evolved hypermutator phenotypes that increased their point-mutation rates by ~ 100 -fold (11). Three of them became hypermutable early in the LTEE (between ~ 2500 and ~ 8500 generations) and had measurable fitness trajectories through at least 30,000 generations (table S2). Our model predicts these populations should adapt faster than those that retained the

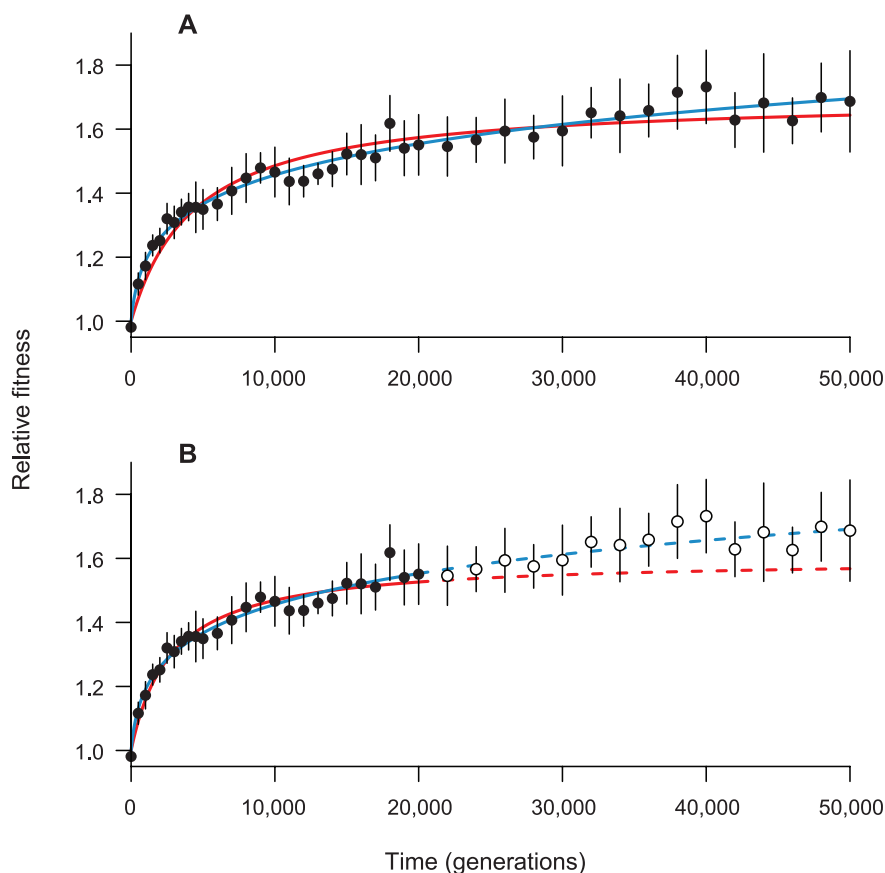


Fig. 2. Comparison of hyperbolic and power-law models. (A) Hyperbolic (red) and power-law (blue) models fit to the set of mean fitness values (black symbols) from all 12 populations. (B) Fit of hyperbolic (solid red) and power-law (solid blue) models to data from first 20,000 generations only (filled symbols), with model predictions (dashed lines) and later data (open symbols). Error bars are 95% confidence limits based on the replicate populations.

ancestral mutation rate. We pooled the data from these early hypermutators and confirmed that their composite fitness trajectory was substantially higher than that of the populations with the low mutation rate (Fig. 4). If the hypermutators' beneficial mutation rate also increased by ~ 100 -fold, the difference in trajectories is best fit by an ancestral rate $\mu = 1.7 \times 10^{-6}$ (95% confidence interval 2.5×10^{-7} to 6.1×10^{-5}), although higher values cannot be ruled out (11). Note that this fit was obtained by using the same initial distribution of fitness effects, α_0 , and epistasis parameter, g , for the hypermutators and the populations that retained the ancestral mutation rate.

Both our empirical and theoretical analyses imply that adaptation can continue for a long time for asexual organisms, even in a constant environment. The 50,000 generations studied here occurred in one scientist's laboratory in ~ 21 years. Now imagine that the experiment continues for 50,000 generations of scientists, each overseeing 50,000 bacterial generations, for 2.5 billion generations total. At that time, the predicted fitness relative to the ancestor is ~ 4.7 based on the power-law parameters estimated from all 12 populations (table S4). The ancestor's doubling time in the glucose-limited minimal medium of the LTEE was ~ 55 min, and its growth commenced after a lag phase of ~ 90 min (20). If the bacteria eliminate the lag, a fitness of 4.7 implies a doubling time of ~ 23 min (fig. S7). Although that is fast for a minimal medium where cells must synthesize most constituents, it is slower than the 10 min that some species can achieve in nutrient-rich media (21). At some distant time, biophysical constraints may come into play, but the power-law fit to the LTEE does not predict implausible growth rates even far into the future. Also, some equilibrium might eventually be reached between the fitness-increasing effects of beneficial mutations and fitness-reducing effects of deleterious mutations (22), although it is impossible to predict when for realistic scenarios with heterogeneous selection coefficients, compensatory mutations, reversions, and changing mutation rates.

Fitness may continue to increase because even very small advantages become important over very long time scales in large populations. Consider a mutation with an advantage $s = 10^{-6}$. The probability that this mutation escapes drift loss is $\sim 4s$ for asexual binary fission (13), so it would typically have to occur 2.5×10^5 times before finally taking hold. Given a mutation rate of 10^{-10} per base pair per generation (23) and effective population size of $\sim 3.3 \times 10^7$, it would require $\sim 10^8$ generations for that mutation to escape drift and millions more to fix. Also, pleiotropy and epistasis might allow a sustained supply of advantageous mutations, because many net-beneficial mutations have maladaptive side effects that create opportunities for compensatory mutations to ameliorate those effects.

The LTEE uses a simple, constant environment to minimize complications and thus illuminates the fundamental dynamics of adaptation by natural selection in asexual populations. The

medium has one limiting resource and supports low population densities (for bacteria) to minimize the potential for cross-feeding on, or inhibition by, secreted by-products. Frequency-dependent interactions are weak in most populations, although stronger in some others (24). Also, such interactions should favor organisms that are more fit than their immediate predecessor, but they are not expected to amplify gains relative to a distant ancestor, as fitness was measured here. In fact, such interactions may cause fitness to fall relative to a distant ancestor (25). In any case, small-effect beneficial mutations should allow fitness to increase far into the future.

At present, the evidence that fitness can increase for tens of thousands of generations in a constant environment is limited to the LTEE, but these findings have broader implications for understanding evolutionary dynamics and the structure of fitness landscapes. It might be worthwhile to examine fitness trajectories from other evolution experiments in light of our results, although data from short-term experiments may not suffice to discriminate between asymptotic and non-asymptotic trajectories. We hope other teams will perform long experiments similar to the LTEE and that theoreticians will refine our models as appropriate.

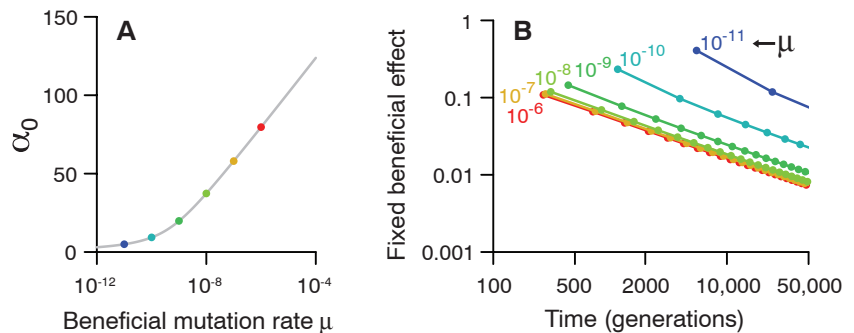


Fig. 3. Theoretical model generating power-law dynamics. (A) Parameter pairs for μ and α_0 that match best fit of power law to fitness trajectories for populations that retained ancestral mutation rate for 50,000 generations. (B) Expected times and beneficial effects of successive fixations for different pairs that match the best fit. The α_0 values corresponding to each μ are shown in (A). In both panels $g = 6.0$, and $N = 3.3 \times 10^7$.

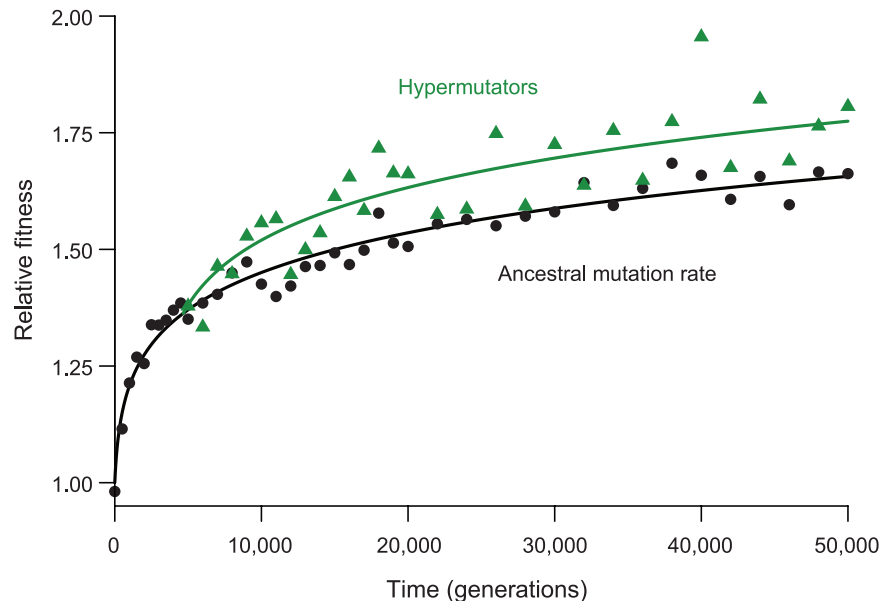


Fig. 4. Effect of hypermutability on observed and predicted fitness trajectories. Black circles: mean fitness of six populations that retained low ancestral mutation rate. Green triangles: mean fitness of three populations that evolved hypermutability early in the LTEE, including one with measurable values through 30,000 generations only. The hypermutators have higher mean fitness at 28 of 31 time points from 5000 to 50,000 generations. Black curve: Predicted trajectory of dynamic model with $\mu = 1.7 \times 10^{-6}$, $\alpha_0 = 85$, $g = 6.0$, and $N = 3.3 \times 10^7$. Green curve: Predicted trajectory with μ increased 100-fold starting at 4667 generations and all other parameters unchanged.

References and Notes

- R. E. Lenski, M. R. Rose, S. C. Simpson, S. C. Tadler, *Am. Nat.* **138**, 1315–1341 (1991).
- C. L. Burch, L. Chao, *Genetics* **151**, 921–927 (1999).
- D. M. Weinreich, N. F. Delaney, M. A. Depristo, D. L. Hartl, *Science* **312**, 111–114 (2006).
- S. Kryazhimskiy, G. Tkačik, J. B. Plotkin, *Proc. Natl. Acad. Sci. U.S.A.* **106**, 18638–18643 (2009).
- H.-H. Chou, H.-C. Chiu, N. F. Delaney, D. Segrè, C. J. Marx, *Science* **332**, 1190–1192 (2011).
- A. I. Khan, D. M. Dinh, D. Schneider, R. E. Lenski, T. F. Cooper, *Science* **332**, 1193–1196 (2011).
- I. G. Szendro, M. F. Schenk, J. Franke, J. Krug, J. A. G. M. de Visser, *J. Stat. Mech.* **2013**, P01005 (2013).
- T. J. Kawecki *et al.*, *Trends Ecol. Evol.* **27**, 547–560 (2012).
- R. E. Lenski, M. Travisano, *Proc. Natl. Acad. Sci. U.S.A.* **91**, 6808–6814 (1994).
- J. E. Barrick *et al.*, *Nature* **461**, 1243–1247 (2009).
- Materials and methods and supplementary text are available as supporting material on Science Online.
- P. Sibani, M. Brandt, P. Alström, *Intl. J. Mod. Phys. B* **12**, 361–391 (1998).
- P. J. Gerrish, R. E. Lenski, *Genetica* **102–103**, 127–144 (1998).
- M. Hegreness, N. Shores, D. Hartl, R. Kishony, *Science* **311**, 1615–1617 (2006).
- S.-C. Park, J. Krug, *Proc. Natl. Acad. Sci. U.S.A.* **104**, 18135–18140 (2007).
- G. I. Lang *et al.*, *Nature* **500**, 571–574 (2013).
- S. Wielgoss *et al.*, *Proc. Natl. Acad. Sci. U.S.A.* **110**, 222–227 (2013).
- R. J. Woods *et al.*, *Science* **331**, 1433–1436 (2011).
- M. M. Desai, D. S. Fisher, A. W. Murray, *Curr. Biol.* **17**, 385–394 (2007).
- F. Vasi, M. Travisano, R. E. Lenski, *Am. Nat.* **144**, 432–456 (1994).
- R. G. Eagon, *J. Bacteriol.* **83**, 736–737 (1962).
- S. Goyal *et al.*, *Genetics* **191**, 1309–1319 (2012).
- S. Wielgoss *et al.*, *G3 (Bethesda)* **1**, 183–186 (2011).
- S. F. Elena, R. E. Lenski, *Evolution* **51**, 1058–1067 (1997).
- C. E. Paquin, J. Adams, *Nature* **306**, 368–370 (1983).

Acknowledgments: This work was supported by grants from the National Science Foundation (DEB-1019989) including the BEACON Center for the Study of Evolution in Action

(DBI-0939454), and by funds from the Hannah Chair Endowment at Michigan State University. We thank three reviewers for comments; I. Dworkin, J. Krug, A. McAdam, C. Wilke, and L. Zaman for discussions; and N. Hajela for technical assistance. R.E.L. will make strains available to qualified recipients, subject to completion of a material transfer agreement that can be found at www.technologies.msu.edu/inventors/mta-cda/mta/mta-forms. Datasets and analysis scripts are available at the Dryad Digital Repository (doi:10.5061/dryad.0hc2m).

Supplementary Materials

www.sciencemag.org/content/342/6164/1364/suppl/DC1
Materials and Methods
Supplementary Text
Figs. S1 to S7
Tables S1 to S4
References (26–40)

17 July 2013; accepted 4 November 2013

Published online 14 November 2013;

10.1126/science.1243357

Exonic Transcription Factor Binding Directs Codon Choice and Affects Protein Evolution

Andrew B. Stergachis,¹ Eric Haugen,¹ Anthony Shafer,¹ Wenqing Fu,¹ Benjamin Vernot,¹ Alex Reynolds,¹ Anthony Raubitschek,^{2,3} Steven Ziegler,³ Emily M. LeProust,^{4*} Joshua M. Akey,¹ John A. Stamatoyannopoulos^{1,5†}

Genomes contain both a genetic code specifying amino acids and a regulatory code specifying transcription factor (TF) recognition sequences. We used genomic deoxyribonuclease I footprinting to map nucleotide resolution TF occupancy across the human exome in 81 diverse cell types. We found that ~15% of human codons are dual-use codons (“duons”) that simultaneously specify both amino acids and TF recognition sites. Duons are highly conserved and have shaped protein evolution, and TF-imposed constraint appears to be a major driver of codon usage bias. Conversely, the regulatory code has been selectively depleted of TFs that recognize stop codons. More than 17% of single-nucleotide variants within duons directly alter TF binding. Pervasive dual encoding of amino acid and regulatory information appears to be a fundamental feature of genome evolution.

The genetic code, common to all organisms, contains extensive redundancy, in which most amino acids can be specified by two to six synonymous codons. The observed ratios of synonymous codons are highly nonrandom, and codon usage biases are fixtures of both prokaryotic and eukaryotic genomes (1). In organisms with short life spans and large effective population sizes, codon biases have been linked to translation efficiency and mRNA stability (2–7). However, these mechanisms explain only a small fraction of observed codon preferences in mam-

malian genomes (7–11), which appear to be under selection (12).

Genomes also contain a parallel regulatory code specifying recognition sequences for transcription factors (TFs) (13), and the genetic and regulatory codes have been assumed to operate independently of one another and to be segregated physically into the coding and noncoding genomic compartments. However, the potential for some coding exons to accommodate transcriptional enhancers or splicing signals has long been recognized (14–18).

To define intersections between the regulatory and genetic codes, we generated nucleotide-resolution maps of TF occupancy in 81 diverse human cell types using genomic deoxyribonuclease I (DNaseI) footprinting (19). Collectively, we defined 11,598,043 distinct 6– to 40–base pair (bp) footprints genome-wide (~1,018,514 per cell type), 216,304 of which localized completely within protein-coding exons (~24,842 per cell type)

(Fig. 1, A and B; fig. S1A; and table S1). Approximately 14% of all human coding bases contact a TF in at least one cell type (average 1.1% per cell type) (Fig. 1C and fig. S1B), and 86.9% of genes contained coding TF footprints (average 33% per cell type) (fig. S1, C and D).

The exonic TF footprints we observed likely underestimate the true fraction of protein-coding bases that contact TFs because (i) TF footprint detection increases substantially with sequencing depth (13), and (ii) the 81 cell types sampled, although extensive, is far from complete; we saw little evidence of saturation of coding TF footprint discovery (fig. S2).

To ascertain coding footprints more completely, we developed an approach for targeted exonic footprinting via solution-phase capture of DNaseI-seq libraries using RNA probes complementary to human exons (19). Targeted capture footprinting of exons from abdominal skin and mammary stromal fibroblasts yielded ~10-fold increases in DNaseI cleavage—equivalent to sequencing >4 billion reads per sample by using conventional genomic footprinting (fig. S3A)—quantitatively exposing many additional TF footprints (fig. S3, B to D). Overall, we identified an average of ~175,000 coding footprints per cell type (fig. S1E), which is 7- to 12-fold more than with conventional footprinting.

Although coding sequences are densely occupied by TFs in vivo, the density of TF footprints at different genic positions varied widely, with many genes exhibiting sharply increased density in the translated portion of their first coding exon (Fig. 1D and fig. S4A). In contrast, internal coding exons were as likely as flanking intronic sequences to harbor TF footprints (Fig. 1D). The total number of coding DNaseI footprints within a gene was related both to the length of the gene and to its expression level (fig. S4, B to D).

Given their abundance, we sought to determine whether exonic TF binding elements were under evolutionary selection. Fourfold degenerate coding bases are frequently used as a model of neutral (or nearly neutral) evolution (20) but

¹Department of Genome Sciences, University of Washington, Seattle, WA 98195, USA. ²Department of Immunology, University of Washington, Seattle, WA 98109, USA. ³Benaroya Research Institute, Seattle, WA 98101, USA. ⁴Agilent Technologies, Santa Clara, CA 95051, USA. ⁵Department of Medicine, University of Washington, Seattle, WA 98195, USA.

*Present address: Twist Bioscience, San Francisco, CA 94158, USA.

†Corresponding author. E-mail: jstam@uw.edu

may exhibit constraint when a functional signal impinges on coding sequence (11). Across the coding compartment, fourfold degenerate bases (4FDBs) within TF footprints show significantly greater evolutionary constraint versus non-footprinted 4FDBs (Fig. 1E and fig. S5, A and B), indicating that TF-DNA recognition constrains the third codon position.

To test for evolutionary constraint at coding footprints in modern human populations, we quan-

tified the age of mutations arising within or outside of coding footprints using exome sequencing data from 4298 individuals of European ancestry (fig. S5C) and 2217 individuals of African American ancestry (fig. S5D) (21). This analysis revealed that mutations within coding footprints were on average 10.2% younger than those outside of footprints (Fig. 1F and fig. S5E), signaling influence of coding TF elements on human fitness.

Both synonymous and nonsynonymous mutations within coding footprints were significantly younger than those outside of footprints (Fig. 1F and fig. S5E), indicating that coding TF binding constrains both codon and amino acid evolution. The genome-wide recognition sequence landscape of each TF has evolved to fit the molecular topography of its protein-DNA binding interface (Fig. 1G) (13). To study how specific TFs influence codon and amino acid choice at

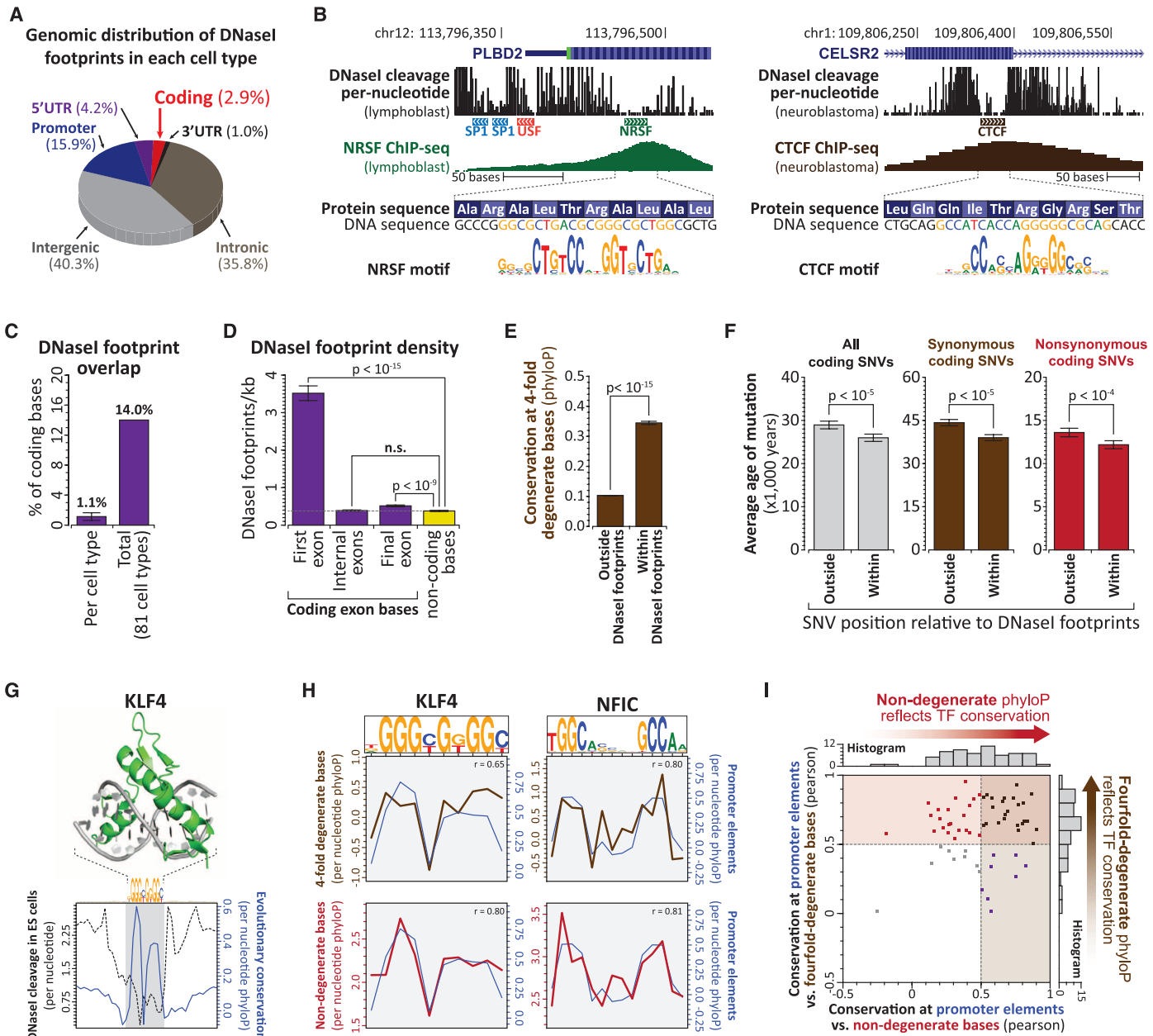


Fig. 1. TFs densely populate and evolutionarily constrain protein-coding exons. (A) Distribution of DNaseI footprints. (B) Per-nucleotide DNaseI cleavage and chromatin immunoprecipitation sequencing (ChIP-seq) signal for coding CTCF (left) and NRSF (right) binding elements. (C) Proportion of coding bases within DNaseI footprints in each of 81 cell types (left), or any cell type (right). (D) Average footprint density within first, internal, or final coding exons [mean \pm SEM; P value, paired t test; nonsignificant (n.s.) indicates $P > 0.1$]. (E) PhyloP conservation at 4FDBs within and outside footprints. (F) Estimated mutational age at all (gray),

synonymous (brown), and nonsynonymous (red) coding SNVs (European) within and outside footprints [P values per (21)] (G) Structure of DNA-bound KLF4 versus average per-nucleotide DNaseI cleavage and evolutionary constraint at KLF4 footprints. (H) Average per-nucleotide conservation at 4FDBs (brown) and NDBs (red) overlapping KLF4 (left) and NFIC (right) footprints [r , Pearson correlation; conservation at promoter bases versus 4FDBs (top) or NDBs (bottom)]. (I) Evolutionary constraint imparted by 63 TFs at promoter elements, 4FDBs and NDBs (Pearson correlations).

their recognition sites, we compared the per-nucleotide evolutionary conservation profiles of TF recognition sequences at noncoding 4FDBs and nondegenerate coding bases (NDBs). For example, the conservation profiles at 4FDBs and NDBs at KLF4 and NFIC recognition sites closely mirror those of recognition sites in noncoding regions (promoter) (Fig. 1H). As such, these TFs constrain both codon choice (via constraint on 4FDBs) and amino acid choice (via NDBs) encoded at their recognition sites. Analysis of conservation profiles for 63 TFs with prevalent occupancy within coding regions (19) showed

that 73% constrain 4FDBs and 51% constrain NDBs (Fig. 1I and figs. S6 and S7). Thus, individual TFs may influence both codon and amino acid choice.

To examine how TF binding relates to codon usage patterns, we examined binding at preferred (biased) versus nonpreferred codons. For example, across all human proteins asparagine is encoded by the AAC codon 52% of the time (versus AAT, 48%), indicating a generalized 4% bias in favor of this codon. However, genome-wide, 60.4% of asparagine codons within footprints are AAC, versus only 50.8% outside of footprints

(a 9.6% occupancy bias toward the preferred codon) (Fig. 2A). Apart from arginine (see below), for all amino acids encoded by two or more codons the codon that is preferentially used genome-wide is also preferentially occupied by TFs (Fig. 2B and table S2).

To determine whether preferential occupancy of biased codons is inherent to TF recognition sequences, we compared trinucleotide frequencies within coding versus noncoding footprints. Trinucleotide combinations favored by TFs within coding sequence were equivalent to those favored in noncoding sequence (Fig. 3C), indicating

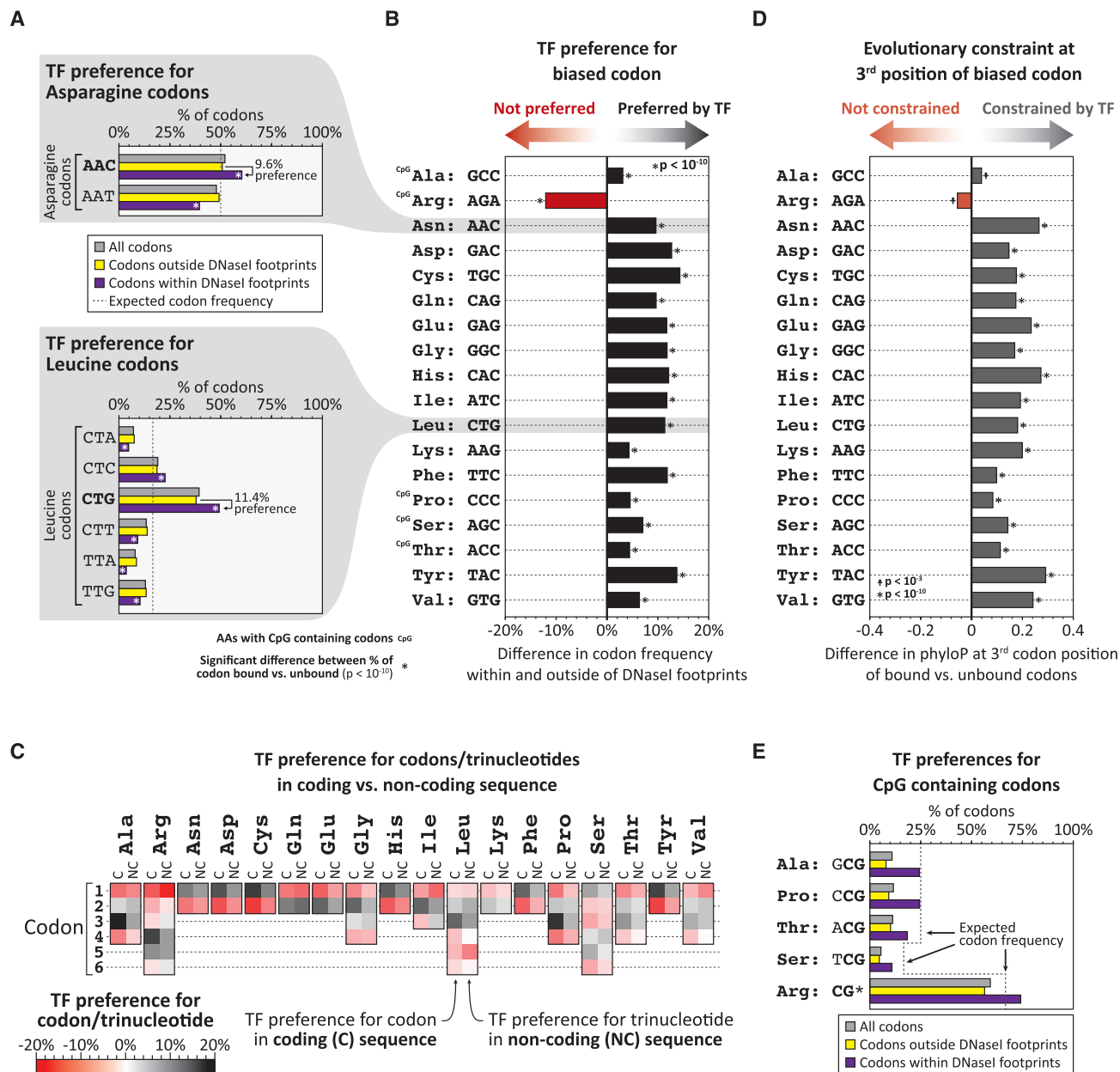


Fig. 2. TFs modulate global codon biases. (A) Proportions of all codons (gray), or codons outside of (yellow) or within (purple) footprints, that encode asparagine (top) or leucine (bottom). Codons with bias (AAC for asparagine and CTG for leucine) preferentially localize within footprints. (B) Preferential footprinting of biased codons, calculated as in (A) (P values, Pearson's χ^2 test). (C) Preferential footprinting

of each codon trinucleotide in coding versus noncoding regions (C, coding; NC, noncoding). (D) Difference in average evolutionary constraint at third positions of biased codons outside versus within footprints (P values, Mann-Whitney test). (E) Proportions of amino acids encoded by CpG-containing codons among all codons (gray), codons outside footprints (yellow), or codons within footprints (purple).

that global TF binding preferences are directly reflected in the frequency of different codons. Of note, baseline trinucleotide frequencies within coding and noncoding sequence are largely independent of one another (table S2). The fact that the third position of preferred codons overlapping footprints is under excess evolutionary constraint (Fig. 2D and table S2) supports a general role for TFs in potentiating codon usage biases through the selective preservation of preferred codons.

Although nearly all codon biases parallel TF recognition preferences genome-wide, arginine—one of the five amino acids encoded by codons containing CpGs (four out of six codons)—was a notable exception. CpGs frequently occur in regulatory DNA (table S2) yet have an elevated mutational rate (22). Consequently, although TFs may favor CpG-containing codons (Fig. 2E) and impart excess constraint thereto (table S2), the higher mutational rate at such codons is likely incompatible with preferential use.

Codons outside footprints still exhibit usage biases (Fig. 2A and table S2); however, it is likely that these biases also reflect the actions of TFs. First, our conclusions above are drawn from a conservative and incomplete annotation of duons. Second, because TF trinucleotide preferences and

codon biases have not changed substantially since the divergence of humans and mice (fig. S8), preferences at any given codon may result from a TF binding element extant in some ancestral species to human. Third, codon usage bias can be exaggerated because of mutual reinforcement with other cellular factors such as tRNA abundances (23, 24). Indeed, such mechanisms could be linked to codon biases created by exonic TF occupancy through a feedback mechanism that potentiates intrinsic TF-imposed biases, resulting in both abundant and rare codons and associated tRNAs, differences that could in turn affect protein synthesis and stability (25–27).

To analyze positional occupancy patterns of specific TFs within coding sequence, we systematically matched TF recognition sequences with footprints, providing an accurate measure of a TF's in vivo occupancy (13, 28). This analysis revealed that a subset of TFs selectively avoid coding sequences (Fig. 3A). Intriguingly, TFs involved in positioning the transcriptional preinitiation complex, such as NFYA and SP1 (29), preferentially avoid the translated region of the first coding exon (Fig. 3A) and typically occupy elements immediately upstream of the methionine start codon (Fig. 3B and fig. S9A).

Conversely, TFs involved in modulating promoter activity, such as YY1 and NRSF, preferentially occupy the translated region of the first coding exon (Fig. 3, A and C) (30, 31). These findings indicate that the translated portion of the first coding exon may serve functionally as an extension of the canonical promoter.

More broadly, the repressor NRSF preferentially occupies and evolutionarily constrains sequences coding for leucine-rich protein domains, such as signal peptide and transmembrane domains (Fig. 3D and fig. S9, B and C). Also, TFs such as CTCF and SREBP1 preferentially occupy and constrain splice sites (fig. S10, A to D), which are otherwise generally depleted of DNaseI footprints (fig. S10E). The above results suggest that specific protein structural and splicing features may undergo exaptation for specific regulatory purposes.

We also found that the occupancy of specific TFs within coding sequence parallels the extent of CpG methylation at their binding site (fig. S11). This raises the possibility that gene body methylation, which is paradoxically extensive at actively transcribed genes (32, 33), may provide a tunable mechanism for thwarting opportunistic TF occupancy within coding sequence during transcription.

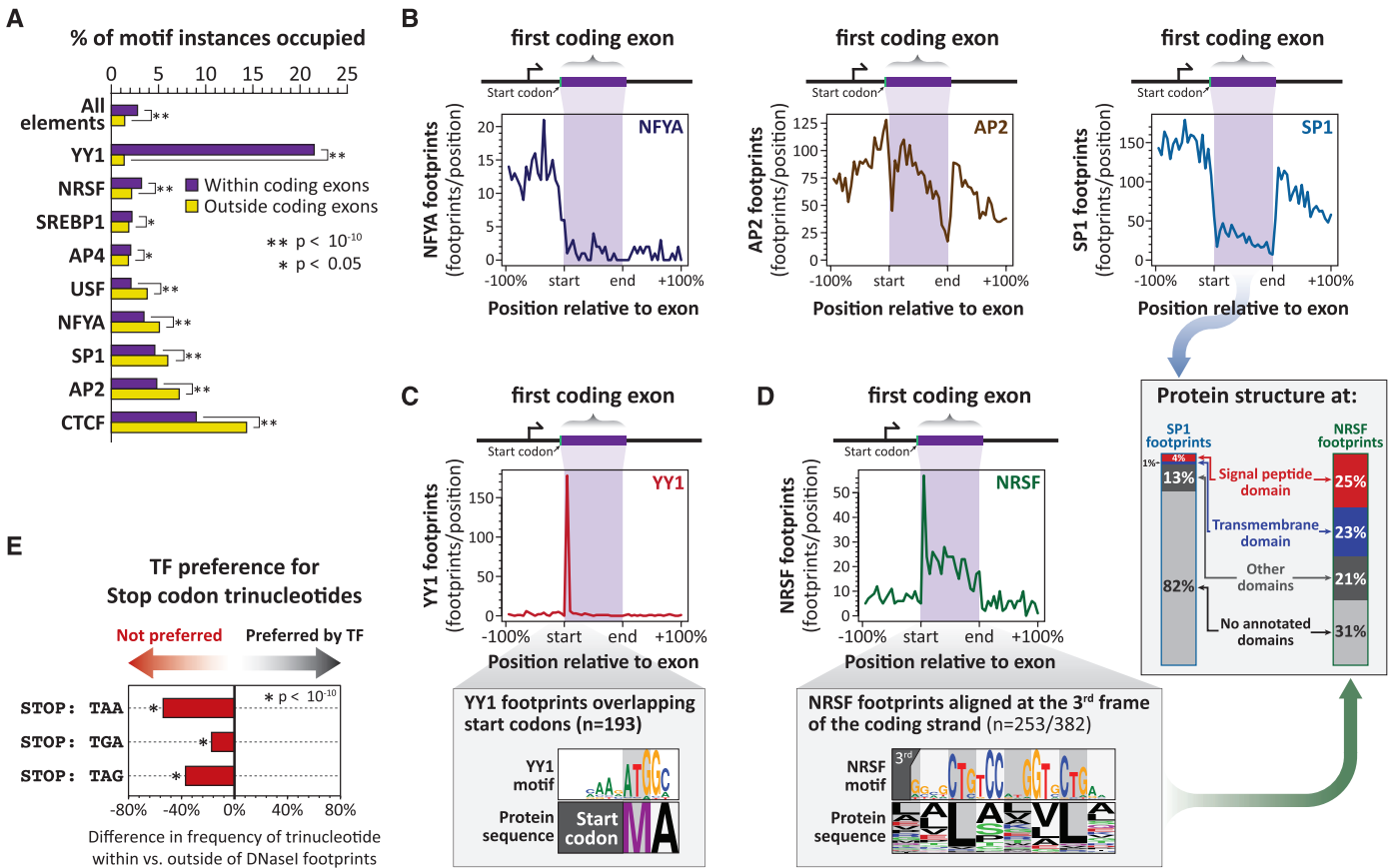


Fig. 3. TFs exploit and avoid specific coding features. (A) Percentage of TF motifs occupied in coding versus noncoding regions (*P* values, paired *t* test). (B) Density of NFYA (left), AP2 (middle), and SP1 (right) footprints relative to translated region of first coding exons. (C) (Top) Density of YY1 footprints across first coding exons. (Bottom) YY1 recognition sequence and corresponding

amino acid sequence within YY1 footprints overlapping start codons. (D) (Top left and bottom) For NRSF as per (C). (Right, arrow) Protein domain annotation of first exon third-frame NRSF footprints versus SP1 footprints. (E) TF preference (avoidance) of stop codon trinucleotides within versus outside footprints in noncoding regions (*P* values, Pearson's χ^2 test).

If TFs, through selective recognition sequences, could impose changes in protein sequence, deleterious consequences could arise if such changes resulted in a nonsense substitution. We observed that TFs generally avoid stop codons (fig. S10E). This finding extends to noncoding regions, in which stop codon trinucleotides (TAA, TAG, and TGA) are selectively depleted within footprints. This indicates that the global TF repertoire has been selectively purged of DNA binding domains capable of recognizing—and thus preferentially stabilizing—nonsense codons (Fig. 3E and fig. S10F).

The high sequencing coverage provided by genomic footprinting revealed 592,867 heterozygous single-nucleotide variants (SNVs) across the 81 cell type samples, and 3% of coding foot-

prints harbored heterozygous SNVs (Fig. 4A). Functional SNVs that disrupt TF occupancy quantitatively skew the allelic origins of DNaseI cleavage fragments (13), and 17.4% of all heterozygous coding SNVs within footprints showed this signature (Fig. 4B and fig. S12), including both synonymous and nonsynonymous variant classes (Fig. 4C). The potential of a coding SNV to disrupt overlying TF occupancy was independent of the class of variant (Fig. 4D) or whether a nonsynonymous variant was predicted to be deleterious to protein function (Fig. 4, E and F).

Of common disease- and trait-associated SNVs identified by genome-wide associated studies (GWASs) in coding sequence (19), 13.5% fall within duons (fig. S13A). GWAS single-nucleotide

polymorphisms in duons encompass both synonymous (12%) and nonsynonymous (88%) substitutions (fig. S13A) and may directly affect pathogenic mechanisms (fig. S13, B to F, and table S3). As such, disease-associated variants within duons may compromise both regulatory and/or protein-structural functions. These findings have substantial practical implications for the interpretation of genetic variation in coding regions.

Our results indicate that simultaneous encoding of amino acid and regulatory information within exons is a major functional feature of complex genomes. The information architecture of the received genetic code is optimized for superimposition of additional information (34, 35),

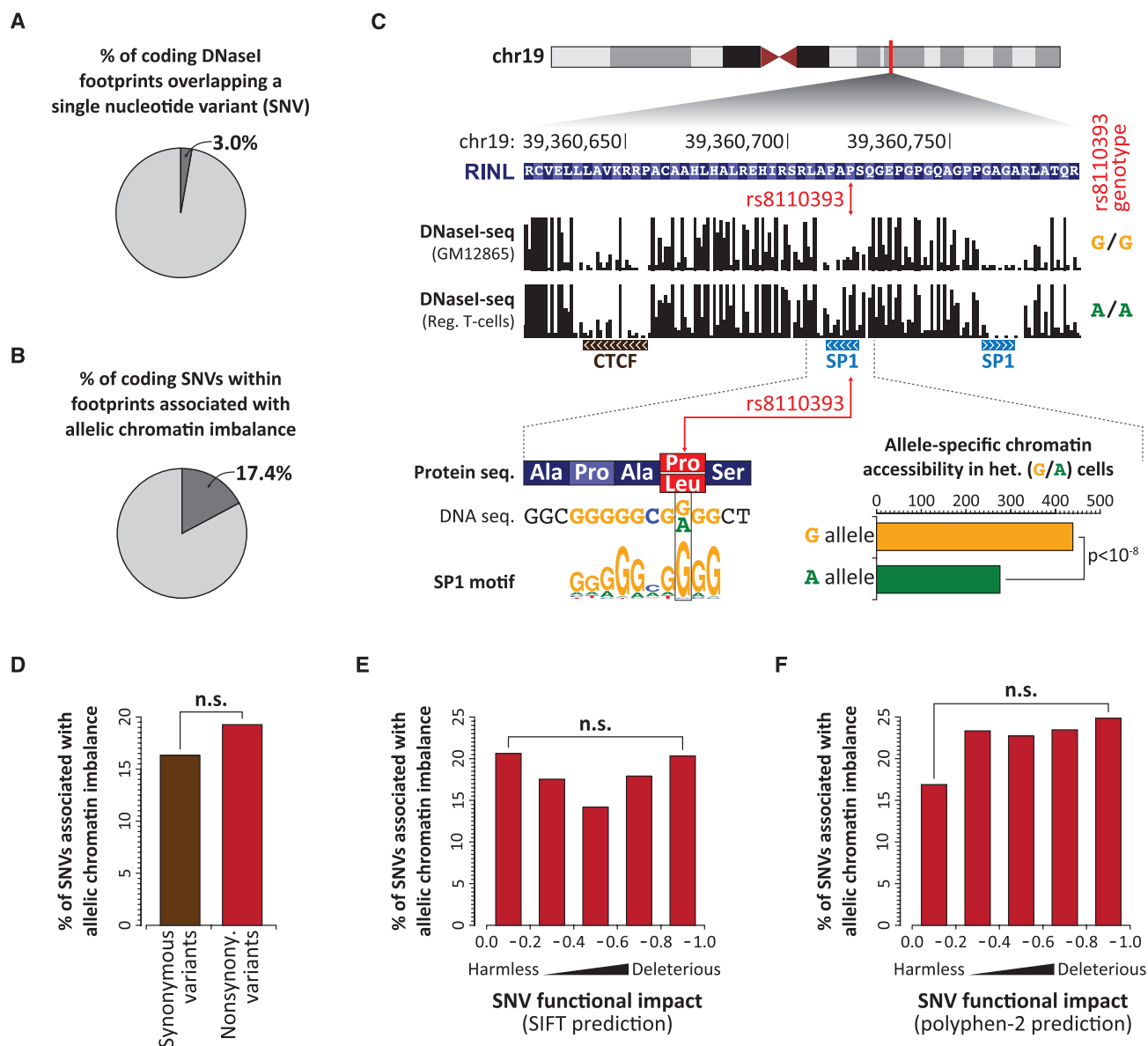


Fig. 4. Genetic variation in duons frequently alters TF occupancy. (A) Proportion of coding footprints overlapping a SNV in any of 81 cell types. **(B)** Proportion of SNVs in duons that allelically alter TF occupancy. **(C)** (Top) Per-nucleotide DNaseI cleavage at common nonsynonymous G→A SNV (rs8110393) in G/G and A/A homozygous cells. (Bottom) Allelic SP1 occupancy in hetero-

zygous (G/A) cells. **(D)** Proportion of synonymous and nonsynonymous variants in duons that allelically alter TF occupancy. **(E and F)** Proportion of nonsynonymous variants from **(D)** grouped by predicted impact of coding variant on protein function using **(E)** SIFT or **(F)** Polyphen-2. None of the bins are significantly different (Fisher's exact test; n.s. indicates $P > 0.1$).

and this intrinsic flexibility has been extensively exploited by natural selection. Although TF binding within exons may serve multiple functional roles, our analyses above is agnostic to these roles, which may be complex (36).

References and Notes

1. R. Grantham, C. Gautier, M. Gouy, R. Mercier, A. Pavé, *Nucleic Acids Res.* **8**, r49–r62 (1980).
2. T. Ikemura, *J. Mol. Biol.* **151**, 389–409 (1981).
3. R. Grantham, C. Gautier, M. Gouy, M. Jacobzone, R. Mercier, *Nucleic Acids Res.* **9**, r43–r74 (1981).
4. M. Gouy, C. Gautier, *Nucleic Acids Res.* **10**, 7055–7074 (1982).
5. A. Eyre-Walker, M. Bulmer, *Nucleic Acids Res.* **21**, 4599–4603 (1993).
6. D. B. Carlini, W. Stephan, *Genetics* **163**, 239–243 (2003).
7. M. dos Reis, R. Savva, L. Wernisch, *Nucleic Acids Res.* **32**, 5036–5044 (2004).
8. J. L. Parmley, J. V. Chamary, L. D. Hurst, *Mol. Biol. Evol.* **23**, 301–309 (2006).
9. T. Warnecke, C. C. Weber, L. D. Hurst, *Biochem. Soc. Trans.* **37**, 756–761 (2009).
10. W. Gu, T. Zhou, C. O. Wilke, *PLOS Comput. Biol.* **6**, e1000664 (2010).
11. M. F. Lin et al., *Genome Res.* **21**, 1916–1928 (2011).
12. Z. Yang, R. Nielsen, *Mol. Biol. Evol.* **25**, 568–579 (2008).
13. S. Neph et al., *Nature* **489**, 83–90 (2012).
14. S. M. Hyder, Z. Nawaz, C. Chiappetta, K. Yokoyama, G. M. Stancel, *J. Biol. Chem.* **270**, 8506–8513 (1995).
15. G. Lang, W. M. Gombert, H. J. Gould, *Immunology* **114**, 25–36 (2005).
16. D. I. Ritter, Z. Dong, S. Guo, J. H. Chuang, *PLOS ONE* **7**, e35202 (2012).
17. A. H. Khan, A. Lin, D. J. Smith, *PLOS ONE* **7**, e46098 (2012).
18. R. Y. Birnbaum et al., *Genome Res.* **22**, 1059–1068 (2012).
19. Materials and methods are available as supplementary materials on Science Online.
20. W.-H. Li, *Molecular Evolution* (Sinauer Associates, Sunderland, MA, 1997).
21. W. Fu et al., *Nature* **493**, 216–220 (2013).
22. C. Coulondre, J. H. Miller, P. J. Farabaugh, W. Gilbert, *Nature* **274**, 775–780 (1978).
23. M. Bulmer, *Nature* **325**, 728–730 (1987).
24. M. Bulmer, *Genetics* **129**, 897–907 (1991).
25. J. Duan et al., *Hum. Mol. Genet.* **12**, 205–216 (2003).
26. J. zur Megede et al., *J. Virol.* **74**, 2628–2635 (2000).
27. J. R. Coleman et al., *Science* **320**, 1784–1787 (2008).
28. R. M. Samstein et al., *Cell* **151**, 153–166 (2012).
29. S. McKnight, R. Tjian, *Cell* **46**, 795–805 (1986).
30. C. Zhang et al., *Nucleic Acids Res.* **34**, 2238–2246 (2006).
31. H. Xi et al., *Genome Res.* **17**, 798–806 (2007).
32. A. Hellman, A. Chess, *Science* **315**, 1141–1143 (2007).
33. D. Zilberman, M. Gehring, R. K. Tran, T. Ballinger, S. Henikoff, *Nat. Genet.* **39**, 61–69 (2007).
34. S. Itzkovitz, U. Alon, *Genome Res.* **17**, 405–412 (2007).
35. S. Itzkovitz, E. Hodis, E. Segal, *Genome Res.* **20**, 1582–1589 (2010).
36. T. R. Mercer et al., *Nat. Genet.*, published online 23 June 2013 (10.1038/ng.2677).

Acknowledgments: We thank many colleagues for their insightful comments and critical readings of the manuscript. We also thank many colleagues who provided individual cell samples for DNaseI analysis. We also thank E. Rynes for his technical assistance. This work was supported by NIH grants U54HG004592, U54HG007010, and U01ES01156 to J.A.S. A.B.S. was supported by grant FDK095678A from the National Institute of Diabetes and Digestive and Kidney Diseases. J.M.A. is a paid consultant for Glenview Capital. All data from this study are available through the ENCODE data repository at UCSC (www.encodeproject.org) and the Roadmap Epigenomics data repository at NCBI (www.ncbi.nlm.nih.gov/epigenomics).

Supplementary Materials

www.sciencemag.org/content/342/6164/1367/suppl/DC1
Materials and Methods
Figs. S1 to S13
Tables S1 to S3
References (37–63)

19 July 2013; accepted 23 October 2013
10.1126/science.1243490

Cryptic Variation in Morphological Evolution: HSP90 as a Capacitor for Loss of Eyes in Cavefish

Nicolas Rohner,¹ Dan F. Jarosz,^{2*} Johanna E. Kowalko,¹ Masato Yoshizawa,³ William R. Jeffery,^{3,4} Richard L. Borowsky,⁵ Susan Lindquist,^{2,6,7} Clifford J. Tabin^{1†}

In the process of morphological evolution, the extent to which cryptic, preexisting variation provides a substrate for natural selection has been controversial. We provide evidence that heat shock protein 90 (HSP90) phenotypically masks standing eye-size variation in surface populations of the cavefish *Astyanax mexicanus*. This variation is exposed by HSP90 inhibition and can be selected for, ultimately yielding a reduced-eye phenotype even in the presence of full HSP90 activity. Raising surface fish under conditions found in caves taxes the HSP90 system, unmasking the same phenotypic variation as does direct inhibition of HSP90. These results suggest that cryptic variation played a role in the evolution of eye loss in cavefish and provide the first evidence for HSP90 as a capacitor for morphological evolution in a natural setting.

A long-standing question in evolutionary biology is the extent to which selection acts on preexisting “standing variation” in a population, as opposed to de novo mutations.

Recent studies have indicated that both mechanisms have contributed to morphological evolution (1, 2). Thus, although de novo mutations may exist and contribute to phenotypic evolution, repeated use of standing variation has played an important role in the evolution in these fish. However, these observations also raise a critical question: How is genetic variation maintained in a population if it is not adaptive before new selective conditions?

Waddington proposed that developmental processes are quite robust and produce the same phenotype regardless of minor genotypic variation, a phenomenon he termed “canalization” (3). In such conditions, cryptic variation can accumulate and can be maintained without consequence. He further proposed that under certain

environmental conditions, this property could be lost (“decanalization”), resulting in expression of the cryptic variation on which selection could act (4).

More recently, Lindquist demonstrated that HSP90 (heat shock protein 90) provides a molecular mechanism for buffering genetic variation and releasing it in response to environmental stress (5–10). The HSP90 chaperone assists in the folding of proteins that are metastable signal transducers, such as kinases, transcription factors, and ubiquitin ligases. HSP90 is normally present at much higher concentrations than needed to maintain these proteins, allowing it to act as a buffer, protecting organisms from phenotypic consequences that would otherwise be caused by genetic variants of these proteins. Because protein folding is so sensitive to environmental stress, changes in the environment can exhaust the chaperone buffer, unmasking vulnerable polymorphisms. And because multiple variants can be unmasked at the same time, this system provides a mechanism to create complex traits in a single step (11).

Besides changes in the activities of kinases, phosphatases, transcription factors, and ubiquitin ligases, other distinct mechanisms have been reported by which changes in HSP90 function can lead to changes in phenotype (5, 10, 12–16).

Evidence strongly suggests that this mechanism has operated in microbial populations (7, 8), but its relevance to the evolution of natural populations of higher organisms remains highly controversial. Thus far, examples of HSP90-mediated canalization in multicellular eukaryotes have been limited to lab strains of various model organisms. Moreover, with the exception of some phenotypes in *Arabidopsis*, the phenotypes of HSP90-released canalization in higher organisms are not

¹Department of Genetics, Harvard Medical School, Boston, MA 02115, USA. ²The Whitehead Institute for Biomedical Research, Cambridge, MA 02142, USA. ³Department of Biology, University of Maryland, College Park, MD 20742, USA. ⁴Marine Biological Laboratory, Woods Hole, MA 02543, USA. ⁵Department of Biology, New York University, New York, NY 10003, USA. ⁶Howard Hughes Medical Institute, Cambridge, MA 02142, USA. ⁷Department of Biology, Massachusetts Institute of Technology, Cambridge, MA 02142, USA.

*Present address: Departments of Chemical and Systems Biology and Developmental Biology, School of Medicine, Stanford University, Stanford, CA 94305, USA.

†Corresponding author. E-mail: tabin@genetics.med.harvard.edu

obviously adaptive. Last, it has been unclear how a heat shock or other environmental factor would feature in the normal context of natural selection.

If a long-term environmental stress were to drive the course of phenotypic evolution, it would plausibly arise when species are confronted with a completely foreign set of conditions. Such circumstances are met when organisms, such as the cavefish *Astyanax mexicanus*, are inadvertently introduced into a cave environment.

Cavefish display many phenotypic differences from their surface conspecifics. We chose to focus on the dramatic loss of eyes in the cave morph, a trait that has been shown to be influenced by at least 14 mapped quantitative trait loci. Moreover, genetic evidence suggests that eye loss is very likely to be adaptive (17, 18). Loss of eyes could have had direct adaptive importance—for example, in the energetic cost of maintaining eyes in an environment where they lack utility and/or could have been selected indirectly through the pleiotropic need to expand other sensory systems

(supplementary text). It is possible that, to some extent, neutral effects could have also contributed to the process by which eyes were lost in the cave populations of *Astyanax*.

To reduce the capacity of HSP90 chaperone activities during development of the fish (mimicking the effects of environmental stress) (5–7, 19, 20), we used the well-characterized and highly specific inhibitor Radicol. When developing, *A. mexicanus* were treated with 500 nM Radicol; this resulted in a strong increase in expression of two marker genes for HSP90 inhibition, *BAG3* and *HSP27* (*HSPB1*), as well as HSP90 itself (Fig. 1A and fig. S1), which is consistent with impairment of chaperone activity. The treated fish displayed an array of different low-penetrance phenotypes in surface, cave, and F2 populations (fig. S2). Similar to previous studies, most of the low-penetrance phenotypes were not obviously adaptive and either not viable or transient. Radicol was not teratogenic for eye development per se. When an inbred laboratory strain of zebrafish was reared

under similar conditions of Radicol exposure (by using a concentration that elicited a similar transcriptional response of target genes), no difference was observed in eye size or morphology (fig. S3). In contrast, when *A. mexicanus* surface fish were raised in the presence of the drug we observed unusually large variation in eye size in larval fish (Fig. 1B).

We initially characterized the effect of HSP90 inhibition on adult stages in an F2 population derived from a cross between a surface fish and a cavefish, allowing us to examine eye size in the simultaneous presence of surface and cave alleles. Indeed, we observed both larger eyes and smaller eyes in the treated fish, leading to a statistically significant increase in the standard deviation (SD) of the treated fish [+58% compared with dimethyl sulfoxide (DMSO)-treated control groups; two-sided *F* test, $P = 0.0004$; Bartlett's test, $P = 0.001$; Levene's test, $P = 0.03$] (Fig. 1, C and D). These experiments were conducted in the dark because Radicol is slightly light sensitive; however, raising *Astyanax* embryos in the presence or absence of light had no effect on eye size (Fig. 1C). Thus, inhibition of HSP90 permits the expression of cryptic variation in eye size present in the *Astyanax* populations.

If the cryptic variation we observed in eye size played a role in the evolution of the reduced eye trait within the caves, one would expect this variation to be present in the modern river population of surface fish (similar to the ancestral form) but to be less prevalent in the cave populations that have undergone selection for this trait. We observed a statistically significant increase in eye size variation (SD, +83% compared with DMSO-treated control fish; two-sided *F* test: $P = 8.1 \times 10^{-6}$; Bartlett's test, $P < 0.001$, Levene's test, $P < 0.001$) in the parental surface populations, again including both larger and smaller eyes than are ever seen in untreated broods (Fig. 2A). The same result was seen whether measuring the eye itself or the infraorbital bones surrounding the eye socket or "orbit" (SD, +108%; two-sided *F* test, $P = 3.4 \times 10^{-6}$; Bartlett's test, $P < 0.001$; Levene's test, $P < 0.001$) (Fig. 2B and fig. S4).

A very different result was observed, however, when we conducted parallel experiments on fish from the Tinaja cave population. Cavefish do not possess visible eyes but still retain a cavity in the skull where the eye would be located (fig. S4), so in this case, we focused on the orbit size. We detected no increase in the variation in orbit size in the inhibitor-treated cavefish (SD, -12%; two-sided *F* test, $P = 0.239$), suggesting that some of the alleles have been selected for in the cavefish population (Fig. 2C). However, we detect a statistically significant decrease in the orbit size in the inhibitor-treated individuals (two-tailed *t* test, $P = 0.002$) (Fig. 2C). This shows that the alleles that have been selected for in cavefish evolution are alleles that, at least in part, are dependent on and responsive to HSP90. Moreover, the HSP90-dependent alleles remaining in the cave population are specifically those contributing to

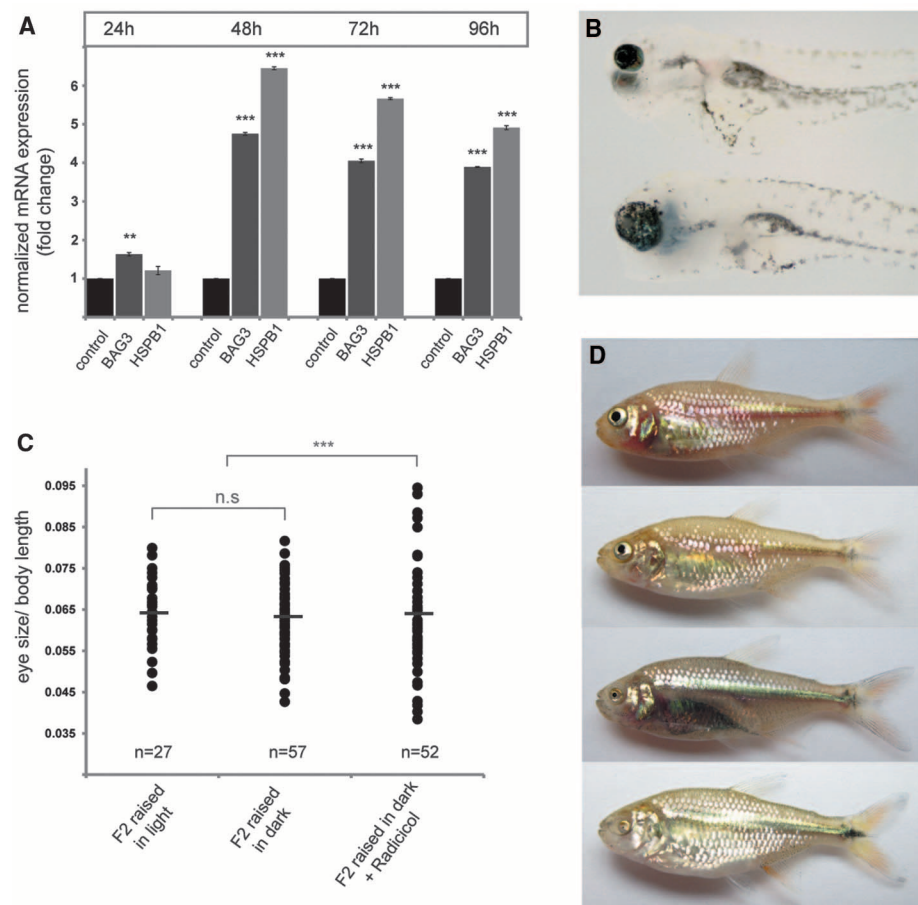


Fig. 1. Reduction of HSP90 levels in *A. mexicanus* using the chemical inhibitor Radicol. (A) Inhibition of HSP90 using 500 nM Radicol leads to activation of *BAG3* and *HSPB1* (two-tailed *t* test, $**P < 0.005$, $***P < 0.0005$). Time scale refers to hours of treatment. (B) Variable eye sizes in surface *A. mexicanus* larvae after treatment. (C) Quantification of eye size in adult F2 hybrids after larval treatment of Radicol reveals a significant increase in SD of eye size, whereas average eye size is not affected (two-sided *F* test: $P = 0.0004$; Bartlett's test, $P = 0.001$; Levene's test, $P = 0.03$). Raising the fish in the dark alone does not affect eye size. Values were corrected for body size by using standard length of the fish. (D) Examples of eye size variation in F2 population of hybrid *A. mexicanus*.

reduced eye sockets. These data are consistent with the possibility that HSP90 played a role in the evolution of eye size in Tinaja cavefish.

To test whether the cryptic variation in eye size uncovered by HSP90 inhibition can be genetically assimilated, we treated a population of embryonic surface fish with Radicol. We then selected for smaller eye size by intercrossing fish from this treated brood whose eye size was smaller than any of the untreated fish raised in parallel. The resultant F2 fish, raised in the absence of the drug, all had eyes and orbit sizes at the lower end of the range of sizes observed in the parental fish and included many individuals with eyes and orbits smaller than any seen in the untreated surface fish and comparable with the smallest of the treated fish (Fig. 3, A and B). Thus, the individuals that develop the smallest eyes in the presence of HSP90 inhibition contain alleles that can contribute to inheritance of small eye size in the absence of treatment.

A critical question, however, is whether a river fish finding itself suddenly trapped in a cave environment would experience a HSP90-related stress response. To characterize abiotic factors that differ between the cave and river environments, we measured pH, oxygen content, temperature, and conductivity in the Tinaja cave and a nearby surface fish habitat in the Sierra de El Abra (table S1). The biggest numerical difference we detected was the much lower conductivity present in the cave water. Further sampling of additional caves revealed conductivities as low as 230 μS (Sabinos cave), compared with the 1300- μS conductivity in adjacent river environments. Low conductivity can elicit a heat shock such as stress response in fish (21), making it a good candidate for a cave-specific stress factor.

To investigate, we raised surface fish at the lowest measured conductivity from the Sabinos cave (230 μS). When fish embryos develop under such conditions, they up-regulate HSP90, showing that they are indeed in a state of physiological stress response and, moreover, activate the same heat shock response genes that are up-regulated with HSP90 inhibition by Radicol (Fig. 4B and fig. S5). Thus, the environment encountered by these fish during their evolutionary transition from surface to cave stresses the protein homeostasis mechanisms of the organism in a manner similar to a specific stress on HSP90 chaperone activities.

Adult river fish placed in low conductivity during larval development displayed statistically significant increases in eye and orbit size variation of 50% (two-sided F test, $P = 0.0018$; Bartlett's test, $P = 0.006$; Levene's test, $P = 0.005$) and 58% (two-sided F test, $P = 5.9\text{E-}4$; Bartlett's test, $P = 0.001$; Levene's test, $P = 0.01$), respectively (Fig. 4, C and D). This demonstrates that a cave-specific environmental stress can elicit similar changes in morphological eye development as biochemical inhibition of HSP90.

We detected an increase in variation in eye size in fish treated with Radicol or in the pres-

Fig. 2. HSP90 inhibition in natural populations of *A. mexicanus*. (A and B) HSP90 inhibition in natural populations of surface *A. mexicanus* leads to an increase of variation in (A) eye size and (B) orbit size. Eye size SD, +83%; two-sided F test, $P = 8.1 \times 10^{-6}$; Bartlett's test, $P < 0.001$; Levene's test, $P < 0.001$; orbit size SD, +108%; two-sided F test, $P = 3.4 \times 10^{-6}$; Bartlett's test, $P < 0.001$; Levene's test, $P < 0.001$. (C) Orbit size decreases after Radicol treatment in Tinaja cave populations (t test, $P = 0.02$), while change in variation is observed (SD, -12%; two-sided F test, $P = 0.239$). Control is DMSO. Asterisks in (A) and (B) compare SDs, whereas in (C), asterisks compare averages.

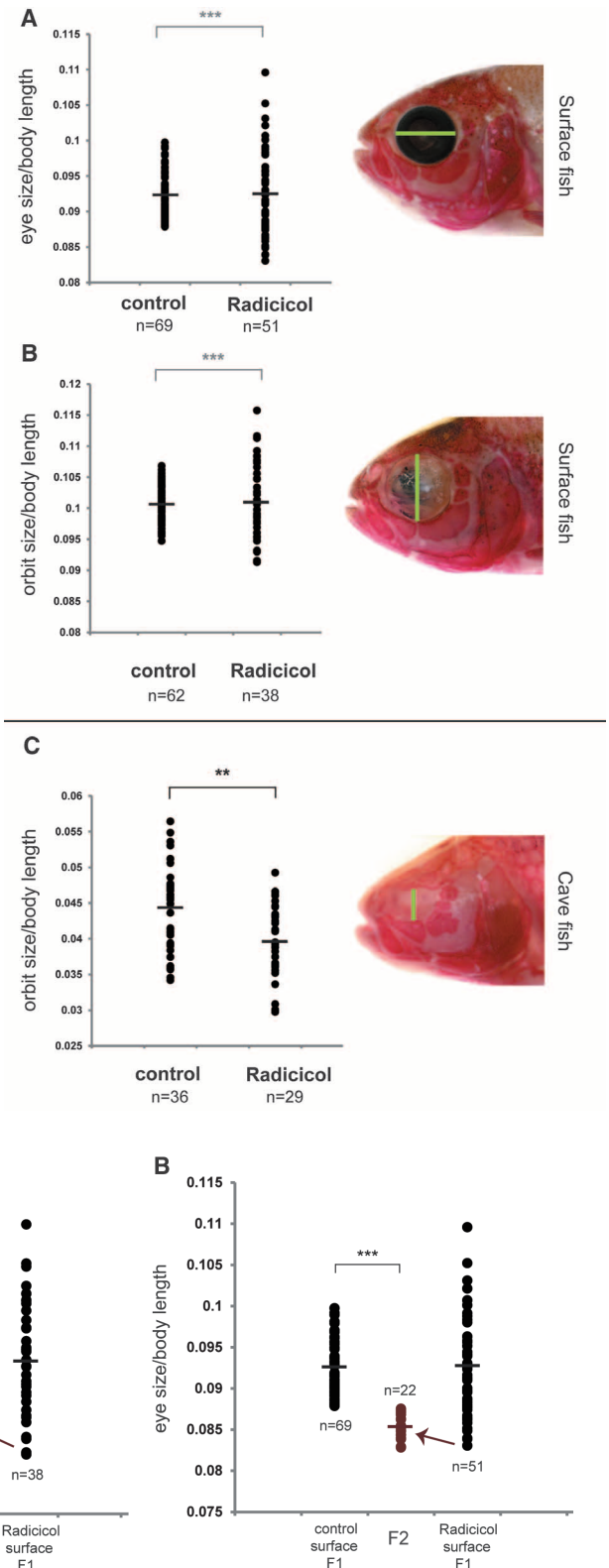


Fig. 3. Genetic assimilation. (A and B) Selection for small eye size in surface fish generated by Radicol treatment resulted in offspring with significantly smaller (A) orbit size and (B) eye size in the absence of treatment (two-tailed t test, $P = 6.5 \times 10^{-13}$ for orbit size; $P = 7.2 \times 10^{-16}$ for eye size). The resultant range exceeded the range seen in any cross of untreated surface fish.

ence of environmental stresses, representing cryptic variation present in the untreated population. We further demonstrated that in cavefish popu-

lations, the alleles that are responsive to HSP90 have undergone selection in the transition from surface to cave forms, leaving only alleles that

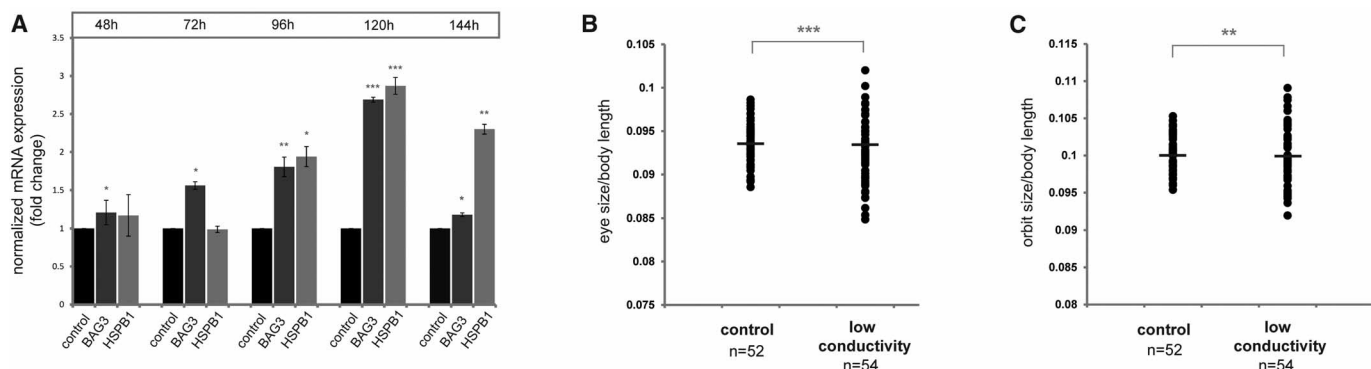


Fig. 4. Low-conductivity conditions in the cave natural habitat have a similar effect to Radicol treatment on surface populations. (A) Quantitative reverse transcription polymerase chain reaction of BAG3 and HSPB1 for surface fish reared under low-conductivity (230 μ S) conditions compared with control conductivity conditions (two-tailed *t* test, **P* < 0.05; ***P* < 0.005;

****P* < 0.0005). Time scale refers to hours of treatment. **(B and C)** Lower-conductivity conditions reveal an increase in variation of (B) orbit size and (C) eye size (eye size SD, +50%; two-sided *F* test, *P* = 0.0018; Bartlett's test, *P* = 0.006; Levene's test, *P* = 0.005; orbit size SD, +58%; two-sided *F* test: *P* = 5.9 $\times 10^{-4}$; Bartlett's test, *P* = 0.001; Levene's test, *P* = 0.01).

produce a smaller orbit when released from their normal HSP90 interactions. This strongly suggests an involvement of HSP90 in cavefish evolution and provides an actual case in nature for Waddington's classic theory of the canalization in evolution. Not all cave-specific traits appear to have relied on HSP90-canalized cryptic variation for their evolution. We examined several other traits and found, for example, that there is no cryptic variation in body size (fig. S6) or in neuromast number (fig. S7) uncovered by HSP90 inhibition in the populations we examined.

It is also reasonable to assume that the change in conductivity is only one factor contributing to the stress response that surface fish might experience after colonizing the caves (such as lower oxygen levels or starvation). However, such environmentally induced stress is likely to have been only transient because the cavefish would have adapted to these new conditions over subsequent generations. Cavefish have higher basal HSP90 levels than those of surface fish (22), potentially rendering them more stress-resistant. However, during the transition period when the fish were adapting to the cave conditions, the HSP90-dependent standing variation in eye size we observed in the surface population of *A. mexicanus* would have helped potentiate a rapid response to the cave environment.

Of course, the extreme environment of the cavefish is exceptional in many ways. Yet, environmental challenges are likely to be a driving force for many other adaptations. For example, temperature increases are extremely common in nature, and even simple starvation affects Hsp expression in European Sea Bass (23).

References and Notes

1. P. F. Colosimo *et al.*, *Science* **307**, 1928–1933 (2005).
2. F. C. Jones *et al.*, *Nature* **484**, 55–61 (2012).
3. C. H. Waddington, *Nature* **150**, 563–565 (1942).
4. C. H. Waddington, *Evolution* **7**, 118 (1953).
5. S. L. Rutherford, S. Lindquist, *Nature* **396**, 336–342 (1998).
6. C. Queitsch, T. A. Sangster, S. Lindquist, *Nature* **417**, 618–624 (2002).
7. D. F. Jarosz, S. Lindquist, *Science* **330**, 1820–1824 (2010).

8. L. E. Cowen, S. Lindquist, *Science* **309**, 2185–2189 (2005).
9. Y. Xu, M. A. Singer, S. Lindquist, *Proc. Natl. Acad. Sci. U.S.A.* **96**, 109–114 (1999).
10. M. Taipale *et al.*, *Cell* **150**, 987–1001 (2012).
11. D. F. Jarosz, M. Taipale, S. Lindquist, *Annu. Rev. Genet.* **44**, 189–216 (2010).
12. V. Sollars *et al.*, *Nat. Genet.* **33**, 70–74 (2003).
13. D. Mittelman, K. Sykoudis, M. Hershey, Y. Lin, J. H. Wilson, *Cell Stress Chaperones* **15**, 753–759 (2010).
14. G. Chen, W. D. Bradford, C. W. Seidel, R. Li, *Nature* **482**, 246–250 (2012).
15. V. Specchia *et al.*, *Nature* **463**, 662–665 (2010).
16. R. Sawarkar, C. Sievers, R. Paro, *Cell* **149**, 807–818 (2012).
17. M. Protas, M. Conrad, J. B. Gross, C. Tabin, R. Borowsky, *Curr. Biol.* **17**, 452–454 (2007).
18. W. R. Jeffery, *Annu. Rev. Genet.* **43**, 25–47 (2009).
19. T. W. Schulte *et al.*, *Mol. Endocrinol.* **13**, 1435–1448 (1999).
20. P. L. Yeyati, R. M. Bancewicz, J. Maule, V. van Heyningen, *PLoS Genet.* **3**, e43 (2007).
21. C. Y. Choi, K. W. An, *Comp. Biochem. Physiol. B Biochem. Mol. Biol.* **149**, 91–100 (2008).
22. T. A. Hooven, Y. Yamamoto, W. R. Jeffery, *Int. J. Dev. Biol.* **48**, 731–738 (2004).
23. E. Antonopoulou *et al.*, *Comp. Biochem. Physiol. A Mol. Integr. Physiol.* **165**, 79–88 (2013).

Acknowledgments: We thank B. Martineau for animal husbandry and T. Luong for assistance in data acquisition; M. Taipale for HSP90 inhibitor and discussions; H. Boldt and M. Harris for providing zebrafish; L. Espinosa for practical support during the caving expedition; L. Legendre for comparison of environmental parameters; and J. Bibliowicz and Y. Elipot for discussions. N.R. was supported by a Deutsche Forschungsgemeinschaft postdoctoral fellowship (RO 4097/1-1). D.F.J. was supported by a postdoctoral fellowship from Damon Runyon Cancer Research Foundation and a Pathway to Independence Award from the NIH. C.J.T. acknowledges the support of a grant from NIH RO1 HD047360.

Supplementary Materials

www.sciencemag.org/content/342/6164/1372/suppl/DC1
Materials and Methods
Supplementary Text
Figs. S1 to S7
Table S1
References (24–29)

8 May 2013; accepted 31 October 2013
10.1126/science.1240276

Progressive Specification Rather than Intercalation of Segments During Limb Regeneration

Kathleen Roensch,^{1,2*†} Akira Tazaki,^{1,2*†} Osvaldo Chara,^{3,4} Elly M. Tanaka^{1,2†‡}

An amputated salamander limb regenerates the correct number of segments. Models explaining limb regeneration were largely distinct from those for limb development, despite the presence of common patterning molecules. Intercalation has been an important concept to explain salamander limb regeneration, but clear evidence supporting or refuting this model was lacking. In the intercalation model, the first blastema cells acquire fingertip identity, creating a gap in positional identity that triggers regeneration of the intervening region from the stump. We used HOXA protein analysis and transplantation assays to show that axolotl limb blastema cells acquire positional identity in a proximal-to-distal sequence. Therefore, intercalation is not the primary mechanism for segment formation during limb regeneration in this animal. Patterning in development and regeneration uses similar mechanisms.

Numerous models to explain proximodistal metazoan limb patterning during regeneration have been proposed. Cell intercala-

tion has become an important concept based on the results of grafting experiments (1–6). Cell intercalation is a patterning process whereby experimentally

induced juxtaposition of cells from disparate parts of an organ (for example, upper arm and fingertip) stimulates a proliferative response that restores the missing, intervening portion of the organ. In arthropods, grafting of the distal leg tip onto an amputated upper leg stump stimulated the leg stump and the leg tip cells at the graft junction to proliferate and restore the missing segments until a normal leg was formed (7). In salamanders, limb amputation results in the formation of a blastema,

a zone of proliferative mesenchymal and epithelial progenitor cells that restores the missing limb elements. When a salamander hand blastema was grafted onto an upper limb stump, intercalation occurred, whereby the upper arm stump regenerated the missing lower arm segment and the grafted hand blastema regenerated the hand (8–10). The intercalation was unidirectional—the hand blastema cells did not contribute to restoration of the missing lower arm. Unidirectional intercalation reflects a cellular determination state, termed “the rule of distal transformation,” in which connective tissue-derived blastema cells can only form limb segments more distal to their original identity (10–13).

An important question is whether intercalation is an integral part of normal limb regeneration (1–4). In such models, the first blastema cells acquire a distal (prospective fingertip) identity. This juxtaposition of fingertip progenitors with upper arm cells were proposed to induce the stump cells to intercalate lower arm cells. Tracking of carbon particles or transiently transfected green flu-

orescent protein (GFP)-expressing limb blastema cells suggested that early- to midstage blastema cells could have distal identity consistent with intercalation (14, 15). However, the data were inconclusive because the labels were not permanently cell-associated.

Expression analysis of posterior *HoxA* family members provided a molecular means to examine the progression of segment identities during limb development and regeneration. During vertebrate limb development, a *HoxA9*⁺*HoxA11*[−]*HoxA13*[−] state reflects progenitor cells for the upper arm, *HoxA9*⁺*HoxA11*⁺*HoxA13*[−] for the lower arm, and *HoxA9*⁺*HoxA11*⁺*HoxA13*⁺ for the hand (16–20). The genes are expressed in a spatial and temporal sequence with *HoxA9* transcripts expressed first throughout the limb bud, followed closely by *HoxA11* more distally and lastly *HoxA13* in the distalmost tip, a phenomenon called temporal and spatial colinearity (21–23). This expression data coupled with functional studies have favored the conclusion that, during limb development,

¹Deutsche Forschungsgemeinschaft (DFG)–Center for Regenerative Therapies Dresden, Technische Universität Dresden, Germany. ²Max Planck Institute of Molecular Cell Biology and Genetics, Dresden, Germany. ³Center for Information Services and High Performance Computing, Technische Universität Dresden, Germany. ⁴Institute of Physics of Liquids and Biological Systems, Consejo Nacional de Investigaciones Científicas y Técnicas (CONICET) and University of La Plata, Argentina.

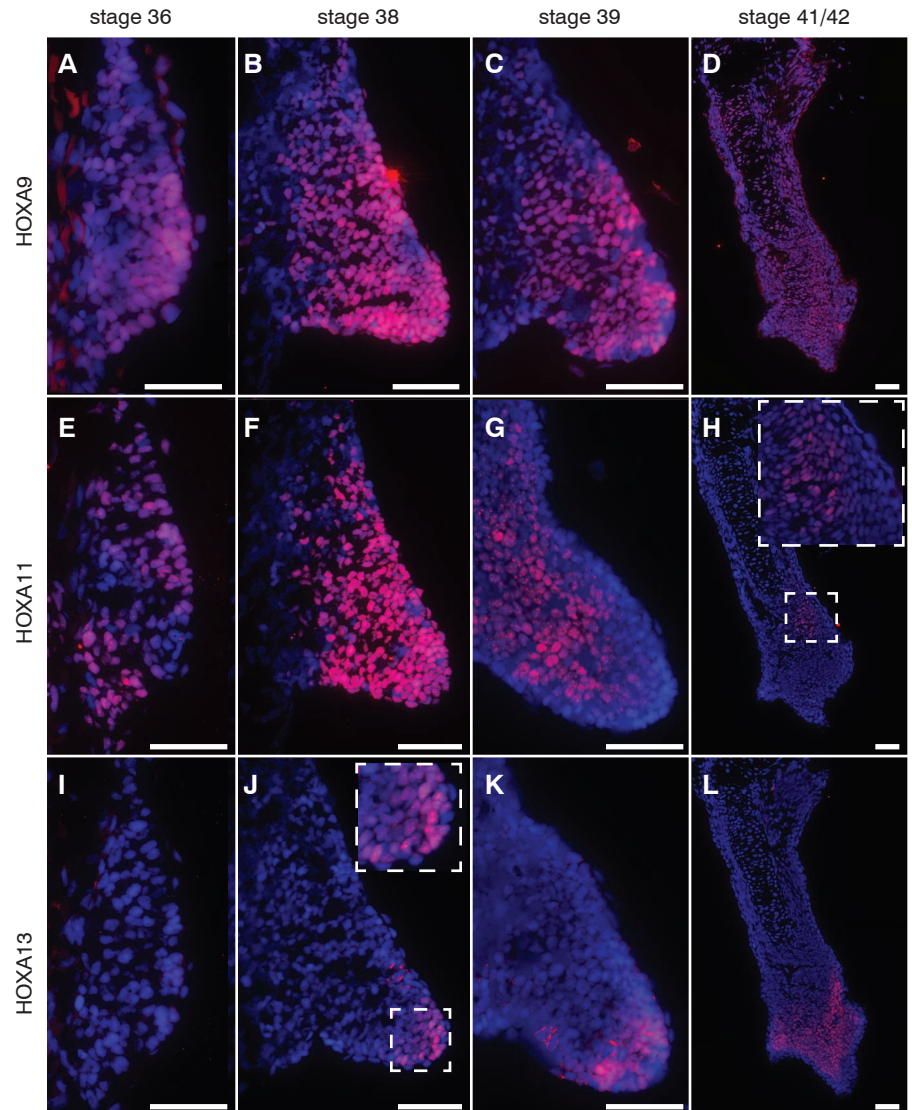
*These authors contributed equally to this work.

†Present address: DFG–Center for Regenerative Therapies Dresden, Technische Universität Dresden, Germany.

‡Corresponding author. E-mail: elly.tanaka@crt-dresden.de

Fig. 1. Sequential expression of HOXA9, HOXA11, and HOXA13 during axolotl limb development.

At stage 36, HOXA9 is expressed in the nascent limb bud (A), onset of HOXA11 expression is evident (E), and HOXA13 is absent (I). At stage 38, HOXA9 is expressed throughout the limb bud (B), HOXA11 is expressed with a more distal expression boundary (F), and HOXA13 is expressed in distal cells (J). At stage 39, HOXA9 is expressed throughout the limb bud (C), HOXA11 is depleted from the distal limb bud (G), and HOXA13 is expressed in distal cells (K). At stages 41/42, HOXA9 is expressed throughout the limb (D), HOXA11 is expressed in a small zone distal to the differentiating humerus and proximal to the emerging hand (H), and HOXA13 is the distal region differentiating hand (L). Hoechst nuclear signal is in blue. Anterior is at top; posterior, down; and distal, right. Scale bars indicate 100 μ m.



progenitor cells are specified in a proximal-to-distal sequence, although some intercalation models have been proposed (24–27).

Important work localizing *HoxA9* and *A13* transcripts in the regenerating *Ambystoma mexicanum* (axolotl) limb described coexpression of *HoxA13* with *HoxA9* at the earliest time points of regeneration, with emergence of a nested pattern later. Such coexpression suggested an unusual violation of colinearity and was consistent with the possibility of intercalation (28). The whole-mount analysis did not, however, yield cellular resolution, so the source of the signal remained unclear. The limb tissue 1 to 2 days postamputation (dpa) is a watery infiltrate of inflammation and clotting-associated material. Immune cells rather than prospective blastema cells could, for example, have

been a source of signal (29). Therefore, despite a historically strong interest in intercalation, definitive molecular or functional evidence for this mechanism was lacking. We reexplored this issue at higher molecular and cellular resolution.

We first examined the progression of HOXA9, A11, and A13 protein expression in axolotl limb development and confirmed spatial and temporal colinear expression (Fig. 1 and fig. S2) (21–23, 28). We next examined the sequence of HOXA protein expression in the regenerating upper limb blastema, including early time points. Because a morphologically defined blastema is not evident at 1 day, we examined limbs in which the relevant blastema precursors (connective tissue cells) expressed enhanced GFP (eGFP). We did not observe HOXA9, A11, or A13 signal in blastema cells at 1 day (Fig. 2,

A and B, and fig. S3). In particular, none of the HOXA13 immunofluorescence signal observed at 1 day colocalized with GFP⁺. HOXA13 was also absent at 4 dpa (fig. S4). By early-bud stage (6 dpa), HOXA9 and HOXA11 expression was evident throughout the blastema, but HOXA13 expression was still absent (Fig. 2, C, E, and G). By medium- and late-bud stages (8 and 12 dpa), a complete nested pattern was observed, with HOXA13 expressed strongly at the distal tip (Fig. 2, D, F, and H, and fig. S4, F to I). The late onset of *HoxA13* expression was corroborated by section in situ hybridization (fig. S5). Therefore, during regeneration posterior HOXA expression occurs colinearly, as in limb development, suggesting that regenerating limb segments are specified in a proximal-to-distal order and not by intercalation.

To confirm the association of HOXA13 expression with hand identity, we examined the onset of HOXA13 expression in hand amputations where we first detected signal already at 4 dpa and strongly by 6 dpa—well before onset of HOXA13 expression in the upper arm blastema (fig. S6). Systemic administration of retinoic acid (RA) is known to convert a hand blastema into an upper arm blastema (30–33). RA-treated hand blastemas at 4 and 6 dpa showed no detectable HOXA13 expression, confirming the sensitivity of HOXA13 immunostaining in detection of a hand determination state.

To functionally assess the order of blastema cell specification, we used transplantation to assay whether early upper-arm blastema cells have already acquired hand identity, as would be predicted by the intercalation model (Fig. 3 and fig. S7). Donor connective tissue-derived cells constitutively expressed eGFP from a genomically inserted transgene (12, 13). Control, medium-bud (8-day) hand blastema cells contributed only to hand structures when transplanted into a 6-day upper-arm blastema (Fig. 3, A, B, I, and J) (12, 33). Transplantation of distal tip cells from medium-bud upper-arm blastemas (HOXA13⁺) yielded distributions very similar to those of the hand blastema transplantations showing commitment of distal (HOXA13⁺) cells to hand by medium-bud stage (Fig. 3, C, D, I, and J). Donor cells from the proximal base of the 8-day upper-arm blastema distributed in both the lower arm and the hand, corresponding to HOXA9⁺HOXA13[−] upper-arm progenitor cell potential (Fig. 3, E, F, I, and J). Last, transplantation of the distal tip of early (4-day) blastema cells (pre-HOXA13) yielded cells in lower arm and hand (Fig. 3, G to J) corresponding to upper arm properties rather than hand-only identity. Taken together, these results indicate that blastema cells are specified in a proximal-to-distal sequence during regeneration rather than through intercalation.

In summary, HOXA protein data and functional assays indicate that, during axolotl limb regeneration, cell identities are specified in a proximal-to-distal order rather than by intercalation, indicating that the patterning mechanisms used in development and regeneration are similar. Although intercalation may not be the patterning mechanism underlying normal limb regeneration, intercalation

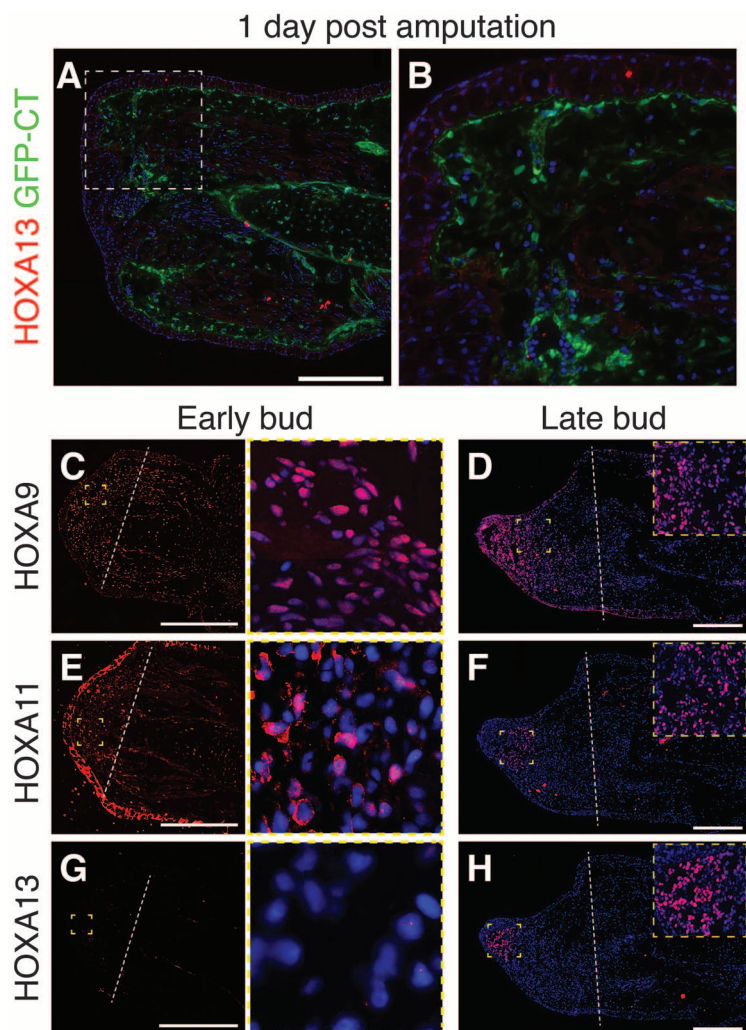
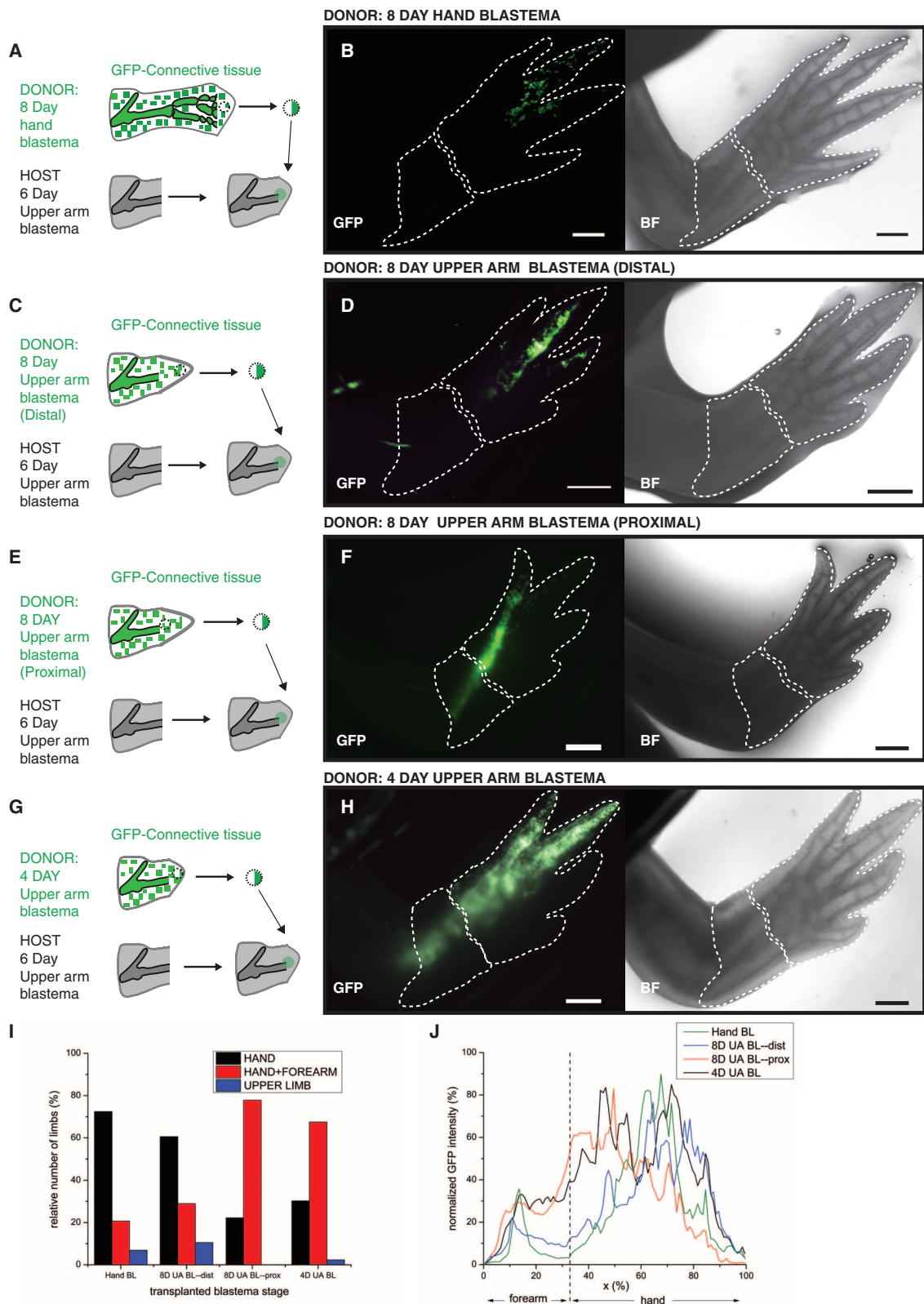


Fig. 2. Sequential expression of HOXA9, A11, and A13 protein during axolotl limb regeneration. Serial longitudinal sections of regenerating upper arm blastemas at 1 dpa, early bud (6 dpa), and late bud (12 dpa) immunostained for AxHOXA9, AxHOXA11, or AxHOXA13. (A) At 1 dpa, GFP-expressing blastema cell precursors from connective tissue (green) do not express HOXA13 (red). Image was taken at same exposure as in (H). (B) Zoom of area outlined in (A). Early bud blastema (6 dpa) expresses robust HOXA9 (C) and nascent HOXA11 (E) but does not express HOXA13 (G). Images at right show nuclei at higher zoom in positive zones. Late-bud blastema (12 dpa) expresses robust HOXA9 (D) and HOXA11 (F) and HOXA13 (H). HOXA9 is positive broadly in the blastema, HOXA11 in a medial band, and HOXA13 at the distal tip. Insets show positive nuclei at higher zoom. Dashed line, plane of amputation; distal, left; proximal, right. Scale bars, 500 μ m.

Fig. 3. Early blastema cells are not committed to a hand fate.

Commitment to hand identity correlates with late onset of *HOXA13* expression. Grafts of GFP-expressing connective tissue-derived blastema cells from different-stage blastemas were made into 6-day upper-arm blastema hosts to assay commitment to hand identity. (A) Schema of 8-day hand blastema (*HOXA13*⁺) transplanted into 6-day upper-arm blastema. (N = 29) (B) Representative experimental result of (A): GFP⁺ cells were found in hand. (C) Schema of a distal region of an 8-day upper arm blastema (*HOXA13*⁺) transplanted into 6-day blastema of a white host (N = 38). (D) Representative experimental result of (C): GFP⁺ cells were detected in the hand. (E) Schema of a proximal region of an 8-day upper arm blastema (*HOXA13*⁺) transplanted into 6-day blastema of a white host (N = 27). (F) Representative experimental result of (E): GFP⁺ cells were found all along the regenerated proximal/distal (P/D) axis. (G) Schema of an early 4-day upper arm blastema (pre-*HOXA13*) transplanted into a 6-day blastema host (N = 43). (H) Representative experimental result of (G). Upon regeneration, GFP⁺ cells were detected all along the P/D axis in the host. Dashed lines in (B), (D), (F), and (H) indicate the outline of the lower arm and hand. Scale bar, 1 mm. (I) The fraction of limbs showing GFP⁺ cells in hand only, hand and forearm, or in the upper arm for each transplantation category. Samples showing upper arm only (blue bar) represent samples where transplant was stuck at amputation plane. (J) Averages of normalized GFP fluorescence along the proximodistal axis for limbs in the different transplantation categories. The normalized lengths of the forearm and the hand calculated for all the limbs studied are indicated. x represents the percent distance between the base of the forearm and the tip of the hand. Standard deviations of the data are in fig. S7. D, day; UA, upper arm; BL, blastema.



and other cell-cell recognition events likely play a role in certain grafting situations and possibly in fine-tuning patterning via segment-specific adhesive properties (34–36).

References and Notes

1. V. French, P. J. Bryant, S. V. Bryant, *Science* **193**, 969–981 (1976).
2. M. Maden, J. Theor. Biol. **69**, 735–753 (1977).
3. S. V. Bryant, V. French, P. J. Bryant, *Science* **212**, 993–1002 (1981).
4. J. E. Mittenthal, *Dev. Biol.* **88**, 15–26 (1981).
5. H. Meinhardt, *J. Embryol. Exp. Morphol.* **76**, 139–146 (1983).
6. H. Meinhardt, *J. Embryol. Exp. Morphol.* **76**, 115–137 (1983).
7. H. Bohn, *Roux's Arch.* **165**, 303–341 (1970).
8. D. L. Stocum, *Dev. Biol.* **45**, 112–136 (1975).

9. L. E. Iten, S. V. Bryant, *Dev. Biol.* **44**, 119–147 (1975).
10. M. J. Pescitelli Jr., D. L. Stocum, *Dev. Biol.* **79**, 255–275 (1980).
11. E. G. Butler, H. F. Blum, *J. Natl. Cancer Inst.* **15**, 877–889 (1955).
12. M. Kragl et al., *Nature* **460**, 60–65 (2009).
13. E. Nacu et al., *Development* **140**, 513–518 (2013).
14. J. Faber, *Arch. Biol. (Liege)* **71**, 1–72 (1960).
15. K. Echeverri, E. M. Tanaka, *Dev. Biol.* **279**, 391–401 (2005).
16. A. P. Davis, D. P. Witte, H. M. Hsieh-Li, S. S. Potter, M. R. Capecchi, *Nature* **375**, 791–795 (1995).
17. Y. Yokouchi et al., *Genes Dev.* **9**, 2509–2522 (1995).
18. C. Fromental-Ramain et al., *Development* **122**, 461–472 (1996).
19. C. Fromental-Ramain et al., *Development* **122**, 2997–3011 (1996).
20. J. Zakany, D. Duboule, *Curr. Opin. Genet. Dev.* **17**, 359–366 (2007).
21. Y. Yokouchi, H. Sasaki, A. Kuroiwa, *Nature* **353**, 443–445 (1991).
22. H. Haack, P. Gruss, *Dev. Biol.* **157**, 410–422 (1993).
23. C. E. Nelson et al., *Development* **122**, 1449–1466 (1996).
24. M. Towers, L. Wolpert, C. Tickle, *Curr. Opin. Cell Biol.* **24**, 181–187 (2012).
25. A. Roselló-Díez, M. Torres, *Dev. Dyn.* **240**, 1203–1211 (2011).
26. C. Tabin, L. Wolpert, *Genes Dev.* **21**, 1433–1442 (2007).
27. F. V. Mariani, C. P. Ahn, G. R. Martin, *Nature* **453**, 401–405 (2008).
28. D. M. Gardiner, B. Blumberg, Y. Komine, S. V. Bryant, *Development* **121**, 1731–1741 (1995).
29. H. J. Lawrence, G. Sauvageau, R. K. Humphries, C. Largman, *Stem Cells* **14**, 281–291 (1996).
30. S. Saxena, I. A. Niazi, *Indian J. Exp. Biol.* **15**, 435–439 (1977).
31. M. Maden, *Nature* **295**, 672–675 (1982).
32. N. Mercader, E. M. Tanaka, M. Torres, *Development* **132**, 4131–4142 (2005).
33. K. Crawford, D. L. Stocum, *Development* **104**, 703–712 (1988).
34. N. Wada, H. Tanaka, H. Ide, T. Nohno, *Dev. Biol.* **264**, 550–563 (2003).
35. S. M. da Silva, P. B. Gates, J. P. Brookes, *Dev. Cell* **3**, 547–555 (2002).
36. M. Barna, L. Niswander, *Dev. Cell* **12**, 931–941 (2007).

Acknowledgments: We are grateful to H. Andreas, J. Michling, B. Gruhl, S. Moegel, and M. Armstead for animal

care; M. Tipword and D. Drechsel for antibody production; D. Gardiner for unpublished *HoxA11* fragment; F. Martin for initial cloning attempts; and J. Rink, J. Currie, and A. Gavalas for comments. National Center for Biotechnology Information accession numbers of axolotl genes are as follows: *HoxA9*, JX975067; *HoxA11*, JX975068; *HoxA13*, JX975069. Grant support came from DFG-SFB655: From Cells to Tissues (DFG TA274/2), DFG TA274/5, central funds of the Max Planck Institute for Cell Biology and Genetics and the Center for Regenerative Therapies, and Human Frontiers Science Program (E.M.T.). A.T. and E.M.T. designed, conceived experiments, and analyzed data. K.R. and A.T. performed experimental work and analyzed data. O.C. developed and performed image analysis. K.R., A.T., and E.M.T. prepared the manuscript. The authors claim no competing interests.

Supplementary Materials

www.sciencemag.org/content/342/6164/1375/suppl/DC1
Materials and Methods

Figs. S1 to S7

References (37–40)

11 June 2013; accepted 1 November 2013

10.1126/science.1241796

EMRE Is an Essential Component of the Mitochondrial Calcium Uniporter Complex

Yasemin Sancak,^{1,2} Andrew L. Markhard,¹ Toshimori Kitami,^{1,2*} Erika Kovács-Bogdán,¹ Kimberli J. Kamer,¹ Namrata D. Udeshi,² Steven A. Carr,² Dipayan Chaudhuri,^{3,4} David E. Clapham,³ Andrew A. Li,¹ Sarah E. Calvo,^{1,2} Olga Goldberger,¹ Vamsi K. Mootha^{1,2†}

The mitochondrial uniporter is a highly selective calcium channel in the organelle's inner membrane. Its molecular components include the EF-hand-containing calcium-binding proteins mitochondrial calcium uptake 1 (MICU1) and MICU2 and the pore-forming subunit mitochondrial calcium uniporter (MCU). We sought to achieve a full molecular characterization of the uniporter holocomplex (uniplex). Quantitative mass spectrometry of affinity-purified uniplex recovered MICU1 and MICU2, MCU and its paralog MCUB, and essential MCU regulator (EMRE), a previously uncharacterized protein. EMRE is a 10-kilodalton, metazoan-specific protein with a single transmembrane domain. In its absence, uniporter channel activity was lost despite intact MCU expression and oligomerization. EMRE was required for the interaction of MCU with MICU1 and MICU2. Hence, EMRE is essential for in vivo uniporter current and additionally bridges the calcium-sensing role of MICU1 and MICU2 with the calcium-conducting role of MCU.

The mitochondrial calcium uniporter is a highly selective channel that moves calcium ions across the mitochondrial inner membrane (1). Although its physiology has been studied for decades, a complete description of its molecular composition has remained elusive. Recently, integrative genomics methods enabled the discovery of the uniporter pore, mitochondrial

calcium uniporter (MCU), and its regulatory subunits, mitochondrial calcium uptake 1 and 2 (MICU1 and 2) (2–5). MCU is an integral membrane protein that is essential for the electrophysiologically defined uniporter current (6); it has two transmembrane domains and orients both its N and C termini into the matrix (3, 7). MICU1 contains EF-hand calcium binding domains and is found in the mitochondrial intermembrane space (IMS), where it serves as a calcium-sensing gatekeeper, keeping the channel closed when calcium levels are low and allowing the channel to open in response to transient rises (2, 5, 8, 9). Its paralog and binding partner, MICU2, has not been extensively characterized (5). Other proteins, including leucine-zipper EF-hand containing transmembrane protein 1 (LETM1), mitochondrial calcium uniporter regulator 1 (MCUR1), mitochondrial sodium calcium exchanger (NCLX), transient receptor

potential 3 (TRPC3), and uncoupling protein 2 and 3 (UCP2 and 3) are also crucial for mitochondrial calcium physiology, but their physical relation to the uniplex are unclear (10–14).

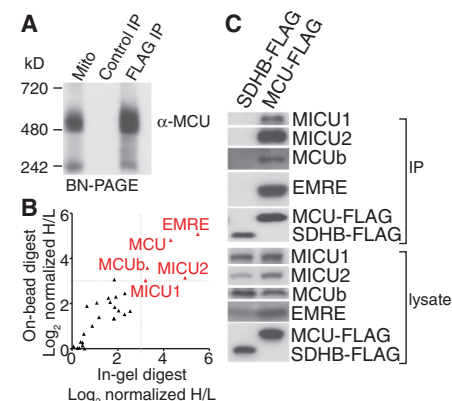


Fig. 1. Affinity purification and proteomic analysis of the uniplex. (A) MCU-FLAG or control SDHB-FLAG was stably expressed in HEK-293T cells. Proteins from digitonin-permeabilized mitochondria from MCU-FLAG-expressing cells and FLAG immunoprecipitations from SDHB-FLAG- and MCU-FLAG-expressing cells were subjected to blue native polyacrylamide gel electrophoresis (BN-PAGE) and immunoblotted with MCU antibody. (B) Identification of proteins that interact with MCU-FLAG. MCU-FLAG-expressing cells were grown in the presence of heavy amino acids; control HEK-293T cells were grown in the presence of light amino acids. FLAG immunoprecipitates from both samples were mixed and analyzed by mass spectrometry. The ratios of heavy and light proteins annotated with mitochondrial localization from two replicates are shown. Proteins that show more than eight-fold enrichment in heavy samples are shown in red. (C) Interaction of MCUB, MICU1, MICU2, and EMRE with MCU. MCU-FLAG or control SDHB-FLAG was immunoprecipitated from HEK-293T cells. Immunoprecipitates and cell lysates were analyzed by immunoblotting for the indicated proteins.

¹Department of Molecular Biology, Massachusetts General Hospital, Department of Systems Biology, Harvard Medical School, Boston, MA, USA. ²Broad Institute of Massachusetts Institute of Technology and Harvard, Cambridge, MA, USA. ³Howard Hughes Medical Institute, Department of Cardiology, Children's Hospital and Department of Neurobiology, Harvard Medical School, Boston, MA, USA. ⁴Cardiovascular Research Center, Massachusetts General Hospital, Boston, MA, USA.

*Present address: RIKEN Center for Integrative Medical Sciences, Yokohama, Japan.

†Corresponding author. E-mail: vamsi@hms.harvard.edu

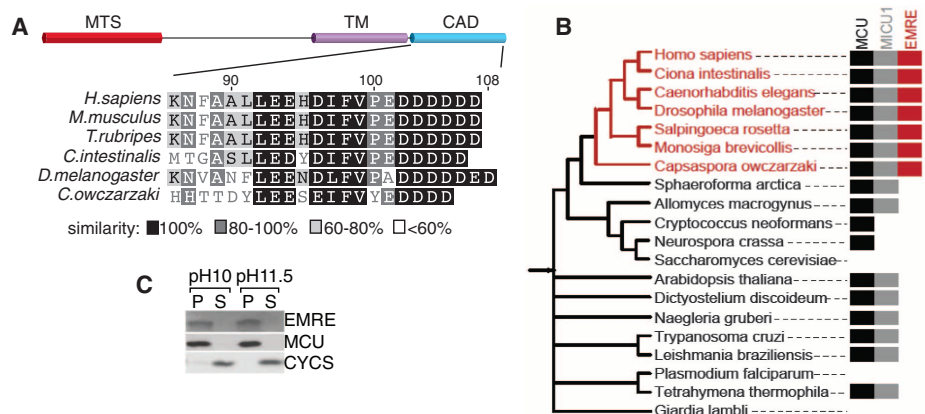


Fig. 2. Domain architecture, phylogeny, and membrane association of EMRE. (A) Schematics showing predicted mitochondrial targeting sequence (MTS), transmembrane (TM), and conserved carboxy terminal acidic domain (CAD) of EMRE. The CAD of EMRE from six species was aligned using Blocks Substitution Matrix (BLOSUM). (B) EMRE is metazoan-specific. Presence of homologs of MCU/MCUB, MICU1/MICU2, and EMRE across 20 selected species spanning the National Center for Biotechnology Information taxonomy tree, indicates that EMRE is a metazoan innovation. (C) EMRE is a membrane protein. HEK-293T cell mitochondria were isolated and proteins were extracted with 0.1 M Na₂CO₃ at pH 10 and pH 11.5. EMRE is observed in the insoluble pellet (P) similar to MCU. Cytochrome c (CYCS) is loosely associated with the inner membrane and is detected in the soluble fraction (S).

We took a biochemical approach to fully characterize the composition of the uniporter complex. We stably expressed MCU tagged with the FLAG epitope at its carboxy terminus (MCU-FLAG) in human embryonic kidney (HEK)-293T cells. MCU-FLAG restored mitochondrial calcium uptake in cells in which MCU was depleted with RNA interference (RNAi) and even caused a gain-of-function phenotype compared with that of cells that expressed a control protein (fig. S1A). MCU exists in a large protein complex when isolated by digitonin permeabilization and native gel electrophoresis of mitochondria from HeLa cells or mouse liver (3). Similarly, in HEK-293T cells that stably expressed MCU-FLAG, MCU migrated at ~480 kD (Fig. 1A). Immunoprecipitation of MCU-FLAG, but not that of a control protein, yielded a protein complex of comparable size (Fig. 1A). Hence, MCU-FLAG associates with the apparent uniporter holocomplex, which we call the uniplex (uniporter complex).

To define the components of the uniplex, we used a quantitative mass spectrometry approach using stable isotope labeling by amino acids in cell culture (SILAC) (15). We grew MCU-FLAG-

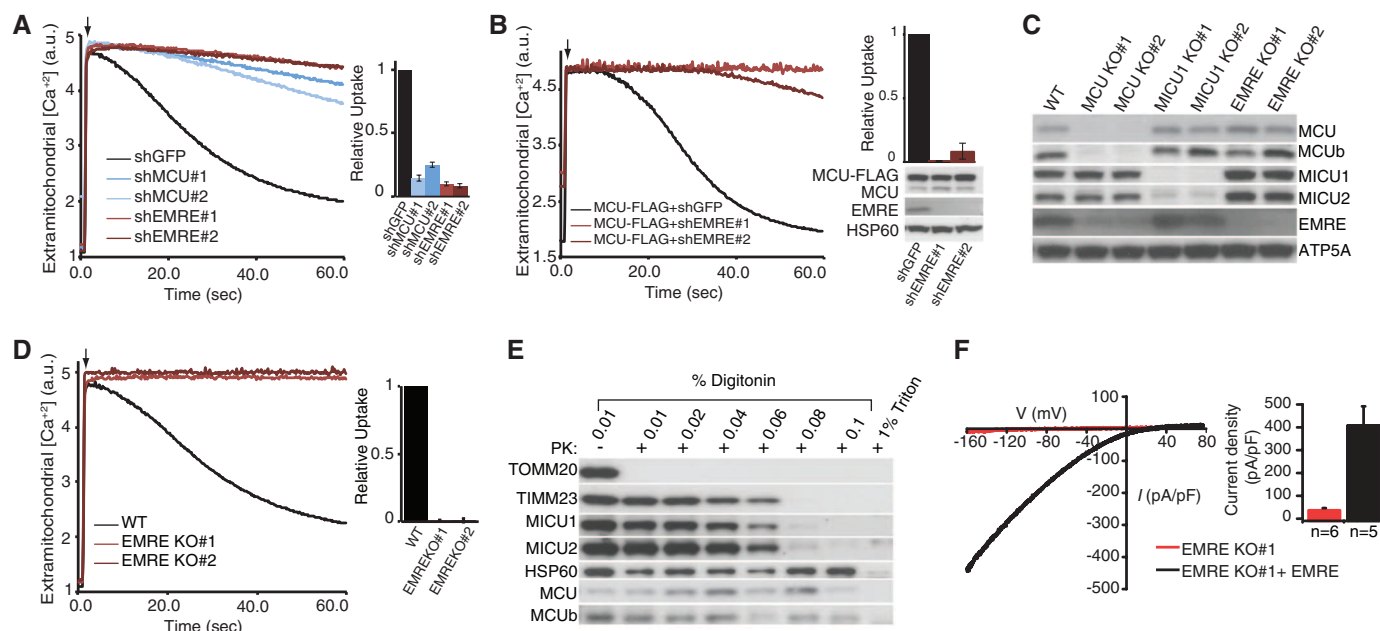


Fig. 3. Requirement of EMRE for uniporter activity. (A) EMRE knockdown impairs mitochondrial calcium uptake. Digitonin-permeabilized HEK-293T cells were incubated with the calcium indicator Oregon green BAPTA 6F (OGB6F). After addition of 50 μ M CaCl₂ (arrow), the depletion of extracellular calcium due to mitochondrial uptake was monitored by OGB6F fluorescence. Representative traces of mitochondrial calcium uptake from HEK-293T cells with green fluorescent protein (GFP) (control), MCU, and EMRE knockdown are shown. The bar graph shows the rate of calcium uptake relative to shGFP (a short-hairpin RNA against GFP) cells (mean \pm SD; $n = 4$ independent experiments). (B) MCU overexpression cannot rescue mitochondrial calcium uptake in EMRE knockdown cells. EMRE was knocked down in HEK-293T cells that overexpress MCU-FLAG. The samples were treated as in (A) ($n = 4$ independent experiments). Lysates were analyzed by immunoblotting for indicated proteins. (C) Loss of MCU decreases EMRE and MCUB abundance. MCU, MICU1, and EMRE knockout (KO) HEK-293T cells were generated using Transcription

Activator-Like Effector Nuclease (TALEN) technology, and cell lysates from wild-type (WT) and two independent knockout clones were prepared and analyzed by immunoblotting for control ATP5A and uniplex proteins (D) Mitochondrial calcium uptake is severely impaired in cells that lack EMRE. Mitochondrial calcium uptake was measured in WT and two independent EMRE KO cell lines as in (A). (E) Loss of EMRE does not change MCU, MCUB, MICU1, and MICU2 submitochondrial localization. Mitochondria were isolated from cells lacking EMRE and incubated with increasing concentrations of digitonin in the presence of proteinase K (PK); samples were analyzed by immunoblotting for outer membrane protein TOMM20, inner membrane protein TIMM23, and matrix protein HSP60, as well as uniplex proteins. (F) Exemplar trace (red) of a mitoplast derived from EMRE knockout cells demonstrates absent calcium current (I_{MiCa}), whereas typical I_{MiCa} is seen after EMRE is knocked back in (black). Voltage ramps were delivered from -160 mV to +80 mV for 750 ms, using a holding potential of 0 mV. (Right) Summary data (mean \pm SEM).

expressing and wild-type HEK-293T cells in medium containing heavy or light amino acid isotopes, respectively, immunoprecipitated proteins with FLAG antibody-conjugated beads and mixed heavy and light samples before they were processed for mass spectrometry. Two independent quantitative mass spectrometry experiments, with two different digestion protocols, reproducibly identified five known or predicted mitochondrial proteins associated with MCU-FLAG. (Fig. 1B and table S1). MCU was enriched in MCU-FLAG samples, as well as its known regulators MICU1 and MICU2. The uniplex also contains MCUb, a paralog of MCU (16). The only other mitochondrial protein revealed through this analysis was C22orf32, a previously uncharacterized protein that we call essential MCU regulator (EMRE). MICU1, MICU2, MCUb, and EMRE were detected by protein immunoblotting after immunoprecipitation of MCU-FLAG from

HEK-293T and HeLa cells, but not with FLAG-tagged succinate dehydrogenase complex subunit B (SDHB-FLAG), a protein also localized to the inner membrane (Fig. 1C and fig. S1B). Moreover, MCU overexpression resulted in increased abundance of MICU1, MICU2, and EMRE (Fig. 1C), probably because it stabilized its binding partners.

EMRE is a ~10-kD protein with a predicted mitochondrial targeting sequence, a predicted transmembrane domain (17, 18), and a highly conserved C terminus rich in aspartate residues (Fig. 2A). MCU and MICU1 are found in all major eukaryotic taxa, with lineage-specific losses in several clades. We did not find EMRE homologs in plants or protozoa. Analysis of recently sequenced opisthokonts and basal fungi revealed that EMRE homologs are not found in any fungi, indicating that it most likely arose in the metazoan lineage (Fig. 2B). EMRE RNA was broadly

expressed in all mouse tissues (fig. S2). Similar to MCU and MICU1, EMRE was identified by proteomic analysis of mitochondria (19), with a pattern suggesting that it is ubiquitously expressed in the mitochondria of all mammalian tissues. EMRE appears to be a bona fide transmembrane protein because it was resistant to carbonate extraction at high pH, as was MCU (Fig. 2C).

We tested the effect of loss of EMRE on uniplex function by RNAi-mediated silencing of EMRE. Depletion of EMRE with each of two sequence-independent hairpins led to loss of mitochondrial calcium uptake equivalent to MCU silencing in permeabilized HEK-293T and HeLa cells, as well as in intact HeLa cells after histamine stimulation (Fig. 3A and fig. S3, A and B). The appearance of the cells and their rates of proliferation were normal after EMRE silencing. The mitochondrial membrane potential was intact and could be depolarized in cells depleted of EMRE (fig. S3C), indicating that loss of calcium uptake was not a trivial consequence of loss of the mitochondrial membrane potential. Overexpression of MCU in cells depleted of EMRE failed to restore mitochondrial calcium uptake (Fig. 3B), suggesting that MCU is not sufficient for *in vivo* uniporter current as previously proposed (4).

To characterize complete loss-of-function phenotypes of uniplex components, we generated HEK-293T cells lacking MCU, MICU1, or EMRE with TALEN technology (Fig. 3C). Surprisingly, in cells lacking MCU, abundance of EMRE was decreased compared with that of wild-type cells (Fig. 3C). However, in these cells, abundance of *EMRE* mRNA was similar to that in wild-type cells (fig. S3D), suggesting that loss of EMRE occurred post-transcriptionally. Thus, EMRE may be destabilized when its binding partner MCU is lost, analogous to the dependence of MICU2 protein expression on MICU1 (Fig. 3C) (5). Cells lacking EMRE, similar to cells lacking MCU, exhibited severe defects in mitochondrial calcium uptake (Fig. 3D and fig. S3E). In cells lacking MICU1, depletion of EMRE also led to loss of mitochondrial calcium uptake (fig. S3F). Digitonin permeabilization of isolated mitochondria from control cell or cells lacking EMRE followed by proteolysis and Western blotting showed that abundance of other uniplex proteins and their mitochondrial localization did not change after loss of EMRE (Fig. 3, C and E, and fig. S3G). These experiments confirmed the topology of MCU (3, 7) and MICU1 (9) and showed that the topology of MCUb is similar to the topology of MCU and that MICU2 localizes to the intermembrane space like MICU1 (Fig. 3E and fig. S3G). To show that loss of EMRE specifically affects the uniporter conductance and not other mitochondrial parameters that will affect mitochondrial calcium uptake (e.g., proton motive force, pH, and buffering capacity), we voltage-clamped mitoplasts isolated from cells lacking EMRE or these same cells after stable expression of EMRE and measured mitochondrial calcium current (I_{MiCa}). Mitoplasts from cells lacking EMRE had dramatically reduced I_{MiCa} ,

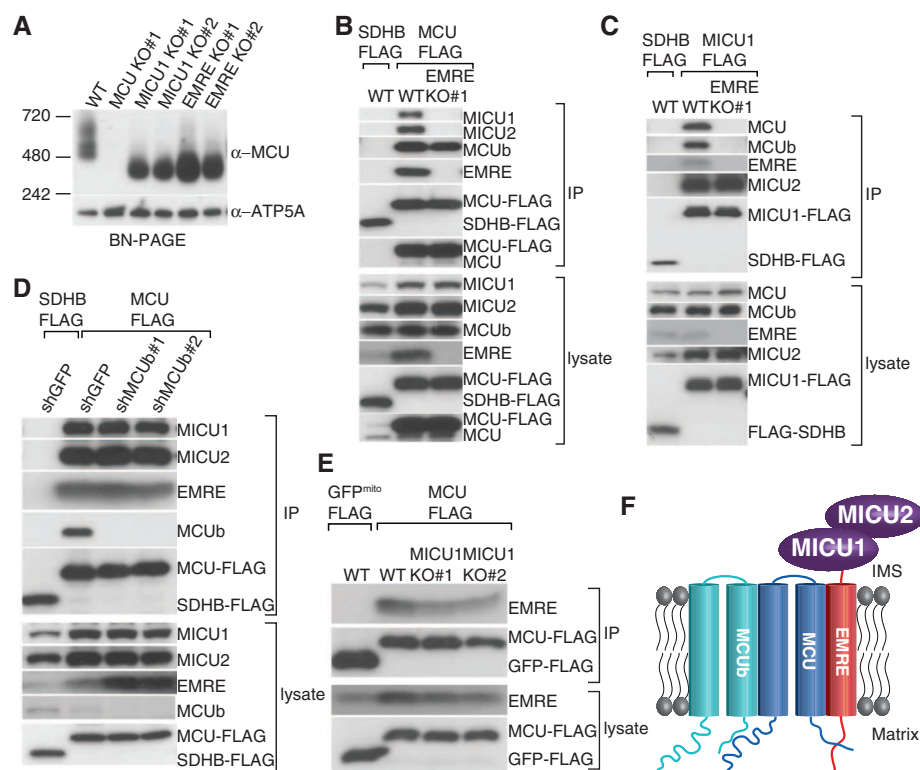


Fig. 4. Requirement of EMRE for the interaction of MCU with MICU1 and MICU2. (A) Loss of EMRE or MICU1 reduces the size of the uniplex to ~300 kD. Mitochondria from indicated cell lines were isolated, digitonin-permeabilized, and immunoblotted for MCU after BN-PAGE. EMRE mediates MCU-MICU1 and MICU2 interaction. Stably expressed SDHB-FLAG (control) or MCU-FLAG (B) or MICU1-FLAG (C) was immunoprecipitated from WT or EMRE knockout cells; lysates and immunoprecipitates were analyzed by immunoblotting for indicated proteins. (D) Loss of MCUb does not alter MCU-EMRE, MICU1, and MICU2 interaction. Stably expressed SDHB-FLAG or MCU-FLAG was immunoprecipitated from cells after GFP (control) or MCUb knockdown with two different hairpins. Samples were treated and analyzed as in (B). (E) Loss of MICU1 does not alter MCU-EMRE interaction. Plasmid for EMRE expression was cotransfected with plasmids for control mitochondrial GFP-FLAG or MCU-FLAG expression in WT and MICU1 knockout cells. Samples were treated and analyzed as in (B). (F) Model showing submitochondrial localization and organization of uniplex proteins. MCU is the pore-forming component of the uniplex; MICU1 and MICU2 reside in the IMS, where they sense outside calcium and regulate MCU through EMRE. EMRE is a single-pass transmembrane protein. It bridges MCU and MICU1 and MICU2 and is essential for the activity of the uniporter. MCU-MCUb interaction is not mediated by EMRE.

whereas typical I_{MiCa} was seen after EMRE re-expression (Fig. 3F) (6).

Consistent with EMRE being a core component of the uniplex, when EMRE was lost, the size of the complex on a native gel was reduced to ~300 kD, similar to that in cells lacking MICU1 (Fig. 4A). The observation that loss of either EMRE or MICU1 reduced the size of the native complex to a similar extent raised the hypothesis that EMRE may mediate interaction between MCU and MICU1 and MICU2. To test this, we stably expressed MCU-FLAG, or a control protein in HEK-293T, or HeLa wild-type cells, or cells lacking EMRE and performed FLAG immunoprecipitations. In wild-type cells, MICU1 and MICU2 immunoprecipitated with MCU-FLAG but not with control SDHB-FLAG (Fig. 4B and fig. S4). However, in cells lacking EMRE, the interaction between MCU-FLAG and MICU1 and MICU2 was completely lost (Fig. 4B and fig. S4). Similarly, MCU was not associated with immunoprecipitated MICU1-FLAG in cells lacking EMRE (Fig. 4C). In the absence of EMRE, MCU still oligomerized (Fig. 4, A and B) and interacted with MCUB. Moreover, in the absence of EMRE, the interaction between MICU1 and MICU2 was intact (Fig. 4C). These data indicate that loss of EMRE specifically interrupted the association of MCU with MICU1 and MICU2. Furthermore, MCUB, MICU1, and MICU2 appear to be dispensable for MCU-EMRE interaction because in cells lacking MCUB or MICU1, EMRE was still associated with immunoprecipitated MCU-FLAG (Fig. 4, D and E).

We propose a model in which EMRE interacts with MICU1 and MICU2 in the IMS and with MCU oligomers in the inner membrane, thus linking the calcium-sensing activity of MICU1

and MICU2 to the channel activity of MCU (Fig. 4F). The fact that our immunoprecipitated complex migrates at the same apparent molecular size as the uniporter from purified mitochondria (Fig. 1A), and recovers the founding members of the complex, suggests that we immunoprecipitated all of its components. It is notable that although other proteins have been reported to participate in mitochondrial calcium handling—such as LETM1, NCLX, UCP2 and 3, MCUR1, and TRPC3—they were not recovered in our proteomic assay, suggesting that they play key roles outside of the uniplex. A key insight from the current work is that EMRE is essential for in vivo uniporter current (I_{MiCa}) and that MCU oligomers alone are not sufficient for in vivo uniporter activity, in contrast to what has been suggested using in vitro bilayer studies (4). Why MCU needs association with EMRE for in vivo calcium conductance requires further investigation. Phylogenetic analyses indicate that the uniporter must have been a feature of the earliest mitochondria because MCU and MICU1 are found within all major eukaryotic taxa, with lineage-specific losses (20). EMRE is unique among human uniplex components in that it appears to have emerged more recently and represents a metazoan innovation. Its identification should help us understand how the activity and regulation of this ancient channel evolved.

References and Notes

1. Y. Kirichok, G. Grapivinsky, D. E. Clapham, *Nature* **427**, 360–364 (2004).
2. F. Perocchi *et al.*, *Nature* **467**, 291–296 (2010).
3. J. M. Baughman *et al.*, *Nature* **476**, 341–345 (2011).
4. D. De Stefani, A. Raffaello, E. Teardo, I. Szabò, R. Rizzuto, *Nature* **476**, 336–340 (2011).

5. M. Plovanich *et al.*, *PLOS ONE* **8**, e55785 (2013).
6. D. Chaudhuri, Y. Sancak, V. K. Mootha, D. E. Clapham, *Life* **2**, e00704 (2013).
7. J. D. Martell *et al.*, *Nat. Biotechnol.* **30**, 1143–1148 (2012).
8. K. Mallilankaraman *et al.*, *Cell* **151**, 630–644 (2012).
9. G. Csordás *et al.*, *Cell Metab.* **17**, 976–987 (2013).
10. R. Palty *et al.*, *J. Biol. Chem.* **279**, 25234–25240 (2004).
11. D. Jiang, L. Zhao, D. E. Clapham, *Science* **326**, 144–147 (2009).
12. K. Mallilankaraman *et al.*, *Nat. Cell Biol.* **14**, 1336–1343 (2012).
13. S. Feng *et al.*, *Proc. Natl. Acad. Sci. U.S.A.* **110**, 11011–11016 (2013).
14. M. Trenker, R. Malli, I. Fertschaj, S. Levak-Frank, W. F. Graier, *Nat. Cell Biol.* **9**, 445–452 (2007).
15. S. E. Ong *et al.*, *Mol. Cell. Proteomics* **1**, 376–386 (2002).
16. A. Raffaello *et al.*, *EMBO J.* **32**, 2362–2376 (2013).
17. A. Krogh, B. Larsson, G. von Heijne, E. L. Sonnhammer, *J. Mol. Biol.* **305**, 567–580 (2001).
18. M. G. Claros, P. Vincens, *Eur. J. Biochem.* **241**, 779–786 (1996).
19. D. J. Pagliarini *et al.*, *Cell* **134**, 112–123 (2008).
20. A. G. Bick, S. E. Calvo, V. K. Mootha, *Science* **336**, 886 (2012).

Acknowledgments: We thank Z. Grabarek and D. M. Shechner for helpful discussions. Y.S. received support from the Helen Hay Whitney Foundation. D.C. received support from NIH F32HL107021. D.E.C. is an Investigator of the Howard Hughes Medical Institute. This work was supported by grants to V.K.M. from NIH DK080261 and a gift from W. Dan and Pat Wright.

Supplementary Materials

www.sciencemag.org/content/342/6164/1379/suppl/DC1
Materials and Methods

Figs. S1 to S4

Table S1

References (21–33)

10 July 2013; accepted 5 November 2013

Published online 14 November 2013;

10.1126/science.1242993

Direct and Reversible Hydrogenation of CO₂ to Formate by a Bacterial Carbon Dioxide Reductase

K. Schuchmann and V. Müller*

Storage and transportation of hydrogen is a major obstacle for its use as a fuel. An increasingly considered alternative for the direct handling of hydrogen is to use carbon dioxide (CO₂) as an intermediate storage material. However, CO₂ is thermodynamically stable, and developed chemical catalysts often require high temperatures, pressures, and/or additives for high catalytic rates. Here, we present the discovery of a bacterial hydrogen-dependent carbon dioxide reductase from *Acetobacterium woodii* directly catalyzing the hydrogenation of CO₂. We also demonstrate a whole-cell system able to produce formate as the sole end product from dihydrogen (H₂) and CO₂ as well as syngas. This discovery opens biotechnological alternatives for efficient CO₂ hydrogenation either by using the isolated enzyme or by employing whole-cell catalysis.

Future energy demands require alternatives for the current energy technologies that are based mainly on fossil fuels. Hydrogen is a promising and widely considered option as alternative energy feedstock, but research on direct hydrogen storage and transportation has not re-

vealed economically usable possibilities (1). A promising alternative is the use of CO₂ as storage material for hydrogen (2). The near-equilibrium hydrogenation of CO₂ leads to formic acid and the corresponding base formate, respectively. This low energy demand is beneficial for a hydrogen

storage application for a hydrogen-using fuel cell. An alternative would be the use of a fuel cell directly using formate (3). Unfortunately, high temperatures and pressures are often required for efficient chemical hydrogenation of CO₂ (4). Recently, progress has been made by using an iridium catalyst to reversibly hydrogenate CO₂ at near-ambient conditions, but still with moderate catalytic rates (5), or by the use of a cobalt-based catalyst in combination with high concentration of an expensive base (6).

Biological systems are often promising alternatives for chemically difficult conversions. Even though the reduction of CO₂ is a widely distributed reaction in nature, little is known about enzymes catalyzing CO₂ reduction activity, and no enzyme is known to catalyze the direct hydrogenation of CO₂ alone (7, 8). One isolated formate dehydrogenase (FDH) could be shown to reduce CO₂ electrochemically, but not with H₂ as the electron donor (9). Acetogenic bacteria are

Molecular Microbiology and Bioenergetics, Institute of Molecular Biosciences, Johann Wolfgang Goethe University Frankfurt/Main, Max-von-Laue-Strasse 9, 60438 Frankfurt, Germany

*Corresponding author. E-mail: vmueller@bio.uni-frankfurt.de

promising candidates for such enzymes based on the physiological use of $\text{H}_2 + \text{CO}_2$ as the sole growth substrate and the production of formate as intermediate (10, 11). One enzyme was reported that can catalyze the hydrogenation of CO_2 at the purified state, but it also uses the reduced form of nicotinamide adenine dinucleotide phosphate (NADPH) and reduced ferredoxin as electron donors in an electron-bifurcating manner (12).

Here, we report the discovery of a bacterial hydrogen-dependent carbon dioxide reductase (HDCR) that directly uses dihydrogen for the interconversion of CO_2 to formate from the acetogenic bacterium *Acetobacterium woodii*. We targeted this bacterium because it grows with $\text{H}_2 + \text{CO}_2$ at ambient conditions using an ancient pathway for energy conservation. It lives under extreme energy limitation, and a direct use of H_2 for CO_2 reduction would be beneficial for the cell. Moreover, an HDCR was predicted from the genome sequence (13).

The HDCR enzyme was purified from cells of *A. woodii* under anaerobic conditions (14). The purified protein complex is composed of four different subunits (fig. S1A). It eluted as a single peak from a gel filtration with an apparent mass around 3500 kD but dissociated during separation by clear native page (fig. S2). The calculated molecular mass of the monomeric complex is 169 kD. Peptide mass fingerprinting

identified four proteins encoded by the gene cluster *Awo_c08190-08260* (fig. S1, B and C). A putative formate dehydrogenase (FdhF1/2) and an iron-iron hydrogenase (HydA2) form the two large subunits accompanied by two small electron transfer subunits (HycB1/2/3). The genome encodes a selenium-containing (FdhF2) and a selenium-free (FdhF1) FDH whose genes are in tandem on the chromosome. Because cells were grown in selenium-containing media, mostly FdhF2 was found. A gene encoding an electron transfer protein follows each FDH gene. The metal content determined by inductively coupled plasma mass spectrometry (ICP-MS) measurements was 0.6 molybdenum, no tungsten, 0.8 selenium, 0.7 zinc and 39 ± 6 iron atoms. These values are in agreement with the predicted cofactors (table S1).

By using the artificial electron acceptor methylviologen, we were able to measure hydrogenase and FDH activity separately. The isolated enzyme catalyzed formate oxidation with an activity of $\sim 600 \mu\text{mol formate min}^{-1} \text{mg}^{-1}$ and hydrogen oxidation with $10,800 \mu\text{mol H}_2 \text{min}^{-1} \text{mg}^{-1}$. Specific activities varied between different enzyme preparations due to the high oxygen sensitivity. The Michaelis constant (K_M) values for formate and hydrogen were determined to be $1 \pm 0.3 \text{ mM}$ (SEM; $N = 2$ independent experiments) and $125 \pm 31 \mu\text{M}$ (SEM; $N = 3$ independent experiments), respectively (fig. S3). The pH range for

maximal activity was between 7 and 9 for both activities (fig. S4). The temperature optimum for hydrogen oxidation was 30°C , that for formate oxidation 40°C (fig. S5). HCO_3^- reductase activity with reduced methylviologen as electron donor was catalyzed with 132 U/mg and a K_M of $37 \pm 4 \text{ mM HCO}_3^-$ (SEM; $N = 3$ independent experiments) (fig. S6).

Searching for an enzyme that directly hydrogenates CO_2 , we investigated whether the purified complex can catalyze this reaction. The enzyme indeed catalyzed the hydrogenation of CO_2 with a rate of $10 \mu\text{mol formate produced min}^{-1} \text{mg}^{-1}$ (Fig. 1A). Recently reported chemical catalysts promote the hydrogenation of CO_2 at comparable conditions with an initial turnover frequency (TOF) of $\sim 70 \text{ hours}^{-1}$ (5). The purified HDCR catalyzes the same reaction at 30°C with a TOF of $101,600 \text{ hours}^{-1}$. Thus, the enzyme is nearly 1500 times as effective as these chemical catalysts. The reverse reaction, formate oxidation to H_2 and CO_2 , was catalyzed with 14 U/mg (Fig. 1B). The enzyme has two advantages in industrial applications. First, it does not need an external cofactor as electron carrier. Cofactor-dependent conversion would raise the cost of such a process even if regeneration systems would be used. Second, the reaction is reversible, and thus the directionality is easy to control by substrate concentrations.

Purified HDCR also catalyzed the reduction of CO_2 with reduced ferredoxin instead of H_2 as electron donor. The rate of ferredoxin-dependent formate production was $0.6 \mu\text{mol formate min}^{-1} \text{mg}^{-1}$ (Fig. 1C). Ferredoxin was reduced by CO dehydrogenase (CODH) from *A. woodii*, leading to formate production from CO. The reverse reaction was catalyzed with rates of $0.6 \mu\text{mol ferredoxin min}^{-1} \text{mg}^{-1}$ and a K_M for ferredoxin of $13 \pm 5 \mu\text{M}$ (SEM; $N = 3$ independent experiments) (fig. S7). Industrially produced hydrogen often contains remaining CO that is a potent inhibitor of fuel-cell catalysts. Considering *A. woodii* HDCR as a catalyst for hydrogen storage, the side activity represents a possible industrial advantage. Using a combination of HDCR and CODH would allow the complete conversion of gas mixtures containing H_2 , CO_2 , and CO (Fig. 2).

To get insights into the reaction mechanism of the HDCR, we searched for compounds that inhibit partial reactions. CO turned out to be a potent inhibitor of the hydrogenase activity alone (fig. S8A). In the presence of 10% CO in the gas phase, only the FDH module is active. Under these conditions, formate-dependent ferredoxin reduction rates increased, showing that the hydrogenase moiety is not involved in this electron transfer (fig. S8B). Ferredoxin reduction with rates of $0.4 \mu\text{mol ferredoxin min}^{-1} \text{mg}^{-1}$ was also observed, with H_2 as electron donor instead of formate when CO_2 was omitted. If CO_2 and ferredoxin were present simultaneously, both were reduced concurrently, although apparently without any coupling because the velocity of

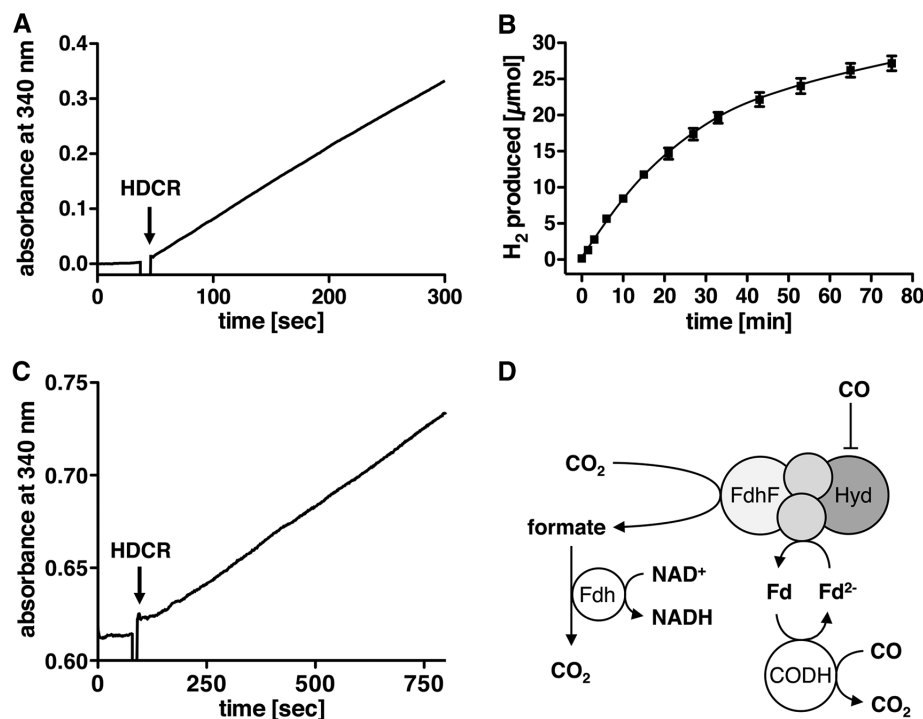


Fig. 1. Reactions catalyzed by the purified HDCR complex. (A) Formate production from $\text{H}_2 + \text{CO}_2$. At the time point indicated, $2 \mu\text{g}$ HDCR was added. Formate was measured using nicotinamide adenine dinucleotide (NAD)-dependent FDH from *Candida boidinii*. (B) Hydrogen production from formate (50 mM) ($10 \mu\text{g}$ HDCR). All data points are mean \pm SEM; $N = 6$ independent experiments. (C) Formate production with ferredoxin as electron donor ($3.5 \mu\text{g}$ HDCR). (D) Set-up of the measurement from (C). Ferredoxin was reduced by CODH with electrons from CO oxidation. Formate was measured as described for (A).

each reaction did not vary in dependence with the other one.

Because the reduction of CO_2 does not require additional cellular electron carriers, the conversion is independent of the cell metabolism. This opens the possibility of using the HDCR in whole-cell catalysis by separating growth and energy conservation from the hydrogenation of CO_2 . To test this, we used whole cells of *A. woodii* that produce acetate as the major end product from $\text{H}_2 + \text{CO}_2$. The energy metabolism of *A. woodii* is strictly sodium ion-dependent and depends on a sodium ion gradient across the cytoplasmic membrane (15). We used this trait to block the energy metabolism by omitting sodium ions from the buffer or by adding a sodium ionophore (fig. S9). Under these conditions, acetate production ceased almost completely, and formate was produced with an initial rate of $2 \mu\text{mol min}^{-1} \text{mg}^{-1}$ cell protein (fig. S10). The formate produced was excreted from the cells. Formate production from $\text{H}_2 + \text{CO}_2$ using whole cells was also observed in other systems, but different enzymes seem to be responsible there (16–18). For further experiments, we used KHCO_3 as substrate; thereby, the overall process is almost pH neutral compared with the production of formic acid from CO_2 . The genome of *A. woodii* encodes for a carboanhydrase that allows the rapid interconversion of CO_2 and HCO_3^- . Up to 0.45 M HCO_3^- , the final formate concentration increased with increasing substrate concentration (Fig. 3). At $1 \times 10^5 \text{ Pa H}_2$, the thermodynamic equilibrium is approximately $[\text{HCO}_3^-] = [\text{HCOO}^-]$. Indeed, up to 0.45 M HCO_3^- the final formate concentration fits well to the theoretic thermodynamic limit of the reaction, underlining the independence of the carboxylation of $\text{CO}_2/\text{HCO}_3^-$ from other cellular processes. There is apparently no substantial loss in unwanted side products or biomass production.

Acetogenic bacteria such as *A. woodii* are also able to use syngas, a mixture of H_2 , CO_2 , and CO , as substrate for acetogenesis. Syngas fermentation is an increasingly considered “green” option for the production of chemicals (19). As a proof of principle, we tested whether syngas can also be used as substrate for the production of formate. Indeed, HDCR in combination with CODH catalyzed formate production from syngas with 1.3 U/mg (Fig. 4A). The whole cell system produced formate from syngas as well, albeit with lower activities compared with $\text{H}_2 + \text{CO}_2$ alone (Fig. 4B). In contrast to $\text{H}_2 + \text{CO}_2$ as substrate, acetate formation could not completely be inhibited in our test system. Based on the results with whole cells, a two-step process can be imagined where the bacteria could be grown using syngas or a mixture of only $\text{H}_2 + \text{CO}_2$ as a substrate, and by disabling the metabolism the hydrogenation of CO_2 could be induced and H_2 could be stored as formate (fig. S11). In this scenario, the greenhouse gas CO_2 is not only used as storage material for H_2 but, additionally, is consumed as growth substrate.

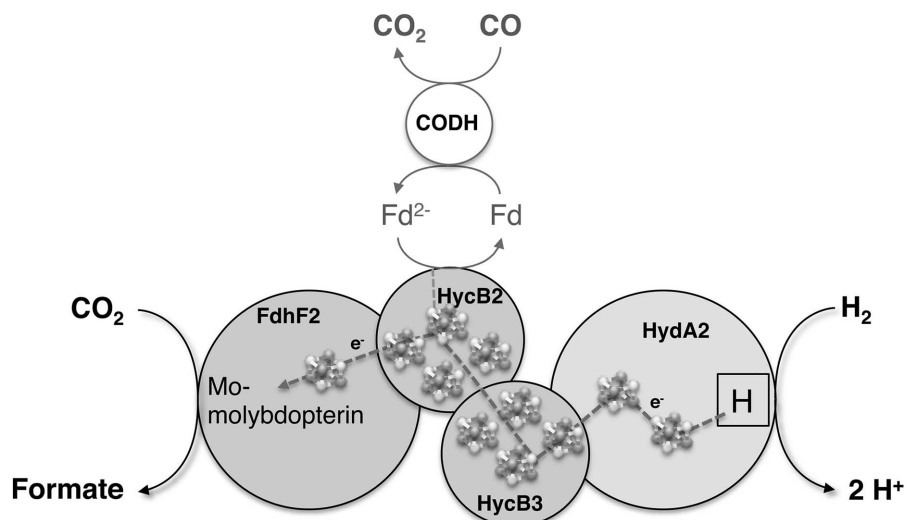


Fig. 2. Model of the HDCR from *A. woodii*. Electrons for CO_2 reduction are either provided by the hydrogenase subunit HydA2, where hydrogen oxidation takes place, or by reduced ferredoxin. The latter can be reduced using carbon monoxide and CODH, for example. Electrons are delivered to the active site for CO_2 reduction in FdhF2 via the electron-transferring subunits HycB2/3. Iron sulfur clusters are indicated.

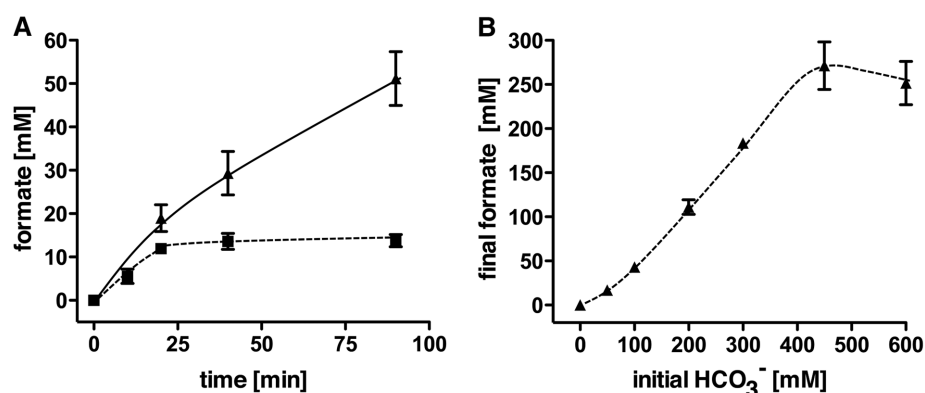


Fig. 3. Production of formate using whole-cell catalysis. (A) Whole cells of *A. woodii* were incubated with H_2 and CO_2 (squares) or H_2 and 0.3 M KHCO_3 in buffer containing $30 \mu\text{M}$ ETH2120 and 20 mM NaCl. (B) The final concentration of formate that was produced by whole cells is plotted against the initial concentration of HCO_3^- used (100% H_2 as gas phase). All data points are mean \pm SEM; $N = 3$ independent experiments.

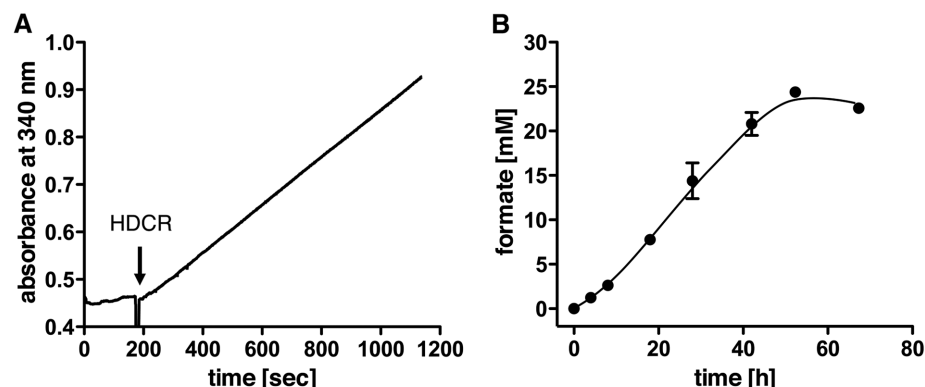


Fig. 4. Formate production from syngas. (A) Purified HDCR ($4 \mu\text{g}$) together with CODH and ferredoxin catalyzed formate production from syngas. Formate was measured using NAD-dependent FDH from *C. boidinii*. (B) Formate was also produced from syngas by whole cells in the presence of ETH2120 and NaCl. At the final time point, 60 mM acetate were produced in addition to formate. All data points are mean \pm SEM; $N = 3$ independent experiments.

We finally want to address the physiological implications of the properties of HDCR. Based on the genome sequence, the two FDHs in the HDCR context seem to be the only enzymes with FDH activity in *A. woodii*. Thus, the HDCR complex is essential for the first step in the reductive acetyl-CoA pathway. In agreement with this notion are data from proteome analysis, which revealed no differential expression between $H_2 + CO_2$ or fructose as substrate (13). Acetogenesis from fructose or other substrates does not yield H_2 directly but reduced ferredoxin. Thus, the second H_2 -independent entry path for electrons is favorable. In addition, CO inhibits the hydrogenase module, but CO-derived electrons can still enter the complex for CO_2 reduction via ferredoxin. The ferredoxin entry path also ensures growth at low H_2 partial pressures. Then the electron-bifurcating hydrogenase may generate reduced ferredoxin for CO_2 reduction (20).

Enzymes similar to the HDCR reported here seem to play an important role in other bacteria as well (see table S2 for the occurrence and previous description of HDCR-like gene clusters in other prokaryotic genomes). A similar gene cluster was predicted in the acetogen *Treponema primitia* (21). HDCR-type enzymes are not restricted to acetogens, but they, for example, have also proposed functions in sulfate reducing or-

ganisms (22) and syntrophic associations (23). Some gene clusters coding for predicted HDCRs vary in the composition compared with the enzyme in the present study—for example, the number of hydrogenase subunits.

References and Notes

- L. Schlapbach, A. Züttel, *Nature* **414**, 353–358 (2001).
- S. Enthaler, J. von Langermann, T. Schmidt, *Energy Environ. Sci.* **3**, 1207–1217 (2010).
- N. M. Aslam, M. S. Masdar, S. K. Kamarudin, W. R. W. Daud, *APCBEE Procedia* **3**, 33–39 (2012).
- E. Fujita, J. T. Muckerman, Y. Himeda, *Biochim. Biophys. Acta* **1827**, 1031–1038 (2013).
- J. F. Hull et al., *Nat. Chem.* **4**, 383–388 (2012).
- M. S. Jeletic, M. T. Mock, A. M. Appel, J. C. Linehan, *J. Am. Chem. Soc.* **135**, 11533–11536 (2013).
- B. R. Crable, C. M. Plugge, M. J. McInerney, A. J. Stams, *Enzyme Res.* **2011**, 532536 (2011).
- A. M. Appel et al., *Chem. Rev.* **113**, 6621–6658 (2013).
- T. Reda, C. M. Plugge, N. J. Abram, J. Hirst, *Proc. Natl. Acad. Sci. U.S.A.* **105**, 10654–10658 (2008).
- S. L. D. H. Drake, C. Matthies, K. Küsel, in *Acetogenesis*, H. L. Drake, Ed. (Chapman and Hall, New York, 1994), pp. 3–60.
- V. Müller, F. Imkamp, A. Rauwolf, K. Küsel, H. L. Drake, in *Strict and Facultative Anaerobes: Medical and Environmental Aspects*, M. M. Nakano, P. Zuber, Eds. (Horizon Biosciences, Norfolk, 2004), pp. 251–281.
- S. Wang et al., *J. Bacteriol.* **195**, 4373–4386 (2013).
- A. Poehlein et al., *PLOS ONE* **7**, e33439 (2012).
- Materials and methods are available as supplementary materials on Science online.
- S. Schmidt, E. Biegel, V. Müller, *Biochim. Biophys. Acta* **1787**, 691–696 (2009).
- S. M. da Silva et al., *Microbiology* **159**, 1760–1769 (2013).
- W. M. Wu, R. F. Hickey, M. K. Jain, J. G. Zeikus, *Arch. Microbiol.* **159**, 57–65 (1993).
- A. M. Klibanov, B. N. Alberti, S. E. Zale, *Biotechnol. Bioeng.* **24**, 25–36 (1982).
- P. C. Munasinghe, S. K. Khanal, *Bioresour. Technol.* **101**, 5013–5022 (2010).
- K. Schuchmann, V. Müller, *J. Biol. Chem.* **287**, 31165–31171 (2012).
- E. G. Matson, X. Zhang, J. R. Leadbetter, *Environ. Microbiol. Rep.* **12**, 2245–2258 (2010).
- I. A. Pereira et al., *Front. Microbiol.* **2**, 69 (2011).
- N. Müller, P. Worm, B. Schink, A. J. Stams, C. M. Plugge, *Environ. Microbiol. Rep.* **2**, 489–499 (2010).

Acknowledgments: We are grateful to M. Herzberg and D. Nies for the ICP-MS measurements and to J. Langer for protein identification via peptide mass fingerprinting. This work was supported by grants from the Deutsche Forschungsgemeinschaft and the German National Academic Foundation. Part of this work is filed as a patent (EP-No. 13172411.4). The data reported in this paper are tabulated in the supplementary materials.

Supplementary Materials

www.sciencemag.org/content/342/6164/1382/suppl/DC1
Materials and Methods
Figs. S1 to S11
Tables S1 and S2
References (24–28)

15 August 2013; accepted 28 October 2013
10.1126/science.1244758

Genetic and Molecular Basis of Drug Resistance and Species-Specific Drug Action in Schistosome Parasites

Claudia L. L. Valentim,^{1,2} Donato Cioli,³ Frédéric D. Chevalier,² Xiaohang Cao,¹ Alexander B. Taylor,¹ Stephen P. Holloway,¹ Livia Pica-Mattocchia,³ Alessandra Guidi,³ Annalisa Basso,³ Isheng J. Tsai,⁴ Matthew Berriman,⁴ Claudia Carvalho-Queiroz,¹ Marcio Almeida,² Hector Aguilar,⁵ Doug E. Frantz,⁵ P. John Hart,^{1,6†} Philip T. LoVerde,^{1,*†} Timothy J. C. Anderson^{2,*†}

Oxamniquine resistance evolved in the human blood fluke (*Schistosoma mansoni*) in Brazil in the 1970s. We crossed parental parasites differing ~500-fold in drug response, determined drug sensitivity and marker segregation in clonally derived second-generation progeny, and identified a single quantitative trait locus (logarithm of odds = 31) on chromosome 6. A sulfotransferase was identified as the causative gene by using RNA interference knockdown and biochemical complementation assays, and we subsequently demonstrated independent origins of loss-of-function mutations in field-derived and laboratory-selected resistant parasites. These results demonstrate the utility of linkage mapping in a human helminth parasite, while crystallographic analyses of protein-drug interactions illuminate the mode of drug action and provide a framework for rational design of oxamniquine derivatives that kill both *S. mansoni* and *S. haematobium*, the two species responsible for >99% of schistosomiasis cases worldwide.

In the absence of effective vaccines for human helminth infections, repeated rounds of mass treatment with drug monotherapies are typically used for control in most developing countries (1, 2). These programs bring enormous health benefits but impose strong selection on parasite populations, and resistance is suspected for several helminth species, including *Onchocerca volvulus*,

cause of river blindness, and *Wuchereria bancrofti*, cause of lymphatic filariasis (3, 4). However, resistance to oxamniquine (OXA) in *Schistosoma mansoni*, a trematode parasite that infects 67 million people in Africa and South America (1), provides the first and clearest example of naturally selected drug resistance in a human helminth parasite. OXA was the first-line drug in Brazil until

the late 1990s and remained in use until 2010. Resistant parasites were isolated from Brazilian patients in the 1970s (5, 6) and also selected in the laboratory from sensitive parasite lines (7). Resistance has a recessive basis and results in a ~500% reduction in drug sensitivity (8). Genetic complementation experiments demonstrate that the same gene determines resistance in both field and laboratory-selected parasites, although whether the same mutations are responsible is unknown (9). OXA is species-specific (10, 11), killing *S. mansoni* (67 million cases) but not other schistosome species (*S. haematobium*, 119 million cases) in Africa or *S. japonicum* (1 million cases) in Asia (1).

We exploited the *S. mansoni* genome sequence (12, 13) and genetic map (14) to identify genome region(s) that underlie OXA-resistance and to determine the basis for species-specific drug action. The complete life cycle of *S. mansoni* can be maintained in the laboratory, and clonal expansion of larval parasites within the snail host allows production of thousands of genetically identical

¹Departments of Biochemistry and Pathology, University of Texas Health Science Center, San Antonio, TX 78229, USA. ²Texas Biomedical Research Institute, San Antonio, TX 78245, USA. ³Institute of Cell Biology and Neurobiology, CNR, Rome, Italy. ⁴Wellcome Trust Sanger Institute, Wellcome Trust Genome Campus, Hinxton, UK. ⁵Department of Chemistry, The University of Texas at San Antonio, San Antonio, TX 78249, USA. ⁶Department of Veterans Affairs, South Texas Veterans Health Care System, San Antonio, TX 78229, USA.

*These authors contributed equally.

†Corresponding author. E-mail: tanderso@txbiomedgenetics.org (T.J.C.A.); loverde@uthscsa.edu (P.T.L.); pjhart@biochem.uthscsa.edu (P.J.H.)

single-sex parasites, which makes this organism well suited to linkage mapping methods. We crossed an OXA-sensitive (LE) (15) and an OXA-resistant (HR) parasite (8) derived by laboratory selection. We used an intercross design: F_1 individuals were crossed to generate 388 F_2 progeny. At each stage, individual parasite genotypes were isolated by infecting snails with a single miracidium larva (Fig. 1A). We measured OXA resistance by exposing adult parasites to 500 $\mu\text{g/ml}$ OXA and monitoring parasite survival. The F_1 individuals and 136 out of 182 (74.7%) F_2 progeny were OXA-sensitive, whereas 36 out of 182 (25.3%) F_2 progeny were OXA-resistant, consistent with recessive inheritance.

We genotyped parental parasites, F_1 individuals, and 144 F_2 progeny using 62 microsatellite markers (14) distributed at 20 cM (± 15 cM) intervals across the genome (table S1). We identified a single quantitative trait locus (QTL) near the end of chromosome (chr.) 6 [logarithm of odds (LOD) = 11.5]. The peak LOD was observed at the terminal marker genotyped, making gene location uncertain. The 1.8-LOD QTL support interval measured 5448 kb (0 to 5,448,149 bp) and contained 184 genes. To finely map this region, we sequenced the genomes of the two parents and two F_1 individuals to 11 to 29 \times coverage (table S2), identifying 558,078 high-confidence single-nucleotide polymorphisms (SNPs) (1.5 every kb) that showed Mendelian segregation in the F_1 parasites. Of these, 6909 were within the chr. 6 QTL, including 5241 SNPs showing fixed differences between the OXA-resistant and -sensitive parents. We genotyped the F_2 progeny using 48 SNPs, including 17 in the QTL region, as well as an addi-

tional nine microsatellite markers surrounding the QTL peak (table S1). Inclusion of these markers increased the peak LOD score to 31 (Fig. 1C), narrowed the 1.8-LOD QTL support interval to 439 kb (positions 1, 149, 128 to 1,587,670 bp) and reduced the number of genes to 16 (Fig. 1D). A secondary screen, in which the marker showing the highest LOD was used as a covariate, removed the chr. 6 QTL and failed to reveal further QTLs, consistent with monogenic trait inheritance (Fig. 1A).

The QTL contains several strong candidate loci. The parasite enzyme that activates OXA has the properties of a sulfotransferase and is found in a 30-kD fraction of soluble worm extracts (16). Three of 16 genes within the QTL are annotated as "cell wall integrity and stress response" or "nicotinamide adenine dinucleotide-dependent epimerase and/or dehydratase" but show structural similarity to sulfotransferases using HHpred (17) and express a predicted protein with a molecular mass close to the expected size (25 to 35 kD) (table S3).

We determined the gene content of the QTL using the genome sequences from the parental parasites. The same genes were present in both parents within the QTL region, which ruled out a gene or exon deletion as the cause of OXA-resistance. We used three approaches to prioritize candidate genes. First, we reasoned that the gene(s) involved would contain fixed nonsynonymous differences (or indels) between the parents. Seven of 16 genes fulfilled this criterion, including one (Smp_089320) of three genes showing homology to sulfotransferases. Second, we measured transcript abundance in OXA-

sensitive and -resistant parental parasites using RNA sequencing (RNAseq). Six of 16 genes within the QTL, including two with homology to sulfotransferases (Smp_089330 and Smp_119060), showed no detectable expression (table S3). Finally, we examined the size of predicted gene products. Four of 16 products had the mass expected (25 to 35 kD) for the OXA-activating factor (16). Only one gene (Smp_089320) fulfilled all three selection criteria (table S3). We also conducted functional analyses on five additional genes within or adjacent to the QTL that satisfied at least two of our selection criteria.

OXA is a prodrug that is enzymatically converted into its active form in sensitive, but not resistant, parasites (18). We used a biochemical complementation assay to determine which of the candidate genes expresses a protein that activates OXA. We quantified OXA activation by measuring covalent binding of tritiated OXA to *S. mansoni* macromolecules in worm extracts (19). We produced recombinant proteins encoded by the six candidate genes, but only the recombinant Smp_089320 protein from the OXA-sensitive parent activated OXA in resistant worm extracts (Fig. 2A). Activation required minimal (1 pM) concentrations of Smp_089320 protein (Fig. 2B). We confirmed the involvement of Smp_089320 in OXA resistance in cultured parasites using RNA interference (RNAi). Double-stranded RNA (dsRNA) targeting Smp_089320 reduced expression by 97% ($\pm 1.5\%$). OXA-sensitive (LE) parasites became resistant to 2 or 4 $\mu\text{g/ml}$ OXA after knockdown of Smp_089320 (Fig. 2C and movie S1). Hence, both biochemical complementation

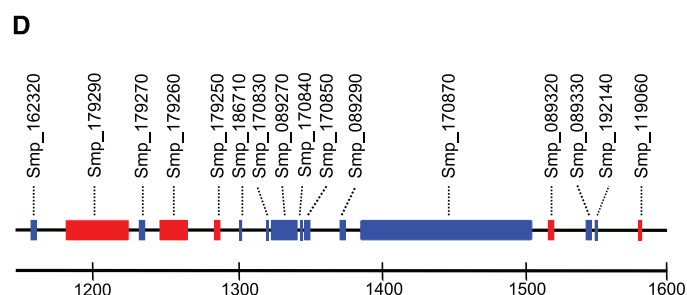
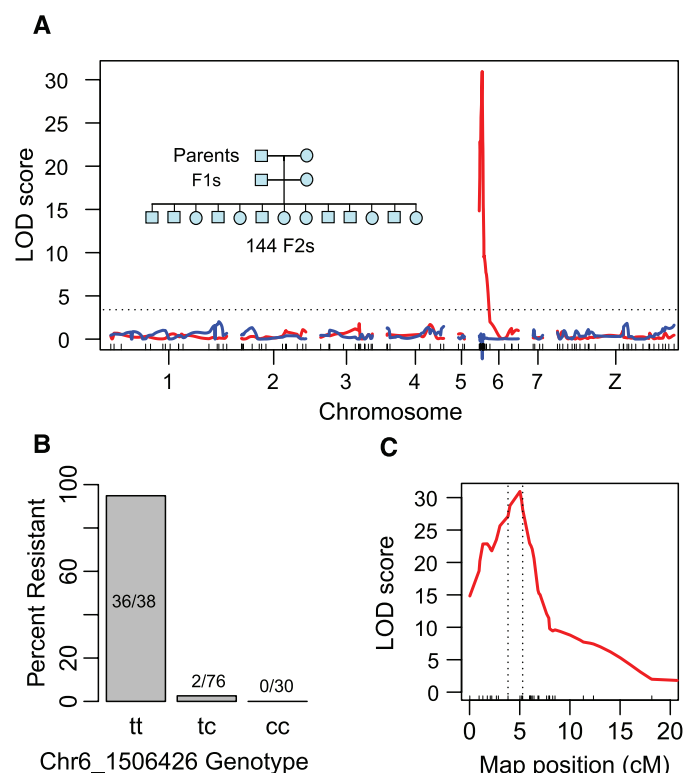


Fig. 1. Linkage mapping of OXA-resistance. (A) OXA-resistance QTL on chr. 6. The red line shows LOD scores plotted across the genome after fine mapping of the chr. 6 QTL region. The blue line represents LOD scores when the marker (Chr6_1506426) showing the peak LOD is used as a covariate. The dotted line marks the 5% significance threshold. The inset shows the three-generation intercross design. (B) Frequencies of resistant parasites in different genotypic classes at marker Chr6_1506426. (C) Close up of chr. 6 QTL peak. The dotted vertical lines show the 1.8-LOD support interval (439 kb, 16 genes) for the location of causative gene. (D) Gene content of the 1.8-LOD support interval. The scale is in kb, genes transcribed on the forward (blue) and reverse (red) strands are shown.

assays and RNAi implicate involvement of Smp_089320 in OXA-resistance.

Smp_089320 from the resistant parent (HR) differs at two positions from the sensitive parent (LE): a substitution of leucine for tryptophan at position 256 (L256W) and a deletion of glutamic acid at position 142 (E142Δ) (20) (Fig. 2D). We conducted complementation assays using recombinant proteins containing either mutation to determine the residue responsible for OXA-resistance. Smp_089320-L256W activates OXA. However, Smp_089320-E142EΔ failed to activate OXA (Fig. 2E), so we identified this deletion as the cause of resistance in the cross. The OXA-resistant parasite (HR) was laboratory-selected (7), so to evaluate whether OXA resistance observed in the field results from the same mutation, we tested an OXA-resistant parasite isolate (MAP) acquired from a Brazilian patient in 1978

(21). Smp_089320 from MAP carried a substitution of cysteine for arginine at position 35 (C35R) (Fig. 2D), and the protein was unable to activate OXA (Fig. 2E). Hence, mutations causing loss of function in Smp_089320 can be independently derived in field- and laboratory-derived OXA-resistant parasites.

The sulfotransferase in sensitive worms extracts activates OXA by transferring sulfate groups from the universal sulfate donor 3'-phosphoadenosine-5'-phosphosulfate (PAPS) to the drug (16). To validate that Smp_089320 is a sulfotransferase, we performed a sulfonation assay (22) using quercetin (16) as substrate. Proteins encoded by Smp_089320 (LE allele), but not Smp_089320_E142Δ or Smp_089320_C35R, were able to transfer a sulfate group from [³⁵S]PAPS to quercetin (Fig. 2F), which provided insights into the resistance mechanism and provided additional evidence for involvement of these mu-

tations in OXA-resistance. Proteins encoded by Smp_089320_L256W show low sulfonation activity (<10% of LE parent), which suggests that this radical substitution may play a compensatory role in restoring functionality with the normal substrate for this enzyme.

To understand the molecular bases for OXA action and resistance, the crystal structure of Smp_089320 from sensitive parasites was determined with 3'-phosphoadenosine-5'-phosphate (PAP) and OXA bound (table S4 and fig. S2). Smp_089320 is 40 residues shorter than human cytosolic sulfotransferases, differs in overall topology, and has an additional α helix (green, Fig. 3A) (23). OXA binds in the central cavity of the L-shaped, predominantly α-helical enzyme (Fig. 3, A and B). The hydroxyl group (the sulfonation target) is precisely positioned adjacent to a shaft running from the surface of the molecule, permitting

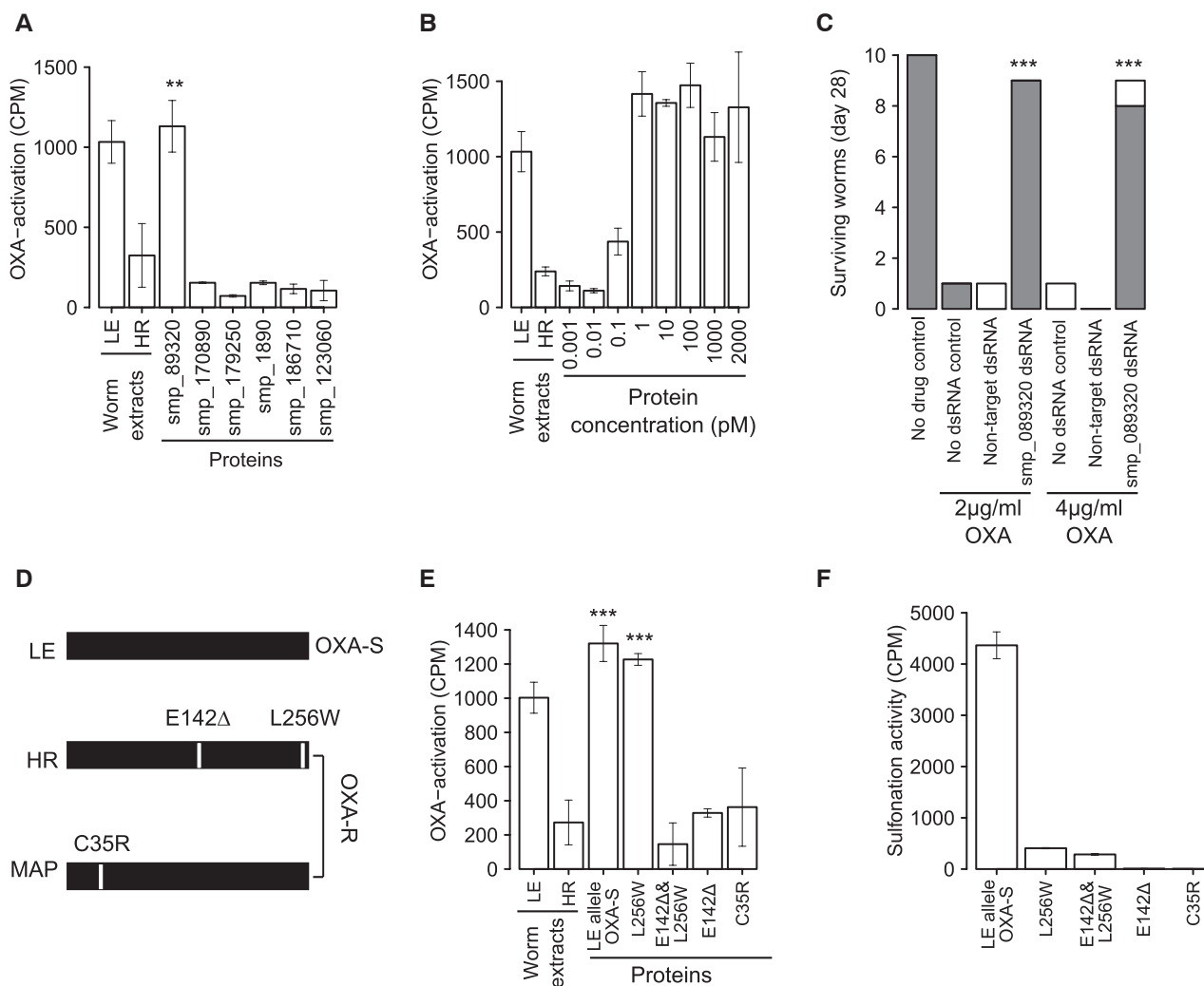


Fig. 2. Identification of gene and mutations underlying OXA-resistance.

(A) Complementation assays to identify proteins that restore OXA-binding in resistant worm homogenates. Extracts of LE (OXA-sensitive) and HR (OXA-resistant) worms were positive and negative controls. Error bars show 1 SD in triplicate assays. Significant increases in activation relative to the HR control are shown (** $P < 0.01$). (B) Complementation using serial dilution of Smp-089320 protein. (C) RNAi knockdown of Smp-089320. Surviving worms were categorized

as vigorous (shaded) or unwell (white) (movie S1). Significant increase in survival relative to treated controls are marked (*** $P < 0.001$). (D) Smp-089320 alleles from LE (OXA-sensitive) and two OXA-resistant parasites (HR, laboratory-selected; MAP, field-derived). (E) Identification of OXA-resistance mutations. Proteins bearing different mutations were used in OXA-complementation assays. Significant increases in activation relative to the HR control are shown (*** $P < 0.001$). (F) Sulfonation activity of Smp-089320 alleles.

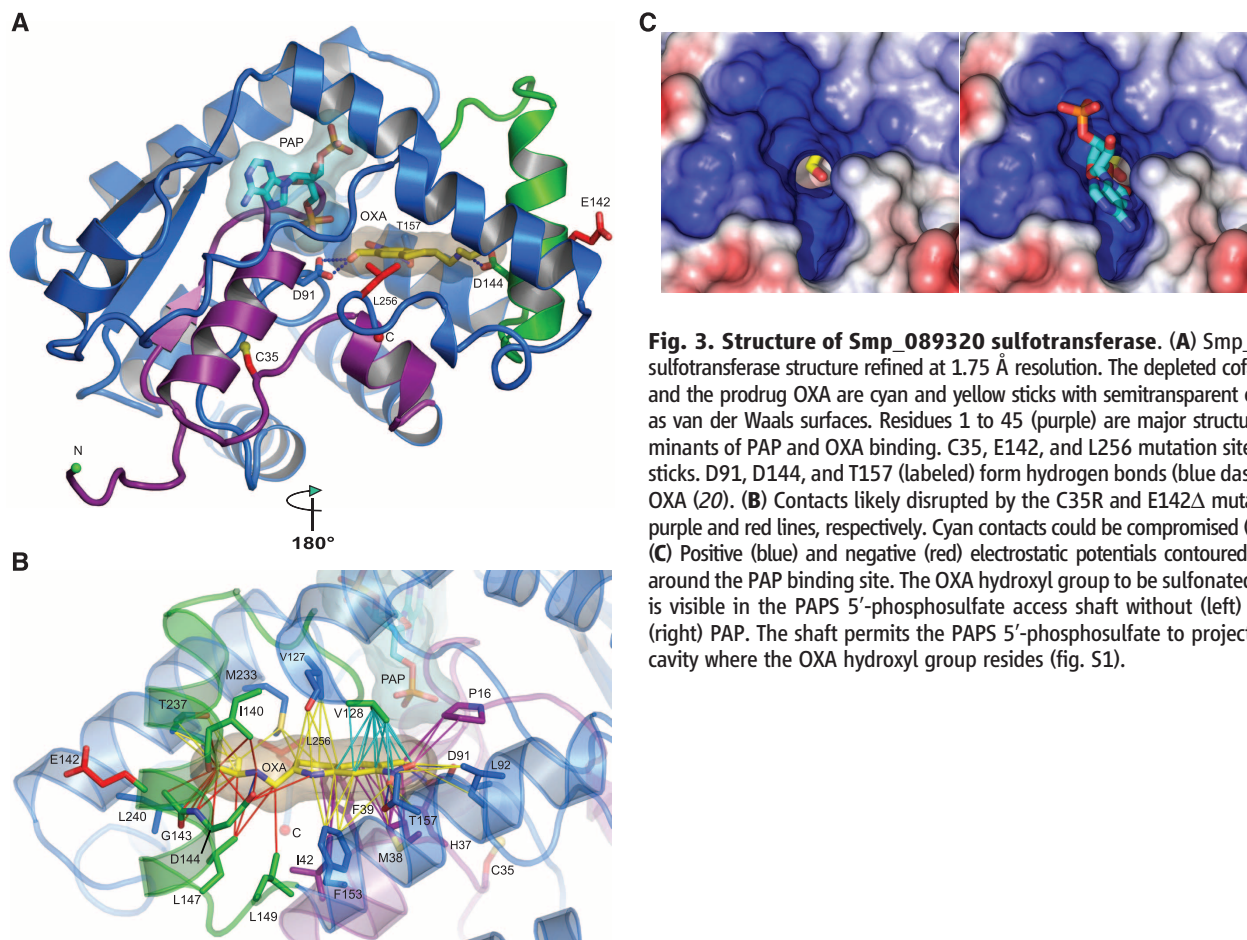


Fig. 3. Structure of Smp_089320 sulfotransferase. (A) Smp_089320 sulfotransferase structure refined at 1.75 Å resolution. The depleted cofactor PAP and the prodrug OXA are cyan and yellow sticks with semitransparent envelopes as van der Waals surfaces. Residues 1 to 45 (purple) are major structural determinants of PAP and OXA binding. C35, E142, and L256 mutation sites are red sticks. D91, D144, and T157 (labeled) form hydrogen bonds (blue dashes) with OXA (20). (B) Contacts likely disrupted by the C35R and E142Δ mutations are purple and red lines, respectively. Cyan contacts could be compromised (table S5). (C) Positive (blue) and negative (red) electrostatic potentials contoured at ± 5 kT around the PAP binding site. The OXA hydroxyl group to be sulfonated (fig. S1) is visible in the PAPS 5'-phosphosulfate access shaft without (left) and with (right) PAP. The shaft permits the PAPS 5'-phosphosulfate to project into the cavity where the OXA hydroxyl group resides (fig. S1).

the PAPS 5'-phosphosulfate access to the sequestered substrate (Fig. 3C). The relative positions of the accepting OXA and donating PAPS groups are consistent with the formation of a sulfonated OXA hydroxyl group (fig. S1). The molecular bases for OXA-resistance are mutation-induced perturbations of enzyme structure that abrogate OXA binding and/or sulfonation. The C35R mutation is in a densely packed region between two critical helices involved in PAPS and OXA binding (fig. S3). Replacement of cysteine with a bulky arginine is predicted to disrupt ≤ 26 interactions and to displace D91, which is critical for OXA binding and sulfonation (Fig. 3A, fig. S3, and table S5). E142Δ occurs in a helix in intimate contact with the OXA tail and is predicted to disrupt 20 to 40 enzyme-OXA interactions (Fig. 3B and table S5).

OXA kills *S. mansoni* but not the other human schistosome species *S. haematobium* and *japonicum* (10, 11). To investigate species-specific drug action, we conducted a phylogenetic analysis. We found 11 genes with homology to Smp_089320 in *S. mansoni*, six in *S. haematobium*, and 11 in *S. japonicum*. Genes in *S. haematobium* (Sha_104171) and *S. japonicum* (Sjp_FN317462.1) share >50% homology with Smp_089320 and form a monophyletic group (Fig. 4 and figs. S4 and S5) with

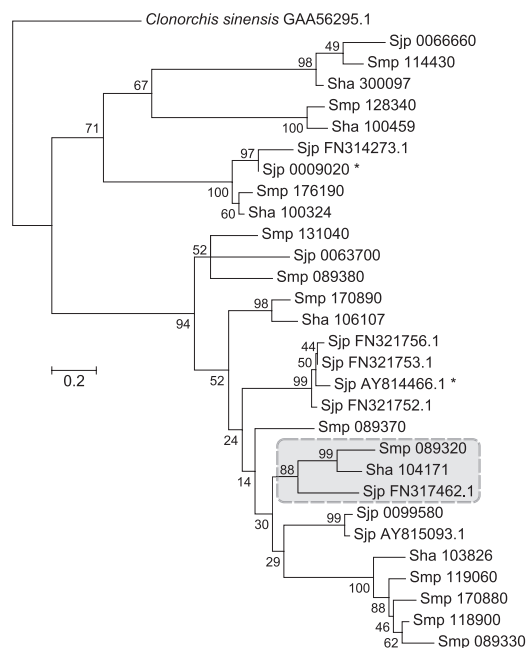


Fig. 4. Identification of homologous genes in *S. haematobium* and *S. japonicum*. Maximum likelihood tree of aligned sequences (fig. S4) showing homology with Smp_089320. The tree is rooted with *Clonorchis sinensis*, branch lengths are numbers of substitutions per site, and percent bootstrap values (1000 replicates) are shown. The cluster containing the homologs of Smp_089320 in *S. haematobium* (Sha) and *S. japonicum* (Sjp) is boxed and was recovered using alternative phylogenetic methods (fig. S5A).

relationships consistent with schistosome phylogeny (24). We sequenced polymerase chain reaction (PCR) products amplified from *S. haematobium* and *S. japonicum* cDNA that showed that these genes are expressed in adult parasites. Comparison of *S. mansoni* and *S. haematobium* is of particular interest, as these two species account for 186 out of 187 million (99.5%) of human schistosome infections (1). *S. haematobium* and *S. mansoni* proteins are 70% identical. Of the 16 residues that contact OXA, three differ in *S. haematobium* (figs. S5B and S6 and table S5). Two of these (T157 *Sm* → S166 *Sh* and I49L *Sm* → I157 *Sh*) are conservative substitutions not predicted to affect OXA binding. However, the third substitution (F39 *Sm* → Y54 *Sh*) results in a change in polarity and size that is predicted to negatively impact OXA binding (fig. S6).

Linkage mapping has been outstandingly successful in protozoan parasites (25–27). Identification of the OXA-resistance locus, which we name SmSULT-OR (*S. mansoni* sulfotransferase-OXA-resistance), extends the utility of this approach to the most important of the human helminth parasites, which paves the way for genetic analyses of biomedically important heritable traits including praziquantel resistance (28, 29), host specificity (30), and virulence (31). New drugs are urgently required for treatment of schistosomiasis because current treatments use praziquantel monotherapy to which partial resistance has been documented (28). Comparative analysis of SmSULT-OR and its *S. haematobium* homolog provides a framework for structure-based redesign of broad-spectrum OXA derivatives active against both *S. mansoni* and *S. haematobium*. Such a drug could be partnered with praziquantel to retard the onset of resistance. More generally, this work demonstrates how genome sequence data can be leveraged for functional genomic analyses of a biomedically important trait in a neglected human helminth parasite.

References and Notes

- P. J. Hotez *et al.*, in *Disease Control Priorities in Developing Countries*, D. T. Jamison *et al.*, Eds. (The International Bank for Reconstruction and Development/The World Bank Group, Washington, DC, ed. 2, 2006), chapt. 24.
- P. J. Hotez, A. Fenwick, L. Savioli, D. H. Molyneux, *Lancet* **373**, 1570–1575 (2009).
- M. Y. Osei-Atweneboana *et al.*, *PLOS Negl. Trop. Dis.* **5**, e998 (2011).
- A. E. Schwab, D. A. Boakye, D. Kyelem, R. K. Prichard, *Am. J. Trop. Med. Hyg.* **73**, 234–238 (2005).
- N. Katz, E. P. Dias, N. Araujo, C. P. Souza, *Rev. Soc. Bras. Med. Trop.* **7**, 381–387 (1973).
- R. Gentile, G. Oliveira, *Acta Trop.* **108**, 175–178 (2008).
- S. H. Rogers, E. Bueding, *Science* **172**, 1057–1058 (1971).
- D. Cioli, L. Pica-Mattoccia, R. Moroni, *Exp. Parasitol.* **75**, 425–432 (1992).
- L. Pica-Mattoccia, L. C. Dias, R. Moroni, D. Cioli, *Exp. Parasitol.* **77**, 445–449 (1993).
- L. Pica-Mattoccia, A. Novi, D. Cioli, *Parasitol. Res.* **83**, 687–689 (1997).
- R. Foster, B. L. Cheetham, *Trans. R. Soc. Trop. Med. Hyg.* **67**, 674–684 (1973).
- A. V. Protasio *et al.*, *PLOS Negl. Trop. Dis.* **6**, e1455 (2012).
- M. Berriman *et al.*, *Nature* **460**, 352–358 (2009).
- C. D. Criscione, C. L. Valentim, H. Hirai, P. T. LoVerde, T. J. Anderson, *Genome Biol.* **10**, R71 (2009).
- F. A. Lewis, M. A. Stirewalt, C. P. Souza, G. Gazzinelli, *J. Parasitol.* **72**, 813–829 (1986).
- L. Pica-Mattoccia *et al.*, *Mem. Inst. Oswaldo Cruz* **101** (suppl. 1), 307–312 (2006).
- J. Söding, A. Biegert, A. N. Lupas, *Nucleic Acids Res.* **33** (Web Server), W244 (2005).
- D. Cioli, L. Pica-Mattoccia, S. Rosenberg, S. Archer, *Life Sci.* **37**, 161–167 (1985).
- L. Pica-Mattoccia, S. Archer, D. Cioli, *Mol. Biochem. Parasitol.* **55**, 167–175 (1992).
- Single-letter abbreviations for the amino acid residues are as follows: A, Ala; C, Cys; D, Asp; E, Glu; F, Phe; G, Gly; H, His; I, Ile; K, Lys; L, Leu; M, Met; N, Asn; P, Pro; Q, Gln; R, Arg; S, Ser; T, Thr; V, Val; W, Trp; and Y, Tyr.
- K. M. Drescher *et al.*, *Mem. Inst. Oswaldo Cruz* **88**, 89–95 (1993).
- L. Varin, D. Barron, R. K. Ibrahim, *Anal. Biochem.* **161**, 176–180 (1987).
- M. Negishi *et al.*, *Arch. Biochem. Biophys.* **390**, 149–157 (2001).

- S. P. Lawton, H. Hirai, J. E. Ironside, D. A. Johnston, D. Rollinson, *Parasit. Vectors.* **4**, 131 (2011).
- L. D. Sibley, *Int. J. Parasitol.* **39**, 915–924 (2009).
- X. Su, K. Hayton, T. E. Wellems, *Nat. Rev. Genet.* **8**, 497–506 (2007).
- L. C. Ranford-Cartwright, J. M. Mwangi, *Int. J. Parasitol.* **42**, 529–534 (2012).
- R. M. Greenberg, *Parasitology* **140**, 1534–1546 (2013).
- M. J. Doenhoff, D. Cioli, J. Utzinger, *Curr. Opin. Infect. Dis.* **21**, 659–667 (2008).
- M. Kalbe, B. Haberl, J. Hertel, W. Haas, *Parasitology* **128**, 635–643 (2004).
- C. M. Gower, J. P. Webster, *Evolution* **58**, 1178–1184 (2004).

Acknowledgments: Funded by NIH (5R21-AI096277, 5R21-AI072704, R01-AI097576) and World Health Organization (HQNTD1206356) in facilities constructed with support from Research Facilities Improvement Program Grant (C06 RR013556) from National Center for Research Resources (NIH). Work at Wellcome Trust Sanger Institute was supported by the Wellcome Trust (grant 098051). P.J.H. was funded by the Robert A. Welch Foundation (AQ-1399). *B. glabrata* snails were supplied by Fred Lewis (Biomedical Research Institute, Rockville, MD) under NIH-National Institute of Allergy and Infectious Diseases contract no. HHSN272201000005I. We thank W. Le Clec'h and C. Valle (capillary sequencing), Z. Lai (RNA sequencing), N. Holroyd (coordinated genome sequencing), Q. Bickle (RNAi support), and G. Anderson (movie compilation). The X-ray Crystallography Core Laboratory is supported by the University of Texas Health Science Center, San Antonio, Office of the Vice President for Research. The authors declare no competing financial interests. Data deposition: Illumina sequence reads (www.ebi.ac.uk/ena/ accession#ERP000160); GenBank accessions (KF733459–61), RNAseq data (www.ncbi.nlm.nih.gov/geo/, GSE51847), structural data (www.wwpdb.org/, accession 4MUA, 4MUB).

Supplementary Materials

www.sciencemag.org/content/342/6164/1385/suppl/DC1
Materials and Methods
Supplementary Text
Figs. S1 to S6
Tables S1 to S5
Movie S1
References (32–58)

12 July 2013; accepted 8 November 2013
Published online 21 November 2013;
10.1126/science.1243106

Fear Learning Enhances Neural Responses to Threat-Predictive Sensory Stimuli

Marley D. Kass,* Michelle C. Rosenthal,* Joseph Pottackal, John P. McGann†

The central nervous system rapidly learns that particular stimuli predict imminent danger. This learning is thought to involve associations between neutral and harmful stimuli in cortical and limbic brain regions, though associative neuroplasticity in sensory structures is increasingly appreciated. We observed the synaptic output of olfactory sensory neurons (OSNs) in individual mice before and after they learned that a particular odor indicated an impending foot shock. OSNs are the first cells in the olfactory system, physically contacting the odor molecules in the nose and projecting their axons to the brain's olfactory bulb. OSN output evoked by the shock-predictive odor was selectively facilitated after fear conditioning. These results indicate that affective information about a stimulus can be encoded in its very earliest representation in the nervous system.

Associative learning can alter cortical and even precortical processing in mammalian sensory systems (1–5). However, the primary sensory input is generally thought to be

determined by the physical stimulus itself, independent of any prior information the subject may have learned about that stimulus. The development of stably expressed optical-activity indicators

in mice now permits longitudinal experiments testing whether sensory inputs to the brain remain constant as an individual mouse learns about specific sensory stimuli.

Associative fear conditioning, in which an animal learns that a neutral sensory stimulus predicts the occurrence of an aversive stimulus, can alter the processing of threat-predictive sensory stimuli (6–8). In the olfactory system, fear learning has been shown to enhance difficult olfactory discriminations (9) and alter odorant-evoked neural activity in the piriform cortex and olfactory bulb (9, 10). We used a trial-based, discriminative olfactory fear-conditioning paradigm consisting of paired, shock-alone control, and odor-alone

Behavioral and Systems Neuroscience Section, Department of Psychology, Rutgers, The State University of New Jersey, 152 Frelinghuysen Road, Piscataway, NJ 08854, USA.

*These authors contributed equally to this work.

†Corresponding author. E-mail: jmcgann@rci.rutgers.edu

control groups that underwent either repeated *in vivo* optical imaging procedures or behavioral testing (Fig. 1A) (see supplementary materials and methods). During each of 3 consecutive days of training, mice assigned to the paired group received five ~15-s presentations of each of two odorants, one of which (the CS⁺ presentation; CS, conditioned stimulus) always coterminated with a foot shock (Fig. 1B) and one of which (the CS⁻) did not. Shock-alone and odor-alone groups underwent identical paradigms but without the odor or shock presentations, respectively. When tested in a novel context, mice in the paired group exhibited preferential freezing to the CS⁺ odorant compared with the CS⁻, with comparatively little freezing observed in the shock- or odor-alone control groups, or to a clean-air control stimulus (Fig. 1C).

For optical imaging, we used a line of gene-targeted mice that express the fluorescent exocytosis indicator synapto-pHluorin (spH, a pH-sensitive green fluorescent protein variant) under the control of the olfactory marker protein (OMP) promoter (11), resulting in spH expression in all mature olfactory sensory neurons (OSNs). We used wide-field fluorescence imaging through an implanted cranial window (12, 13) to visualize *in vivo* odorant-evoked spH signals, which indicate neurotransmitter release from OSN terminals into olfactory bulb glomeruli, both before and after behavioral training (Fig. 1A). Olfactory fear conditioning induced a

robust increase in the magnitude of spH responses evoked by the CS⁺ odorant compared with the preconditioning baseline, whereas no changes were observed in the spH responses evoked by the CS⁻ or three nonpresented control odorants (Fig. 2, A, D to G, and K). Odorant-evoked spH signals did not differ across imaging sessions in the shock- and odor-alone control groups (Fig. 2, B to D and H to K). We obtained identical results, regardless of whether glomerular responses were pooled across mice (Fig. 2) or averaged within each individual mouse (fig. S1). Although fear learning augmented CS⁺-evoked spH signals, there was no change in the spatial arrangement of CS⁺-evoked glomerular response maps (fig. S2). In a parallel control experiment, we observed no changes in respiration during CS⁺ and CS⁻ presentations in identically anesthetized, fear-conditioned mice (fig. S3).

Each OSN in the mouse olfactory epithelium expresses one out of hundreds of odor receptor types (14). As OSN axons project ipsilaterally to

the olfactory bulb, they segregate by receptor type so that each glomerulus receives projections exclusively from OSNs expressing a specific odor receptor (15). Odorants bind to a subset of olfactory receptor types in the epithelium and thus drive OSN synaptic output into a corresponding subset of olfactory bulb glomeruli. Consequently, the global configuration of odorant-evoked OSN input to glomeruli across the bulb represents the chemical identity of that odorant (16, 17). Because the CS⁺ and CS⁻ odorants were both esters, they drove OSN input to distinct but overlapping populations of glomeruli, reflecting their excitation of partially overlapping populations of OSNs. Some glomeruli selectively received OSN output evoked by the CS⁺ odorant, whereas others were selective for the CS⁻, and some responded to both odorants (dual-responsive). Separating the odorant-evoked OSN synaptic output based on the odorant-selectivity of each glomerulus revealed that the OSN input to CS⁺-selective glomeruli was greatly enhanced, whereas OSN input to glomeruli

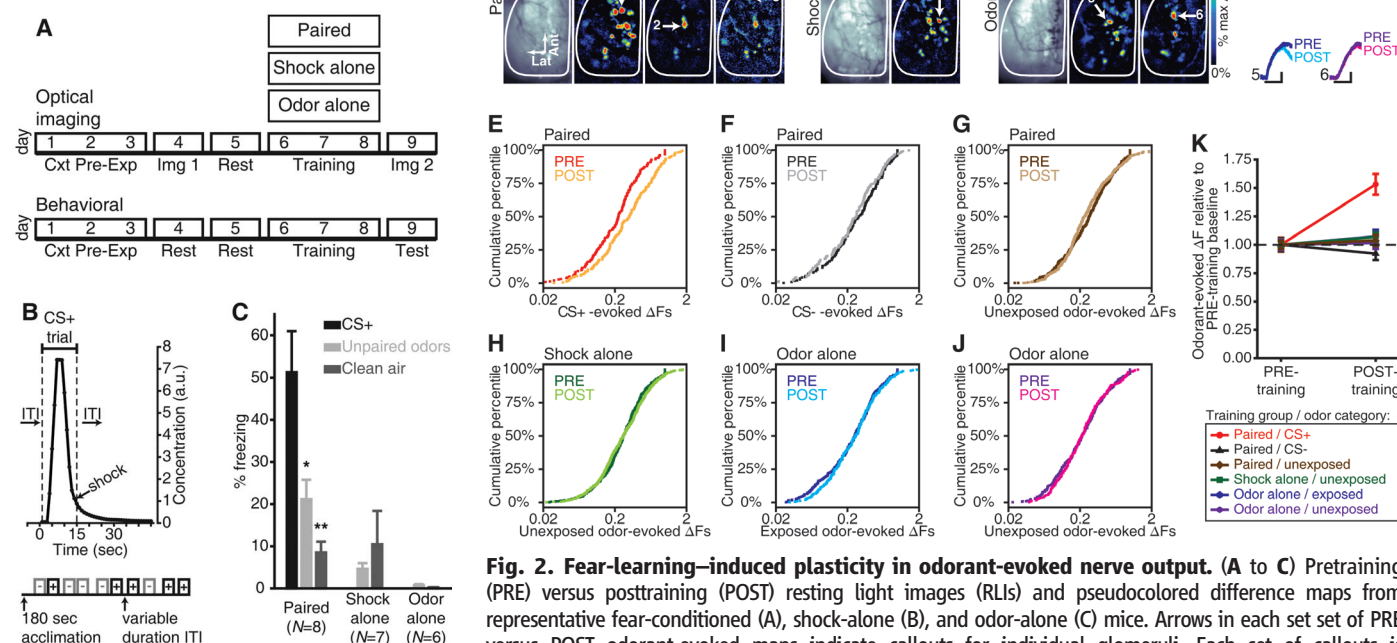


Fig. 2. Fear-learning-induced plasticity in odorant-evoked nerve output. (A to C) Pretraining (PRE) versus posttraining (POST) resting light images (RLIs) and pseudocolored difference maps from representative fear-conditioned (A), shock-alone (B), and odor-alone (C) mice. Arrows in each set of PRE versus POST odorant-evoked maps indicate callouts for individual glomeruli. Each set of callouts is numbered and corresponds to the numbered traces in (D). MV, methyl valerate; BA, butyl acetate; IAA, isoamyl acetate. Lat, lateral; Ant, anterior. (D) Odorant-evoked change in fluorescence (ΔF) corresponding to callouts in (A) to (C). Black scale bars shown under traces; horizontal, 6-s stimulus; vertical, 25% max of PRE. (E to J) Cumulative probability plots showing the distributions of PRE versus POST ΔF values that were evoked by the CS⁺ [(E); $P \leq 0.001$], CS⁻ [(F); $P > 0.05$], and all other unexposed odorants [(G); $P > 0.05$] in the paired group; all unexposed odorants in the shock-alone group [(H); $P > 0.05$]; and all exposed [(I); $P > 0.05$] and unexposed [(J); $P > 0.05$] odorants in the odor-alone group. P values were determined by Kolmogorov-Smirnov tests. (K) Mean ± SEM ΔF values pooled across glomeruli (the black dashed line denotes the baseline). Number (N) of glomeruli contributing to data in (E) to (K): paired, $N_{\text{PRE}} = 267$, $N_{\text{POST}} = 285$; shock-alone, $N_{\text{PRE}} = 163$, $N_{\text{POST}} = 173$; odor-alone, $N_{\text{PRE}} = 209$, $N_{\text{POST}} = 180$.

selective for the CS⁻ was unchanged (Fig. 3, A and B). In dual-responsive glomeruli, there was a selective enhancement when the OSN glomerular inputs were evoked by the CS⁺ odorant, but not when they were evoked by the CS⁻ (Fig. 3, A and B). This differential enhancement was not attributable to scattered light from the responses of CS⁺-selective glomeruli (fig. S4).

The selective enhancement of CS⁺-evoked OSN synaptic output in glomeruli whose OSNs are driven by both the CS⁺ and the CS⁻ odorants was unexpected. This discrimination presumably requires that information about the activity of other

OSN populations reaches the dual-responsive OSNs to modulate their output. Because this could require feedback from other brain regions, we separated the spH signals into four 1-s time bins (fig. S5) and tested whether the degree of enhancement varies across the duration of the odorant presentation. We observed the CS⁺-specific enhancement of OSN output, not only at the peak of the spH response but also in constant proportion throughout the entire odorant presentation (Fig. 3, C and D, and figs. S5 and S6). No changes were observed for CS⁻-evoked synaptic input to CS⁻-selective or dual-responsive

glomeruli (Fig. 3, C and D, and fig. S6), nor were changes observed for time-binned shock- or odor-alone control data (fig. S7).

Fear conditioning with acetophenone increases the number of OSNs expressing its cognate M71 odorant receptor and, consequently, increases the cross-sectional area of the OSNs' target glomeruli when observed 3 weeks later (18). However, after fear conditioning we did not observe a change in the cross-sectional area of OSN output signals from CS⁻-selective, CS⁻-selective, or dual-responsive glomeruli (Fig. 3E), or in the distributions of glomeruli among these selectivity categories (Fig. 3F). Moreover, the present results cannot be explained by changes in OSN number, because an increase in the number of cells in OSN populations excited by both the CS⁺ and the CS⁻ would not selectively facilitate the response of that population to the CS⁺ (Fig. 3B). In addition, only 3 days elapsed between fear conditioning and imaging (Fig. 1A), which is less than the 7 days required for newborn OSNs to mature and express OMP [whose promoter drives spH expression in these mice (11, 19)]. It is also insufficient time for enhanced survival of mature CS⁺-responsive OSNs [which typically survive for months (20)] to disproportionately increase their numbers. Thus, the locus of plasticity may lie in the glomerular circuit that presynaptically modulates OSN output (21), instead of in changes in the population of OSNs.

Fear learning enhanced CS⁺-evoked OSN output, on average, across glomeruli (Fig. 2 and Fig. 3, A to D), but in fact, each mouse receives OSN input to many glomeruli at once. For each mouse, we thus quantified the differences in the overall patterns of OSN input evoked by the CS⁺ odorant, the CS⁻ odorant, and an unexposed ester both before and after fear learning. The differences (quantified as Euclidean distances in vector space) between the primary sensory representations for the CS⁺ and CS⁻ odorants and between the CS⁺ and an unexposed odorant were increased by fear learning (Fig. 3G and fig. S8). When calculated as a function of time, the fear-conditioning-induced difference in representations [presumably predictive of odor discriminability (17)] was most pronounced during the first second of the stimulus presentations (Fig. 3H and fig. S8).

Olfactory stimuli typically do not include sharp onsets and offsets. Instead, their concentration varies over time and with distance from the source. OSN firing frequency increases with higher odorant concentrations (22), resulting in more neurotransmitter release from axon terminals into olfactory bulb glomeruli (11). It is possible that the CS⁺-selective enhancement of OSN output after fear conditioning is concentration-dependent, such that only OSN responses above some threshold evoke the enhancement. Alternatively, the augmented response to the CS⁺ odorant could be concentration-independent, thus enhancing sensitivity to the threat-predictive odorant. We tested these possibilities by presenting the CS⁺ and CS⁻ odorants at three different concentrations—including the training concentration (Fig. 1B), as

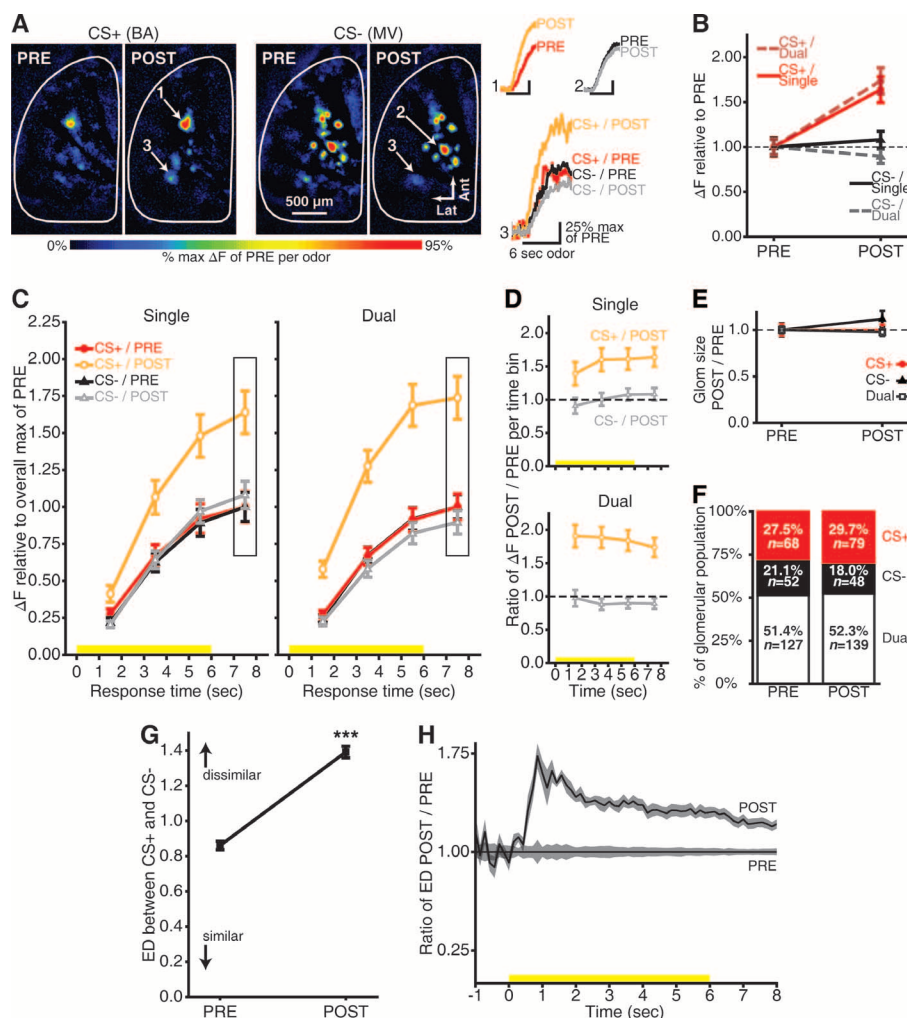


Fig. 3. Stimulus-specific enhancement of nerve output. (A) PRE versus POST CS⁺- and CS⁻-evoked maps from a representative mouse. Numbered callouts show example traces from single- and dual-responsive glomeruli. (B) Peak odorant-evoked change in fluorescence (ΔF) separated by selectivity (the black dashed line denotes the baseline). (C) Time-binned odorant-evoked ΔF for single- and dual-responsive glomeruli. Boxed regions indicate the bin corresponding to peak responses in (A) and (B). Yellow stimulus bars show odorant presentations. (D) Ratio of CS⁺- and CS⁻-evoked ΔF values during POST relative to those during PRE (POST/PRE) per bin per selectivity category (black dashed line, baseline). (E) Glomerulus response size shown relative to PRE (dashed line). (F) Percent of pre- and posttraining glomerular populations per selectivity category. $P > 0.05$, by χ^2 ; n , number of glomeruli contributing to means \pm SEM in (B) to (E). (G and H) Example network-level analysis from one mouse. (G) PRE versus POST mean \pm SEM Euclidean distance (ED) between CS⁺- and CS⁻-evoked maps pooled across trial pairs and response times (0 to 8 s). *** $P < 0.001$ by factorial analysis of variance. (H) Proportional increase in dissimilarity between odor representations as a function of time. Solid lines \pm shading represent mean \pm SEM.

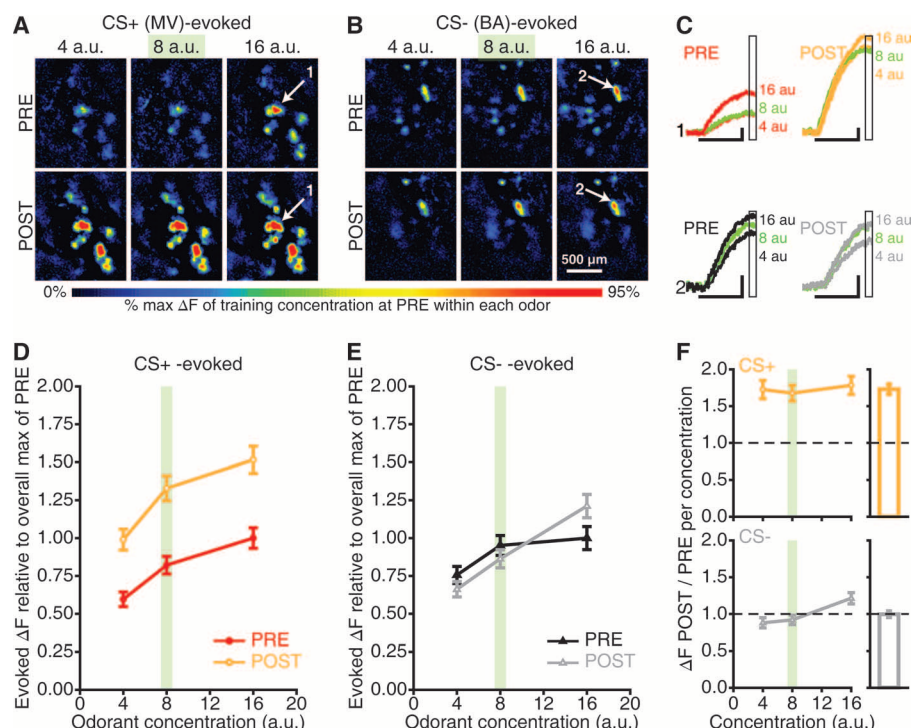


Fig. 4. Enhanced sensitivity to the CS⁺ odorant. (A and B) Maps evoked by three concentrations of the CS⁺ and CS[−] odorants before and after this example mouse underwent fear conditioning. (C) Response amplitudes (ΔF values) for callouts in (A) and (B). Black scale bars shown under traces; horizontal, 6-s stimulus; vertical, 25% max of PRE. Boxed regions indicate the bin used to generate peak maps [(A) and (B)] and concentration analyses [(D) to (F)]. (D and E) PRE versus POST CS⁺- and CS[−]-evoked concentration-response functions. (F) Ratio of CS⁺- and CS[−]-evoked ΔF values during POST relative to those during PRE (POST/PRE) within each concentration (dashed lines, baselines). Outsets are scaled to the main y axis and show overall ratios pooled across concentrations. Data are pooled across glomeruli (mean \pm SEM) in (D) to (F). The training concentration is indicated in green in (A) to (F).

well as half and double that concentration—during both imaging sessions.

During baseline imaging, the size of the peak spH signals increased as a function of concentration (Fig. 4, A to C). After fear conditioning, CS⁺-evoked OSN output was enhanced at all three concentrations (Fig. 4, A, C, and D), whereas CS[−]-evoked OSN output was unchanged (Fig. 4, B, C, and E). The magnitude of spH signals stimulated by the training CS⁺ concentration (Fig. 4, D and F) was ~68% larger than before conditioning, comparable to the increase at the lower (~73% larger) and higher (~78% larger) concentrations. Similar results were obtained when concentration-response functions were measured earlier in the odorant presentation (fig. S9). No differences were observed in the concentration-response functions that were evoked by the CS[−] odorant (99.6% of baseline)

(Fig. 4, E and F) or in the shock- or odor-alone control groups (fig. S10). Notably, after conditioning the OSN output that was evoked by the lowest concentration of the CS⁺ odorant [4 arbitrary units (a.u.)] was equivalent to the OSN output evoked by the highest concentration of that odorant (16 a.u.) before conditioning. This suggests that the effect of fear conditioning on OSN output was comparable to the effect of quadrupling the odorant concentration (Fig. 4D and fig. S9).

These data demonstrate that fear learning can change the neural representation of threat-predictive odors at the synaptic output of the OSNs, which provide the primary olfactory input to the brain. This plasticity may serve to enhance the system's sensitivity to odors associated with an aversive event, perhaps by initiating a large alarm signal specific to the CS⁺ presentation. Such an enhance-

ment could potentially underlie sensory symptoms of anxiety and affective disorders (23), including attentional bias or even hallucinations similar to those of posttraumatic stress disorder (6, 24).

References and Notes

1. C. F. Chen, D. C. Barnes, D. A. Wilson, *J. Neurophysiol.* **106**, 3136–3144 (2011).
2. W. Doucette *et al.*, *Neuron* **69**, 1176–1187 (2011).
3. J. M. Edeline, N. M. Weinberger, *Behav. Neurosci.* **105**, 618–639 (1991).
4. A. Gdalyahu *et al.*, *Neuron* **75**, 121–132 (2012).
5. L. M. Kay, G. Laurent, *Nat. Neurosci.* **2**, 1003–1009 (1999).
6. L. F. Barrett, M. Bar, *Philos. Trans. R. Soc. London Ser. B Biol. Sci.* **364**, 1325–1334 (2009).
7. E. A. Krusemark, W. Li, *J. Neurosci.* **33**, 587–594 (2013).
8. D. B. Headley, N. M. Weinberger, *J. Neurosci.* **33**, 5705–5717 (2013).
9. W. Li, J. D. Howard, T. B. Parrish, J. A. Gottfried, *Science* **319**, 1842–1845 (2008).
10. M. L. Fletcher, *Front. Syst. Neurosci.* **6**, 16 (2012).
11. T. Bozza, J. P. McGann, P. Mombaerts, M. Wachowiak, *Neuron* **42**, 9–21 (2004).
12. L. A. Czarnecki *et al.*, *Toxicol. Sci.* **126**, 534–544 (2012).
13. M. D. Kass, A. H. Moberly, M. C. Rosenthal, S. A. Guang, J. P. McGann, *J. Neurosci.* **33**, 6594–6602 (2013).
14. L. Buck, R. Axel, *Cell* **65**, 175–187 (1991).
15. P. Mombaerts *et al.*, *Cell* **87**, 675–686 (1996).
16. B. Malnic, J. Hirono, T. Sato, L. B. Buck, *Cell* **96**, 713–723 (1999).
17. S. L. Youngentob, B. A. Johnson, M. Leon, P. R. Sheeha, P. F. Kent, *Behav. Neurosci.* **120**, 1337–1345 (2006).
18. S. V. Jones, D. C. Choi, M. Davis, K. J. Ressler, *J. Neurosci.* **28**, 13106–13111 (2008).
19. F. Miragall, G. A. Monti Graziadei, *Brain Res.* **239**, 245–250 (1982).
20. V. M. Carr, A. I. Farbman, *Exp. Neurol.* **124**, 308–314 (1993).
21. J. P. McGann, *Chem. Senses* **38**, 459–474 (2013).
22. J. Reiser, H. R. Matthews, *J. Physiol.* **530**, 113–122 (2001).
23. A. T. Beck, D. A. Clark, *Behav. Res. Ther.* **35**, 49–58 (1997).
24. K. L. Felmingham, C. Rennie, E. Gordon, R. A. Bryant, *Biol. Psychol.* **90**, 224–227 (2012).

Acknowledgments: This work was supported by NIH grants DC009442, MH101293, and DC013090 to J.P.M. M.D.K., M.C.R., and J.P.M. conceived and designed the experiments. M.C.R., M.D.K., and J.P.M. collected and analyzed the behavioral and imaging data. J.P. and J.P.M. collected and analyzed the respiration data. J.P.M., M.D.K., M.C.R., and J.P. prepared the manuscript. All data are reported in the main article and in the supplementary materials. We thank T. Otto, L. Matzel, and L. Czarnecki for helpful comments.

Supplementary Materials

www.sciencemag.org/content/342/6164/1389/suppl/DC1
Materials and Methods
Figs. S1 to S10
References (25–28)

19 August 2013; accepted 5 November 2013
10.1126/science.1244916



The Scientific World Journal

Hindawi Publishing Corporation
<http://www.hindawi.com>

Volume 2013



Hindawi

- ▶ Impact Factor **1.730**
- ▶ **28 Days** Fast Track Peer Review
- ▶ All Subject Areas of Science
- ▶ Submit at <http://www.tswj.com>

Add your expertise to ours. Expand the impact of **data science.**

As a global leader in network research, Northeastern is seeking new faculty to pursue innovations in smart modeling, machine learning, and the growing applications of Big Data. Join us.

northeastern.edu/faculty-positions

Northeastern University

We're reimagining
the future of data science.
Put yourself in this picture.

Albert-László Barabási
Distinguished Professor of Physics, Biology,
and Computer Science

Scale-free networks and dynamic network modeling, error and attack tolerance and robustness of complex networks, and network theory applied to biological systems

David Lazer
Professor of Political Science and Computer
and Information Science

Computational social science, political networks and 21st century democracy, collective cognition, and understanding how patterns of institutional relations yield functional or dysfunctional systems

Alessandro Vespignani
Sternberg Family Distinguished University
Professor of Physics, Computer Science,
and Health Sciences

Analytical and computational models for the coevolution and interdependence of large-scale social, technological, and biological networks

Miriam Leeser
Professor of Electrical and
Computer Engineering

Biocomputing, reconfigurable hardware and hardware design tools, description languages, and implementation of image and digital processing algorithms

Yizhou Sun
Assistant Professor of Computer and
Information Science

Data mining, database systems, statistics, machine learning, information retrieval, and network science, focused on modeling novel problems for large-scale applications

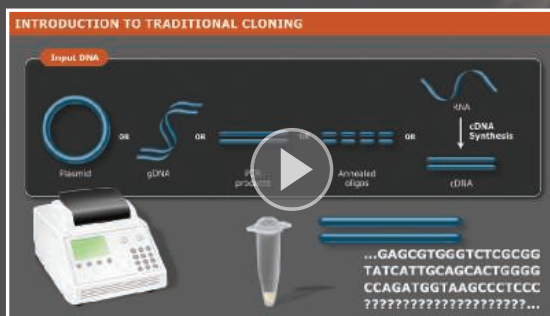


Clone with Confidence.

Whether you are performing your first cloning experiment, or constructing multi-fragment gene assemblies, NEB[®] has the solution for you. Our high quality reagents are available for every workflow, and include specialized enzymes, competent cells, and novel solutions – such as Gibson Assembly[®]. When you are looking to clone with confidence, think of NEB.

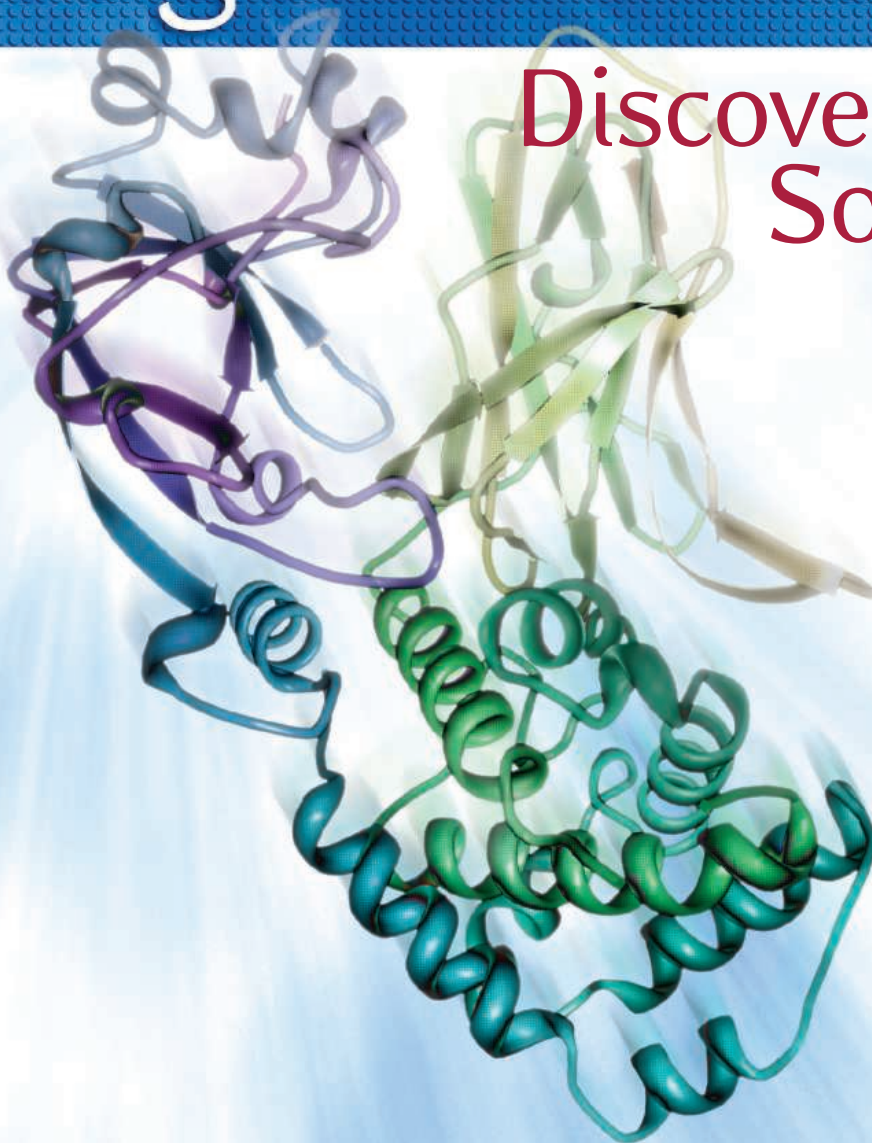
Explore the wise choice at
CloneWithNEB.com.

Visit **CloneWithNEB.com** to view online tutorials describing various cloning workflows.



Reagent Proteins

Discover the
Source



Reagent Proteins is the source

With over 5,000 recombinant proteins available, *Reagent Proteins* provides seamless access to the highest quality reagent, pre-clinical and cGMP grade proteins for research purposes.



"What I do with my Octet HTX time? Ride."

Epitope binning studies in days, not weeks.

Are your antibody epitope binning experiments just getting bigger and bigger? The new Octet HTX system lets you get them done in days, not weeks. Start a 32 x 32 cross-competition matrix in the morning, then analyze your data with a few mouse clicks before you leave the lab for the day. Can your ELISA or SPR system do that?

Lauren gets out of the lab more often now to ride. What will you do with your extra time?



fortéBIO
A Division of **Pall Life Sciences**

PALL Life Sciences

fortebio.com | 888-OCTET-75

Fast. Accurate. EASY.

Better results — on any sequencing platform

Get the most from your NGS

Discover new and innovative solutions,
dedicated for use with any NGS workflow



Streamline your next-generation sequencing (NGS) workflow and achieve high-quality results you can rely on.

- Highly specific and selective nucleic acid purification and target enrichment
- Unbiased whole genome amplification from a single cell
- High DNA library yields using optimized workflows that allow ~50% time-savings
- Outstanding results on any sequencing platform
- Intuitive, knowledge-based data interpretation for deeper insight into NGS results

Visit www.qiagen.com/goto/NGS to learn more!



Sample & Assay Technologies

Add your expertise to ours. Advance the **nanotechnology** revolution.

Northeastern is creating interdisciplinary faculty teams to identify groundbreaking solutions in biomaterials, drug delivery, energy transmission, and nanoengineered structures. Join us.

northeastern.edu/faculty-positions

Northeastern University

Ahmed Busnaina
William Lincoln Smith Chair
Professor, Mechanical and
Industrial Engineering

Directed assembly used in the manufacturing of nanoscale structures for applications in energy, electronics, biomedicine, and materials



Heather Clark
Associate Professor of
Pharmaceutical Sciences

Fluorescent nanosensors for in vitro and in vivo analyte detection to advance medical diagnostics and health monitoring



Mansoor Amiji
Distinguished Professor and Chair of
Pharmaceutical Sciences

Nanomedicine, drug discovery, chemo toxicity and resistance, modular drug systems and specialized carrier complexes for targeted drug delivery



We're reimagining the
future of nanotechnology.
Put yourself in this picture.



Vince Harris
University Distinguished Professor of
Electrical and Computer Engineering

Characterization, design, and processing of advanced magnetic materials with emphasis on materials for high-frequency applications to strengthen wireless communications resilience



Hicham Fenniri
Professor of Chemical Engineering

Development of nanoscale materials for medical and electronics applications, with a current focus on self-assembling organic nanotubes



THE ROCKEFELLER UNIVERSITY

celebrates ten years of the

PEARL MEISTER GREENGARD PRIZE

An International Award Recognizing Outstanding Women in Biomedical Research

Congratulations to Dr. Huda Zoghbi
who was awarded the Greengard Prize on December 5

For more information, please visit:
www.rockefeller.edu/greengardprize



2013 RECIPIENT

Huda Zoghbi, M.D.

*Ralph D. Feigin Professor, Baylor College
of Medicine
Investigator, Howard Hughes
Medical Institute*

For her discoveries in neurogenetics,
which contain implications for
Rett Syndrome and Autism



PRIZE PRESENTER

Ursula von Rydingsvard

*Sculptor, Brooklyn, NY
Co-Founder, with Nobel Laureate Paul Greengard,
of the Pearl Meister Greengard Prize*



PAST RECIPIENTS: JOAN STEITZ • BRENDA MILNER • JANET ROWLEY • MARY-CLAIRE KING • SUZANNE CORY
ELIZABETH BLACKBURN • CAROL GREIDER • VICKI LUNDBLAD • GAIL MARTIN • BEATRICE MINTZ
ELIZABETH ROBERTSON • MARY LYON • PHILIPPA MARRACK • NICOLE LE DOUARIN

Introducing the new BD FACSAria™ Fusion

Integrated cell sorting and biosafety.



The fusion of safety,
performance, and sorting.

The BD FACSAria™ Fusion cell sorter is built on the solid foundation of patented technologies, exceptional multicolor performance and ease-of-use that was first brought to the world of sorting by the launch of the BD FACSAria™ cell sorter in 2003.

Now this sorting know-how is combined with best-in-class biosafety expertise to create the BD FACSAria Fusion, a fully integrated advanced cell sorter and biosafety solution for research laboratories.



Helping all people
live healthy lives

The BD FACSAria Fusion has been verified to meet personnel and product protection standards for a Class II Type A2 biosafety cabinet, the National Sanitation Foundation International Standard 49, the European Standard 12469, and the Australian Standard AS 2252.2–2009.

Choose up to six laser wavelengths and 20 detector positions to measure up to 18 colors simultaneously.

Learn more at bdbiosciences.com/go/fusion.

WESTERN BLOT DETECTION SYSTEM

The ScanLater Western Blot Detection System combines Western blot membrane detection with a multimode microplate reader platform, eliminating the need to acquire a separate dedicated Western blot system, saving both lab space and budget. The system is compatible with Molecular Devices' SpectraMax i3 and SpectraMax Paradigm Platforms. ScanLater System uses time-resolved fluorescence (TRF)-based Western blot detection, an optimal detection method that reduces stray excitation light, resulting in lower background noise and higher sensitivity. The system comprises the ScanLater Western Blot Detection Cartridge, ScanLater Western Blot Kit, and image acquisition software powered by SoftMax Pro Software. ScanLater Western Blot Kits contain europium-labeled secondary antibodies designed to work with existing primary antibodies without further optimization. This substrate-free method of Western blot detection not only outperforms traditional chemiluminescence and fluorescence-based Western blot detection, but also allows membrane detection at any time.

Molecular Devices

For info: 800-635-5577 | www.moleculardevices.com/westernblot



ELISA KITS

The new range of SimpleStep ELISA kits have a greatly simplified protocol when compared with standard multistep enzyme-linked immunosorbent assays (ELISAs), providing significant time-savings and ease of use. Offering enhanced performance, SimpleStep ELISA kits are single wash, colorimetric sandwich ELISAs which retain the familiar process and data outputs of a traditional ELISA kit. The kits require no specialized training or instrumentation and, in contrast to standard ELISA, achieve increased accuracy due to reduced sample handling steps. Additionally, a more efficient in-solution binding process provides superior sensitivity and specificity. The SimpleStep kits are ideal for studying intra- or extracellular signaling pathways or for cancer biomarker research. Numerous new kits are being added to the already extensive range each month. The kits are available in convenient off-the-shelf one-, two-, or four-target conformations. Custom multitarget kits are also available, allowing customers to select analyte combinations specific to their research.

Abcam

For info: 888-772-2226 | www.abcam.com/simplestep

MASS DETECTOR

The ACQUITY QDa Detector is the first mass detector to bring high-quality, mass spectral data to chromatographic separations. Designed as a synergistic component of a chromatographic system, the ACQUITY QDa Detector is compatible with ACQUITY UltraPerformance LC (UPLC), ACQUITY UltraPerformance Convergence Chromatography (UPC2), Alliance high-performance liquid chromatography (HPLC), and supercritical fluid chromatography (SFC) and LC-based purification systems. The ACQUITY QDa Detector addresses the barriers of complexity, size, and cost that have hindered the adoption of mass spectrometry for everyday use. It is purposefully designed for analytical scientists who need mass spectral data without the complexity of a mass spectrometer. With the on/off simplicity that analytical scientists have long wanted from mass spectrometry, the ACQUITY QDa Detector fully automates sample analysis and eliminates sample-specific adjustments for certainty in sample results, from user to user and system to system.

Waters Corporation

For info: 800-252-4752 | www.waters.com/separate

AUTOMATED PROTEIN DENATURATION SYSTEM

The new Model 2304 Automated Protein Denaturation System completely automates protein stability determinations using chemical denaturation. Developed to facilitate the formulation of biologics in a safe and stable form, the system uses intrinsic or extrinsic fluorescence to monitor the conformational changes associated with protein unfolding (denaturation) and automatically generates complete protein stability curves. Up to 96 different formulations, process conditions, or individual protein constructs can be evaluated for relative stability, and an individual stability curve generated for each. Sample preparation, data collection, data analysis, and stability report generation are all automated. The free energy (ΔG) of protein unfolding is automatically calculated for each formulation condition or each individual protein construct. Chemical denaturation, a well-established technique, provides reliable thermodynamic values for protein stability and allows solution conditions such as buffer composition, buffer strength, pH, ionic strength, excipient composition, excipient concentration, and protein concentration to be effectively assessed and optimized.

AVIA Biosystems

For info: 413-658-5426 | www.aviabiosystems.com

HRP CHEMILUMINESCENT SUBSTRATE KITS

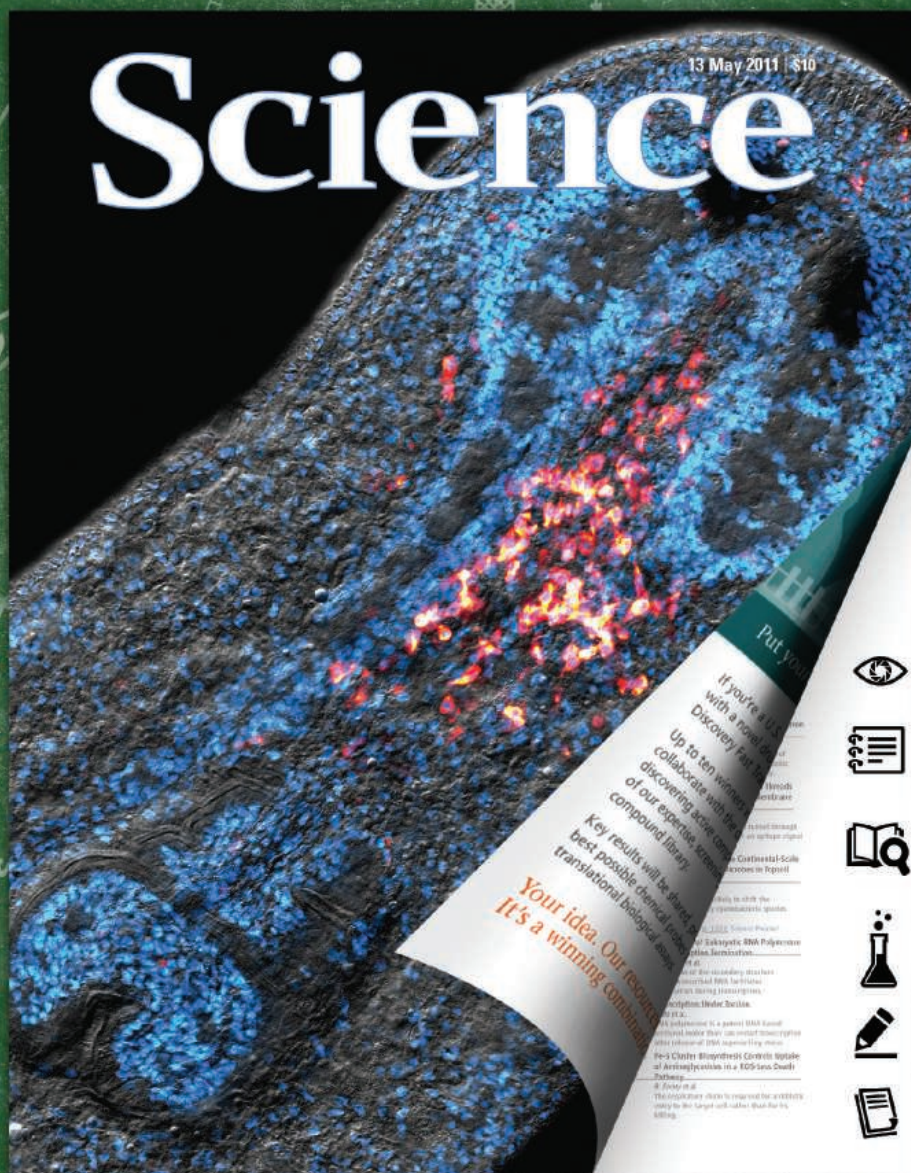
The VisiGlo HRP Chemiluminescent Substrate Kit with picogram sensitivity is now one of three VisiGlo options available after the addition of VisiGlo Prime and VisiGlo Select HRP Chemiluminescent Substrate Kits to their repertoire. The different formulations, from low to high sensitivity, allow HRP detection across a broad range of Western blotting conditions. The new VisiGlo Prime HRP Chemiluminescent Substrate Kit is ideal for accurate protein quantitation, with a linear dynamic range of signal versus protein concentration encompassing over three orders of magnitude. VisiGlo is best suited for moderate- to high-abundance protein detection, while VisiGlo Select offers the most intense signal for use in blotting with low-abundance targets. For sensitivity and accurate quantitation, VisiGlo Prime's wide dynamic linear range is an ideal choice. The chemiluminescent signals of the three VisiGlo options are all compatible with CCD and film imaging. VisiGlo Select also works with fluorescent imaging systems.

AMRESCO

For info: 800-448-4442 | www.amresco-inc.com

Electronically submit your new product description or product literature information! Go to www.sciencemag.org/products/newproducts.dtl for more information.

Newly offered instrumentation, apparatus, and laboratory materials of interest to researchers in all disciplines in academic, industrial, and governmental organizations are featured in this space. Emphasis is given to purpose, chief characteristics, and availability of products and materials. Endorsement by Science or AAAS of any products or materials mentioned is not implied. Additional information may be obtained from the manufacturer or supplier.

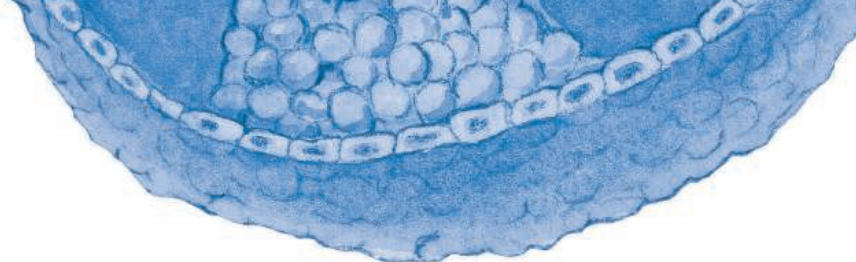


Online tools to help your students analyze a professional research paper!

Tell me and I forget. Teach me and I remember. Involve me and I learn. -- Benjamin Franklin

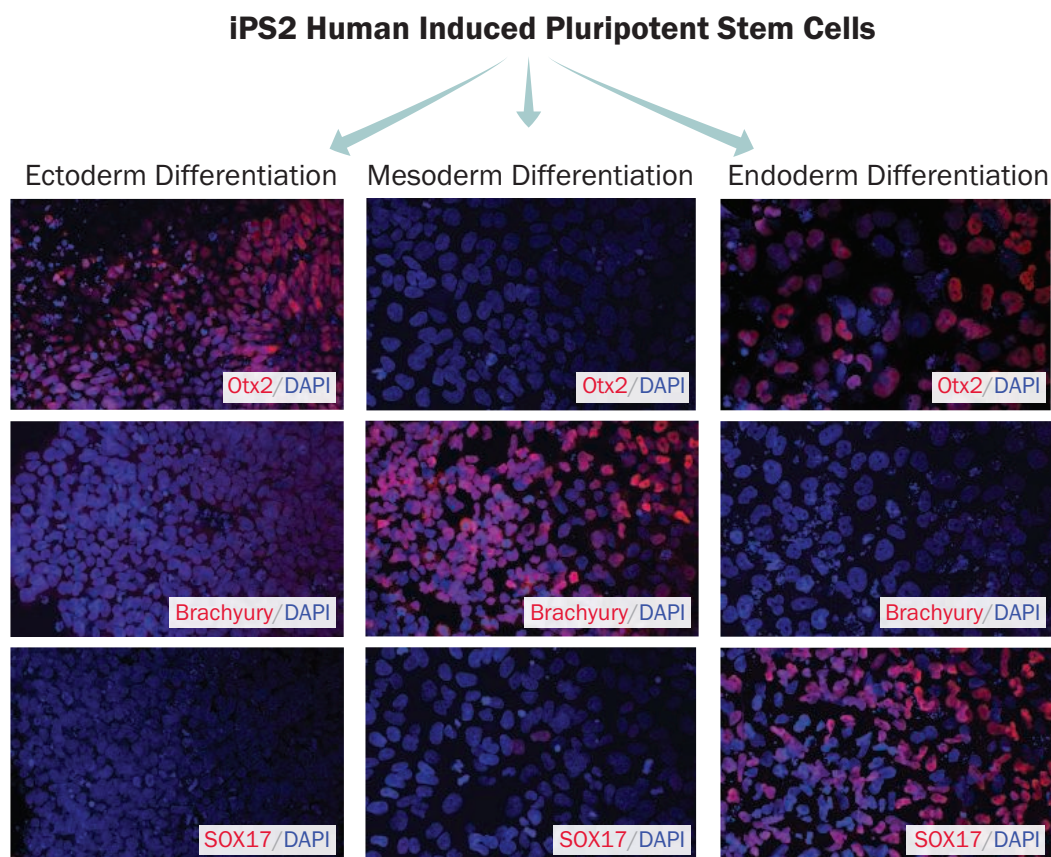
Featuring over 6 research papers at any given time, *Science* in the Classroom is specifically designed to help young researchers understand the structure and workings of professional scientific research.

Learn for yourself how *Science* in the Classroom can help your students deepen their understanding of scientific research. **Visit scienceintheclassroom.org today.**



Move Forward with Confidence

Verify stem cell potency with Functional Identification Kits from R&D Systems



Verification of iPS2 human induced pluripotent stem cells by directed differentiation using R&D Systems Human Pluripotent Stem Cell Functional Identification Kit.

Kits are available for verification of pluripotent, mesenchymal, and neural stem cells

- ✓ Save valuable time and reagents
- ✓ Reduce experimental variation
- ✓ Functionally verify stem cell potency

Find the right tools to verify
potency by stem cell type

[RnDSystems.com/stemcellverification](https://www.RnDSystems.com/stemcellverification)

R&D
SYSTEMS®

There's only one

Science



Science Careers Advertising

For full advertising details, go to ScienceCareers.org and click For Employers, or call one of our representatives.

Tracy Holmes

Worldwide Associate Director
Science Careers
Phone: +44 (0) 1223 326525

THE AMERICAS

E-mail: advertise@sciencecareers.org
Fax: 202-289-6742

Tina Burks

East Coast/West Coast/South America
Phone: 202-326-6577

Marci Gallun

Midwest/Canada
Phone: 202-326-6582

Candice Nulsen

Corporate
Phone: 202-256-1528

Online Job Posting Questions

Phone: 202-312-6375

EUROPE / INDIA / AUSTRALIA / NEW ZEALAND / REST OF WORLD

E-mail: ads@science-int.co.uk
Fax: +44 (0) 1223 326532

Axel Gesatzki

Phone: +44 (0)1223 326529

Sarah Lelarge

Phone: +44 (0) 1223 326527

Kelly Grace

Phone: +44 (0) 1223 326528

JAPAN

Yuri Kobayashi

Phone: +81-(0)90-9110-1719
E-mail: ykobayas@aaas.org

CHINA / KOREA / SINGAPORE / TAIWAN / THAILAND

Ruolei Wu

Phone: +86-1367-1015-294
E-mail: rwu@aaas.org

All ads submitted for publication must comply with applicable U.S. and non-U.S. laws. Science reserves the right to refuse any advertisement at its sole discretion for any reason, including without limitation for offensive language or inappropriate content, and all advertising is subject to publisher approval. Science encourages our readers to alert us to any ads that they feel may be discriminatory or offensive.

Science Careers

From the journal *Science*



ScienceCareers.org



GROUP ON
EARTH OBSERVATIONS



MARTIN-LUTHER-UNIVERSITÄT
HALLE-WITTENBERG

GEO BON (Group on Earth Observations Biodiversity Observation Network) is a "community of practice" within the **Global Earth Observation System of Systems - GEOSS** (<http://www.earthobservations.org/geobon.shtml>). As of January 1st, 2014, the secretariat of GEO BON will be based in iDiv, German Center for Integrative Biodiversity Research (Leipzig, Germany).

Executive Director

(full-time employment, initially limited till September 30th, 2016 with possibility of extension, salary up to Entgeltgruppe 13 TV-L)

We seek highly motivated candidates with a PhD in ecology or a related field, fluency in English and excellent communication skills and experiences with executive leadership in organizations or project management. The successful candidate will be expected to provide visible leadership for GEO BON with the science community, create funding opportunities for GEO BON activities and coordinate the activities of the GEO BON Working Groups and Regional Observation Networks. For further information please visit <http://www.idiv.de/idiv-global/positions> or <http://personal.verwaltung.uni-halle.de/jobs/wissmi/>. Applications are accepted until January 6th, 2014.

Severely disabled persons are encouraged to apply and will be given preference in the case of equal suitability. Women are strongly urged to submit an application.



The UC Davis MIND Institute, School of Medicine, and the Genome Center

invite applications for one or more tenure-track faculty positions in the area of human genetics and genomics. Applicants interested in genomic approaches to autism or related disorders who employ large-scale, technology-driven approaches that complement existing strengths at UC Davis are particularly encouraged to apply. Ideal candidates would combine bioinformatics with wet bench approaches in human studies or animal models. Candidates should be strongly motivated by the biological

and medical importance of their research and should value the opportunity to work in close collaboration with both clinical and research faculty.

The UC Davis MIND Institute (*Medical Investigation of Neurodevelopmental Disorders*) is a collaborative international research center, committed to the awareness, understanding, prevention, care, and cures of neurodevelopmental disorders. Its mission is to find effective treatments and cures for autism and other neurodevelopmental disorders. The MIND Institute is an administrative unit within the UC Davis School of Medicine. The UC Davis Genome Center integrates experimental and computational approaches to address key problems at the forefront of genomics. The Center faculty build on and enhance the unique strengths and unmatched breadth of the life sciences on the UC Davis campus.

Candidates may be at any academic level. At the senior level, we invite applications from prominent scientists with distinguished records of research, including extramural funding, teaching, and leadership in genomics. At the junior level, we invite applications from candidates whose accomplishments in innovative research and commitments to teaching demonstrate their potential to develop into the future leaders in human genetics and genomics.

This position requires a Ph.D., M.D./Ph.D., or equivalent. The appointment will be at the Assistant, Associate or Full Professor level in an appropriate academic department in the School of Medicine. The position will remain open until filled. For fullest consideration, applicants should submit a letter of application, a curriculum vitae, statements of research and teaching interests, and the names of at least five references to the UC Davis Recruit Website <https://recruit.ucdavis.edu/apply/JPF00196> by **January 4, 2014**.

The University of California is an Affirmative Action/Equal Opportunity Employer.

December 2nd, 2013

Group leader positions in the *Imagine* Institute of Genetic Diseases

The new *Imagine* Institute of Genetic Diseases, affiliated with the Necker Enfants malades Hospital campus in the heart of Paris, is inviting applications for group leader positions.

Imagine is an interdisciplinary research center with excellent core facilities for genomics, cell imaging, flow cytometry, bioinformatics, pathophysiology and animal housing for transgenic mice and zebra fish. The new tailor-made building (to be opened in early January 2014) will offer cutting-edge research facilities.

Imagine is affiliated with Paris Descartes University, the INSERM national institute for medical research and the Paris Public Hospitals Group (*Assistance Publique-Hôpitaux de Paris*). It has recently been designated by the French government as a University Hospital Institute (*Institut Hospitalo-Universitaire*, IHU) supported by a Foundation. The Institute focuses on rare diseases, their genetic architecture and life-long outcomes. *Imagine* intends to address unmet basic and clinical research questions related to rare diseases, in order to increase knowledge in a major medical field that is currently insufficiently covered. This will result in the development of new biological concepts, diagnostic tools and innovative therapeutics. *Imagine* has a tradition of high-quality research and provides an outstanding, international research environment and a well-regarded graduate program. The Institute is currently composed of 300 staff members from 21 labs in the fields of genetics, immunology, infectious diseases, hematology, nephrology, developmental defects, metabolic diseases/encephalopathy, dermatology and gastroenterology. Applications can focus on any field directly linked or related to the basis, pathophysiology and treatment of genetic diseases, with special emphasis on:

- 1- Development, stem cells and neuroscience
- 2- Computational biology and/or bioinformatics.

Applications in these two areas will be separately evaluated.

Appointments will be made at a junior or senior level, depending on experience.

Applications should be submitted to Professor Alain Fischer at the address below and must include:

- a full CV, including a list of publications
- past and current research interests (2 pages)
- future research proposals (5 pages)
- letters of recommendation by referees (3 pages in all) should be submitted with the application.

Further information can be found at www.institutimagine.org

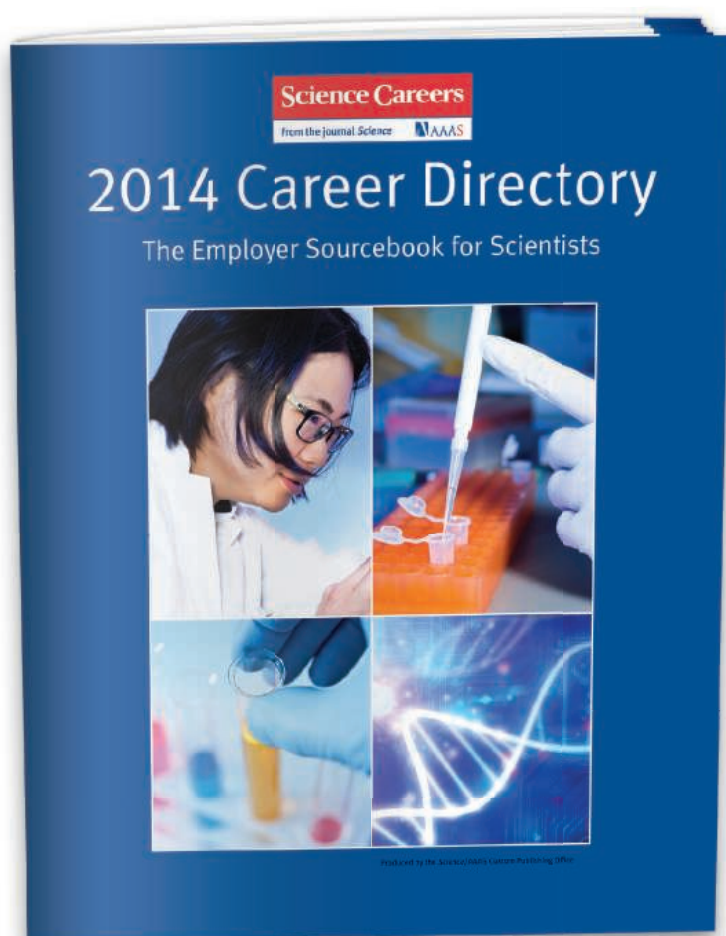
Address: newgroups@institutimagine.org

Applications must be received by May 15th, 2014.

Recruit and Promote Your Brand All Year Long

Science Careers will publish a 2014 Career Directory that will be promoted and distributed all year long.

A combination of career development content alongside your branding ads makes this the perfect place to promote your organization's mission and the areas where you typically recruit. With bonus distributions to meetings and career fairs throughout the year and push marketing including banner ads and e-mail blasts to potential candidates, your company receives ongoing exposure to scientists eager to know about career opportunities.



Benefits to your company

- Opportunity to brand your organization to scientists beyond your normal reach.
- Print bonus distribution of 3,500 copies to career fairs and meetings around the globe.
- Digital copy e-mailed to 100,000 scientists including all *Science Careers* registrants.
- Your logo included in two Career Path newsletters.
- A PDF of the booklet will also be posted on *Science Careers* for one year with marketing to drive readers to the booklet. Marketing includes banners, e-mail blasts, and promotion across AAAS/*Science* newsletters.

To book your ad or for more information:

E-mail: advertise@sciencecareers.org

Or telephone us:

US/Canada/South America:
202-326-6582

Europe/India/Australia/New Zealand/Rest of World: +44 (0) 1223 326500

Japan: +81-(0)90-9110-1719

China/Korea/Singapore/Taiwan/Thailand: +86-1367-1015-294

Reserve space by December 20, 2013

Ad materials due January 10, 2014

Rate: US\$2,995

For recruitment in science,
there's only one **Science**



The Faculty of Medicine at Heinrich-Heine University Düsseldorf and the University Hospital of Düsseldorf invite applications for the permanent position of

Professor (W3) of human genetics
(Succession of Prof. Dr. Royer-Pokora)

The applicant should be a specialist in human genetics, have extensive experience in an executive position, as well as have broad clinical experience in diagnosis and in the counselling of patients with human genetic diseases. The candidate is expected to demonstrate successful acquisition of publication record in nationally or internationally renowned specialized journals and competitive third-party funding. The applicant should also possess an international and innovative research profile. "Habilitation" or an equivalent academic achievement, as well as the ability to lead a department economically and administratively, will be assumed. International research experience will be an advantage. The position combines a professorship with the management of the Department of Human Genetics. An expected future focus will be on the topics of oncology and rare human genetic diseases.

The appointee is expected to cooperate with and contribute to the Comprehensive Cancer Centre (UTZ), which is funded by the German Cancer Research Foundation, and with the different departments of the University hospital (Collaborative Research Centre 974 "Communication and Systemic Impact in Liver Damage and Regeneration"; Clinical Research Group: 217 "Hepatobiliary Transport and Liver Disease"; DFG Research Unit: 729 "Anti-infectious Effector Programmes: Signals and Mediators"; Research Training Groups: 1033 "Molecular Targets of the Aging Process and Strategies for the Prevention of Aging" and IRTG 1902 "Intra- and Interorgan Communication of the Cardiovascular System". Cooperation with the clinical and pre-clinical institutes of the Faculty of Medicine and other research departments of the Heinrich-Heine University of Düsseldorf is also expected.

The Heinrich-Heine University searches for applicants with long-standing experience in teaching human genetics, as well as experience in coordinating and networking of teaching. Appointees should also be willing to further develop the curriculum of the faculty of medicine at HHU and contribute to the School of Oncology in Düsseldorf.

The university will employ a professor with clinical duties on a private contract basis (privatrechtliches Dienstverhältnis) according to an agreement on objectives with the State Ministry of Innovation, Science and Research of North Rhine-Westphalia. Exceptions are possible in case the appointee already holds a tenured professorship (W2/W3, C2/C4). The university or the university hospital will not offer liquidation proceeds. The clinical duties of the professorship will be settled within a separate contract, with a performance-linked salary granted.

Conditions for employment are, in addition to general administrative conditions in accordance with § 36 of the North Rhine-Westphalia University Act (Gesetz über die Hochschulen des Landes Nordrhein-Westfalen), an aptitude for teaching, exceptional competence in research, and additional scientific achievements.

Female candidates are encouraged to apply; they will be given preference in cases of equal aptitude, ability, and professional achievements unless there are exceptional reasons for choosing another applicant.

Applications from suitably qualified severely disabled persons or disabled persons regarded as being of equal status according to Book IX of the German Social Legal Code (SGB –

Soziales Gesetzbuch) are encouraged to apply and will be given preferential consideration in the case of equal aptitude. Heinrich Heine University of Düsseldorf offers a Dual Career Service and is a member of the Rhineland Dual Career Network (Dual Career Netzwerk Rheinland). Further information can be found under www.dualcareer-rheinland.de.

Applications comprising all relevant documents (for further information please see <http://www.medicin.hhu.de/akademische-verfahren/berufungen/informationen-bewerber/informationen-fuer-bewerberinnen-und-bewerber.html>) must be sent in electronic form as PDF (max. 15 MB) within 4 weeks of publication of this announcement to **Professor Joachim Windolf M.D.**, Dean of the Faculty of Medicine at Heinrich-Heine University of Düsseldorf, at the following email address: berufungsverfahren@med.uni-duesseldorf.de.

We are offering a

Postdoctoral Position in Bioinformatics

The Max Planck Institute of Immunobiology and Epigenetics in Freiburg, Germany is offering a Postdoctoral Position in Bioinformatics in the Laboratory of Chromatin Regulation (Head: Dr. Asifa Akhtar). The Position is available for an initial two-year appointment with the possibility of extension.

The MPI in Freiburg is an international research institute at the cross-road of Southern Germany, Switzerland and France. The working language is English. State-of-the-art infrastructure and service units, including transgenesis, mass spectrometry, proteomics, flow cytometry, fly and imaging facilities are available.

Your tasks:

The research focus of the Akhtar laboratory includes mechanisms underlying chromatin and epigenetic regulation. We are particularly interested in X chromosomal regulation using flies and mouse models employing multidisciplinary approaches such as genetics, biochemistry, functional genomics as well as cell biology and structural biology.

We are looking for enthusiastic, highly-motivated, science-driven and experienced postdoctoral fellows to join our team to unravel the molecular mechanisms that regulate gene expression.

Your qualifications:

Applicants should have a PhD or equivalent doctoral degree with at least 3 years of proven research experience in bioinformatics and analyses of genomewide data (ChIPseq, RNA seq). Prior experience in working with *Drosophila* or mammalian models is highly encouraged. Candidates must have a strong publication record. Furthermore, the ability to work in a team, communication skills and experience in the supervision of graduate students are an asset.

Please submit your application, including a statement of research interests, and a CV to our homepage <http://www.ie-freiburg.mpg.de/jobs>.

Please also ask three referees to send recommendation letters directly to schmidl@ie-freiburg.mpg.de.

We offer:

Salaries will be according to postdoctoral fellowships of the Max Planck Society or TVöD and will commensurate with experience.

Application deadline: 15.01.2014

Our Institute investigates the molecular basis of the immune response and other topics of the developmental biology, such as the origin and differentiation of the immune cells as well as the development of vertebrate embryos. Another main focus of the Institute is Epigenetic. This area deals with inheritable traits, which are not caused by changes in the DNA sequence.

Handicapped applicants with equal qualifications will be given preferential treatment. The Max Planck Society seeks to increase the number of women in areas, where they are underrepresented, and therefore explicitly encourages women to apply. A childcare facility is directly attached to the institute.

If you would like to work in a dedicated team, please convince us now by sending us your complete application documents together with your salary expectations and your earliest possible date of joining the Institute.

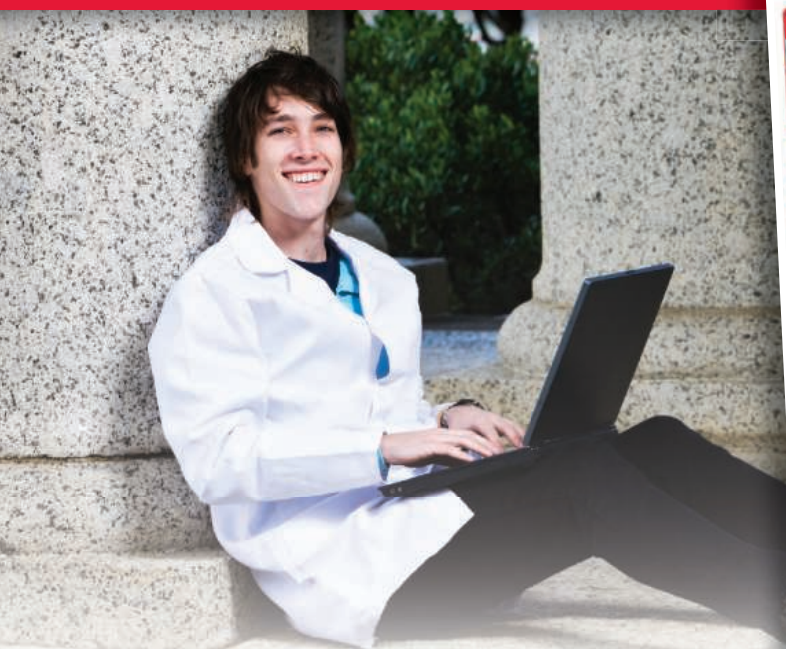
Max Planck Institute of Immunobiology and Epigenetics
Ms. Kanisch

Have we sparked your interest? Please apply online via the Jobmarket on our website. We are looking forward to getting your complete application documents.

<http://www.ie-freiburg.mpg.de/jobs>

For your career in science, there's only one **Science**

A career plan customized
for you, by you.



myIDP.sciencecareers.org



Recommended by leading professional societies and endorsed by the National Institutes of Health, an individual development plan will help you prepare for a successful and satisfying scientific career.



In collaboration with FASEB, UCSF, and the Medical College of Wisconsin and with support from the Burroughs Wellcome Fund, AAAS and *Science* Careers present the first and only online app that helps scientists prepare their very own individual development plan.

Visit the website and
start planning today!
myIDP.sciencecareers.org

In partnership with:



IOWA STATE UNIVERSITY

Helping you become your best.

Faculty Positions in Infectious Diseases

Iowa State University has launched the Presidential High Impact Hires Initiative to support targeted faculty hiring in areas of strategic importance. As part of the initiative, the College of Veterinary Medicine at Iowa State University is seeking qualified candidates for three tenure-track or tenured faculty positions in infectious diseases to strengthen its leadership in animal health, human health, and One Health research. The three faculty positions include two in Translational Health and one in Big Data. The College of Veterinary Medicine has a dynamic faculty representing disciplines of bacteriology, virology, parasitology, immunology, pathology, and public health. Modern laboratory space and animal facilities are available in the college as well as full service large and small animal teaching hospitals. Excellent opportunities exist for collaboration with faculty in other colleges and a number of interdepartmental programs/centers and with researchers at national laboratories and other institutions. The university offers a competitive start-up package and salary.

Translational Health (Assistant, Associate, or Full Professor)

The College of Veterinary Medicine invites applications for two positions at the rank of Assistant, Associate, or Full Professor in Translational Health. The position responsibility statement will include 80% effort in developing and sustaining a vigorous, extramurally funded research program that focuses on infectious diseases in the areas of bacteriology, virology, immunology, pathology, or parasitology. Special emphasis will be given to the areas of research on pathogen-host interaction, disease mechanisms, protective immunity, and translational medicine. 15% effort will be dedicated to the instruction of infectious diseases courses. The remaining 5% effort will include university service components and outreach responsibilities expected of all faculty members. The successful candidates will possess the experience and skills necessary for conducting research, teaching, and mentoring professional and graduate students.

Big Data (Assistant, Associate, or Full Professor)

The College of Veterinary Medicine invites applications for a faculty position at an Assistant, Associate, or Full Professor rank in the area of microbial bioinformatics, pathogenomics, and diagnostic genomics. The position responsibility statement will include 80% effort in developing and sustaining a vigorous, extramurally funded research program that focuses on genomic and bioinformatic approaches to studying microbial infections, pathogen evolution, emergence of disease, or detection of new and emerging pathogens. 15% effort will be dedicated to the instruction of genomics, functional genomics, and bioinformatics courses. The remaining 5% effort will include university service components and outreach responsibilities expected of all faculty members.

For all three positions, a PhD or an equivalent degree in a relevant discipline is required. Demonstrated potential or history for competitive funding and a minimum of two-years postdoctoral training experience are required for an appointment at the Assistant Professor rank. Preference will be given to a nationally or internationally recognized investigator in a relevant field with a record of sustained publication and extramurally funded research for an appointment at the rank of Associate or Full Professor. Review of applications will start on **February 15, 2014** and will continue until the positions are filled. The proposed start date is August 15, 2014 and is negotiable. To submit an application, please visit www.iastatejobs.com and follow the online application instructions for vacancies **131332 (Translational Health)** and **131333 (Big Data)**. Questions regarding the positions should be directed to **Dr. Qijing Zhang, Search Committee Chair. zhang123@iastate.edu; 515-294-9348.**

Iowa State is an Affirmative Action/Equal Opportunity Employer.



Multiple Faculty Hires for a Food Systems Hub at the University of Florida

The University of Florida (UF) announces the availability of seven faculty positions with the aim of forming a "Food Systems Hub" to consolidate and synergize campus-wide interests and efforts in food security, food safety, and food transportation. This interdisciplinary effort includes positions in the College of Engineering, College of Public Health and Health Professions, The Florida Climate Institute, the Emerging Pathogens Institute, and the Institute of Food and Agricultural Sciences (IFAS). Of particular interest are individuals with capabilities in systems modeling that can advance integrative thinking and research to link existing disciplinary-specific strengths in food safety and security at UF. We anticipate such integration will be key to making high-impact scientific advances in understanding the complexities of food systems, and providing a more holistic approach to feeding a growing population in a changing world. Applications of the Food Systems Hub will include strategic foresight assessments of decisions on investments in technologies for sustainable food systems and on policies to help meet future societal needs for safe and nutritious food.

Areas of high interest include, but are not limited to:

- Socio-economic assessment and modeling of food systems at regional to global scales
- Integrative food systems modeling
- Crop/livestock modeling of responses to climate variability, extreme events, and climate change
- Agro-ecological issues as they affect the food supply, production, and land use
- Microbial risk analysis as a predictor of food safety
- Modeling pests and diseases of crops and livestock
- Incorporating genomics information in modeling food production
- Epidemiology and surveillance
- Systems engineering to address food security, safety, processing, and distribution
- Modeling of human nutritional & health impacts of alternative food systems and policies
- Application of technologies and practices that address food safety, security, processing and distribution

Successful candidates for these positions will have a proven track record of publication in top journals, recognition as current or emerging leaders in their disciplines, demonstrated ability to establish or work effectively in interdisciplinary collaborations, and success in obtaining significant extramural funding.

Interested individuals may self-nominate or be nominated by their peers by submitting a letter of interest, along with a brief summary of research accomplishments and ongoing research, and a Curriculum Vitae to: **Douglas L. Archer, Chair, Food Hub Steering Committee, 1022 McCarty Hall, PO Box 110200, Gainesville, FL 32611-0200; dlarcher@ufl.edu.**

This will be a rolling search for these positions and we anticipate inviting potential candidates to Gainesville present seminars in January and February 2014. Interviews will continue until all positions are filled.

The University of Florida is an Equal Opportunity Institution dedicated to building a broadly diverse and inclusive faculty and staff.



AAAS is here – helping scientists achieve career success.

Every month, over 400,000 students and scientists visit ScienceCareers.org in search of the information, advice, and opportunities they need to take the next step in their careers.

A complete career resource, free to the public, *Science Careers* offers a suite of tools and services developed specifically for scientists. With hundreds of career development articles, webinars and downloadable booklets filled with practical advice, a community forum providing answers to career questions, and thousands of job listings in academia, government, and industry, *Science Careers* has helped countless individuals prepare themselves for successful careers.

As a AAAS member, your dues help AAAS make this service freely available to the scientific community. If you're not a member, join us. Together we can make a difference.

To learn more, visit aaas.org/plusyou/sciencecareers





THE MOLECULAR & BEHAVIORAL
NEUROSCIENCE INSTITUTE
UNIVERSITY OF MICHIGAN

FACULTY POSITION

The Molecular and Behavioral Neuroscience Institute (MBNI) at the University of Michigan is recruiting an Assistant Professor (tenure track) whose research program focuses on fundamental aspects of nervous system development and function. We are especially interested in candidates applying molecular, cellular and genetic techniques to investigate mechanisms underlying synaptic plasticity, neural circuits, behavior or disease. We seek highly motivated and interactive individuals that will establish an internationally recognized, independently funded research program. Applicants must have a Ph.D. and/or M.D. and a strong record of research accomplishments. For more information on the MBNI see: <http://www.mbni.med.umich.edu/mbni/search.html>.

Interested candidates should send cover letter, curriculum vitae and a 3-5 page statement of current and future research directions as a single PDF to MBNI_2014@umich.edu. Candidates should also arrange to have 3 letters of recommendation sent as PDFs to the above email address. Applications and letters of recommendation will be considered up until **February 1, 2014**.

Women and underrepresented minorities are encouraged to apply. The University of Michigan is supportive of the needs of dual career couples and is an equal opportunity employer.

Northeastern University

College of Engineering



Learn more
bit.ly/NUCOErecruit
northeastern.edu/coe

53 ENGINEERING FACULTY HIRES SINCE 2010...and counting

Northeastern's College of Engineering seeks outstanding faculty candidates for appointments at the associate or full professor level, both within the college and in conjunction with interdisciplinary positions across the university. We will also consider exceptional candidates at the assistant professor level. Successful applicants will lead internationally recognized research programs that complement existing expertise aligned with one or more of Northeastern's strategic research themes—health, security, and sustainability—or in the enabling fields of nanotechnology and materials, and data science. Our Boston campus facilitates collaborations with major medical centers, research labs, neighboring academic institutions, and industry.

Northeastern is an Affirmative Action/Equal Opportunity Educator and Employer committed to excellence through diversity.



MAX-PLANCK-GESELLSCHAFT

Max Planck Institute for Developmental Biology

The **Max Planck Institute for Developmental Biology** in Tübingen is seeking candidates for a position as

DEPARTMENT DIRECTOR

in the area of Organismic Biology, including evolutionary biology, ecology and interactions among organisms. The successful candidate will be expected to have a strong molecular and mechanistic research profile in these areas and to bridge to existing Departments at the Institute.

The Max Planck Institute for Developmental Biology has a general interest in understanding biological complexity, from protein evolution and molecular machines to development and evolution. The Institute addresses these questions using various methods, which all focus on the molecular principles of life.

The Max Planck Society for the Advancement of Science is an independent, non-profit research organization that primarily promotes and supports basic research. The Max Planck Society is an equal opportunity employer and is committed to diversity and inclusion in all aspects of recruiting and employment. The Max Planck Society is aiming at increasing the percentage of women among its scientific leadership, particularly at the director level. Therefore, we strongly encourage expression of interest from and nominations of qualified female scientists.

Applications, letters of interest, and nominations of candidates should be sent to the Managing Director, Ralf J. Sommer, Max Planck Institute for Developmental Biology, Spemannstrasse 37, 72076 Tübingen, Germany (ralf.sommer@tuebingen.mpg.de) by **January 31st, 2014**.

POSITIONS OPEN

ASSISTANT/ASSOCIATE PROFESSOR
Department of Nutrition and Food Science
College of Agriculture and Natural Resources
University of Maryland

The Department of Nutrition and Food Science at the University of Maryland, College Park invites applications for a nine-month, tenure-track position as assistant or associate professor in nutrition.

Responsibilities: (1) The successful candidate will be expected to sustain/develop an independent nutrition research program that focuses on the role of nutrition and dietary factors in the etiology, prevention, and treatment of chronic diseases such as obesity, cardiovascular disease, diabetes, or cancer. (2) This individual will develop an outstanding research program that employs modern laboratory and/or clinical approaches to prevent and ameliorate human chronic disease by dietary means. (3) The location of the university provides excellent opportunities for collaboration with scientists at several nearby institutions including the National Institutes of Health, the U.S. Department of Agriculture Beltsville Human Nutrition Research Center, and the University of Maryland Medical School. (4) The successful candidate must also have demonstrated ability or potential to teach and mentor graduate students as well as undergraduate dietetics and nutrition students effectively, possess excellent interpersonal and communication skills, and have the ability to work with others in a collegial team atmosphere.

Qualifications: Required—Candidates must have an earned doctorate in nutrition or related field. Preferred—postdoctoral experience is desirable; Certification as a Registered Dietitian is desirable.

Salary/Benefits: Salary will be commensurate with education and experience. The University of Maryland offers an extensive benefits package.

Apply online at **website: <https://jobs.umd.edu>** by sending a current (signed) curriculum vitae, representative publications, official transcripts, and the names and contact information for three professional references (include mailing address, telephone number, and e-mail address), and a cover letter describing the candidate's strengths, accomplishments, and future research plans. If you have further questions contact **David K. Y. Lei**, Chair of Search Committee, at **e-mail: dlei@umd.edu**. Closing Date: January 25, 2014 or until an acceptable candidate is identified.

The University of Maryland is an Equal Opportunity/Affirmative Action Employer. Minorities and Women are encouraged to apply.

☒ **More scientists agree—we are the most useful website.**

Science Careers

From the journal *Science* AAAS

www.ScienceCareers.org

Get your questions answered.
Careers Forum
www.ScienceCareers.org

Download your free copy today.

ScienceCareers.org/booklets



From technology specialists to patent attorneys to policy advisers, learn more about the types of careers that scientists can pursue and the skills needed in order to succeed in nonresearch careers.

Science Careers

From the journal *Science* AAAS